Collective and Collisional Properties of the Rubidium Quantum Gas

ACADEMISCH PROEFSCHRIFT

ter verkrijging van de graad van doctor
aan de Universiteit van Amsterdam,
op gezag van de Rector Magnificus
prof. mr. P.F. van der Heijden
ten overstaan van een door het college voor promoties ingestelde
commissie, in het openbaar te verdedigen in de Aula der Universiteit
op dinsdag 11 oktober 2005, te 10:00 uur

door

Christian Buggle
geboren te Hannover, Duitsland

Promotiecommissie:

Promotor	Prof. Dr. J.T.M. Walraven
Overige leden	Prof. Dr. M. Leduc Prof. Dr. G.V. Shlyapnikov Prof. Dr. H.B. van Linden van der Heuvell Prof. Dr. M.S. Golden Prof. Dr. M. Weidemüller
Faculteit	Faculteit der Natuurwetenschappen, Wiskunde en Informatica

Cover: Exploded schematic view of the trap-coil arrangement, combined with CCD images from the experiment.

The work described in this thesis is part of the research programme of the Stichting voor Fundamenteel Onderzoek der Materie (FOM), which is financially supported by the Nederlandse Organisatie voor Wetenschappelijk Onderzoek (NWO).

The work described in this thesis was carried out at the
FOM Institute for Atomic and Molecular Physics (AMOLF)
Kruislaan 407, 1098 SJ Amsterdam, The Netherlands.

This thesis was written at the
Van der Waals-Zeeman Institute, University of Amsterdam
Valckenierstraat 65-67, 1018 XE Amsterdam, The Netherlands.

A digital Version of this thesis can be downloaded from
http://staff.science.uva.nl/∼walraven

Ουκοῦν κάν
ει πρὸς αυτὸ τὸ φῶς αναγκάζοι αυτὸν βλέπειν,
αλγεῖν τε αν τὰ ομματα καὶ φεύγειν
αποστρεφόμενον πρὸς εκεῖνα, α δύναται καθορᾶν
καὶ νομίζειν ταῦτα τῶ όντι σαφέστερα τῶν δεικνυμένων;

And is it not true,
that if one might force one to watch into the light itself,
that he suffers pain in his eyes and that he flees
turning back to what he is capable of seeing,
believing that this was more certain than what he has been shown?

Plato

Contents of this thesis have been published in:

Chapter 4
Shape oscillations in non-degenerate Bose gases - transition from the collisionless to the hydrodynamic regime, Ch.Buggle, P.Pedri, W.von Klitzing, and J.T.M.Walraven, arXiv:cond-mat/0505136, accepted for publication in Physical Review A (2005)

Chapter 5
Interferometric Determination of the s and d-Wave Scattering Amplitudes in ^{87}Rb, Ch.Buggle, J.Léonard, W.von Klitzing, and J.T.M.Walraven, Physical Review Letters **93**, 173202-1 (2004)

Chapter 6
Focusing of Bose-Einstein condensates in free flight,
I.Shvarchuck, Ch.Buggle, W.von Klitzing, and J.T.M.Walraven, in: Interactions in ultracold gases, Wiley-VCH, ISBN 3-527-40389-2 pg. 415 (2003)

Other publications of the author:

Hydrodynamic clouds and Bose-Einstein Condensation, Ch.Buggle, I.Shvarchuck, W.von Klitzing and J.T.M.Walraven, Journal de Physique IV France **116**, EDP Sciences, ISBN 2-86883-718-2, pg. 211-217 (2004)

Hydrodynamic behavior in expanding thermal clouds of ^{87}Rb, I.Shvarchuck, Ch.Buggle, D.S.Petrov, M.Kemmann, W.von Klitzing, G.V.Shlyapnikov, and J.T.M.Walraven, Physical Review A **68**, 063603 (2003)

Bose-Einstein condensation in a magnetic double-well potential, T.G.Tiecke, M.Kemmann, Ch.Buggle, I.Shvarchuck, W.von Klitzing and J.T.M.Walraven, Journal of Optics B: Quantum and Semiclassical Optics **5** S119-S123 (2003)

Bose-Einstein condensation into non-equillibrium states, studied by condensate focusing, I.Shvarchuck, Ch.Buggle, D.S.Petrov, K.Dieckmann, M.Zielonkowski, M.Kemmann, T.G.Tiecke, W.von Klitzing, G.V.Shlyapnikov, and J.T.M.Walraven, Physical Review Letters **89**, 270404-1 (2002)

Low-cost setup for generation of 3 GHz frequency difference phase-locked laser light, F.B.J.Buchkremer, R.Dumke, Ch.Buggle, G.Birkl, and W.Ertmer, Review of Scientific Instruments **79**, 3306 (2000)

Previous thesis for attainment of title "Diplom-Physiker":

Construction of a miniaturized storage ring for neutral atoms,
Diploma thesis under the supervision of Prof.Dr. W.Ertmer, University of Hannover, Germany (2000) (text in German language)

Preface

The work, described in the following does not stand on it's own, it is in fact the third Ph.D. thesis, that has been worked out using the experimental setup for Bose-Einstein condensation at the AMOLF institute under the supervision of Professor J.T.M. Walraven. The work described herein is based on the the achievements of my preceding colleges, and this short historical summary shall link the efforts together.

The construction of the setup was started in April 1996 by Kai Dieckmann as a Ph.D. student together with Matthias Weidemüller as a post-doc at the University of Amsterdam. The experiment moved to AMOLF in December 1996, where in March 1997 the first MOT was achieved, only shortly before Matthias Weidemüller left the group. A major development, the ^{87}Rb source MOT for the loading of the main MOT, was documented in *Two-dimensional magneto-optical trap as a source of slow atoms*, Phys. Rev. A **58**, 3891 (1998). Igor Shvarchuck joined the group as a second Ph.D. student in October 1997. In February 1999 Martin Zielonkowski started his term as post-doc, and it was in 2000 that the first BEC was achieved. A newly designed key-component of the experiment was the main cooling laser source, described in the publication *Broad-area diode-laser system for a rubidium Bose-Einstein condensation experiment*, Appl. Phys. B **71**, 475-480 (2000). Wolf von Klitzing joined the group as a second post-doc in September 2000, shortly before Martin Zielonkowski left AMOLF in December 2000. In February 2001 Kai Diekmann promoted to Ph.D. after having summarized the building process of the experiment with a detailed description in his thesis **Bose-Einstein condensation with high atom number in a deep magnetic trap**. He left the group only a few weeks later.

On the very day of Kai Dieckmanns defense, I joined the group in February 2001. Minor optimizations were done on the apparatus in the following and the formation of Bose-Einstein condensates under the boundary condition of high atom numbers in the thermal cloud could be investigated, resulting in the publication *Bose-Einstein condensation into non-equillibrium states, studied by condensate focusing*, Phys. Rev. Lett. **89**, 270404-1 (2002). The BEC-focusing technique, proposed in this experiment, was also described in the workshop proceedings *Focusing of Bose-Einstein condensates in free flight*, Interactions in ultracold gases, Wiley-VCH, ISBN 3-527-40389-2 pg. 415 (2003). In September 2001 Mark Kemmann joined the group as a third Ph.D. student. The experiments continued with the observation of the expansion behavior of thermal clouds in the hydrodynamic regime, resulting in the publication *Hydrodynamic behavior in expanding thermal clouds of ^{87}Rb*, Phys.Rev.A **68**, 063603 (2003). Igor Shvarchuck described the experiments summarized in the previous 3 publications to greater detail in his Ph.D. thesis **Bose-Einstein condensation into non-equilibrium states** (2003)

and was promoted to Ph.D. in May 2003. Mark Kemmann unfortunately decided to quit from the project in July 2003.

The experiments continued in the direction of hydrodynamic effects, i.e the observation of the oscillation behavior of thermal clouds. At the same time the trap modulation technique was implemented into the setup, which is described in the publication *Bose-Einstein condensation in a magnetic double-well potential* J. Opt. B: Quantum Semiclass. Opt. **5** (2003) S119-S123. This method was technically worked out for use in the oscillation experiments as well as for the s- and d-wave collision in the course of 2003. Acquisition of systematic measurements was first focused on the quadrupole oscillations and then on the collisions. During this process Jeremi Léonard joined the group as Post-Doc in March 2004. The final experiments on the collisions of two Bose Einstein condensates were historically conducted after the oscillation experiments, namely February till May 2004, but still published before in *Interferometric Determination of the s- and d-Wave Scattering Amplitudes in* ^{87}Rb, Phys. Rev. Lett **93**, 173202-1 (2004). The publication of the results of the quadrupole oscillation followed in *Shape oscillations in non-degenerate Bose gases - transition from the collisionless to the hydrodynamic regime*, submitted to Phys. Rev. A in May 2005. As a third, independent line of experiments, the BEC focusing technique was more systematically investigated in the time between May and July 2004, but none of its results was published. These 3 major experiments and all changes done on the set-up after Igor's leave are described in **this thesis**.

The setup was shut-down in July 2004 and in the following disassembled in order to be moved to the University of Amsterdam, which is the reason, why the publications had to follow the experiments with some delay. Since no other Ph.D. student was working on the setup at that moment (Paul Cleary (Ph.D.) and Steve Gensemer (Post-Doc) had joined the group during summer, but they did not work on the BEC-setup), no further thesis will be published with contents involving BEC experiments conducted at AMOLF. Both Post-Docs, that were present during the last experiments performed with the apparatus, left Amsterdam before the writing of this thesis, Wolf von Klitzing in September, Jeremi Léonard in December 2004. Therefore, one may consider this trilogy of theses, with this one being the third, as a closed description of all experimental measurements and major building efforts, that have been carried out at the AMOLF institute.

Electronic copies of all mentioned theses can be downloaded from the groups homepage, which is at the moment (August 2005) staff.science.uva.nl/∼walraven/. For physical copies contact Prof. J.T.M. Walraven or the authors themselves.

Contents

Chapter 1
Introduction

1.1 Background

The occurrence of Bose-Einstein condensation (BEC) was predicted by A. Einstein as early as 1924, as a consequence of the work of S.N. Bose, out of statistical considerations [Bose24, Eins24]. The consequence of their argumentation is, that if an ensemble of particles, that obey Bose-statistics, is sufficiently cold and sufficiently dense, a major fraction is not contained in the classical, thermal distribution but traverses into the lowest quantum mechanical state. This high occupation of a quantum mechanical state in a statistical consideration (Quantum mechanics was still under development during that time [Beth99]) was the only way to explain, what would happen to the particles that could not be contained in the thermal distribution [Eins25].

The importance of this concept shows in the wide-spread application: The superfluidity of liquid helium is considered the result of Bose-Einstein condensation of a part of the helium into a single quantum state [Legg99]. Also superconductivity is considered the result of the presence of pairs of electrons (Cooper pairs) which act as Bosons and form a Bose-Einstein condensate [Bard57]. This concept of composite Bosons plays also a role in nuclear physics and astronomy, where pairing and Bose-Einstein condensation of nucleons allows explanation of excitation spectra of the nucleus; also superfluidity in neutron stars should be mentioned [Dean03, Mish97, Kapl02].

The historical development in the course of the 20th century is closely linked to the investigation of superfluidity in liquid Helium [Legg04]. However, the observation of the Bose-condensed fraction is hindered by high atom densities, which results in strong interactions and suppresses high condensate fractions.
All other substances condense to solids at low temperatures before Bose-Einstein condensation sets in. An alternative approach became realistic in the mid 70's, when Etters and co-workers calculated, that in spin-polarized hydrogen the attractive interaction would be too weak to form a bound state, and the system would remain metastable and gaseous for the time of the experimental observation [Ette75]. This turned the focus of research to spin polarized hydrogen and confinement of cold clouds of atomic hydrogen at low densities. Successful stabilization of spin-polarized hydrogen was first reported by I.F. Silvera in 1980 [Silv80] and first wall-free magnetic trapping by H.F. Hess in 1987 [Hess87]. First attempts to reach Bose-Einstein condensation in atomic hydrogen were based on cryogenic cooling, magnetic trapping and subsequent evaporative cooling [Hess86, Roij88, Masu88, Luit96]. However, subsequent analysis of the relaxation kinetics showed that the condensate fraction is in the case of hydrogen marginal [Hijm93, Seti93]. Moreover, evaporative cooling in the cryogenic geometries was hindered by low dimensionality [Pink98]. It took until 1998, before the first successful realization of a BEC of atomic hydrogen could be reported [Frie98].

In the mean time, the development of laser cooling techniques, magnetic trapping of alkali atoms [Migd85] and forced, rf-induced evaporative cooling [Davi95a] had allowed the successful realization of BEC in Rubidium [Ande95], Sodium [Davi95b] and Lithium [Brad95] in 1995. In the case of hydrogen, laser cooling is difficult to apply, due to the lack of sufficiently strong light sources at 122nm still today [Seti93, Eike01]. These break-throughs of the alkali gases were awarded Nobel prices in 1997 to S. Chu, C. Cohen-Tannoudji and W.D. Phillips for laser-cooling [Phil98], and in 2001 to E.A. Cornell, W. Ketterle, and C.E. Wieman for Bose-Einstein condensation [Corn02]. This success triggered a rapid expansion of this subdiscipline of physics. Within the recent years, also Bose-Einstein condensation of larger objects, i.e. molecules was shown [Grei03, Joch03b, Zwie03].

The particular importance of quantum gases and Bose-Einstein condensation lies in the fundamental concept, that is planted in many-body theory and quantum mechanics. But also first applications like clocks [Weit94, Hind99b, Sant99] and atom-interferometers [Gust97, McGu02] are under development. A particular advantage of this field lies in the exclusive possibility, to make direct images of a quantum-mechanical waveform [Andr97].

Recent developments of this experimentally relatively young field point into the direction of exploiting the advances in controlled manipulation of ultra-cold thermal or Bose-condensed clouds with the help of radiative or magnetic forces, e.g. in the formation of optical lattices to tailor model crystals [Grei02].

Another specific aspect of this technology is the isolation of the investigated cloud from the environment: a BEC of alkali vapor rests at a temperature of $\approx 1\mu$K in a magnetic field only centimeters apart from the vacuum container wall at room temperature $\approx$ 300K. This makes quantum gases ideal objects of investigation even prior to the onset of Bose-Einstein condensation. The atom number and cloud temperature can be extremely well controlled by high precision evaporation, while on the other hand, 'relatively' high densities of up to 10^{15} particles per cm^3 can be achieved (which is still very small as compared to the atmospheric average density of 10^{19}cm^{-3}). For typical collisional cross sections, this density regime lies in the cross-over regime between hydrodynamic and collisionless behavior, which is an interesting regime in its own right.

Direct observation of the scattering behavior in the ultra-low temperature regime [Datz99] forms the low-temperature limit of accelerator experiments [Burn02]. Further, the atomic scattering properties in these systems can be tuned by varying the containing magnetic fields [Inou98]. The exploitation of the coherent properties of matter waves raises analogies with applications of laser-light: elements for beam shaping and manipulation ('atom-optics') [Roac95, Hols97, Lau99, Bloc01, Birk01] as well as continuous sources of coherent matter waves ('atom-lasers') [Pfau02, Laha04] are under development.

1.2 This thesis

This thesis addresses three different lines of independent research topics. In the first two chapters, the fundamentals of this particular experimental device are addressed in both theoretical and technological aspects. Each of the remaining chapters addresses one of the mentioned specific experiments.

In chapter 2 we present some basic theoretical aspects of experiments with ultra-cold gases, where a selection is focused on the use in the experiments of the following chapters. The fundamentals of thermal clouds in harmonic traps both in-trap and in expansion is presented for use in the observation of thermal, hydrodynamic clouds in chapter 4 and the behavior on release from the trap, addressed in chapter 6. The fundamentals of the Bose-Einstein condensed state both in-trap and in expansion are presented for use in the collision experiment, presented in chapter 5 (as it is conducted with BEC's) and the matter wave focusing experiment presented in chapter 6. An overview of the quantum mechanical treatment of ultra-cold collisions is presented, as it forms the basis for the BEC-collision experiment, presented in chapter 5.

Chapter 3 gives a summary of the devices and methods that are used in the path towards the creation of ultra-cold thermal clouds and Bose-Einstein condensates, as this is common to all experiments of this thesis. Further, descriptions of the devices, that have been added or rebuilt since the writing of the thesis by Igor Shvarchuck are given. Details of the experimental device, that have been presented before in [DiecTh] and [ShvaTh] are neglected.

Chapter 4 is dedicated to the collective behavior in shape oscillations of thermal clouds in the cross-over from collisionless to hydrodynamic regime. The technological progress in recent years has increased the typical atom numbers and density (e.g. the number of atoms in the JILA-BEC from $2\,10^3$ in [Ande95] to $3.5\,10^6$ in [Simu05]), usually aimed at more successful evaporation and higher atom numbers in the BEC. With rising density in the trapped vapors or by tuning the collisional properties [Ties93, Fedi96b, Moer96, Mari98], the collective behavior can venture into the crossover region towards hydrodynamic behavior. In such cases, the collective behavior shows collisionally hydrodynamic behavior, which is closely related to the superfluid hydrodynamics of the degenerate state in both Bosonic and Fermionic systems. Great care must be taken, to enable a clear distinction in the analysis of experiments. Theoretical descriptions of collisional hydrodynamics in the cross-over regime have been developed in the recent years. First experiments, that allow a fully conclusive confirmation of the underlying theory are presented here.

Chapter 5 addresses the scattering behavior of colliding BECs with the goal of determination of the s-wave scattering length. The collisional properties of a gas is the most important material constant to be investigated prior to any further experiment in the ultracold temperature regime. The scattering behavior in the zero-temperature limit is expressed in the s-wave scattering length. Its sign and value is decisive for thermalization and evaporation (the essential technique to achieve Bose-Einstein condensation), the stability of the formed BEC [Kaga96] and the strength of the mean field, that defines its collective properties. The importance of the scattering length is indicated in more

detail in chapter 2. Next to being the first direct imaging of quantum mechanical d-wave scattering of colliding BEC's (direct imaging of s-wave scattering has been reported in [Chik00] (CCD-image) and [Gibb95] (velocity distribution), d-wave scattering in thermal clouds parallel to the observation in this group [Thom04]), a new method to extract the scattering length is presented.

Chapter 6 describes a technique for matter wave focusing in free expansion, in short also called: BEC-focusing. The investigation of the most intriguing feature of Bose-condensed clouds, the internal phase coherence, is one of the key interest and the most direct link to the theory building of quantum mechanics in experiments with Bose-Einstein condensates. The internal phase coherence of a single BEC is difficult to extract from in-trap images, because the chemical potential suppresses phase distortions to appear as observable density fluctuations. BEC-focusing is presented as a method to probe the internal state of a BEC, but also as a tool in quantum optics. This principle was developed before and presented partly in [ShvaTh], but the focusing effect was not triggered actively. In this part the first results on an *active* BEC focusing technique are presented along with a detailed description of the underlying theory.

Chapter 2
Theoretical aspects of ultra-cold gases

In the 80 years following the prediction of Bose-Einstein condensation and preceding the presentation of this thesis, a very rich construct of theory has been developed, to describe the quantum-degenerate state of atomic and molecular gases at ultra-low temperatures. In this chapter a summary of the basics will be given to introduce the notation and to build upon in the next chapters.

2.1 Classical limit

In the classical theory of gases the concept of phase space has been developed as a tool, to describe the development of an ensemble of particles in time. In this concept, the state of any 3 dimensional distribution of particles is represented as a 6-dimensional volume (3-space dimensions plus 3-momentum dimensions), and any dynamic development from one configuration to another must preserve certain quantities as stated in Liouvilles theorem [Cha-Cow, LandauS].

In the ideal gas limit, i.e. the assumption of interaction free particles, the energy of a cloud of particles is distributed according to the Maxwell-Boltzmann statistics

$$f(E) = \mathcal{C} \exp\left(\frac{-E}{k_B T}\right), \tag{2.1}$$

where $\mathcal{C}$ is a normalization constant. For the case of a free gas (no potential energy) all energy is included in kinetic energy $\frac{1}{2}mv^2$ and we have the well known thermal velocity distribution

$$f(v) = \mathcal{C}' 4\pi v^2 \exp\left(\frac{-mv^2}{2k_B T}\right), \tag{2.2}$$

which is a good approximation only for systems of very big real-space size. This is because integrating a distribution over phase space should result in the particle number, but in this case the spatial dimension is unbounded and therefore its integral value is infinitely large.

2.1.1 Trapped case

By adding a harmonic trapping potential of the form $U(\vec{r}) = \sum_j \frac{1}{2}m\omega_j^2 r_j^2$, one adds potential energy to the kinetic energy

$$E = \sum_j \frac{1}{2}mv_j^2 + \sum_j \frac{1}{2}m\omega_j^2 r_j^2 \quad (j = x, y, z), \tag{2.3}$$

and the phase space distribution is given by

$$f_j(r_j, v_j) = \mathcal{C} \exp\left(\frac{-mv_j^2 - m\omega_j^2 r_j^2}{2k_B T}\right) = \mathcal{C} \exp\left(\frac{-r_j^2}{r_0^2} + \frac{-v_j^2}{v_0^2}\right), \tag{2.4}$$

where r_0 and v_0 are the thermal $1/e$-sizes of position and velocity, given by

$$r_0 = \sqrt{2k_BT/(m\omega_j^2)} \quad \text{and} \quad v_0 = \sqrt{2k_BT/m}. \tag{2.5}$$

The term "thermal $1/e$-size" refers to the mathematical form of equ.(2.4), which is a Gaussian. A thermal cloud in a harmonic trap appears as an object with this density profile. If the harmonic frequencies ω_j are known, one can thus determine the temperature directly from the density profile in the trap.

2.1.2 Expanding clouds

In the experimental device, described later, it is possible to instantly remove the confinement, and observe the development of the density profile in free expansion. Also from this time development the temperature can be deduced, because the velocity distribution is equal for any point in real space in the trap. Since in the ideal case the atoms are assumed to have no interaction, the velocity distribution will not change during expansion and the time-development of the real space density distribution can be calculated by a convolution integral of the initial cloud distribution with the velocity distribution. All axes decouple and each axis j takes the form

$$n_j(r_j,t) = n_0 \iint \exp\left(\frac{-r_j'^2}{r_{j,0}^2} + \frac{-v_j^2}{v_{j,0}^2}\right) \delta(r_j - r_j' - v_j t)\, dr_j' dv_j, \tag{2.6}$$

where the $r_{j,0}$ and $v_{j,0}$ are the $1/e$-sizes in real and velocity space and n_0 is the peak density, given by the normalization of the 3D volume to the particle number. For convenience, we leave out the index j in the following. We calculate further

$$\begin{aligned} n(r,t) &= \int n_0 \exp\left(\frac{-r'^2}{r_0^2} + \frac{-(r-r')^2}{(t\,v_0)^2}\right) dr' && (2.7)\\ &= \int n_0 \exp\left(-r'^2\left(\frac{1}{r_0^2} + \frac{1}{t^2v_0^2}\right) + \frac{2\,r\,r'}{t^2v_0^2} - \frac{r^2}{t^2v_0^2}\right) dr'. && (2.8) \end{aligned}$$

We define the abbreviation

$$A^2 = \left(\frac{1}{r_0^2} + \frac{1}{t^2v_0^2}\right), \tag{2.9}$$

expand the second term and a zero and continue

$$n(r,t) = \int n_0 \exp\left(-(r'A)^2 + 2\,r'\,A\left(\frac{r}{At^2v_0^2}\right) - \left(\frac{r}{At^2v_0^2}\right)^2 + \left(\frac{r}{At^2v_0^2}\right)^2 - \frac{r^2}{t^2v_0^2}\right) dr' \tag{2.10}$$

$$= \int n_0 \exp\left(-\left(r'\,A - \frac{r}{At^2v_0^2}\right)^2 + \left(\frac{r^2}{A^2t^4v_0^4} - \frac{r^2}{t^2v_0^2}\right)\right) dr'. \tag{2.11}$$

The first term in the argument of the exponential will be integrated together with n_0 into some (time-dependent) number, which can be merged with the normalization constant $\mathcal{C}$.

The second term factors out and yields the time dependency, and we find

$$n(r,t) = \frac{\mathcal{C}}{\sqrt{A(t)}} \exp\left(\frac{-r^2}{w(t)^2}\right) \tag{2.12}$$

$$\text{with} \quad w(t)^2 = \frac{A^2 t^4 v_0^4}{A^2 t^2 v_0^2 - 1} = \frac{t^2 v_0^2}{1 - (t^2 v_0^2 / r_0^2 + 1)^{-1}} = t^2 v_0^2 + r_0^2. \tag{2.13}$$

which is another Gaussian function. So we find, that the shape of a thermal cloud during expansion remains a Gaussian one, whose $1/e$-sizes scale with $w_j(t) = [t^2 v_{j,0}^2 + r_{j,0}^2]^{1/2}$. With the definitions of v_0 and r_0 in equ.(2.5), one realizes that v_0 is independent of any trap parameters. Therefore the expansion velocity is isotropic and for large expansion times the cloud will approach unit aspect ratio. By fitting the time development of an expanding thermal cloud one can determine the temperature of the sample without the uncertainty in the determination of the trap parameters, which makes this method the commonly favored one. For a more detailed description see e.g. [You96].

However, this approach in combination with equ.(2.12) is based on the assumption of ideal, collionless gas behavior and that the cloud is in equilibrium at the moment of release. This implies that during expansion the temperature does not change and the expansion of the gas in one axis does not influence any of the others. This is not the case, if the collisional density rises to values, where the cloud exhibits hydrodynamic behavior. Then the initial phase of expansion results in a decrease of temperature, just like in expansion of compressed gases. This isentropic cooling ceases, as the density drops into the collisionless regime, so the manifested temperature reduction is limited. A non-unity aspect ratio of the trapped cloud then causes different timescales, on which the cloud becomes collisionless for the different axes. This reduces the cloud expansion velocity unequally in the spatial directions, resulting in anisotropic expansion. This effect has been predicted in [Wu98] and demonstrated in [Shva03a].

2.2 The Bose-Einstein prediction

In 1924 an as yet unsolved problem was to derive Planck's radiation without making arbitrary or classical assumptions. S. Bose wrote a manuscript with that intention, which came into the hands of A. Einstein, who translated and published it in a German science journal [Bose24]. The starting point of Bose's derivation is to assume a total amount of radiative energy E enclosed in a Volume V. The total energy E will be split into N^s quanta of energy $h\,\nu^s$ (with $s \in [0, \infty]$ being a summation index, not a power), so the total energy is

$$E = \sum_s N^s\, h\, \nu^s. \tag{2.14}$$

The second law of thermodynamics implies, that the system will self-arrange to maximize the probability of the distribution of all N^s under the boundary condition of equ.(2.14). To calculate this probability, we must first find the total number of cells in phase space. Due to the frequency-impulse relation of photons

$$p_x^2 + p_y^2 + p_z^2 = \frac{h^2\,\nu^2}{c^2} \tag{2.15}$$

the quanta are forced to remain on a hypersurface in phase space. It is straightforward to calculate the total number of cells for a frequency interval $d\nu$, which is

$$8\pi V \frac{h\nu^2\, d\nu}{c^3}. \tag{2.16}$$

For N^s, the number of quanta belonging to the interval $d\nu^s$, we write the number of permutations W, to distribute these into the cells as

$$\ln(W) = \sum_s A^s \ln(A^s) - \sum_s \sum_r p_r^s \ln(p_r^s), \tag{2.17}$$

where p_r^s is the number of cells in the frequency interval s that contain r photons, and for the number of photons N^s itself

$$N^s = \frac{A^s e^{-\frac{h\,\nu^2}{\beta}}}{1 - e^{-\frac{h\,\nu^s}{\beta}}} \qquad \text{with} \qquad A^s = 8\pi V \frac{h\,\nu^2\, d\nu^2}{c^3} \tag{2.18}$$

Inserting this into the energy relation equ.(2.14) we find

$$E = \sum_s N^s\, h\,\nu^s = \sum_s \frac{8\pi\, h\,\nu^{s3} d\nu^s}{c^3} \frac{V}{e^{-\frac{h\,\nu^s}{\beta}} - 1}. \tag{2.19}$$

To make this consistent with the definition of entropy, one finds immediately $\beta = k_B T$, which makes equ.(2.19) equivalent to Planck's radiation law.

Einstein extension to Bose's theory lies in the Ansatz to use instead of equ.(2.15) the energy-impulse relation for massive particles

$$p_x^2 + p_y^2 + p_z^2 = 2mE, \tag{2.20}$$

with m being the mass of the particle [Eins24, Eins25]. The continuation follows the same argumentation as S. Bose presented. A. Einstein draws the following conclusion from the resulting system of equations (translation by Ch.Buggle): *In the theory of the ideal gas, it appears to be a valid demand, that volume and temperature of a gaseous ensemble can be arbitrarily chosen. Theory then allows to calculate energy and pressure of the gas. But the study of the equation of state (...) shows, that at a given number of molecules n and a given temperature T the volume* ***cannot*** *be made arbitrarily small. (...) It follows then, that the number of molecules in such a gas at a given volume V cannot be greater than*

$$n = \frac{(2\pi\, m\, k_B\, T)^{3/2} V}{h^3} \sum_{\tau=1}^{\infty} \tau^{-3/2} = \frac{(2\pi\, m\, k_B\, T)^{3/2} V}{h^3}\, 2.61... \tag{2.21}$$

But what happens now, if I let the density of the gas at this temperature of n/V keep growing further, e.g. by iso-thermal compression? I claim, that in this case a growing number of molecules (growing with the overall density) *will traverse into the first quantum state, while the remaining ones will redistribute according to unit degeneracy.* This fraction, which condenses into the first quantum state, was later-on named: the Bose-Einstein condensate.

2.3 Cold and ultracold collisions

The Bose-Einstein theory predicts the condensation of an ideal gas. The term 'ideal' implies, that the particles do not interact with each other, which is an extreme case, which is in practice never strictly realized. Particles interact with each other via collisions. At room temperatures ($\sim$ 300K), these collisions can be described classically. At low temperatures, i.e. low relative velocities, scattering shows a significantly different behavior and a quantum mechanical treatment is necessary [Wein99].

To describe a collision between two distinguishable particles a and b let $\vec{R}$ be the vector, that connects particle a with particle b. In a collision the two approach each other, so that their interaction potential takes effect. At the turning point $R_{t.p.}$ the potential energy is equal to the relative kinetic energy E and they separate again. We reduce the two-body problem to the problem of one body of reduced mass $\mu = (m_a\, m_b)/(m_a + m_b)$ in the potential $V(\vec{R})$. The atoms move with the relative momentum $\vec{k}$, so the energy of the collision is $E = \hbar^2 k^2/2\mu$. If Ψ_a and Ψ_b represent the quantum mechanical wave functions of the internal states of the particles and there is no interaction ($V(\vec{R}) = 0$) then the relative motion is described by the simple wave function

$$\Psi(\vec{R}) \propto e^{i\vec{k}\vec{R}} \Psi_a\, \Psi_b. \tag{2.22}$$

The existence of an interaction potential will add to the free propagating wave an outgoing, scattered wave, which at distances of R bigger than the range of the potential $V(\vec{R})$ can be described by the total wave function

$$\Psi(\vec{R}) \propto \left[e^{i\vec{k}\vec{R}} + \frac{e^{i\,|k|\,|R|}}{R} f(E, \vec{k}_{in}, \vec{k}_s) \right] \Psi_a\, \Psi_b. \tag{2.23}$$

The function $f(E, \vec{k}_{in}, \vec{k}_s)$ reflects the amplitude of the scattered wave in the direction $\vec{k}_s$, which can exhibit a complicated angular distribution. Expanding the incident wave into spherical harmonics Y_{lm} yields

$$e^{i\vec{k}\vec{R}} = 4\pi \sum_{l=0}^{\infty} \sum_{m=-l}^{+l} i^l\, Y^*_{lm}(\vec{k}_{in})\, Y_{lm}(\vec{k}_s)\, j_l(kR), \tag{2.24}$$

where the spherical Bessel-function j_l has the following form for $R \to \infty$:

$$j_l(kR) \sim \frac{\sin(kR - (\pi/2)l)}{k\,R}. \tag{2.25}$$

We also expand the scattering amplitude into Legendre polynomials $P_l(\cos(\theta))$

$$f(E, \theta) = \frac{-i}{2|k|} \sum_{l=0}^{\infty} (2l+1) \left(e^{i\,2\eta_l} - 1 \right) P_l(\cos(\theta)), \tag{2.26}$$

where θ is the angle between $\vec{k}_{in}$ and $\vec{k}_s$. Here we introduce η_l as the phase shift, caused by the potential $V_g(R)$ on an incident wave of collisional energy E, that varies for different angular momenta ($l = 0, 1, 2, 3, ...$). This simplification is valid, if the scattering potential

$V(\vec{R})$ is spherically symmetric, which is the case for all alkali atoms in their electronic ground state when they are fully polarized, because the magnetic dipolar interaction is negligibly small. In the case of identical Bosons only the even partial waves contribute (as we will show in chapter 5).

The overall intensity of the scattered wave, i.e. the scattering cross section $\sigma(E)$, is given by the integral of $f(E, \vec{k}_{in}, \vec{k}_s)$ over all spatial directions, averaged over all incident directions $\vec{k}_{in}$, which is then

$$\sigma(E) = \frac{1}{4\pi} \int_{4\pi} \int_{4\pi} |f(E, \vec{k}_{in}, \vec{k}_s)|^2 \, d\vec{k}_{in} d\vec{k}_s \tag{2.27}$$

$$= 2\pi \int_0^{2\pi} \sin(\theta) |f(E, \theta)|^2 \, d\theta = \frac{4\pi}{k^2} \sum_{l=0}^{\infty} (2l+1) \sin^2 \eta_l. \tag{2.28}$$

The wave functions before and after collision will both have the form of equ.(2.25). The entire wavefunction of the collision can be calculated numerically by computing the Schrödinger equation to trace the development of the phase from a point far away from the turning point $R_0 \gg R_{t.p.}$ into the potential $V(R)$ to the turning point $R_{t.p.}$ and then back out to R_0, which allows to extract the phase shift η_l.

A principal modification to the scattering process is given by the fact, that at temperatures in the mK-regime the thermal DeBroglie wavelength

$$\lambda_{dB}(T) = \sqrt{\frac{2\pi\hbar^2}{m k_B T}} \tag{2.29}$$

of the scattering atoms a and b reaches values of the order of $\lambda_{dB} > 100 a_0$, while the typical range of the interaction potential (defined via $\hbar^2/(mR_0^2) = V(R_0)$) is of the order of $R_0 \approx 25 a_0$ (see fig.2.1)[1]. The resulting implications have been extensively discussed in the context of neutron scattering in nuclear physics [Beth35]. In particular, in the limit of $k \to 0$, we find two relations that link the phase shift η_l to the new parameter a_l. Its limiting behavior for $k \to 0$ is linked to the power of the long-range potential n and the quantum number of angular momentum l:

$$a_l^{-1} = \begin{cases} \lim_{k\to 0} k^{2l+1} \cot \eta_l & \text{for } 2l \le n-3 \\ \lim_{k\to 0} k^{n-2} \cot \eta_l & \text{for } 2l \ge n-3. \end{cases} \tag{2.30}$$

Note, that for $2l = n-3$ both options are equal. The collision of ground-state atoms implies that for $k \to 0$ all higher partial waves $l \ge 1$ vanish, and only the contribution of the s-wave, $l = 0$ remains. From equs.(2.27) and (2.30) and realizing that we have $n = 6$ and $l = 0$ (as will be argued below), we find that the scattering cross sections approaches a constant

$$\sigma(E) \to 4\pi a_s^2 \quad \text{with} \quad \lim_{k\to 0} a_s = -\tan \eta_0(k)/k \simeq -\eta_0(k)/k, \tag{2.31}$$

which defines the s-wave scattering length a_s. For identical Bosons this becomes $8\pi a_s^2$. The parameter a_s is a key material constant, from which all scattering properties in the

[1] 1 atomic unit ('a.u.' or a_0) is 0,053 nm

ultracold regime and many properties of Bose-condensed fractions can be calculated. Due to its connection to the phase shift η_0, which appears in the argument of the sine-function of the free-space wave function equ.(2.25), the scattering length a_s can be interpreted as a real-space displacement of the scattered wave function relative to the incident wave function at large distances $R \gg R_0$.

To determine the scattering length, three approaches are apparently feasible: either finding a sufficiently exact description of the interaction potential $V(\vec{R})$ by ab-initio calculations [Kolo65] or by adaptive calculations [Magn93] and deriving a_s from a combination of experiment and potential calculation, or by conducting experiments from which the scattering length can be extracted directly [Wein99]. We will return to this point in chapter 5.

For simplicity the potential can be treated in two parts: a long-range part $V_L(R)$, and a short range part $V_S(R)$. A clear distinction is difficult to make and depends on the purpose of the calculation. As a first, simple approximation, one can make use of the fact, that most of the phase shift η_l is generated in the outer region of the potential, where the potential is shallow. This is because in the short range part, the potential depth is much greater than the collision energy and dominates the phase development for all collision energies in the same way. Making the approximation of neglecting all repulsive forces, the molecular bound states are given as quantum mechanical states in the potential, formed solely by the interactions in the long-range part $V_L(R)$ of the potential, which are predominantly attractive. This ansatz reads

$$V_L(R) = c_{e1} \exp\left(\frac{c_{e2}}{R}\right) + \sum_{n=2}^{\infty} \frac{c_n}{R^n}, \tag{2.32}$$

where the coefficients c_n reflect various types of interactions. As an assignment of the coefficients c_n to the interaction type and a best approximation or the long range behavior, the interaction power n depends on the multipole order (monopole=0, dipole=1, quadrupole=2 etc.) of the interacting atoms n_1 and n_2 like

$$n = n_1 + n_2 + 1 \qquad \text{for resonant interactions} \tag{2.33}$$

$$n = 2\,(n_1 + n_2 + 1) \qquad \text{for non} - \text{resonant interactions.} \tag{2.34}$$

The first term in equ.(2.32) represents the exchange interaction, which is a purely quantum-mechanical effect [LandauQ]. For the case of ^{87}Rb it adds a repulsive interaction, particularly for collisions of atoms in excited states, but contributes only to a minor extent to ground state collisions. For the ^{87}Rb-dimer, where two atoms in the spherical symmetric s-state interact, symmetry allows only interactions of even n. Only the non-resonant monopole-monopole interaction can yield a total n=2 (neglecting the centrifugal barrier with a $1/r^2$-behavior here), but this is the electrostatic interaction and the atoms are not charged in this experiment. The resonant dipole-quadrupole interaction with n=4 is attractive but results from a second order perturbation and is negligibly small. Therefore, the non-resonant dipole-dipole interaction, commonly known as the van der Waals interaction with $n = 6$ represents the dominant attractive interaction. The molecular states in this potential will form a series of possible molecular states, that can be spectroscopically observed [Lett95]. By adjusting the parameters $c_n \geq 6$, one can model a potential

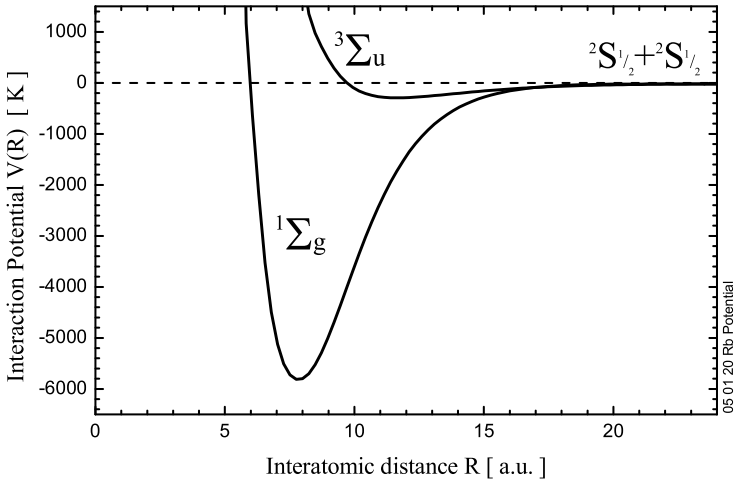

Figure 2.1: View of the ^{87}Rb interaction if both atoms are in the ground-state $^2S_{1/2}$ (Figure taken from [Wein99]). The energy is scaled by k_B to display K. For infinite separation the molecular state converges to the atomic state, here scaled to zero. Note the significant depth of both molecular potentials $> 10^2$K as compared to the typical temperature regime of ultracold collisions $< 10^{-3}$K.

to match the available spectroscopic data. This method, first proposed by LeRoy and Bernstein [LeRo70], can often provide a sufficiently good model of the potential for many applications.

For a more complete description that includes the repulsive, short range part of the potential $V_S(R)$ more elaborate methods are necessary. The first successful precision ab-initio calculation of a full potential was performed for the hydrogen-dimer in 1965 [Kolo65] due to its simple structure, but for all other elements, no analytical solutions are available so far. For the alkali atoms, Li, Na, K, Rb and Cs ab-initio calculations exist at least for the long-range interactions, i.e. the long range part of the potential [Buss85]. To retrieve also the inner part, multiple computational algorithms have been designed, to match the entire potential to spectroscopic data. The chemical bond region, i.e. the region, where $V(R) < 0$ holds, is often retrieved by using the RKR algorithm [Rees47]. A higher degree of precision can be obtained, by iteratively fitting to the result of the RKR-method, and adding adaptive corrections to the potential, to match the resulting states. This iterative process is referred to as the inverted perturbative approach (IVP), which was generallly introduced by Vidal [Vida79]. From such algorithms the potential shown in fig.2.1 was computed.

The molecular notations $^1\Sigma_g$ and $^3\Sigma_u$ refer to the total angular momentum.[2] Their distinction results from the two possible symmetries of the wave function describing the dimer. The singlet state $^1\Sigma_g$ corresponds to an antisymmetrical spin wave function and a symmetric coordinate wave function and the triplet state $^3\Sigma_u$ vice versa [LandauQ]. A purely quantum mechanical calculation does not yield the local minimum in the $^3\Sigma_u$ state, that is just perceivable in fig.2.1, unless the attractive van der Waals and other at-

[2]Similar to the notation in atomic states, the projection of angular momentum of $L = 0, 1, 2, 3$, *etc.* onto the axis connecting the atoms is labelled by capital Greek letters Σ, Π, Δ *etc.*.

tractive forces of minor strength are included. The triplet interaction potential contains 3 potentials, because of the possible permutations of the projection of the interacting dipole momenta, which are lifted out of degeneracy by the trapping magnetic field [Mill93]. In the magnetic trap used in all experiments, presented in this thesis, the atoms are spin-polarized in the trapping field in the fully stretched $F=2, m_F=2$ hyperfine state state. Thus the interaction via the singlet potential is prohibited, and the triplet state $^3\Sigma_u$ with the proper polarization projection represents the only possible interaction potential for collisions in the trap in all experiments described further on.

2.4 The condensed state

As we showed in the previous section, the Bose-condensed atoms interact with each other via the Van der Waals-interaction. As mentioned, we work solely with ^{87}Rb in the fully stretched $F=2, m_F=2$ hyperfine state, where no Feshbach resonances are reported yet [Mart02], so we restrict our description to the case of a constant, positive scattering length (the actual value being in this case $98.99(2)\,a_0$ [Mart02, Kemp02]) which results in a repulsive interaction. The consequences of a negative scattering length (collapse of the BEC) are pointed out in ref. [Kaga96, Dodd96] and demonstrated in ref. [Gert00]. The easiest observable feature of the particle interaction becomes visible in the density profile of the condensed fraction in trap and during expansion, which we will present here. For a more elaborate introduction to the Bose-condensed state see e.g. [Dalf99, Legg01, Pet-Smi, Pit-Str].

As argued in section 2.2, all condensing atoms traverse into the ground state of the confining potential $U(\vec{r})$. The magnetic trapping potentials is to good approximation harmonic

$$U_{ext}(\vec{r}) = \frac{m}{2}\sum_j \omega_j^2\, r_j^2 \qquad (j=x,y,z), \tag{2.35}$$

with m being the mass of the trapped particle and ω_j the trapping frequency. The solution of the Schrödinger equation for the resulting Hamiltonian

$$H = -\frac{\hbar^2}{2m}\nabla^2 + U_{ext}(\vec{r}), \tag{2.36}$$

yields the well-known system of energetically equally spaced eigenvalues

$$\epsilon_j = \sum_j \left(\frac{1}{2} + n_j\right)\hbar\omega_j \qquad (n_j = 0,1,2,...), \tag{2.37}$$

and the ground state wave function for $n_j = 0$, for all $j = x,y,z$ is

$$\Phi(\vec{r}) = \left(\frac{m\,\omega_{gm}}{\pi\,\hbar}\right)^{3/4} \exp\left(\frac{-m}{2\hbar}\sum_{j=x,y,z}\omega_j r_j^2\right), \tag{2.38}$$

with the geometric mean of the trapping frequencies $\omega_{gm} = (\omega_x\omega_y\omega_z)^{1/3}$. The observable density profile is given by

$$n_{BEC}(\vec{r}) = |\Phi(\vec{r})|^2, \tag{2.39}$$

so in this case the profile would be Gaussian, which is identical to the distribution of a thermal cloud at a certain lower temperature, as shown in equ.(2.5). So there would be no qualitative difference between the observed density profiles of the condensed and uncondensed fractions in the absence of the particle interaction.

The starting point for a treatment of the interacting gas is the many body Hamiltonian in second quantization

$$\hat{H} = \int \hat{\Psi}^\dagger(\vec{r}) \left[\frac{-\hbar^2}{2m} \nabla^2 + U_{ext}(\vec{r}) \right] \hat{\Psi}(\vec{r})\, d\vec{r} + \frac{1}{2} \int \hat{\Psi}^\dagger(\vec{r}) \hat{\Psi}^\dagger(\vec{r'})\, U(\vec{r} - \vec{r'})\, \hat{\Psi}(\vec{r}) \hat{\Psi}(\vec{r'})\, d\vec{r}\, d\vec{r'}, \tag{2.40}$$

where $\hat{\Psi}^\dagger(\vec{r})$ and $\hat{\Psi}(\vec{r})$ are the Boson creation and annihilation operators and $U(\vec{r} - \vec{r'})$ is the interparticle potential, as described in the previous section. When this Hamiltonian is inserted into the Schrödinger equation for systems of interest, i.e. samples with $\sim 10^6$ atoms, one retrieves a system of equations, where the mere number of coupled equations turns this into an analytically and numerically practically unsolvable task. The Schrödinger equation for this problem can be greatly simplified to an analytically solvable one, by approximating the integral over all Boson field operators in equ.(2.40) by the overall expectation value and thereby introducing the condensate wave function

$$\Phi(\vec{r}, t) \equiv \langle \hat{\Psi}(\vec{r}, t) \rangle. \tag{2.41}$$

This approximation effectively replaces the sum of all two-body interactions by a mean interaction, that represents the average of all individual ones. Therefore it is referred to as the mean-field approximation. It results in the Gross-Pitaevskii equation for N atoms in an external potential [Gold81]

$$\begin{gathered} i\hbar \tfrac{\partial}{\partial t} \Phi(\vec{r}, t) = \left(\tfrac{-\hbar^2}{2m} \nabla^2 + U_{ext}(\vec{r}) + g\, |\Phi(\vec{r}, t)|^2 \right) \Phi(\vec{r}, t) \\ \text{with } g = 4\pi\hbar^2\, a_s\, m^{-1}, \end{gathered} \tag{2.42}$$

where g is the interaction parameter of a simplified model interaction $U_{coll}(\vec{r}) = g\delta(\vec{r})$ that links the collisional interaction to the scattering length a_s. We can further simplify it by separating out the time development with the ansatz $\Phi(\vec{r}, t) = \phi(\vec{r}) \exp(-i\mu\, t/\hbar)$ to

$$\mu\, \phi(\vec{r}) = \left(\frac{-\hbar^2}{2m} \nabla^2 + U_{ext}(\vec{r}) + g\, |\phi(\vec{r})|^2 \right) \phi(\vec{r}), \tag{2.43}$$

where μ is the chemical potential. In the case of repulsive interaction, i.e. $a_s > 0$ and high particle number N in a not too strong confinement, such that $N|a_s|{a_{ho}}^{-1} \gg 1$, the condensate wavefunction is dominated by the interaction energy, and the kinetic energy term is negligible [Pit-Str]. Neglecting the kinetic energy term in equ.(2.43) is referred to as the Thomas-Fermi approximation. In this approximation we immediately find, that the density profile of a Bose-Einstein condensate is given by

$$|\phi(\vec{r})|^2 = \begin{cases} g^{-1}(\mu - U_{ext}(\vec{r})) & \text{for r.h.s.} > 0 \\ 0 & \text{otherwise} \end{cases} \tag{2.44}$$

In the Thomas-Fermi approximation, μ is defined by the normalization of $\phi(\vec{r})$

$$\mu = \frac{\hbar\,\omega_{gm}}{2}\left(15Na_s\sqrt{\frac{m\omega_{gm}}{\hbar}}\right)^{2/5}, \tag{2.45}$$

with ω_{gm} the geometric mean as introduced in equ.(2.38). Therefore the density profile mirrors the shape of the trapping potential, and for the potential $U_{ext}(\vec{r})$ in equ.(2.35) the density profile is parabolic [Gold81]. The distance, at which the density profile equ.(2.44) goes to zero in a parabolic trap,

$$R_{TF,j} = \frac{1}{\omega_j}\sqrt{\frac{2\mu}{m}} \propto \begin{cases} \omega_\rho^{-3/5}\omega_z^{1/5} & \text{for } j=\rho \\ \omega_\rho^{2/5}\omega_z^{-4/5} & \text{for } j=z \end{cases} \tag{2.46}$$

is referred to as the Thomas-Fermi radius. A precise treatment that includes the interaction of the condensed with the thermal fraction shows corrections, that tend to smooth the edges of the parabolic envelope [Hutc97].

2.5 BEC in expansion

Analogously to the release of a thermal cloud, also the release of a Bose-condensed cloud is an essential tool to probe the internal state (see section 2.1.2). To calculate the behavior of a BEC in time after release or more generally after a sudden change of trapping frequency from $\omega(0)$ to $\omega(t)$, we have to return to the time dependent Gross-Pitaevski equation [Cast96, Kaga96]

$$i\hbar\,\partial_t\Phi(\vec{r},t) = \left(\frac{-\hbar^2}{2m}\nabla^2 + U_{ext}(\vec{r}) + g\,|\Phi(\vec{r},t)|^2\right)\Phi(\vec{r},t). \tag{2.47}$$

Here and in the following we use for convenience the abbreviation $\partial/\partial_\chi = \partial_\chi$ for any variable χ.

As a first, classical model, the external potential and collision interaction terms on the r.h.s. of equ.(2.47) can be perceived as a potential energy whose spatial derivative results in a force

$$\vec{F}(\vec{r},t) = -\nabla\,\left(U_{ext}(\vec{r}) + g\,n_{BEC}(\vec{r},t)\right), \tag{2.48}$$

where the density profile $n_{BEC}(\vec{r},t)$ can now vary in time starting out from the in-trap shape $n_{BEC}(\vec{r},0)$ as in equ.(2.44). A classical gas experiences a dilation of its Gaussian profile, as shown in section 2.1.2, and as a first approximation, we assume a similar behavior in this case. As in real space the position of an infinitesimal part of the cloud moves on a trajectory $r_j(t) = r_j(0)\,b_j(t)$ $(j = x, y, z)$, where $r_j(0) \equiv r_j$ is the position at the moment of release, the cloud shape is inversely scaled by the scaling parameters $b_j(t)$ to

$$n_{BEC}(\vec{r},t) = \frac{1}{b_x(t)b_y(t)b_z(t)}\,n_{BEC}\Big(\frac{r_j}{b_j(t)},0\Big), \tag{2.49}$$

where the prefactor maintains proper normalization during scaling. In general, the time evolution for $t \gg 0$ of the b_j is not equal for the different $j = x, y, z$, unlike in the case of

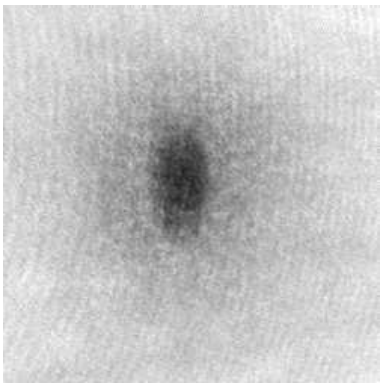

Figure 2.2: Typical image from the BEC experiment. The BEC is imaged by absorption imaging 4ms after release from the trapping potential. Clearly visible is the sharply edged condensed fraction in the center surrounded by the more fuzzy thermal fraction.

a classical gas (see sec.2.1.2). Applying Newtons law to the force equ.(2.48) and realizing that equ.(2.44) implies $\partial_r n_{BEC} = -g^{-1}\partial_r U(r)$ we find

$$m\ddot{b}_j(t)r_j = -\partial_{r,j}U(\vec{r},t) + \frac{1}{b_x(t)\,b_y(t)\,b_z(t)}\partial_r U(r_j,0). \tag{2.50}$$

With the harmonic potential equ.(2.35) this simplifies to

$$\ddot{b}_j = -\omega_j^2(t)b_j(t) + \frac{\omega_j^2(0)}{b_j(t)\,b_x(t)\,b_y(t)\,b_z(t)} \qquad (j = x,y,z). \tag{2.51}$$

Since the initial sizes r_j factor out, the scaling ansatz of equ.(2.49) yields a correct description, if the scaling parameters obey this differential equation.

We now try to construct a similar scaling solution in a more rigorous way that satisfies the Gross-Pitaevski equ.(2.47) at all times during expansion. An appropriate ansatz is

$$\varphi\left(\frac{r_k}{b_k(t)},t\right) = \frac{e^{i\theta}}{b_x(t)\,b_y(t)\,b_z(t)}\tilde{\varphi}\left(\frac{r_k}{b_k(t)},t\right). \tag{2.52}$$

Together with the dilatation of the condensate occurs an increase in velocity which is equivalent to a phase shift built-up, so the scaling ansatz must also contain a unitary gauge transform of the initial wavefunction φ. By proper choice of this phase θ to

$$\theta = -\theta_1 + \frac{m}{2\hbar}\sum_j r_j^2\frac{\dot{b}_j(t)}{b_j(t)} \tag{2.53}$$

$$\text{with } \theta_1 \text{ such, that} \quad \dot{\theta}_1(t) = \frac{\mu}{\hbar\,b_x(t)\,b_y(t)\,b_z(t)}, \tag{2.54}$$

we arrange the coefficients in the ansatz such that we find after inserting this scaling ansatz into equ.(2.47) and some algebra

$$\left[i\hbar\partial_t + \frac{\hbar^2}{2\,m}\sum_j \frac{1}{b_j^2(t)}\partial_{r,j}^2\right]\tilde{\varphi}(\vec{r},t) = \frac{[-\mu + U(\vec{r},0) + g|\tilde{\varphi}(\vec{r}),t|^2]}{b_x(t)\,b_y(t)\,b_z(t)}\tilde{\varphi}(\vec{r},t), \tag{2.55}$$

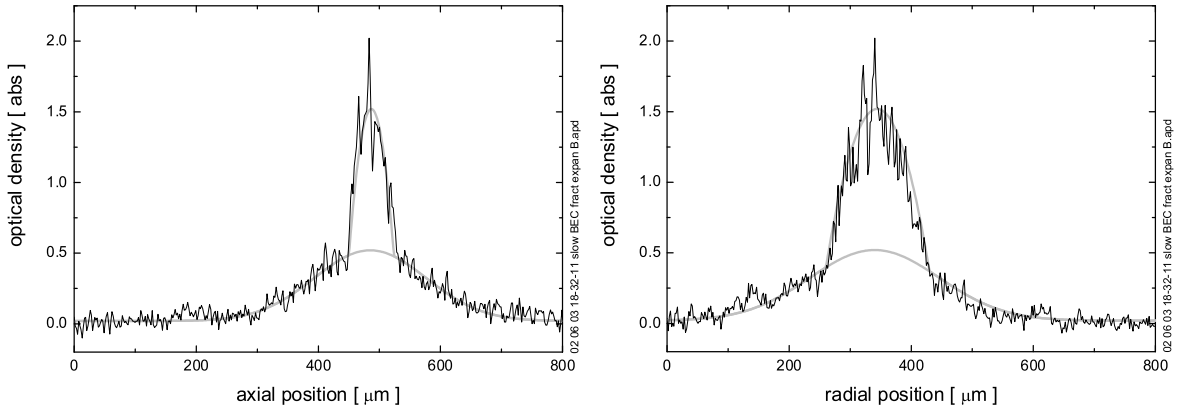

Figure 2.3: Cross section of the density profile in the horizontal and vertical direction through the center of the cloud shown in fig.2.2. The grey full lines indicate fitting lines corresponding to an inverted parabola and a Gaussian shape. The noisy structure of the profile around the fitting lines originates predominantly from imaging noise.

with the initial condition $\tilde{\varphi}(\vec{r},t) = \varphi(\vec{r},0)$. It can be shown that $\tilde{\varphi}(\vec{r},t) \approx \varphi(\vec{r},t)$ for all times to very good approximation. Again doing a Thomas-Fermi like approximation, i.e. neglecting the derivatives on the l.h.s. of equ.(2.55), we find

$$N|\varphi(\vec{r},t)|^2 = \begin{cases} \frac{\mu - \frac{m}{2}\sum_j \omega_j^2(0)\, r_j^2/b_j^2(t)}{g\, b_x(t)\, b_y(t)\, b_z(t)} & \text{for r.h.s} > 0 \\ 0 & \text{otherwise} \end{cases} \tag{2.56}$$

which is the rescaled equivalent of equ.(2.44). So the initially parabolic shape remains parabolic for any change in trap frequency, or any time development, triggered by it, in particular shape oscillations or a free expansion.

The time development of the scaling parameters themselves can be most easily extracted, if one assumes, that the trap is completely switched off, so $\omega_j(t) = 0$ for all $j = x, y, z$ and $t > 0$. Then the differential equation of the scaling parameters equ.(2.51) simplifies to

$$\ddot{b_z}(t) = \frac{\omega_z^2}{b_z(t)^2\, b_\rho(t)^2} \qquad \text{and} \qquad \ddot{b_\rho}(t) = \frac{\omega_\rho^2}{b_z(t)\, b_\rho(t)^3}, \tag{2.57}$$

where we model the trap used for this thesis, i.e. $\omega_x = \omega_y = \omega_\rho$ and $\omega_z/\omega_\rho \ll 1$ (the actual value is $1/23$). By making use of this small parameter, one can solve this set of equations by adding to the initial conditions $b_j(t) = 1$, $\dot{b}_j(t) = 0$ and $\ddot{b}_z(t) = 0$ and solving the remaining radial equation in equ.(2.57). We find

$$b_\rho(t) = \sqrt{1 + (\omega_\rho t)^2}. \tag{2.58}$$

Now we can drop the constraint $\ddot{b}_z(t) = 0$ and insert this result in equ.(2.57). In doing so we use only the zeroth order of $b_z(t) = 1 + O(\omega_z^2/\omega_\rho^2) \simeq 1$ for all t. By integrating twice the resulting differential equation $\ddot{b_z}(t) = \omega_z^2/(1 + \omega_\rho^2 t^2)$ we find

$$b_z(t) = 1 + \left(\frac{\omega_z}{\omega_\rho}\right)^2 \left(\omega_\rho t \, \arctan(\omega_\rho t) - \frac{1}{2}\ln\left(1 + \omega_\rho^2 t^2\right)\right). \tag{2.59}$$

So we find, that for non-unit aspect ratios the weakly confined dimension expands slowly, while the stronger confined dimension expands rapidly. The aspect ratio therefore rises from ω_z/ω_ρ to 1 within a time of $t \approx \omega_z^{-1}$ and keeps rising linearly in time towards infinity. This stands in contrast to the expansion behavior of thermal clouds (see section 2.1.2), and is one of the major signatures of degeneracy in the experiment. The fact that during expansion the parabolic shape of a cloud expanding from a harmonic trap is conserved is presented in fig.2.3, which shows the density profile of the BEC absorption image in fig.2.2 after 4 ms of free expansion.

Equ.(2.58) is identical to the expansion behavior of a minimum uncertainty wave packet (a derivation will be presented in sec.6.1.2), and describes the expansion of the $1/e$-size of the ground state wavefunction. On applying it to an experimental situation, one has to be aware, that by multiplying equ.(2.58) directly with the Thomas-Fermi radius of a Bose-Einstein condensate with large atom number, i.e. equ.(2.46), one overestimates the expansion velocity for large expansion times by a factor of $\sqrt{3/2}$, because the Thomas-Fermi size R_{TF} in the trap is broadened by the mean-field pressure [Pet-Smi].

Chapter 3
Experimental device and methods

In the following a description of the pathway to BEC as realized in the experimental apparatus of this experiment shall be given. Since certain parts of the experiment have not been modified during my presence in AMOLF, no description about those will be given here. For the vacuum system, see sections 3.3 in [ShvaTh] and 3.2 in [DiecTh]. For the ^{87}Rb-source see sections 3.2 in [ShvaTh] and chapter 4 in [DiecTh]. A precise treatment that includes the interaction of the condensed with the thermal fraction shows corrections, that tend to smooth the edges of the parabolic envelope [Hutc97].

3.1 Laser cooling

Laser cooling exploits the particle nature of photons, i.e. their impulse $h^2\,\nu^2 c^{-2} = |\vec{p}|^2$. Every absorption or emission causes a change in the motion of the interacting atom. By arranging a configuration, where all absorptions occur from one certain direction, while emissions distribute randomly - and thus average to zero - one creates a net-force, that can reduce the average velocity of an ensemble of atoms, i.e. their temperature. As the photon impulse is weak ($\approx 8.5 \cdot 10^{-28}$ kg m s^{-1}) as compared to the impulse of a thermal atom ($\approx 6.3 \cdot 10^{-23}$ kg m s^{-1}), intense light sources, with great spatial and spectral purity are necessary (as we explain later). Though coherence is not an issue for this simple scheme, lasers are the only sources, that satisfy these criteria.

In order to achieve a considerable effect, atoms must scatter many photons, and cycle through a certain path in the system of states shown in fig.3.1. This cycle starts from state $(5S_{1/2}, F=2)$ with a photon to pump[1] it to the $(5P_{3/2}, F=3)$ state. The photons in this step provide the cooling mechanism, and the laser is referred to as the MOT-cooling laser. Re-emission can return the atom to the initial state, or to $(5S_{1/2}, F=1)$, where they would be lost from the cooling cycle. A re-pumping laser pumps atoms, that arrived in state $(5S_{1/2}, F=1)$ to $(5P_{3/2}, F=2)$, from where they can either return, or decay to the correct $(5S_{1/2}, F=2)$ state.

3.1.1 Level scheme of ^{87}Rb

Fig.3.1 indicates, what laser frequencies are necessary, to drive transitions between a selection of states in ^{87}Rb. As the "Master"-laser we refer to in the following as a laser, that is spectroscopically stabilized to the $(5S_{1/2}, F=2) \leftrightarrow (5P_{3/2}, F=1\,c.o.\,3)$ cross-over line generated by the spectroscopy. With the help of acousto-optical modulators (AOM), fractions of its laser light are frequency shifted to derive the correct laser frequencies for magneto-optical cooling $(5S_{1/2}, F=2) \leftrightarrow (5P_{3/2}, F=3)$, with detuning adjustable

[1] As 'pumping from state a into state b' we refer to causing an optical transition from quantum state $|a\rangle$ to quantum state $|b\rangle$.

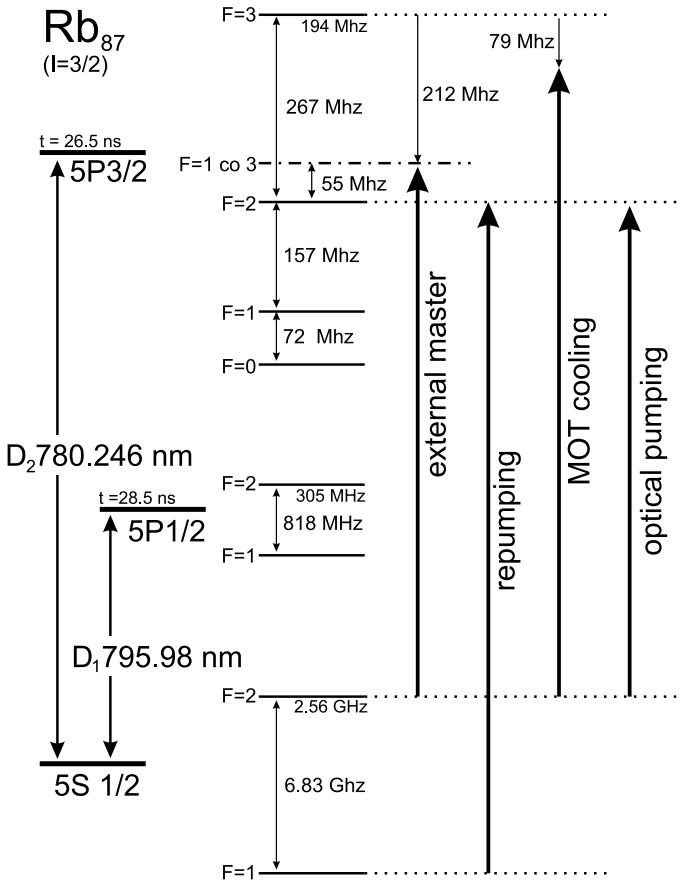

Figure 3.1: Selected atomic transition lines of ^{87}Rb. The spacing on the graphic reflects the energetic spacing only between the F-substates of the $5P_{3/2}$ state. All transitions, involved in this experiment, lie within the ^{87}Rb D_2-line.

from -79MHz to -17MHz, optical pumping $(5S_{1/2}, F=2) \leftrightarrow (5P_{3/2}, F=2)$, and imaging $(5S_{1/2}, F=2) \leftrightarrow (5P_{3/2}, F=3)$. The imaging detuning is adjustable from -20 to $+15MHz$ via an AOM, or by using a separate laser, stabilized by a RF-beat lock from -3GHz to +3GHz. For the repumping laser $(5S_{1/2}, F=1) \leftrightarrow (5P_{3/2}, F=2)$ acousto-optical modulators (AOM) or RF-beat lock schemes, bridging 6.8GHz, would be possible [Buch00] but challenging, and was implemented as a dedicated spectroscopic stabilization for easier handling. The function of these transitions in the cooling process will be explained in section 3.2.3, their technical implementation in the following.

3.1.2 Laser system layout

The experiment makes use for all laser systems of grating stabilized diode lasers [Wiem91], where in some cases AOM shifter lines, in other cases RF-beat locks were used, to derive the desired frequency from the Master-laser. Injection locked slave diode lasers provide power amplification and stabilization for laser beams, that passed through AOM-lines [Bond00]. RF-beat locks control the stabilization electronics of grating and current stabilized diode lasers. In the theses of Kai Dieckmann and Igor Shvarchuck, major parts of the laser setup have already been described. See fig.3.1 in [DiecTh], pg.27 or fig.3.3 in [ShvaTh], pg.22. The schematic shown there is still valid, with the exception, that

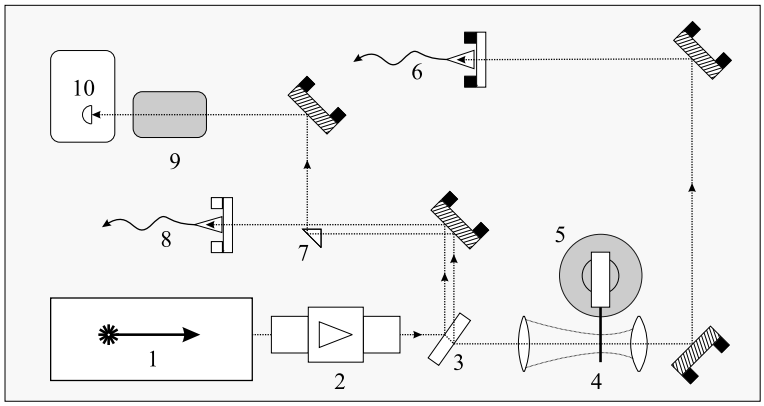

Figure 3.2: TIGER set-up. 1.) TIGER Laser head, 2.) 60dB-Faraday isolator, 3.) 2%-Beam splitter, 4.) Compression telescope, 5.) Mechanical shutter, 6.) Primary out: single mode optical fibre to MOT, 7.) 90°-Prism, 8.) Secondary out: single mode optical fibre mixer, with second input from external master for beat signal, leading to photodiode, 9.) Rb vapor cell, 10.) Photodiode to monitor doppler broadened absorption signal. Real size of base plate: 450 × 250mm.

the Master laser was together with all optical and spectroscopic components mounted on the same optical table. After the writing of the last thesis [ShvaTh] this monolithic principal was abandoned and lasers (Master, MOT and Phase contrast imaging) were redesigned and migrated to isolated breadboards, connected to the remaining system by optical fibres. For maximized stability, either commercial breadboards are used (External Master) or the base plates are custom made from 50mm thick aluminum (Tiger and PhC imaging), and rest either on vibration isolating feet on the main optical table or in a separate location. For RF and sound isolation, the setups are enclosed in aluminum casings. The Broad-Area diode Laser (BAL) (see chapter 4 in [ShvaTh] or [Shva00]) was replaced by a new type of high-power laser (TIGER, ® Sacher GmbH).

TIGER The TIGER laser system (only the laser head, object 1 in fig.3.2) is commercially available at Sacher-Lasertechnik[2]. Its implementation into the set-up is sketched in fig.3.2. A small amount of power is diverted to a Doppler-broadened absorption spectroscopy and another optical fibre output. The major amount of power is directly sent through a mechanical shutter arrangement into a single-mode optical fibre. The simple absorption spectroscopy allows coarse frequency monitoring while scanning the feedback grating in the laser head. The secondary optical fibre is one out of 2 inputs of an X-fibre mixer[3]. It mixes the laser beams from the two inputs 50-50 into both outputs. One output is sent into a fast photodiode to generate an electronic beat signal, the other output is used for monitoring. The electronic scheme, to derive a signal for the locking circuits is sketched in fig.3.3. The scheme is assembled from commercial parts, purchased from Minicircuits[4]. Its principal of operation is, that in a homodyne spectroscopy the phase shift, created by a fixed length delay line, is frequency

[2]Sacher Lasertechnik GmbH, Hannah Arendt Straße 3-7, D-35037 Marburg, Germany, www.sacher.de

[3]Custom made, based on splitter model 904P (fixed ratio coupler), Canadian Instrumentation and Research LTD, E-8-1155 Appleby Line, Burlington, Ontario, L7L5H9 Canada, www.cril.ca.

[4]Mini-Circuits Europe, Dale House Wharf Road, Frimley Green, Camberley, Surrey GU16 6LF, United Kingdom, www.minicircuits.com

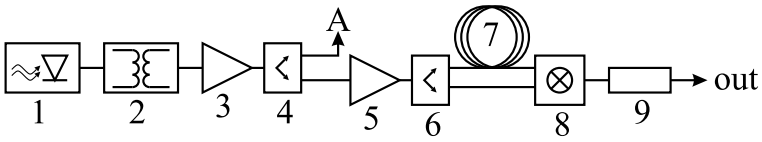

Figure 3.3: Electronic schematics for beat-lock of TIGER. 1.) Photodiode, 2.) Transformation isolator FTB-1-1, 3.) Amplifier ZFL-500, 4.) Power Splitter ZSCJ-2-1, 5.) Power Amplifier ZFL-500, 6.) Power Splitter ZSCJ-2-1, 7.) Delay line cable, 4.5m 8.) Phase Detector ZRPD-1 9.) Low-Pass filter 1.9MHz. Secondary output A leads to an RF-counter. All type specifications refer to the Mini-circuits catalogue Ver.2004.

dependent; the implementation described here is derived from ref.[Schü99]. The signal from 2 super-imposed lasers at frequency ω_1 and $\omega_2 = \omega_1 + \delta\omega$, creates a detected intensity proportional to

$$[\sin(\omega_1 t) + \sin(\omega_2 t)]^2 = \sin(\omega_1 t)^2 + \sin(\omega_2 t)^2 + \cos((\omega_1 - \omega_2)t) - \cos((\omega_1 + \omega_2)t). \quad (3.1)$$

As for light at 780nm, the frequency is $\nu = 3.83\,10^{14}$Hz, which is beyond the bandwidth of the photodiode it detects only the AC-part of the difference frequency $\omega_1 - \omega_2 = 2\pi\,\delta\nu$. It is passed through an rf-transformer, that filters the DC-offset. The difference frequency is amplified and sent through two separate cables, whose lengths differ by an amount l. The delay line causes a phase shift of $\phi = 2\pi\,l\,\delta\nu/c_g$, where c_g is the group velocity of an electric signal in the cable ($\approx 2/3\,c$). The phase detector passes the cosine of the phase through, so the zero-crossings of the voltage[5] signal

$$U(\delta\nu) \propto \cos\left(2\pi\frac{l\,\delta\nu}{c_g}\right) \quad (3.2)$$

can be used for locking (see fig.3.6 for a sample locking signal). The signal drops to zero around $\delta\nu = 0$ and also for large $|\delta\nu|$ due to the limited range of the used rf-components (e.g. ZFL-500: 0.5 - 500MHz). A special forward-backward rolling of the cable, a full-metal casing and an additional low-pass filter are necessary, to keep the signal clean from stray rf-noise, since the delay line cable acts as an antenna. The cable length $l = 4.5$m was chosen such, that the first zero crossing with rising slope signifies a frequency difference of $\delta\nu$=33MHz, which was the usual lock-point. This scheme generates a locking signal in a simple fashion, but does not provide great accuracy. The FWHM of the locked frequency is ≈ 2 MHz, while the TIGER is specified to sub-MHz-linewidth. However, for its purpose, a MOT at -33MHz and optical molasses at -79MHz detuning, a narrower linewidth is not required. The laser beam has good Gaussian shape and an aspect ratio of 1.5. Due to the great excess power (up to 800mW after the laser head, while only 140mW are required for the MOT), the resulting lower coupling efficiency of ≈ 60 % into the fibre was accepted. A single mode fibre guides the power to the MOT and also provides mode cleaning.

Phase contrast imaging laser The laser setup for phase contrast imaging (in short called Ph.C. imaging, for the imaging setup and theory see section 3.4.2) as pictured in fig.3.4 incorporates a grating and current stabilized diode laser, intensity switching and optics for beat-offset locking. The intensity is controlled by an electro-optical modulator (EOM) for fast, adjustable switching and an additional mechanical shutter for total

[5]Note, that U denotes in this section a voltage, whereas usually it denotes potential energy.

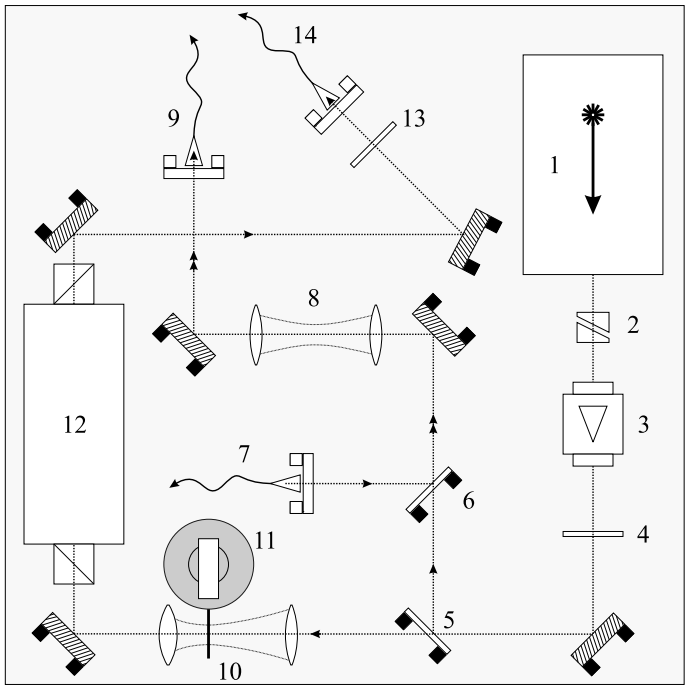

Figure 3.4: Phase contrast imaging laser setup. 1.) Grating stabilized diode laser, 2.) anamorphic prism pair, 3.) 30dB-Faraday isolator, 4.) $\lambda/2$-plate, 5.) 50%-beam splitter, to divert power to beat lock, 6.) 50%-Beam splitter, to overlay PhC-laser with external reference, coming from 7.) single mode optical fibre from reference laser, 8.) 1:1 telescope, intentionally mal-adjusted to mode match beam, 9.) Secondary out: single mode optical fibre to fast photo diode, 10.) Compression telescope, 11.) Mechanical shutter, 12.) Electro-optical modulator for fast intensity switching, 13.) $\lambda/2$-plate, 14.) Primary out: single mode, polarization maintaining optical fibre to experiment. Real size of base plate: 380×380mm.

extinction, since the EOM (specified to 30dB) provides extinction ratios of maximally 38dB, measured behind the primary output optical fibre. A beat signal is generated by overlaying in a secondary output fibre some amount of laser light from the Ph.C. laser with light, guided to the unit by another optical fibre from an external reference, in our case a fraction from the external master (see next subsection). The secondary fibre out leads directly to a fast photodiode. The electronic schematics, that generates an electronically usable signal for locking the laser with an adjustable frequency offset to the reference laser, is sketched in fig.3.5. Its principle of operation is similar to the one explained in more detail during the description of the TIGER-locking scheme, with two major extensions. To lock on higher beat frequencies, the beat signal can be passed to a high frequency counter. This specific counter (see caption of fig.3.5 for type) operates by mixing the incoming frequency with an internal reference oscillator at 250MHz. The displayed input frequency f_{count} is internally represented as $f_{count} = n \times 250\text{MHz} + f_{interm}$ with the highest possible $n = 1, 2, 3, \ldots$. The intermediate frequency f_{interm} is passed out, and can be used as input for the beat-lock circuit. Thus the maximum achievable offset frequency between reference laser and locked laser is limited by the bandwidth of the counter and the components before it. All components after the counter were chosen for a bandwidth of 500MHz for low frequency range operation. In this mode, the beat signal is directly wired to the phase lock line.

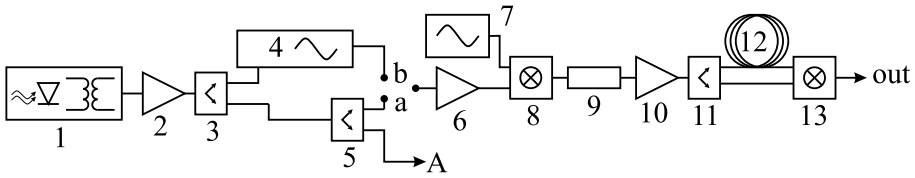

Figure 3.5: Electronic schematics for Phase contrast imaging laser. 1.) Fibre-coupled photodiode with internal transformation isolator, New Focus, Model 1534 (6GHz) 2.) Power Amplifier ZKL-2R5, 3.) Power Splitter ZFSC-2-2500, 4.) High frequency counter Hewlett-Packard 53508 with intermediate frequ. out, 5.) Powersplitter, ZSC-2-4, 6.) Power Amplifier ZKL-1R5, 7.) Tunable Marconi VCO 50-300MHz, 8.) Mixer ZAD-2, 9.) Low-pass filter 50MHz, 10.) Power amplifier ZFL-500, 11.) Power splitter ZSCJ-2-1 12.) Delay line cable, 13.) Phase detector ZRPD-1. All type specifications refer to the Mini-circuits catalogue Ver.2004. Secondary out A leads to a spectrum analyzer. At point *ab*, either the signal from a or from b can be wired into power amplifier 6.

As a second major extension a voltage controlled oscillator (Marconi VCO, $f_{VCO} = 50 - 300$MHz) is mixed with the beat signal, prior to the delay line. This mixing creates sidebands at the sum and difference frequency, given by equ.(3.1). The resulting locking voltage signal contains two AC signals $U(\delta\nu + f_{VCO}) + U(\delta\nu - f_{VCO})$, with $U(\delta\nu - f_{VCO})$ as in equ.(3.2), which is sketched in fig.3.6. Tuning the VCO-control voltage shifts the two signals in opposite fashion, and with it the locking point, that can be chosen at any zero crossing of a rising flank, so the offset frequency between reference and locked laser can be continuously tuned. Usually the two sides interfere with each other, resulting in undesired behavior, including partial vanishing of the signal. To avoid this, a low pass filter before the delay line cable (in the experiment 50MHz were chosen), is inserted. If the VCO is tuned to a high frequency and the locking point is chosen on a far out flank, the low-pass filter is removed, to maximize the range of the locking scheme. The length of the delay line cable was occasionally changed to achieve faster or slower phase wrapping and thus shift the zero crossings. Also here all VCO components and the cable have to be specially shielded in a full-metal casing. As mentioned in the previous TIGER section, the absolute stability of this locking scheme is not outstanding (≈ 2 MHz FWHM), but must be compared to the total tuning range of 6GHz. The mounted laser diode provides 40mW, for imaging only 2.5 mW after the fibre were used.

External Master The expression 'External Master' refers to the facts, that this laser provides the overall frequency reference, and second, that it is the only experiment optics component that was stored in a separate location. The set-up, as depicted in fig.3.7, incorporates the laser head, spectroscopy, an injection locked slave [Bond00] and a scanning cavity, to check proper lock of the slave. The principal of the spectroscopy is similar to modulation spectroscopy with the variation, that not the laser is modulated, but the magnetic field in the Rb-vapor cell. Sidebands are thus imprinted on the two σ components of the light, that pass through the cell, whereas the laser itself shows none. Since in weak magnetic field, the Zeeman-sublevels are shifted with opposite sign (see fig.3.8), the σ^+ and σ^--components are modulated with opposite sign. For retrieving a locking signal from the modulated laser beam, only one of the σ-components is necessary. Constant magnetic fields add with opposite sign to the σ-components. By

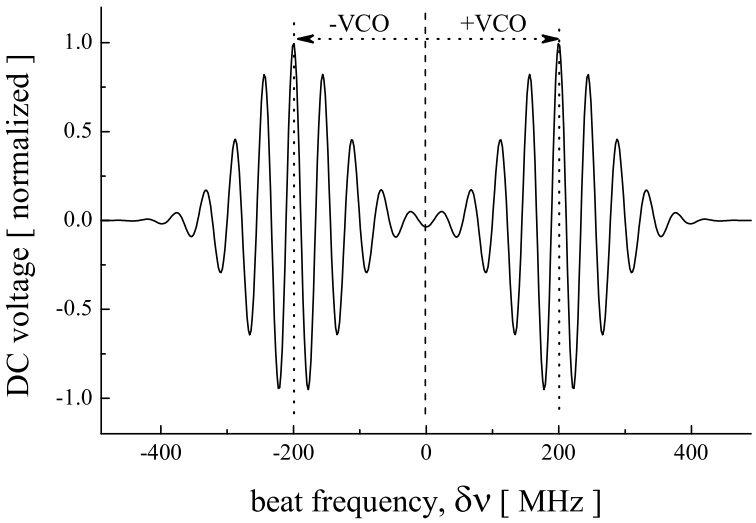

Figure 3.6: Qualitative representation of the locking signal for the phase contrast imaging laser. One of the two signals alone, centered around $\delta\nu = 0$MHz, would sketch the locking signal of the TIGER. A low-pass filter avoids overlap of the two signals. In reality the signal drops sharply to zero at zero beat frequency and at both centers of the shifted wrapping signals, as the mixer electronics do not transmit DC signals.

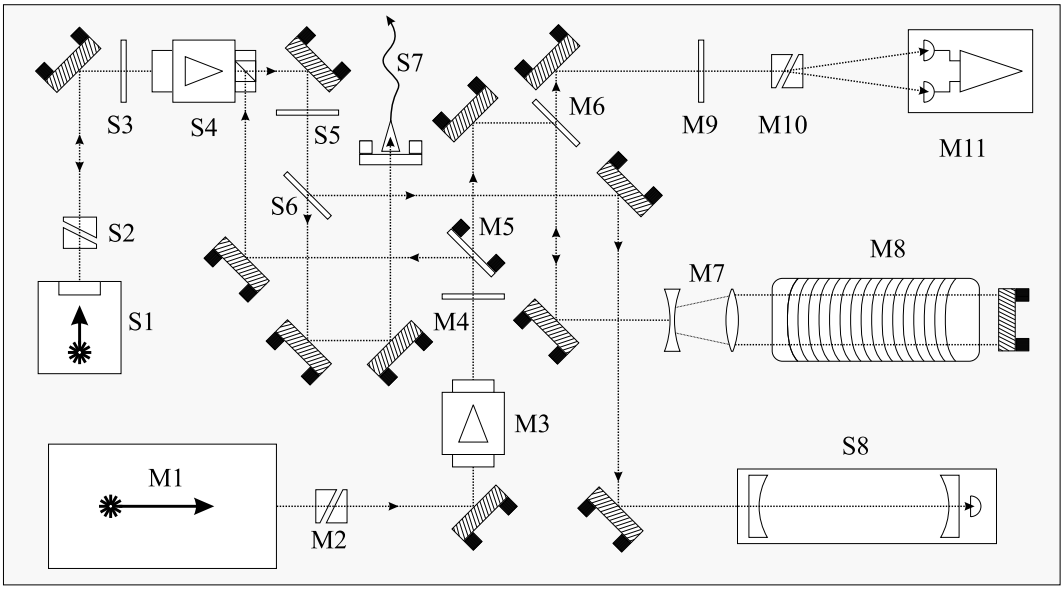

Figure 3.7: External Master set-up. Master components: M1.) Grating stabilized diode laser, M2.) Anamorphic prism pair, M3.) 30dB-Faraday isolator, M4.) $\lambda/2$-plate, M5.) 10%-Beam splitter to direct power to injection lock slave diode, M6.) 95%-Beam splitter, M7.) Expansion telescope, M8.) Rb-vapor cell, surrounded by coil wires to generate ac-magnetic field (1.9MHz), M9.) $\lambda/4$-plate, M10.) Wollaston prism, M11.) differential photodiode. Slave components: S1.) Free running slave diode in custom made mount, S2.) anamorphic prism pair, S3.) $\lambda/2$-plate, S4.) 30dB-Faraday isolator, rotated by 45° along opt. axis to have injection lock input in plane, S5.) $\lambda/2$-plate, S6.) 4%-Beam splitter, to divert power to monitoring cavity, S7.) Single mode, polarization maintaining optical fibre to experiment, S8.) Scanning, confocal cavity, to check lock of slave. Real size of base plate: 600×300mm.

detecting the two σ-components in two differential photodiodes, ambient magnetic fields cancel out.

3.2 Confinement

In order to pre-cool, collect and ultimately confine a cloud of atoms, a magneto-optical trap (MOT) and a magnetic trap are used. Both concepts make use of magnetic fields.

3.2.1 ^{87}Rb in magnetic fields

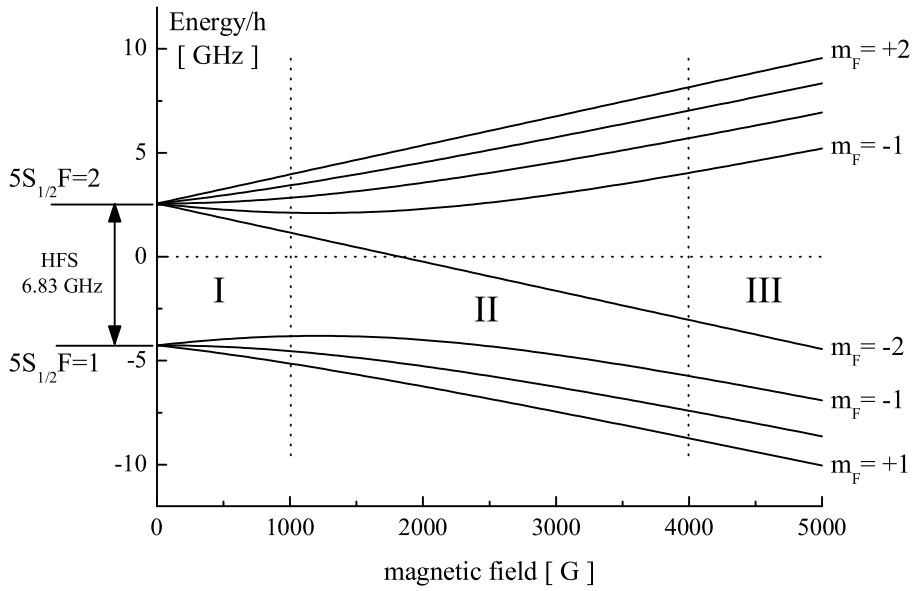

Figure 3.8: Splitting of energy levels for the $5S_{1/2}$ $F = 1$ and $F = 2$ states in ^{87}Rb. **I**: Zeeman region, **II**: transitional region, **III** Paschen-Back region. Note the field strength, required to leave region **I**.

An atom has 3 internal angular momenta that create a resulting magnetic field, which interacts with the external one: the nuclear spin $\vec{I}$, the orbital angular momentum of the shell electron $\vec{L}$, and the spin of the electron $\vec{S}$ (with $S = 1/2$ and the two projection options $\pm 1/2$), where atoms can undergo transitions between spin and orbital angular momentum states. The coupling of these 3 angular momenta gives rise to the rich level structure of atoms. In weak external fields $\vec{S}$ and $\vec{L}$ couple to a resulting $\vec{J}$ ($J = L + S$), and then with $\vec{I}$ to $\vec{F}$ ($F = I + J$). The nucleus of the isotope ^{87}Rb is comprised of 37 protons and 50 neutrons, where each one carries a spin $\frac{1}{2}\hbar$. Their arrangement in the nucleus creates a total nuclear spin of $I = \frac{3}{2}$. The fact, that the sum of all elementary particles (37 protons + 37 electrons + 50 neutrons) is even, gives this isotope Bosonic properties. From its 37 electrons, 36 are arranged in the closed shells with main quantum numbers $n = 1$ to $n = 4$, only the remaining one with $n = 5$ contributes to S and L. The ground state is therefore the $5^2S_{1/2}$-state. In the S state we have $L = 0$, so $J = 0 \pm \frac{1}{2}$ and $F = \frac{3}{2} \pm \frac{1}{2}$, which makes the state a doublet. The total magnetic moment $\vec{\mu_F}$ of the atom

is given (in the assumption of spin-orbit coupling $\vec{J} = \vec{S} + \vec{L}$) by

$$\vec{\mu_F} = \vec{\mu_J} + \vec{\mu_I} = -\frac{g_J\,\mu_B}{\hbar}\vec{J} + \frac{g_k\,\mu_k}{\hbar}\vec{I}, \tag{3.3}$$

where g_J is the Landé-factor

$$g_J = 1 + \frac{J(J+1) + S(S+1) - L(L+1)}{2J(J+1)}, \tag{3.4}$$

$g_k = 0.995\,10^{-3}$ the nuclear Landé-factor, $\mu_B = 0.579\,10^{-4}\mathrm{eVT}^{-1}$ Bohr's magneton and $\mu_k = 3.152\,10^{-8}\mathrm{eVT}^{-1}$ the nuclear magneton. For atoms with $L = 0$ it follows $J = S$ and therefore $g_J = 2$. Any atomic state with $\vec{J},\ \vec{I} \neq 0$ experiences an energy shift, dependent on the state of the spin projections L and S. The magnitude of this shift is dependent on the interval factor

$$A = -\frac{\mu_I \mu_K\, B_n}{I\,J}, \tag{3.5}$$

with μ_I the magnetic moment of the nucleus and B_n the magnetic field, caused by the hull electrons in the spatial region of the nucleus. For ^{87}Rb in the S-state A has the value $2\pi\hbar\,3.415$ GHz. For alkali atoms in their ground state, where $F = I \pm \frac{1}{2}$ holds, the shift is well described by the Breit-Rabi formula [MaKu97]

$$E^{HFS}_{F,m_F}(B) = -\frac{A}{4} + m_F g_K \mu_K B + (-1)^F \frac{\Delta E_0}{2}\sqrt{1 + \frac{4\,m_F}{2\,I+1}\,\xi + \xi^2} \tag{3.6}$$

$$\text{with} \quad \xi = \frac{g_J\mu_B - g_K\mu_K}{\Delta E_0}B, \quad \text{and} \quad \Delta E_0 = A\Big(I + \frac{1}{2}\Big), \tag{3.7}$$

which extends equ.(3.3) beyond a linear approximation, where m_F represents the projections of the Zeeman-substates onto the external field vector, and can take the values $m_F = 0, \pm 1, \ldots \pm F$. Due to the small value of μ_K one can neglect the second term in equ.(3.6) and approximate in equ.(3.7) $\xi \approx 2\mu_B/\Delta E_0$. The resulting group of graphs is displayed in fig.3.8. The change in the approximative power-law of the energy curves in the intermediate region II in fig.3.8 is caused by re-ordering of preferred momentum coupling, which makes the assumption of equ.(3.3) invalid. As can be seen from the graph, for the field strengths, achievable with the experimental setup ($\ll$ 1000G) a linear approximation for the shift of the m_F states relative to the undisturbed $F = 2$ state is well sufficient:

$$\Delta E^{HFS}_{F,m_F}(B) = \frac{1}{2} m_F \mu_B B, \tag{3.8}$$

so the linear coefficient in frequency units has a value of $\mu_B/2\,h \approx 700$kHz/G. Above a temperature of 1mK the atoms venture into regions, where the quadratic Zeeman effect causes deviations from this linear approximation, and forced evaporative cooling becomes less efficient, as the resonance condition varies for transitions between different m_F states. However, in our experiment, evaporation starts at a temperature of 600μK and proceeds efficiently.

3.2.2 Magnetic field configuration

In order to confine atoms by the force of a magnetic field, a spatially localized field extremum must be provided. As can be seen from fig.3.8, some m_F-states are energetically

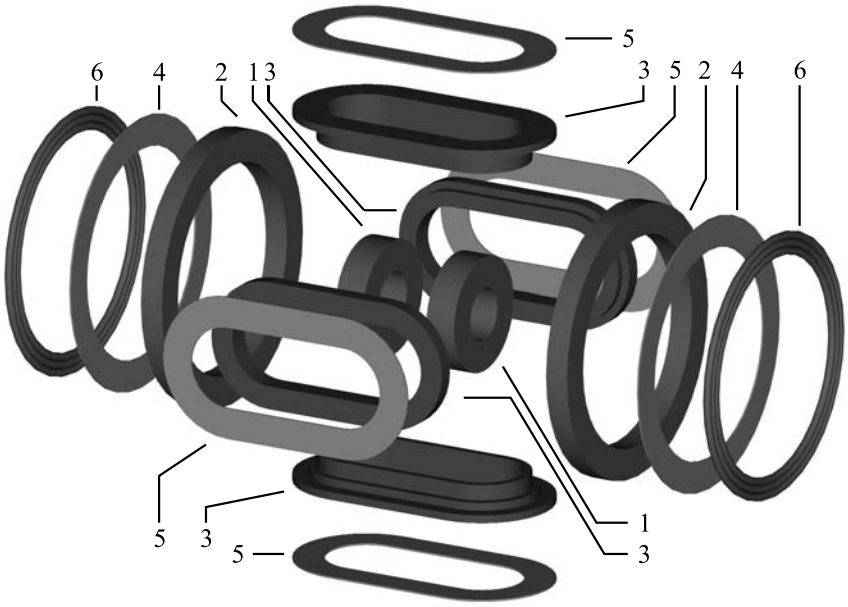

Figure 3.9: Exploded schematic view of coil arrangement. All coils are sets of 2, symmetric to the center. 1.) Pinch, 2.) Compensation, 3.) Ioffe bars, 4.) Axial PCB trim coil, 5.) Radial PCB trim coil, 6.) Axial wire trim coil. Supply wires, carrying current to the coils are left out.

lower for higher fields and others for lower fields (atoms in those states are named accordingly high-field seekers and low-field seekers), while the states with $m_F = 0$ experience no magnetic force and are dragged by gravity out of any field configuration. A local, static field maximum contradicts Maxwells equations [Wing84], only a local field minimum can be realized. The force, that an atom experiences in a magnetic field is given by the spatial derivative of equ.(3.6)

$$\vec{F} = -\nabla E^{HFS}_{F,m_F}(B(\vec{r})) \approx -\mu_F \nabla B(\vec{r}), \tag{3.9}$$

which is to very good approximation proportional to the negative gradient of the magnetic field via the effective magnetic moment of the atom μ_F, as discussed in section 3.2.1.

The coil arrangement used in this experiment is referred to as the Ioffe-Pritchard type configuration, which was originally designed for plasma confinement [Gott62] and later adapted for neutral atoms [Prit83]. The configuration and the naming conventions are displayed in fig.3.9. Their real arrangement is shown in fig.3.10. In order to create a quadrupole field, as required for magneto-optical trapping (see next section), the two pinch coils can be adjusted to have current running in opposite direction. This configuration must be switched to identical direction, in order to create a "magnetic bottle", a configuration designed to trap a hot plasma in strong fields. The arrangement of the coils is similar to a Helmholtz configuration, but the distance is greater, which results in a local field minimum at high field offset. A quadrupole field in the radial plane is exerted by the Ioffe bars in the orthogonal plane to add radial confinement. A second set of axial coils counteracts the pinch field to compensate the magnetic field offset of the pinch coils. A sophisticated electronic system controls the currents and current directions in the coils to allow changes in configuration and compression (see sec.3.5).

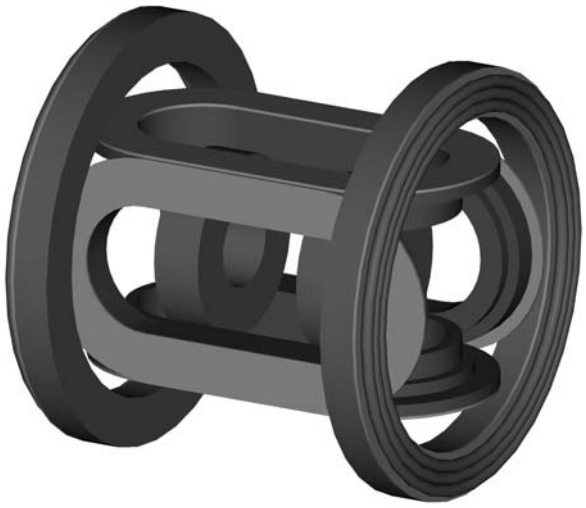

Figure 3.10: Schematic view of trapping coil arrangements with all coils in proper position. Supply wires, carrying current to the coils are left out. We identify the axis through the center of the pinch and compensation coils as the 'axial' or z-direction ($\vec{e}_z$). The orthogonal plane is referred to as the (x-y)- or ρ-, i.e. 'radial' plane ($\vec{e}_\rho$), where the three Cartesian vectors form an orthonormal system $\vec{e}_x \perp \vec{e}_y \perp \vec{e}_z$. We define $\vec{e}_x$ as the axis of imaging, that points through the center of the horizontal Ioffe bars. The real space distance of the compensation coils is ∼110mm, their outer diameter ∼140mm.

The used power supplies can exert up to 400 A, which resulted in a power dissipation of 5.4 kW in the coils and 4.4 kW in the switching IGBT's, so a water cooling for all components was devised. The balance between the fields of pinch and compensation coils was adjusted to tune the field strength at the field center to zero. The trap bottom magnetic field strength at the center B_0 is generated by a separate set of coils, that is merged with the earth-field compensation, a cubic arrangement of coils of 1.5 m cubic length, which is not pictured in figs.3.9 and 3.10. A more complete description of the current circuits is given in section **3.3** in [DiecTh].

The magnetic field configuration at full current is well described by

$$B(x,y,z) = B_0\sqrt{(1+\beta z^2)^2 + (\alpha^2-\beta)(x^2+y^2) + \alpha\beta xyz}, \tag{3.10}$$

with the scaled trap parameters $\beta = \beta_{real}/B_0$ and $\alpha = \alpha_{real}/B_0$ [Berg87]. Note, that the third term in the square-root of equ.(3.10) represents a tetrahedron-like distortion, which becomes noticeable only at large off-axial distances. However, it avoids certain analytic calculations due to its non-rotational structure, and therefore it is the following neglected. It plays a role solely in the experiment, presented in chapter 5.

The central z-axis coincides with the zero-crossing of the radial quadrupole field, so B_0 originates solely from the axial field coils, that form part of the earth field compensation. The parameters α_{real} and β_{real} represent the unscaled radial gradient of the quadrupole field $\alpha_{real} = 353\,\mathrm{Gcm}^{-1}$ and the unscaled axial curvature $\beta_{real} = 136\,\mathrm{Gcm}^{-2}$ (see table 3.2 in [DiecTh]. Note the difference in definition and usage of the parameter β_{real} here and there). Close to the center, this can be approximated by an harmonic potential of the

form

$$B(x,y,z) = \frac{1}{2} m \sum_j \omega_j^2 r_j^2 \quad (j = x,y,z) \tag{3.11}$$

with m being the mass of ^{87}Rb ($1.45 \cdot 10^{-25}$ kg). The trapping frequencies can be retrieved by calculating the second derivatives of equ.(3.10), and we find

$$\omega_x = \omega_y = \omega_\rho = \sqrt{\frac{\mu_B}{m}\left(\frac{\alpha_{real}^2}{B_0} - \beta_{real}\right)} = 2\pi\, 476\,\mathrm{Hz} \tag{3.12}$$

$$\omega_z = \sqrt{\frac{\mu_B}{m} 2\beta_{real}} = 2\pi\, 21.0\,\mathrm{Hz} \tag{3.13}$$

In axial direction, the curvature of the field remains to good approximation in agreement with equ.(3.11) for ≈1cm, which is much larger than the usual exploited range. In radial direction the harmonic approximation turns into the linear slope of the quadrupole field on a distance, which is dependent on the value of B_0. For the usual value of $B_0 = 0.9$G the deviation between equ.(3.10) and equ.(3.11) reaches 1% at a distance of 14μm, which is the equivalent of the $1/e-$size of a thermal cloud at 10μK.

An added modification, which is important for the understanding of later experiments, is the arrangement of trim coils, that were installed during construction of the magnetic coil setup but have not been mentioned in [DiecTh] or [ShvaTh] and neither been used until the experiments described herein. These trim coils allow trimming and modulation of the main field configuration.
On the outer surface of each coil, except the pinch coils, a standard PCB-board is mounted, which is on both sides covered by a 100μm thick layer of copper. By cutting gaps and proper wiring, each PCB-board acts as a magnetic field coil with 2 windings. They are in the following referred to as the PCB-trim coils. Due to their low inductance they can exert only minor fields, but in return can be switched very fast ($< 1\mu$s). The radial trim coils produce a field of 0.221 GA^{-1} in a Helmholtz like current configuration. This calibration was measured by the displacement of the cloud in situ due to the shift of the quadrupole field zero-crossing. The axial PCB-trim coils generate a field of

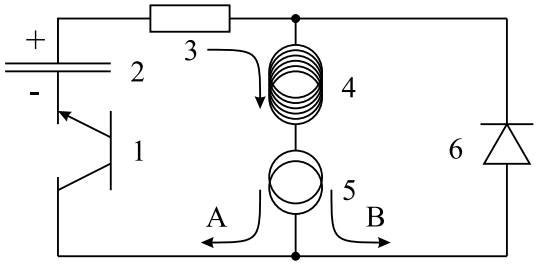

Figure 3.11: Current switching circuit for adjustable decay time. 1.) Main switching FET, IRFK-4H450, 2.) Power supply, 3.) Resistor to simulate voltage drop of diode, only for low currents, 4.) Added coil of wound copper wire, 2mm diameter, various lengths, for additional, variable inductance, 5.) Axial PCB- or wire-trim coil, 6.) Diode USD940. In power supply driven mode, the current follows path A. When the FET gate closes, self inductance drives the current through path B. The decay time can be tailored by choice of the inductance 4.

0.120 GA^{-1}, calibrated by the shift of the trap bottom magnetic field, i.e. the point, at which under rf-evaporation no atoms remain trapped (for rf-evaporation see section 3.3). Due to the advantageous surface to volume ratio, the PCB-trim coils can endure more than 20 A for multiple seconds, with minor heating. However, due to heat built-up in the soldered connectors, the use of more than 5 A becomes critical after ≈30s.

In order to apply more axial modulation or trimming field, a second set of axial coils was added, formed by 10 turns of wound copper wire with 2mm diameter, which is in the following referred to as 'axial wire trim coils'. They are calibrated to 0.495 GA^{-1} in the same way as the axial PCB-trim coils. These coils can withstand up to 80 A of DC current for up to a minute, limited by heat built up in the supply wires and FET switching circuits.

The trim coils current directions were reconfigured for various purposes, but are during the experiments reported in this thesis used only in one configuration: the radial helper coils are set to exert a homogeneous field and powered in AC mode such, that a constant amplitude field vector rotates at a certain frequency in the radial (x-y)-plane. The rotation is generated by two DDS (direct digital synthesis) arbitrary waveform generators (type 33120A and 33250A ® Agilent) in phase-locked and external amplitude controlled mode. The amplitude is controlled via AOs (analogue out) from the experiment control system. The signal is amplified by a home-built AC-amplifier, based on MTP1306 (® Motorola) high density power FET's. To assure total current switch-off digitally controlled mechanical relais are additionally implemented.
The axial trim coils are powered (solely with DC) by either a Delta-SM15-200D (200A max.) or a Delta-SM70-20D (20A max.) power supply (® Delta Elektronika B.V.) in voltage limited, current stabilized mode, occasionally also in current control via voltage-in mode from another AO. The control via AOs (see section 3.5) allowed precise control over current sweeps and timing, which is essential for some experiments.

All PCB and wire trim coils switch off on a timescale below 10μs when switched directly by a FET-circuit. This results in some switch-off depolarization and loss of atoms, since off-axis magnetic field vectors suddenly change direction. Therefore the switching circuit, sketched in fig.3.11 was devised, to tailor the current decay time to ≈200μs.

3.2.3 Magneto-optical and magnetic trapping

To capture and precool atoms in a finite region of space, we make use of a magneto-optical trap (MOT). A 1-dimensional schematics is shown in fig.3.12, which can be easily extended to 3 dimensions; the caption text describes the capture process [Raab87]. The trapping mechanism of a magneto-optical trap is complex and encompasses multiple light scattering processes, so a detailed description is beyond the scope of this thesis. For a more detailed description see e.g. [Town95, Phil98, Met-Str].

In the initial stage of the experiment the pinch coils (see fig.3.9) are used in anti-Helmholtz like current configuration at low current (40 A) to provide the quadrupole field for the MOT. The required laser power for the MOT is 120 mW for all 6 cooling beams, and 6 mW for the repumping beams, which are mixed only into the 4 incident directions in the horizontal plane.

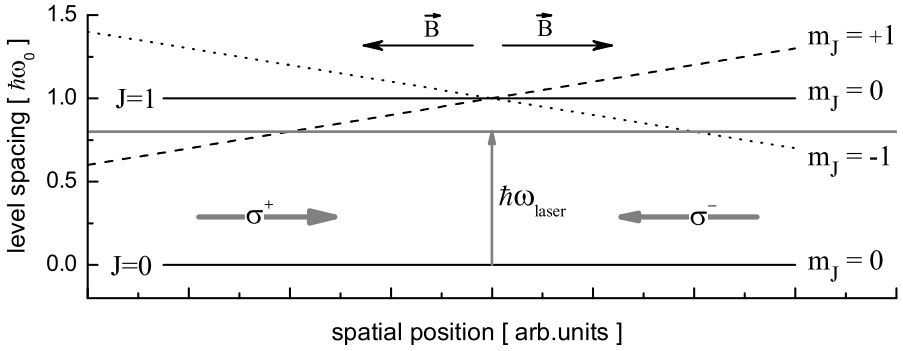

Figure 3.12: MOT scheme for simplified model system for one dimension. Note, that in this representation the trap axis is chosen as quantization axis. A magnetic field gradient creates a spatial dependent Zeeman shift to lift the degeneracy of the m_J-states. Incident light beams with opposite helicity σ^+ and σ^- are supplied with red detuning in order to break the symmetry of transition probability for the m_J-states. Atoms scatter photons solely from the beam, whose helicity and detuning allows a transition, which due to the magnetic field is spatially dependent. By proper arrangement of helicity and magnetic field, a situation can be arranged, where an effective restoring force is present, because only incoming photons are scattered. In the center the light scattering cross section is equal for all incident and passing beams, and the net-force vanishes.

Since a MOT does not polarize the atoms into a single m_F-state, a recapture of a cloud from a MOT directly into a Ioffe-Pritchard configuration would yield low transfer efficiency. With 'recapture' we refer to a sudden switch-off of all laser light and a sudden switch from quadrupole to Ioffe-Pritchard current configuration, which also poses certain requirements to the electronic control circuits (see section 3.5). To increase the recapture efficiency, a 15 ms stage of optical molasses cooling is inserted between MOT switch-off and magnetic trap switch-on to further reduce the cloud temperature [Lett88]. In this stage, the laser detuning of the MOT beams (left at full power) is increased from the MOT value of -33 MHz to -72 MHz, whereas all magnetic fields are off during this time. After optical molasses we switch to a homogeneous magnetic field along the trap z-axis. As the quantization of the atomic momentum is in the following counted versus this axis, it is also referred to as the polarization axis.
Then we shine σ^+ polarized light along the $z-$axis of the trap for 300μs for polarization pumping. Each absorption of a σ^+-polarized photon pumps the atoms one step closer to the $(5S_{1/2}, F=2, m_F=2)$-state. In order to maintain resonance condition for all m_F-states, optical pumping has to occur on a transition to a state with identical slope coefficient of the Zeeman-effect (see fig.3.8), which holds for the $(5S_{1/2}, F=2) \leftrightarrow (5P_{3/2}, F=2)$ transition. Since the last step to the $(5S_{1/2}, F=2)$ state is not a stimulated emission, the decay can occur to the $(5S_{1/2}, F=1)$ or $(5S_{1/2}, F=2,_{m_F}=1)$ state, which limits the efficiency. For this stage 60μW of pumping light was used. For the same reasons as explained in the context of laser-cooling, 200μW of repumping light are added.

Magnetic trap loading sequence In the experiment typically 10 billion ^{87}Rb atoms are loaded from the source described in [Diec98] into the MOT. By applying optical molasses and optical pumping we typically capture 5×10^9 atoms. The initial field strength is chosen such, that low-field seeking atoms in the $m_F = 1$-state are not

effectively trapped, since the gravitational pull is stronger. In the following, the cloud is compressed by ramping up the current in the power supplies that feed the field coils from 40 A to 400 A. This compression increases the temperature of the sample from 40 μK to more than 600 μK, but also increases the collisional density of the cloud, thus speeding up thermalization, which is essential, to prepare for the following step of forced evaporative cooling.

Losses by spin-depolarization The $(5S_{1/2}, F=2)$-state is most favorable for magnetic trapping, since the coupling constant of atomic magnetic momentum to field is greatest, resulting in tighter confinement. However, since it is not the state of minimal possible energy in a magnetic field, losses can occur by spin-reorientation to the other m_F-states. The magnetic moments $\vec{\mu}$ of the trapped atoms precess around the magnetic field $\vec{B}$ at the the Larmor frequency, $\omega_L = \vec{\mu}\vec{B}/\hbar$. Changes in the vector projection should occur slow as compared to the timescale of this frequency, to allow the magnetic moment to follow adiabatically and avoid losses from the trap.

This condition can be violated by two processes, occurring in the experiments described herein: first, any sudden change of field vectors in the trap, which becomes an issue for atoms, which are located off-axis while the compensation magnetic field is changed. The vector field in off-axis regions then changes also orientation, since the pinch and compensation coils are not geometrically in the same position. Second, when atoms cross due to their thermal motion through regions of low $\vec{B}$ the probability to undergo a spin transition scales with $\exp(-B_{min})$, where B_{min} represents the lowest encountered value in a trajectory. This problem has been first studied in the context of ultracold neutrons [Golu79, Rabi36, Majo32] and has acquired the name 'Majorana' depolarization in the context of trapped neutral atoms. Due to the geometry [Prit83], we have $B_{min} \geq B_0$, so by supplying sufficient central field strength B_0, Majorana depolarization is effectively avoided.
Transitions to the $(5S_{1/2}, F=1)$-state in the absence of laser light are significantly less probable, since the orbit angular momentum has to change by 1, and dipole transitions are forbidden, so the trapped state is metastable.

3.3 Evaporative cooling

Due to limitation of cooling with optical methods (in particular the Doppler limit and the recoil limit) forced evaporative cooling has been devised as a powerful tool to lower the temperature of a gaseous sample. Evaporative cooling was first realized in experiments with atomic hydrogen [Hess86, Hess87]. A review of evaporative cooling is presented in [Walr96, Kett96], for an example of a numerical simulation see e.g. [Wu96, Wu97].

Evaporative cooling is based on the preferential removal of atoms from the high energy tail of a Maxwellian energy distribution equ.(2.1) with subsequent thermalization via collisions [Kroo76]. The energy value ϵ_t at which the distribution equ.(2.1) is truncated, i.e. above which the atoms are 'evaporated' out of the trap, scaled to the sample temperature at

the moment of truncation k_BT is defined as the truncation parameter

$$\eta = \frac{\epsilon_t}{k_BT}. \tag{3.14}$$

The evaporation rate per atom can be expressed by

$$\tau_{ev}^{-1} = \frac{\dot{N}}{N} = n(0)\overline{v}_{th}\sigma_{el}\,\frac{V_{ev}}{V_{ef}}\,e^{-\eta}, \tag{3.15}$$

where $\sigma_{el} = 7.9\,10^{-16}\mathrm{m}^2$ is the elastic collisional cross section, as introduced in equ.(2.31) and $\overline{v}_{th}$ the mean thermal velocity

$$\overline{v}_{th} = (8k_BT/\pi\,m)^{1/2}. \tag{3.16}$$

The ratio of evaporated volume V_{ev} to the effective volume $V_{ef} = N/n(0)$, with $n(0)$ being the real space density at the trap center, is for experimental parameters of this thesis close to unity [Walr96]. As elastic collisions re-thermalize the gas, atoms are promoted to higher energy, which eventually causes them to be evaporated as well, if the evaporative effect is left in operation. As the temperature lowers, η rises and the evaporation rate drops exponentially, so the temperature approaches a lower, but finite value. This method of evaporation under a constant evaporation is referred to as 'plain evaporation'.

If the achieved temperature after a single evaporation step is not sufficient, the evaporation energy ϵ_t can be step-wise or continuously further lowered, forcing evaporation to continue at constant rate, i.e. constant η, which is referred to as 'forced evaporative cooling'. It can be shown, that in this case the temperature remains proportional to the number of atoms N

$$T \propto N^{\alpha_{ev}}, \tag{3.17}$$

if the efficiency parameter

$$\alpha_{ev} \equiv \frac{d\,\ln(T)}{d\,\ln(N)}, \tag{3.18}$$

depends only on η. Evaporative cooling of atoms is inevitably linked to losses in real space density, which for a cubic shaped confinement, where the volume is independent of temperature, would result in dropping density and collision rates and therefore rising thermalization times. But due to the dependancy of thermal size on temperature in harmonic traps, as shown in equ.(2.5), the real space cloud volume V_e decreases. For the Ioffe-Pritchard quadrupole trap of this thesis, the dependency is given by

$$V_e \sim \begin{cases} T^{5/3} & \text{at high temperatures (linear limit)} \\ T^{3/2} & \text{at low temperature (harmonic limit).} \end{cases} \tag{3.19}$$

By combining equ.(3.17) and (3.19) we find, that real density at the trap center can be arranged to rise during evaporation, provided

$$\alpha_{ev} > \delta^{-1}. \tag{3.20}$$

The combination of decreasing temperature and increasing real space density results in a significant increase of phase space density, which allows Bose-Einstein condensation

to set in, as soon as it's value rises above 2.6 (compare to equ.(2.21)) [Gard97]. Under conditions of low collision rates, the BEC formation occurs as a continuous growth [Mies98, Gard98, Koeh02]. Under hydrodynamic conditions, the growth occurs fast as compared to the decay of phase-fluctuations and the BEC forms out of equilibrium [Shva02, Bugg04a].

In order to arrange a continuous growth, a large η and therefore slow evaporation is necessary. On the other hand, the cloud density decreases by other loss mechanisms, most profoundly collisions with untrapped background gas atoms, which are present in the vacuum chamber due to limits in achievable pressure by the vacuum pumps and seals. These losses are not energy selective, and lead mainly to particle loss, so a balance between high η and swift evaporation has to be chosen. If the rise in real space density is strong enough to result also in rising collision rates $\tau_{el}^{-1} \propto n(0)v_T \propto n(0)T^{1/2}$ the so called 'runaway' evaporation regime is reached: evaporation may proceed faster for decreasing temperatures. The conditions for entering this regime are experimentally mainly given by high initial number of atoms N and tight compression in the trap.

The technical implementation of forced evaporation is given by an AC-magnetic field in the radio-frequency (RF) range, that transfers atoms from the trapped ($F=2, m_F=2$) state into any of the untrapped states ($F=2, m_F=0, -1, -2$) at the resonance condition

$$\hbar\, 2\pi\, \nu_{RF} = \frac{1}{2}\mu_B |B(\vec{r})| = 700\mathrm{kHzG}^{-1} \times |B(\vec{r})| \tag{3.21}$$

where ν_{RF} is the frequency of the oscillating field in the range from 500 kHz to 50 MHz. As shown in section 3.2.1, the Zeeman shift in low magnetic fields is to good approximation linear, and with the resonance condition met, each m_F-state is coupled to all other ones, which efficiently transforms low field seeking $m_F=2$ into high field seeking $m_F=-2$ atoms.

By evaporating to the bottom of the trap, and dividing the frequency ν_0, at which no atoms remain trapped by the linear coefficient, the value of B_0 is experimentally measured. It is important to be aware, that the presence of the RF-field also deforms the trapping potential in the region close to where the resonance condition is met. When evaporating close to the trap bottom, the actual value of B_0 is shifted down ($\approx$5kHz). Experimentally this effect is compensated by measuring the atom number at various ν_{RF} close to the suspected ν_0 and extrapolating for the zero crossing.

With ν_0 known, the truncation energy ϵ_t is related to the RF-frequency by the simple relation

$$\epsilon_t = m_F 2\pi\hbar\,(\nu_{RF} - \nu_0)\,. \tag{3.22}$$

The resonance condition is not linked directly to the thermal energy of an atom, since atoms are only evaporated if their trajectory in the sample brings them into regions of the magnetic potential, where the resonance condition is met. Therefore evaporation does not occur on a sphere in phase space, but only on a sphere in real-space. The probability of a transition from the trapped into an untrapped state is dependent on the amplitude of the evaporating RF-field and the speed, at which an atom passes through the resonance region. This problem was solved for a two level atom [Zene32] and is discussed in ref. [Rubb81]. Additional studies for the particular case of this

experiment have been carried out in the group [ValcMs]. The probability is a function of the Landau-Zener parameter, which is proportional to the square of the Rabi frequency. At a certain amplitude of the RF-field, the transition probability saturates to unity, and excess RF-power only leads to power broadening of the resonance condition.

Forced evaporative cooling is started after full compression of the trapped cloud, to assure entering the runaway-evaporation regime. The evaporation frequency starts at 50MHz, which is equivalent to an RF-photon energy, higher than the depth of the trapping potential. It is then swept to values $\geq \nu_0 = 630$kHz in a duration of 10.6 seconds. During this time, the amplitude is also lowered from $30\,\mu\mathrm{T_{pp}}$ down to $8\,\mu\mathrm{T_{pp}}$.

Under usual conditions these steps results in a Bose-Einstein condensate of up to 10^6 atoms with 80% BEC fraction at a final RF-frequency of $650kHz = \upsilon_0 + 10$kHz.

3.4 Imaging

In this experiment the atoms in the vacuum chamber are detected by their interaction with light. A laser beam exiting a single mode, polarization maintaining optical fibre, that provides a clean Gaussian beam profile, is expanded, collimated and sent onto the cloud. On its path it also traverses two quartz glass walls, that are part of the vacuum chamber, in which the cloud resides. These glass walls are anti-reflection coated on the outside, but not on the inside, and therefore give rise to fringe patterns, that must be compensated by image processing. The cast shadow of the cloud inside the chamber and a major part of the light, that does not traverse the cloud is collected by a relay telescope with $\times 2$ magnification and creates a virtual image outside the vacuum chamber, as sketched in fig.3.13. This virtual image is then projected by a microscope objective with $\times 4$ magnification onto the CCD-chip (chip type EEV 512×512 FMTR) of the camera (camera model TE/CCD-512EFT by Princeton Instruments). The numerical aperture and optical quality of the imaging components results in a total resolution limit of $\approx 4\mu$m FWHM.

Detection is (for all experiments described further on) done with a $40\,\mu$s flash of

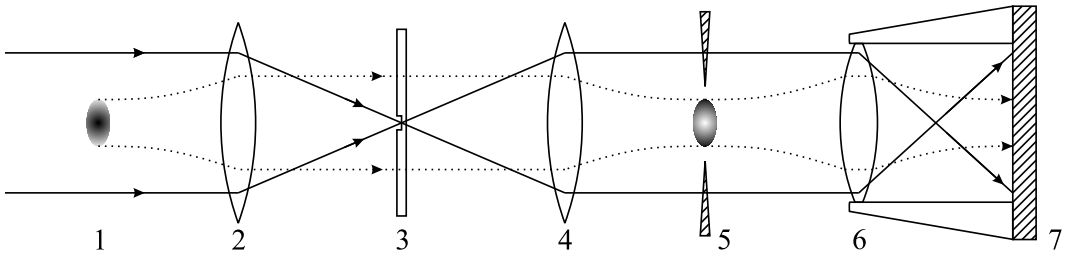

Figure 3.13: Imaging optics setup. The cloud at 1 resides in the focus of the confocal relay telescope formed by the achromats 2 and 4. In reality it had $\times 2$ magnification. The light, traversing the cloud is collimated, while the background light is focused. For phase contrast imaging a phase advancer in the focus 3 and two shadowing blades in the image plane 5 could be inserted. The telescope creates the image 5 of the cloud, which is then projected by a fixed mounted microscope objective 6 onto the CCD-chip 7. In reality this objective had $\times 4$ magnification.

linearly polarized light and for absorption imaging detunings chosen to keep the peak optical density at ~ 2. The polarization and propagation vectors are both orthogonal to the trap axis. The intensity is ≈ 2 mW/cm^2. The effects of saturation and optical pumping arise only at small detunings and are corrected for to first order where necessary.

The chip has a real size of 7.7×15.4mm with 512×1024 pixels, but one half of it is covered by a physical shield from incident light, so only a maximal surface of 7.7×7.7mm can be illuminated at once, i.e. an area of 512×512 pixels. This division is necessary to allow the brightness information stored in the built up charge in each well to be swiftly shifted to the covered region (the CCD chip can shift charges by 1 line per μs) where it is then read-out without collecting any additional light. A CCD surface read-out can only be performed as a full surface read-out and consumes $\approx$ 600ms, which is too long for any reasonable experimental timescale to be performed multiple times during an experiment. The maximum field of view covers a region of $962 \times 962\,\mu$m with each well collecting photons passing through a surface in the object plane of $1.88 \times 1.88\mu$m. The camera is mounted on a 3-D translation stage, so the focus point and field of view can be shifted by micrometer screws by up to ≈2cm in each direction.

Each CCD-well is specified to collect up to 130000 electrons with a quantum efficiency of 0.45 electrons per photon at 780nm. The detection flash time was chosen as 40μs to avoid blur of the image, i.e. imaging of the same atom in two pixels e.g. during imaging a thermal cloud in expansion. This detection flash is controlled by EOMs mounted in the absorption and phase contrast detection laser systems (see e.g. fig.3.4). The total intensity of the detection laser power was chosen as 2.2mW, i.e. 175μW/cm^2 peak intensity in a Gaussian beam with $1/e$-size of 2.5cm. Therefore the well depth is exploited only to a minor fraction. This low-detection power was chosen to avoid saturation affects in absorption imaging at resonance (see [ShvaTh]). The collected charge information of the CCD wells is converted into a brightness information encoded with 10bit resolution, resulting in a grey-level image of the field of view.
The imaging system was mounted in the horizontal plane, orthogonal to the trap z-axis, imaging through the Ioffe bars (see fig.3.9 and 3.10). It provided a view of the vertical and axial (y, z)-plane of the magnetic trap.
The polarization of the incident light was linear and orthogonal to the magnetic field vector during imaging. Therefore imaging occurred with π-polarization.

The propagation of the light wave in the optical system can be best understood by assuming, that the cloud generates light of a certain phase and intensity, that interferes with the incident light as sketched in fig.3.13. The phase and intensity of the incident electromagnetic wave can be represented by a complex number, where we define its phase as the reference and therefore zero:

$$E_{in} = E_0 e^{i\,\omega t}. \tag{3.23}$$

The cloud generates light which at resonance is in anti-phase with the incident light and therefore interferes destructively, resulting in a shadow.
The interaction of the light wave with the atoms can be directly calculated by evaluating the energy loss as the electromagnetic wave oscillating at frequency ω drives the oscillator, formed by the valence electron of the atom, which is characterized by the dipole moment and the resonance frequency ω_0. For this simple one oscillator model (which is

a good approximation for alkali with only one electron in the s-state) we find the linear susceptibility $\chi(\omega)$ as [Loudon]

$$\chi(\omega) = \frac{\lambda^3 n}{(2\pi)^2}\left(\frac{1}{\delta - i}\right), \tag{3.24}$$

where λ is the wavelength of the light and n the atom density, and $\delta = 2(\omega - \omega_0)/\Gamma$ the detuning scaled to half-linewidths (note the opposite sign of the definition here compared to ref.[Loudon]). The susceptibility is linked to the (complex) refractive index $n_{ref} = n_i + i\,n_i$ as $\chi = n_{ref}^2 - 1$. By comparing real and imaginary parts we find

$$n_{ref} = \frac{\lambda^3 n}{2(2\pi)^2}\left(\frac{-\delta}{1+\delta^2} + \frac{i}{1+\delta^2}\right). \tag{3.25}$$

The optical density that the light wave passes before falling on the camera is spatially dependent because we image 3 dimensional structures $n(x, y, z)$. The 2 dimensional density profile $n_{2D}(y, z)$ is given by the integral of the 3-D density along the direction of the camera (here the x-axis)

$$n_{2D}(y, z) = \int_{-\infty}^{\infty} n(x, y, z)dx. \tag{3.26}$$

where we assume the x-direction to be the direction of imaging. We take the fact into account, that we use π-polarized light by averaging over all Clebsch-Gordon coefficients, and find that the cross section is reduced by a factor of 7/15. In the thin-lens approximation and assuming Lambert-Beers law of intensity attenuation, we find for the amplitude transmission coefficient

$$\tau(y, z) = \exp\left(\frac{-\sigma_\pi}{2}\left(\frac{1}{1+\delta^2}\right) n_{2D}(y, z)\right), \quad \text{where we define} \quad \sigma_\pi = \frac{7}{15}\,\frac{\lambda^2}{2\pi}. \tag{3.27}$$

To retrieve the phase shift, we realize, that a light wave passing through a medium of length D with index of refraction n_{ref} undergoes a total phase wrap of $2\pi D n_{ref}/\lambda$. The phase difference compared to light progressing through vacuum is $\phi = 2\pi D\,(n_{ref} - 1)/\lambda$. For large detuning $|\delta| \gg 1$ the imaginary part of n_{ref} is negligible and we find

$$\phi(y, z) = \frac{\sigma_\pi}{2}\left(\frac{-\delta}{1+\delta^2}\right) n_{2D}(y, z) \tag{3.28}$$

The light ΔE that the cloud generates must interfere with the incident light to yield the absorption imaging signal, so

$$\Delta E = E_0 e^{i\omega t}(\tau e^{i\phi} - 1). \tag{3.29}$$

3.4.1 Absorption Imaging

In absorption imaging the virtual light ΔE interferes with the incident light E_{in} on the CCD-chip surface. The resulting intensity is given by

$$I = |E_{in} + \Delta E|^2 = E_0 e^{i\omega t}\left(1 + \tau e^{i\phi} - 1\right) \times c.c. = I_0\,\tau^2. \tag{3.30}$$

By inverting the Lambert-Beers law of absorption, that defines the intensity in the imaging plane when imaging with the absorption imaging detuning δ_{Abs}

$$I(y,z) = I_0 \exp\left(\frac{-\sigma_\pi}{1+\delta_{Abs}^2}\int_{-\infty}^{\infty} n(x,y,z)dx\right) \tag{3.31}$$

one can retrieve the particle density, integrated over the column at the spatial position (y,z) in the image plane, provided, that the detuning δ_{Abs}, linewidth Γ and absorption cross section σ_π of the used transition are known (including shifting and broadening effects, e.g. Zeeman shifts induced by stray magnetic fields).

In absorption imaging the entire exposed surface of the camera CCD-chip is used for imaging and one single shift operation (consisting of 512 individual line-shift operations) moves the whole image under the shield for read-out. Since absorption imaging implies scattering of resonant or near-resonant photons, the cloud is destroyed by one imaging flash. With the available laser systems, that were described in sections 3.1.2, absorption imaging can be conducted using the $(5S_{1/2}, F=2, \leftrightarrow 5P_{3/2}, F=3,\ F=2,\ F=1)$ transitions in the D_2 line. In practice only the $(5S_{1/2}, F=2, \leftrightarrow 5P_{3/2}, F=3)$ transition with various detuning was used.

3.4.2 Phase Contrast Imaging

For phase contrast imaging the incident light is phase shifted by a glass plate with a spot of increased or decreased thickness that resides in the focus of the relay telescope (see fig.3.13). The resulting intensity is given by the interference between the virtual electromagnetic wave ΔE with the phase shifted wave $E_p = E_0 e^{i\omega t \pm \pi/2}$:

$$\begin{aligned} I_{phc} &= (E_p + \Delta E)^2 = E_0 e^{i\omega t}(e^{\pm i\pi/2} + \tau e^{i\phi} - 1) \times c.c. \qquad (3.32)\\ &= I_0\left(2 + \tau^2 + \tau\left(e^{i\phi \mp i\pi/2} + e^{-i\phi \pm i\pi/2}\right) - \tau\left(e^{i\phi} + e^{-i\phi}\right)\right)\\ &= I_0\left(2 + \tau^2 - \tau\left(\left(e^{i\phi} + e^{-i\phi}\right)\cdot\left(1 - e^{\mp i\pi/2}\right)\right)\right)\\ &= I_0\left(2 + \tau^2 - 2\sqrt{2}\tau\cos(\phi \pm \pi/4)\right), \qquad (3.33) \end{aligned}$$

For phase contrast imaging with great detuning $|\delta_{PhC}| \gg 1$ (in the experiment δ_{PhC} was -500), the transmission τ is ≈ 1 and we can simplify this to

$$I_{phc} = I_0\left(3 - 2\sqrt{2}\cos(\phi \pm \pi/4)\right) \simeq I_0\left(1 \pm 2\phi\right). \tag{3.34}$$

Inserting the phase shift equ.(3.28) we find

$$I_{phc}(y,z) = I_0\left(1 \pm \left(\frac{-\delta_{PhC}\,\sigma_\pi}{1+\delta_{PhC}^2}\right)\int_{-\infty}^{\infty} n(x,y,z)dx\right). \tag{3.35}$$

The near unit transmission implies low photon scattering rates, which makes this imaging method non-destructive [Andr96], and allows multiple images to be taken of the same cloud.

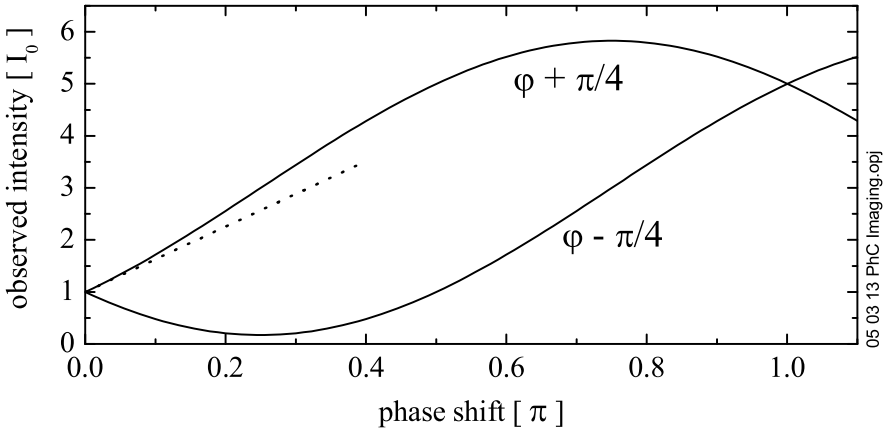

Figure 3.14: Transmitted intensity in phase contrast imaging for quarter phase retarder ($-\pi/2$) and advancer ($+\pi/2$), assuming negative, i.e. "red" detuning. The dotted line represents the approximation of equ.(3.34) with positive sign. The bright imaging branch offers a greater dynamic range, if the full form of equ.(3.34) is used. Higher column density results in more phase build up, less detuning in faster phase wrapping per unit density.

By choice of the phase plate the phase shift built up during passage of the cloud therefore results in intensity de- or increase, as shown if fig.3.14. The phase plate used in the experiment had a spot of 200μm diameter with increased height, retarding the background light wave, therefore advancing it's phase relative to the object light resulting in a phase shift of $+\pi/2$ for light at 780nm. According to the refractive index equ.(3.25), negative "red" detuning results in positive phase shift in the object light, which upon interference with phase advanced reference light results in a bright image, i.e. the cloud appears in the image as an object with a brightness higher than the background level I_0.

From a 2 level system model, the usage of large detuning Γ results in non-destructive imaging, as the photon scattering rate drops $\propto \Gamma^{-2}$. In a real experiment the atoms approach during collision and form interaction potentials as described in section 2.3, which gives rise to photon scattering rates also for large detuning. Shining light with detuning of the order of the interaction potential depth into the cloud is equivalent to conducting a photoassociation experiment (as has been demonstrated for the D_1-transition in Rb_2 in ref. [Mill93]). On the blue detuning side the repulsive branches of the interaction potentials shift into resonance with any positive laser detuning at some interatomic distance during a collision [Suom95]. This causes significant trap losses, as the 2 atoms use the absorbed photon energy to repel each other out of the trap.

We found in the experiment[6] that phase contrast imaging in the region from -2.8 GHz up to resonance is destructive with frequency dependent levels of particle losses per imaging flash. We attribute this to bound states in the molecular interaction asymptotes of the $(5S_{1/2} - 5P_{3/2})$ transition [Kemm04] and assume, that atoms are photoassociated during detection. These lines are hard to avoid in view the linewidth of our phase contrast imaging laser ($\sim$ 2MHz FWHM) and the density of lines close to the dissociation limit.

[6] The phase contrast imaging system was used solely in the quadrupole oscillation experiment, described in chapter 4.

Using blue detuning we observe a similar loss-mechanism. We attribute this to the continuum states of the repulsive branch of the molecular interaction potentials.
The only satisfactory result was obtained for maxumum detuning of -3GHz, as here the particle loss after 31 imaging shots was below our typical relative error in the particle number determination of 1%. Due to this limitation, the advantages of non-destructive multiple shot imaging in one experimental run can only be exploited for high atom densities.

For using the camera in multiple shot mode during phase contrast imaging, only an area of 512×32 pixels at the top-edge of the chip is used for imaging. A shift operation moves the charges of all wells on the CCD by 32 lines towards the shield on a timescale of 32μs, which is much faster than e.g. the radial oscillation period (2ms). Shift operations cannot be applied to lines individually, but affect all lines simultaneously. Since here one shift does not move the information under the shield mounted in the camera, additional shields must be installed, to avoid the wells collecting photons from the next imaging flash. These shields are formed by a pair of blackened razor blades, that are mounted in the focal plane of the virtual cloud image, and leave only the part of the field of view open, that is imaged by the 512× 32 pixels stripe (see fig.3.13). Therefore the total height of 1024 pixels can be subsequently illuminated in stripes of 32pixels, yielding a total of 32 independent images. Since read-out starts at the moment of the first collected stripe reaching the bottom of the CCD surface, the 32nd stripe cannot be shifted into the covered region and is over-exposed by background light during read-out, so a maximum of 31 images can be used. Due to the critical alignment of the shadowing blades, at the top and bottom of each image stripe 3 pixel are neglected, since dust particles on the razor blades occasionally disturb the image pixels in their vicinity, so out of each stripe only the central 26 pixels are taken into account, offering an image height of 50μm. Since typical cloud diameters in experiments, that used phase contrast imaging (see chapter 4) are of the order of 30μm this scheme could not be extended to more image stripes per experimental sequence without loosing the radial $1/e$-size information.

3.4.3 Resolution and lensing

The optical system that is sketched in fig.3.13 transports the shape information, stored in the light intensity and phase, to the CCD chip. If any curvature is introduced to an (idealized) flat phasefront [Self83], i.e. the imaging laser beam, the light partly focuses or defocuses, as - according to Huygens-principle - the propagation direction of the lightwave is orthogonal to the phasefront. If parts of the wavefront are not recollected, the image suffers quality degradation, equivalent to failing to recollect all components in a Fourier-transformation [Bech67]. This is principally limited as the imaging optics have finite size. This limit is expressed in terms of the numerical aperture NA and the maximum collection angle γ of an optical system

$$NA = \frac{r}{f}, \qquad \gamma = \arcsin(NA), \tag{3.36}$$

where r is the radius of the lens and f its focal length [Hecht]. The front imaging achromat in this experiment has a focal length of 100mm and a diameter of 30mm, so the numerical aperture is $NA = 0.15$ and the collection angle $\gamma = 8.6°$, limited by the

geometrical distance between the vacuum cell center and the volume of the magnetic trap coils. The remaining optics are designed not to degrade the numerical aperture further.

Two main effects have to be taken into account:
Object size As every object acts as an aperture, diffraction occurs at the object edges, which introduces wavefront curvature at the edges. As the diffraction angle increases as the object size decreases, the quality of the imaging system is expressed in terms of smallest resolvable object size. Insufficient resolution results in washing out of edges of imaged objects or patterns.
The optical resolution limit in this experiment is measured with a positive 1951 USAF resolution target[7]. A stripe pattern is defined as resolved if the transmitted intensity is modulated at least by 20%. The smallest resolved pattern has a repetition period of 6.9 μm, which corresponds to a resolution of 3.3 μm (1/e-halfwidth).
Lensing As the wavefront experiences a density and detuning dependent phase shift as described by equ.(3.28), the wavefront acquires a profile proportional to the integrated cloud shape. For the case of a thermal cloud, the 3-D profile is Gaussian in all directions, as argued in section 2.1.1, and on integration over one Cartesian dimension it remains Gaussian. By calculating the point of largest phase front angle from flat phase, the maximum angle of the propagation direction of the light wave phase front from the forward vector after passing the cloud can be retrieved. As this value depends on atom density, detuning and cloud diameter, it has to be recalculated for the individual experimental conditions. Due to the fact, that in this case the whole cloud acts as a lens, this effect is referred to as 'lensing' (a more extensive treatment is presented in [Brad97]; to realize the importance of lensing see the related article [Brad95]). Lensing shows as a redistribution of light within the image. In extreme cases the cloud appears to have bright or dark halos around it, depending on the sign of detuning. This effect can be avoided, by using large or zero imaging detuning, as suggested by equ.(3.28), if experimental conditions allow this.

3.4.4 Image processing

For creating a scaled, background free image, the usual sequence of taking 3 images with subsequent image subtraction and division is performed [Kett99]. The first image is called the object image P_{obj}, which contains the absorption or phase contrast image of the cloud, where the latter one consists of 31 stripes with cloud images, as explained in the previous section. After removal of the cloud from the field of view (in absorption imaging the detection light flash removes the cloud, during phase-contrast imaging this has to be done actively) a second image with a detection flash identical to the object imaging flash is acquired, called the reference image P_{ref}. The background image P_{bgr} is acquired where no detection flash is applied. During phase contrast imaging for both reference and background image the whole sequence of 31 stripes is re-done. A single reference and background stripe would be sufficient, but for compatibility reasons in the control software it had to be done as described. By performing pixel-wise the operation

$$P(y,z) = \frac{P_{obj}(y,z) - P_{bgr}(y,z)}{P_{ref}(y,z) - P_{bgr}(y,z)}, \tag{3.37}$$

[7]Such a target consists of a glass plate with a collection of aequi-distant aluminum stripe patterns with various sizes.

one retrieves a background free picture, where all static noise patterns, like fringes caused by the vacuum cell or other optics, are divided out. This image is also normalized to the incident intensity I_0. Some fringe noise remains due to non-static disturbances.

The resulting image is pixel-wise converted to particle column density, by inverting either equ.(3.31) or equ.(3.34). For phase contrast images, one can alternatively also combine equs.(3.31) and (3.34) (there with '-' chosen out of '$\pm$' as argued before) to find

$$P_{virt}(y,z) = \exp\left(\frac{(P_{PhC}(y,z)-1)\cdot(1+\delta_{PhC}^2)}{(1+\delta_{Abs}^2)\cdot\delta_{PhC}}\right), \tag{3.38}$$

where the choice of sign is in accordance to the phase plate of the experiment. Conveniently, the photon scattering cross section σ_0 divides out. By applying this transformation pixel-wise to a phase contrast image P_{PhC} after preprocessing by equ.(3.37) at known phase contrast detuning δ_{PhC}, one can transform the image into a virtual absorption image, where one can adjust the resulting optical density $[(-1)\ln(P_{virt}(x,y))]$ by choice of δ_{Abs}, here the 'virtual' absorption imaging detuning. This allows to re-use analysis code that is designed for absorption images also for phase contrast images, by passing the virtual absorption image with the virtual absorption detuning to it, which is the method, used in the experiment analysis[8].
The resulting density profile is then fitted by a 2 dimensional representation of a Gaussian for a thermal cloud (see section **1.1**), an inverted parabolic function for a Bose-Einstein condensate (see section **1.6**) or a combination of both, for clouds that contain fractions of both. With known expansion time t_{exp}, trapping frequencies $\omega_i\,(i{=}x,y,z)$ and photon scattering cross sections σ_0, particle densities and cloud temperatures can be extracted.

3.5 Experimental control

The experimental sequence (loading, MOT, recapture, compression, evaporative cooling, the experiment itself, image acquisition and processing) is controlled by a PC system with μs timing precision. The control system consists of 2 PC's, out of which one (in Lab-jargon called Messknecht) controls the experiment, whereas the second (in Lab-jargon called Zeus) receives the acquired image and some other parameters of the command script for that particular experiment, and performs instant image fitting and data logging routines[9].

Zeus is a standard PC, linked to Messknecht by a 100Mbit network connection.
Messknecht is an industrial, self designed PC system: a passive PICMG Bus backplane with 7 ISA and 7 PCI slots (type BP-PX14S1) is mounted in a 19" rack with a PC-card (type SCA-IB740, Intel Pentium III, 1.0GHz) in one of it's 2 PC-card slots. The Data Acquisition (DAQ) hardware, mounted in the remaining slots consists of:

[8] This approach was chosen, since the image fitting routines contained advanced intensity levelling and noise reduction features, that are too extensive to reprogram, particularly, as the image quality suffers no degradation in this transformation.

[9] The control system was previously - i.e. for the theses of Igor Shvarchuck and Kai Dieckmann, where no information regarding the PC-control is given - distributed over 3 standard PCs, but apart from that nearly identical.

type	bus	manufacturer	connectors
DIO-128	ISA	Viewpoint solutions	100 DO
Lab-PC 1200	ISA	National Instruments	2 WO, 8 AI
AT-AO 10	ISA	National Instruments	8 AO, 2 WO
PCI-6711	PCI	National Instruments	4 WO
P.PCI Interface	PCI	Princeton Instruments	P.I. Camera Control
PCI-6713	PCI	National Instruments	8 AO
PCI-6534	PCI	National Instruments	32 DO (dedicated for DDS)

where AO stands for analog out, DO for digital out, AI for analog in, and WO for waveform out[10]. The AI are used only for monitoring external parameters, e.g. the laboratory ambient temperature and the lock of lasers. No experimental parameters were measured, except the image. All DO's are buffered by opto-couplers to prevent damage to the DIO-128 because fast switching of high currents via FET's controlled by DO's can cause voltage spikes travelling back the line. The AO's and WO's are partly buffered by isolation amplifiers, partly left unprotected.

Two self developed LabView-programs (®National Instruments), running under the operating system on Windows2000 (®Microsoft corp.), on Messknecht and Zeus operate synchronized via the network. Their network communication protocol allows Messknecht to perform an experimental run, while Zeus analyzes the previous image, so no delay for analysis is created between experimental runs.

To execute an experiment the LabView program interprets an input file (in Lab-jargon called the timeframe) that forms a list of ≈250 individual subsequent or parallel events, that define an experiment, create all digital patterns for the DAQ-boards, load these patterns into their on-board memories, and start the execution by the DIO-128. The stepping of the analog boards to the next output value is triggerd and synchronized by TTL pulses from DO's of the DIO-128. Thus an experiment execution occurs at hardware timing, independently of the PC hard- or software, which also secures all experimental devices from eventual OS-failures. By automatically modifying the timeframe file the system is capable of scanning experimental parameters without human interaction.

3.6 Image acquisition and analysis control

The camera CCD chip illumination and read-out is triggered by TTL pulses, send from the DOs of the DIO-128. The images are transferred from the camera hardware to the PC by the WinView (®Princeton Instruments) camera driver, that is linked to LabView via Active-X.

A typical run takes about 50 seconds, so the Zeus PC has only limited time at disposal

[10]In order to get this amount of boards to operate without resource conflicts, IRQ's, DMA's and Base-I/O's had to be manually assigned by setting in the BIOS IRQ's as reserved, thereby disabling a few unnecessary PC features, and manually overriding the Windows DMA and Base-I/O assignment routine.

to complete his analysis before the arrival of the next image. Therefore only simple cross-section fitting routines or pixel counting orientated methods based on the transformations given in section 3.4.4 are executed on line with software written in LabView. More complex image fitting, based on full 2-D surface fits of the images is performed by separate standard PC's off-line. As these routines are programmed in the mathematical package Mathematica (® Wolfram research), which is not optimized for such procedural tasks, a fit result requires ≈2 minutes per image to complete.

Chapter 4
Hydrodynamic shape oscillations

4.1 Introduction

Collisional hydrodynamics has gradually become an important issue for the understanding of experiments with dilute quantum gases [Pit-Str]. When the atomic mean-free-path is smaller than the characteristic dimensions of typical elongated atomic clouds, the gas properties depend on the local density field and exhibit collisional hydrodynamics rather than the collisionless dynamics of a nearly ideal gas [Pit-Str, Lifsch]. For Bose gases and Bose-Fermi mixtures it is difficult to penetrate deeply into this collisional hydrodynamic regime as three-body molecule formation will give rise to fast decay of the samples [Pit-Str]. Therefore, also the transition region between collisionless and hydrodynamic conditions is of substantial practical importance.

The hydrodynamic flow of classical fluids was described as early as 1755 by the equation of motion of Euler [LandauF]. The opposite limit of collisionless flow is equally well understood since the work of Maxwell and Boltzmann and the investigation of rarefied gas dynamics around the turn of the last century [Lifsch]. The transition regime between collisionless and hydrodynamic conditions deserves special attention as the crossover behavior is often non-intuitive as was already noted by Knudsen in 1908 [Knud09]. With the availability of trapped ultracold gases there is a renewed interest in the collisional hydrodynamics. For non-degenerate quantum gases in harmonic traps the absence of the familiar wall-boundary condition of zero hydrodynamic flow at the sample edges gives rise to a very close phenomenological similarity with the superfluid hydrodynamics of Bose-Einstein condensates [Pit-Str, Kaga97, Grif97, Niku98]. Collisional hydrodynamics also has to be considered in two-component Fermi gases near inter-component Feshbach resonances, where the intercomponent scattering length is tuned to large values in order to optimize thermalization [Stri04, OHar02a, Rega03, Bour03].

The onset of collisional hydrodynamics was first observed at MIT in measurements of the damping and frequency shifts of the low-lying $M = 0$ quadrupole shape oscillation of cigar-shaped samples of the ^{23}Na quantum gas, just above the Bose-Einstein transition temperature T_c [Stam98]. Similar results were obtained at the ENS-Paris with clouds of metastable triplet helium (He^*) [Ledu02]. A demonstration of the collisional crossover was given at JILA by measuring, for varying density, the damping of the center of mass oscillations of two distinguishable clouds of ^{40}K, passing in anti-phase [Gens01, Tosc04]. At AMOLF we showed how hydrodynamic conditions affect the BEC-formation process in elongated samples [Bugg04a] and can give rise to substantial shape oscillations of the condensates being formed [Shva02]. Further, hydrodynamic conditions were shown to give rise to anisotropic expansion of thermal Bose gases after switching off the confining field, which has important consequences for time-of-flight thermometry [Shva03a, Gerb04]. Hydrodynamic effects were observed more pronouncedly in the expansions of two-component Fermi gases tuned near an inter-component Feshbach resonance [OHar02a, Rega03, Bour03]. Also the investigation of the macroscopic dynamics of two-component Fermi gases in

the BCS-BEC transition region requires detailed understanding of the hydrodynamics [Grei03, Joch03b, Zwie03, Cubi03].
In this paper we study the crossover from collisionless to hydrodynamic conditions in non-degenerate clouds of ^{87}Rb by measuring both the frequency shift and the damping of the low-lying $M = 0$ quadrupole shape oscillation as a function of density. In accordance with theory [Kaga97, Grif97, Niku98], the frequency shifts down from $2\omega_z$ in the collisionless regime to $1.55\omega_z$ for collisionally hydrodynamic clouds, with ω_z the axial frequency of our trap. Most of the shift occurs over a narrow range of densities around the crossover density, where the mean-free-path becomes comparable to the axial size of the sample. At this density also the strongest damping is observed. All our data were taken for temperatures $T > 2T_c$ to avoid precursor phenomena close to the BEC transition [Niku04]. Hence, although the collisions are quantum (i.e. s-wave), the gas is statistically classical. As we observed a temperature dependence of the oscillation frequencies, we derive theoretical expressions to include the influence of trap anharmonicities, which cause this effect. These expressions allow numerical evaluation for regular potentials. Further, they allow us to derive convenient analytic approximations that apply to *any* elongated Ioffe-Pritchard trap.

4.2 Background

4.2.1 Mode structure

For quantum gases well-above the degeneracy temperature, all oscillatory modes are solutions to the classical Boltzmann equation [Pit-Str, Cha-Cow]

$$\frac{\partial f}{\partial t} + \mathbf{v} \cdot \nabla_{\mathbf{r}} f + \frac{\mathbf{F}}{m} \cdot \nabla_{\mathbf{v}} f = I_{\text{coll}}[f], \tag{4.1}$$

where $f = f(t, \mathbf{r}, \mathbf{v})$ is the phase-space distribution-function with $\mathbf{r} = \{r_j\} = (x, y, z)$ and $\mathbf{v} = \{v_j\}$ the position and momentum vectors, m is the atomic mass and $\mathbf{F}(\mathbf{r}) = -\nabla_{\mathbf{r}} U(\mathbf{r})$ the force of the trapping potential $U(\mathbf{r})$; $I_{\text{coll}}[f]$ is the collisional integral [Cha-Cow].
For *isotropic* harmonic traps the normal modes are multipoles of order $(L; M)$ [Grif97]. Oscillations in the dipole mode ($L = 1$) are commonly used for measuring trap frequencies by observing the motion of the center of mass of trapped clouds as a function of time. In harmonic traps these oscillations are undamped, since for any pair of atoms also their center of mass oscillates at the trap frequency ω. As noted in ref. [Grif97, Niku98], Boltzmann obtained in 1897 the surprising result that for isotropic harmonic traps also the monopole (or 'breathing') mode ($L = 0$) is undamped, oscillating at frequency 2ω, *independent* of the density. The next normal mode solutions are shape oscillations ($L \geq 2$). In the hydrodynamic limit they are (like the dipole mode) both irrotational and divergence-free [Grif97, Niku98], and therefore also undamped. They oscillate at frequency $\sqrt{L}\,\omega$. Because the flow is irrotational shear viscosity plays no role and viscous damping is absent. Because the flow is divergence-free the temperature is constant.

In the collisionless regime they are again undamped but oscillate at frequency $L\,\omega$. This difference in frequency results in damping in the transition regime [Kavo98] due to collisional relaxation towards equilibrium.

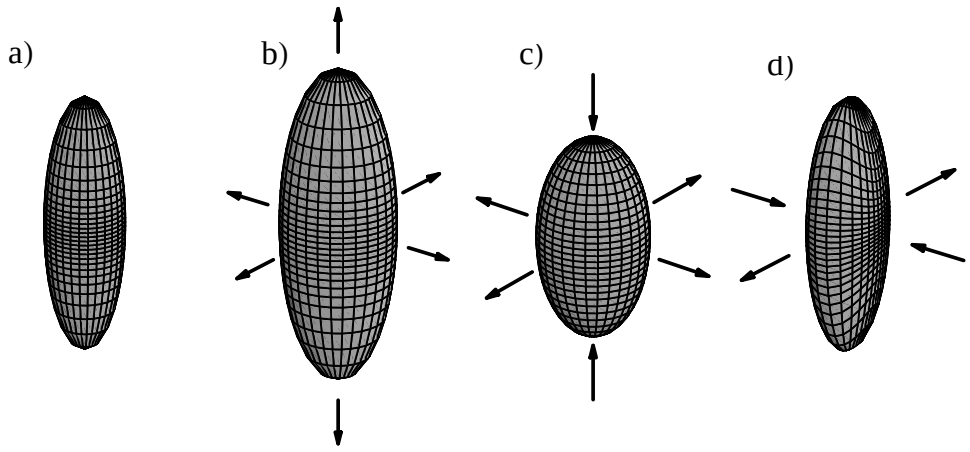

Figure 4.1: Graphical representation of the surface deformation under shape oscillations for a model cloud, shown at rest in a). The following images show one extremal amplitude position (maximal extension or compression of each axis) for an amplitude of 30%. The breathing mode (L=0;M=0) pictured in b) shows an all in phase oscillation of the cloud in all directions. In the quadrupole mode (L=2;M=0) in c) the radial dimensions dilate in anti-phase with the axial one (here in vertical direction). In the M=±2 mode the x- and y- dimension oscillate in anti-phase, whereas the axial size remains static.

For *elongated* harmonic traps, with axial direction z and radial coordinate $\rho = (x^2 + y^2)^{1/2}$, we distinguish three ($L = 1; M = 0, \pm 1$) dipole modes, oscillating uncoupled and undamped at frequencies ω_z and ω_ρ. In the hydrodynamic limit, the monopole mode is coupled to the ($L = 2; M = 0$) quadrupole mode. Fig.4.1 shows the 3-dimensional amplitude structure exemplary for the ($L = 0; M = 0$)-'breathing', ($L = 2; M = 0$)-'quadrupole' and ($L = 2; M = \pm 2$) mode. Decoupling in terms of irrotational solutions yields [Kaga97, Grif97, Niku98]

$$\omega^2 = \frac{1}{3}\left[5\omega_\rho^2 + 4\omega_z^2 \pm \sqrt{25\omega_\rho^4 + 16\omega_z^4 - 32\omega_\rho^2\omega_z^2}\,\right]. \tag{4.2}$$

In the experiment described in this paper, we study the low-lying $M = 0$ coupled monopole-quadrupole mode, corresponding to the minus sign in equ. (4.2). In this mode the radial size oscillates in anti-phase with the axial size. For shortness we will refer to it as the 'quadrupole' mode with frequency ω_Q in all regimes, although in the collisionless limit the axial and radial motion decouple and the overall behavior is to be considered as a superposition of '1D-breathing modes', showing dephasing behavior. This dephasing can be avoided by exciting a pure axial oscillation. As follows directly from equ. (4.2), in the limit of very elongated clouds ($\omega_\rho \gg \omega_z$) we have $\omega_Q = \sqrt{12/5}\,\omega_z \approx 1.55\,\omega_z$.

4.2.2 Quadrupole dispersion relation

The transition regime is less obvious. Describing the oscillation phenomenologically by $e^{-i\,\omega t}$ the crossover takes the form [Kavo98]

$$\omega^2 = \omega_{\rm cl}^2 + \frac{\omega_{\rm hd}^2 - \omega_{\rm cl}^2}{1 - i\,\omega\tilde{\tau}}, \tag{4.3}$$

where $\omega = \omega' + i\omega''$ is the complex quadrupole frequency for a given thermal relaxation time $\tilde{\tau}$; $\omega_{\rm hd}$ and $\omega_{\rm cl}$ are the (real) frequencies of this mode in the hydrodynamic ($\omega'\tilde{\tau} \ll 1$) and collisionless ($\omega'\tilde{\tau} \gg 1$) limits, respectively.

Expansion solution By separating complex and imaginary part of $\omega_q = \omega' + i\omega''$ we expand equ.(4.3) to

$$\left(\omega'^2 - \omega''^2\right) + i\,2\omega'\omega'' = \omega_{cl}^2 + \frac{(\omega_{hd}^2 - \omega_{cl}^2)\,(1+\omega''t)}{1 + 2\omega''t + \omega''^2t^2 + \omega'^2t^2} + i\frac{(\omega_{hd}^2 - \omega_{cl}^2)\,\omega'^2t}{1 + 2\omega''t + \omega''^2t^2 + \omega'^2t^2}. \tag{4.4}$$

Assuming, that the square of the real part is positive and therefore contains no contribution of the imaginary part, we find a simplified equation for the real part

$$\omega'^2 - \omega''^2 = \omega_{cl}^2 + \frac{(1+\omega''t)\,(\omega_{hd}^2 - \omega_{cl}^2)}{1 + 2\omega''t + \omega''^2t^2 + \omega'^2t^2}, \tag{4.5}$$

and for the imaginary part

$$2\omega'' = \frac{t\,(\omega_{hd}^2 - \omega_{cl}^2)}{1 + 2\omega''t + \omega''^2t^2 + \omega'^2t^2}. \tag{4.6}$$

These can be resolved analytically with some algebraic efforts. A relatively simple, yet precise approximation is, neglecting the ω''^2-terms in both parts, which yields an equation of 2nd order in ω'^2 and one of 2nd order in ω'', which are resolved by

$$\omega' = \sqrt{\frac{\omega_{cl}^2}{2} - \frac{1}{2t^2} - \frac{\omega''}{t} + \sqrt{\frac{1}{4}\left(\omega_{cl}^2 - \frac{1}{t^2}\right)^2 + \frac{\omega_{hd}^2}{t^2} + \frac{\omega''}{t}\left(\omega_{hd}^2 + \frac{1}{t^2}\right) + \frac{\omega''^2}{t^2}}} \tag{4.7}$$

$$\omega'' = \frac{-1}{4t} - \frac{\omega'^2t}{4} + \sqrt{\left(\frac{1}{4t} + \frac{\omega'^2t}{4}\right)^2 + \frac{1}{4}\,(\omega_{hd}^2 - \omega_{cl}^2)}, \tag{4.8}$$

where the positive sign of both square-roots was chosen to yield a non-diverging solution. At this level of approximation real and imaginary part are still coupled to each other, which can be easily resolved by a recursive calculative algorithm, that starts interpolating from any extremal regime, where the solution is known. Both approximations agree with a full solution to better than 2.5%.

Intuitive Picture To have an intuitive picture of the solutions of equ.(4.3) one can separate the real and imaginary parts of ω and make the identification ($\omega_Q = \omega'$, $\Gamma = -\omega''$). For $\Gamma/\omega_Q \ll 1$ we can approximate the imaginary part of the solution by the convenient form

$$\Gamma \simeq \frac{\tilde{\tau}}{2}\frac{\omega_{\rm hd}^2 - \omega_{\rm cl}^2}{1 + \omega_{\rm cl}^2\tilde{\tau}^2}, \tag{4.9}$$

which underestimates the maximum damping by 23%. The solution for the real part of equ. (4.3) can be heuristically, but fairly accurately (±0.3%) described by

$$\omega_Q \simeq \omega_{\rm hd} + (\omega_{\rm cl} - \omega_{\rm hd})\,(2/\pi)\arctan\!\left(\omega_{\rm cl}^2\tilde{\tau}^2\right). \tag{4.10}$$

We define the 'cross-over point' as the point where maximum damping occurs and the frequency is at the intermediate value $\omega_Q = 1/2\,(\omega_{cl} + \omega_{hd})$. From Eqs. (4.9) and (4.10) this is seen to occur at the relaxation time $\tilde{\tau} = \tilde{\tau}_0$, where $2\omega_z\tilde{\tau}_0 = 1$.

4.2.3 Role of relaxation

Equ. (4.3) can be obtained from the Boltzmann equation in the relaxation time approximation [Guer99, AlKh00], where the collisional integral is replaced by

$$I_{\rm coll}[f] \simeq -\,(f - f_{\rm le})\,/\tau. \tag{4.11}$$

Here τ is the relaxation time and $f_{\rm le} = f_{\rm le}(t, x, v)$ the local thermal distribution, which has an isotropic momentum distribution [Pedr03]. For harmonic traps one has [Guer99]

$$\tau^{-1} = \frac{\sqrt{2}}{5}\tau_c^{-1}, \quad \text{where} \quad \tau_c^{-1} = \sqrt{2}\,n_0\overline{v}_{th}\sigma \tag{4.12}$$

is the elastic collision rate at the trap center [Cha-Cow], with $\overline{v}_{th} = (8k_BT/\pi\,m)^{1/2}$ the mean thermal velocity at temperature T, n_0 the central density and σ the elastic-scattering cross section. To arrive at equ. (4.3) the relaxation time has to be renormalized by a factor that depends both on the cloud shape and the mode considered. For the $M = 0$ quadrupole mode in very elongated harmonic traps one finds $\tilde{\tau} = 6/5\,\tau$ [Guer99, AlKh00].

4.3 Driving technique

Any type of oscillation can be triggered by preparing the cloud in a state, which is equivalent to a phase space configuration, that represents a certain moment in the phase development of the oscillation, and then observing the oscillation in the standard trapping geometry. In principal, any configuration in phase space can be chosen as a starting point, but configurations, where there are kinetic components to prepare are technically difficult to realize (as done e.g. by parametric driving). An extremal cloud-shape at rest, e.g. a moment, when all parameters are at a turning point, is preferable.

A monopole mode oscillation can be triggered by preparing the cloud in a trapping geometry, with uniformly up- or downscaled trap-frequencies, and then allowing the cloud to start it's oscillatory motion with a contraction or expansion, when the trap diabatically returns to its standard configuration. A dipole mode can be realized by a sudden displacement of the trapping potential. Also a Quadrupole mode can achieved by such an approach, since axial and radial cloud size oscillate in anti-phase and therefore come to a turning point at the same moment. Such an approach is complicated by the fact, that the amount of oscillatory amplitude in the radial direction varies with the hydrodynamicity of the sample. However, in the hydrodynamic limit, rapid

thermalization will enforce the proper oscillatory mode on a short timescale, even if only the axial dimension experiences a sudden change in frequency. Moreover, modification of the tight, radial confinement gives more easily rise to higher modes in the axial direction, since the involved frequency is higher. Also constrains about timing and precision make operation in this way experimentally more critical.

Therefore the following approach (which is the proper one for the collisionless limit) has been chosen: the cloud is prepared at rest in a trap, where the axial frequency ω_z is lowered. Then the axial confinement is re-tightened, and the cloud starts the oscillation by contracting in the axial dimension. During this process, the radial frequency ω_ρ is kept constant. The definite knowledge of the starting phase and amplitude of the shape oscillation is the most striking advantage of this driving technique.

In order to deform the trapping potential in the described way, the method of Time Averaged Potential has been developed and applied. The principal is based on the fact, that any recursive modification of the trapping geometry, that occurs fast as compared to the mobility of the trapped atoms, is experienced only in its cycle average. Since this modification has to be applied to the magnetic field, the modulation must occur at a timescale short as compared to the Larmor frequency to avoid depolarization of the sample, but this does not impose a tight constrain and the successful realization has been demonstrated before [Petr95].

4.3.1 TAP deformation

The time average of a magnetic field $B(z, \rho, t)$ due to a time dependent modulation with a cycle time T is given by

$$\overline{B(x,y,z)} = \frac{1}{T}\int_0^T B(x(t), y(t), z(t))\, dt, \tag{4.13}$$

where the unmodulated magnetic field is given by

$$B(x,y,z) = B_0\sqrt{(1+\beta z^2)^2 + (\alpha^2-\beta)(x^2+y^2)}, \tag{4.14}$$

with the scaled trap parameters $\beta = \beta_{real}/B_0$ and $\alpha = \alpha_{real}/B_0$ (see section 3.2 and equ.(3.10)). The modulation is introduced by a homogeneous magnetic field B_m, whose field vector rotates in the radial plane: $\vec{B}_m(t) = B_m[\sin(2\pi\, f\, t)\vec{e}_x + \cos(2\pi\, f\, t)\vec{e}_y]$ with the modulation frequency $f = 1/T$. The field B_m results in a shift of the potential minimum by an amount

$$\rho_m = B_m/\alpha_{real} = B_m/(\alpha\, B_0). \tag{4.15}$$

Therefore all momentary positions with respect to the magnetic field are shifted by

$$x(t) = x + \rho_m \sin(2\pi\, f\, t) = x + \rho_m s_\phi \tag{4.16}$$

$$y(t) = y + \rho_m \cos(2\pi\, f\, t) = y + \rho_m c_\phi, \tag{4.17}$$

where the abbreviations $\sin(2\pi f\, t) = \sin(\phi) = s_\phi$ and cos alike are introduced for convenience. According to equ.(4.13) the scaled, time averaged magnetic field configuration is

given by:

$$\frac{B(x,y,z)}{B_0} = \frac{1}{2\pi}\int_0^{2\pi}\sqrt{(1+\beta z^2)^2+(\alpha^2-\beta)((x+\rho_m s_\phi)^2+(y+\rho_m c_\phi)^2)}\,d\phi \tag{4.18}$$

$$= \frac{1}{2\pi}\int_0^{2\pi}\sqrt{\mathbf{C}+(\alpha^2-\beta)2\rho_m(x\,s_\phi+y\,c_\phi)}\,d\phi, \tag{4.19}$$

with the abbreviation

$$\mathbf{C} = (1+\beta z^2)^2+(\alpha^2-\beta)(x^2+y^2+\rho_m^2). \tag{4.20}$$

By further introducing the new variables, $x = \xi\, s_\chi$, $y = \xi\, c_\chi$, where $\xi^2 = x^2+y^2$ (χ can be precisely defined as well, but is irrelevant since it is integrated over), we can make use of the well-known identity

$$\sin(\phi)\cos(\chi)+\cos(\phi)\cos(\chi) = \cos(\phi-\chi) \tag{4.21}$$

and find

$$\frac{B(x,y,z)}{B_0} = \frac{1}{2\pi}\int_0^{2\pi}\sqrt{\mathbf{C}+(\alpha^2-\beta)2\rho_m\,\xi\,c_{\phi-\chi}}\,d\phi \tag{4.22}$$

$$= \frac{1}{2\pi}\int_0^{2\pi}\sqrt{\mathbf{C}+\mathbf{D}\,c_{\phi-\chi}}\,d\phi = \frac{1}{2\pi}\int_0^{2\pi}\sqrt{\mathbf{C}+\mathbf{D}\,c_\phi}\,d\phi, \tag{4.23}$$

where the abbreviation $\mathbf{D} = (\alpha^2-\beta)2\rho_m\,\xi$ has been introduced. We shift the variable $\phi \to \theta$ and find after a few arithmetic transformations:

$$\frac{B(x,y,z)}{B_0} = \frac{1}{2\pi}\int_0^{2\pi}\sqrt{\mathbf{C}+\mathbf{D}\,c_\phi}\,d\phi \tag{4.24}$$

$$= \frac{4}{2\pi}\sqrt{\mathbf{C}+\mathbf{D}}\int_0^{\pi/2}\sqrt{1-\mathbf{M}\,s_\theta^2}\,d\theta, \tag{4.25}$$

with $\mathbf{M} = (2\mathbf{D})/(\mathbf{C}+\mathbf{D})$. Thus we find on the r.h.s. the well-known elliptic integral, which is tabulated in books on mathematics and is also available in mathematical packages like Mathematica (®Wolfram Research). The last group of transformations and therefore equ.(4.25) is valid only, if $\mathbf{D} \le \mathbf{C}$ holds. This is equivalent to

$$0 \le \mathbf{C}-\mathbf{D} = (1+\beta z^2)^2+(\alpha^2-\beta)(x^2+y^2+\rho_m^2-2\rho_m\sqrt{x^2+y^2}) \tag{4.26}$$

$$= (1+\beta z^2)^2+(\alpha^2-\beta)(\rho_m-\rho_m\sqrt{x^2+y^2})^2, \tag{4.27}$$

which is valid f.a. $x,y,z,\rho_m \in \mathbb{R}$ if $\alpha^2 > \beta$ holds, which is true, since $\alpha^2 = 1.2\,10^5 cm^{-2} >> \beta = 1.4\,10^2 cm^{-2}$.

Expressions for the harmonic trap frequencies in the trap center, i.e. for $x,y,z = 0$ can be analytically derived by time averaging directly the second derivative, based on the assumption

$$\omega_{x,y,z} = \sqrt{\frac{\partial^2_{x,y,z}U(x,y,z,\rho_m)}{m}}. \tag{4.28}$$

The scaled, second derivative of the potential in equ.(3.10) with respect to x (y would be analogous) is given by

$$\partial_x^2 \frac{B(x,y,z)}{B_0} = \frac{(\alpha^2-\beta)}{[(1+\beta z^2)^2+(\alpha^2-\beta)(x^2+y^2+\rho_m^2-2\rho_m)(x\,s_\phi+y\,c_\phi)]^{1/2}} - \frac{(\alpha^2-\beta)^2(x-\rho_m\,s_\phi)^2}{[(1+\beta z^2)^2+(\alpha^2-\beta)(x^2+y^2+\rho_m^2-2\rho_m)(x\,s_\phi+y\,c_\phi)]^{3/2}}.$$

Calculating the time average, we find

$$\overline{\partial_x^2 \frac{B(x,y,z)}{B_0}} = \frac{(\alpha^2-\beta)}{[(1+\beta z^2)^2+(\alpha^2-\beta)(x^2+y^2+\rho_m^2)]^{1/2}} - \frac{(\alpha^2-\beta)^2(x-\frac{1}{2}\rho_m)^2}{[(1+\beta z^2)^2+(\alpha^2-\beta)(x^2+y^2+\rho_m^2)]^{3/2}}. \tag{4.29}$$

In the previous step, the assumption of

$$\frac{1}{2\pi}\int_0^{2\pi} \frac{1}{\sqrt{1+2\rho_m(\alpha^2-\beta)(x\,s_\phi+y\,c_\phi)}}\,d\phi = 1 \qquad \text{f.a. } x,y,\rho_m \in \mathbb{R} \tag{4.30}$$

has been made, which is not strictly valid, and for great x and y can even lead to an undefined integral[1]. Therefore any equations resulting from this derivation can only be applied in the limit of small x and y. Proceeding in the identical way, we find for the axial second derivative

$$\overline{\partial_z^2 \frac{B(x,y,z)}{B_0}} = \frac{2\beta+6\beta^2 z^2}{[(1+\beta z^2)^2+(\alpha^2-\beta)(x^2+y^2+\rho_m^2)]^{1/2}} - \frac{4(\beta z+\beta^2 z^3)^2}{[(1+\beta z^2)^2+(\alpha^2-\beta)(x^2+y^2+\rho_m^2)]^{3/2}}. \tag{4.31}$$

For the trap center where $x,y,z=0$ we thus find the modulated radial and axial frequencies

$$\overline{\omega}_{\rho,m} = \omega_\rho \frac{(1+\frac{1}{2}(\alpha^2-\beta)\rho_m^2)^{1/2}}{(1+(\alpha^2-\beta)\rho_m^2)^{3/4}} \tag{4.32}$$

$$\overline{\omega}_{z,m} = \omega_z\,(1+(\alpha^2-\beta)\rho_m^2)^{-1/4} \tag{4.33}$$

which is the result, presented as equ.(14) in [Tiec03].

4.3.2 Parameter choice

Starting from equs.(4.32) and (4.33) a variety of field configurations and jumps between various confinement frequencies can be realized by appropriate choice of oscillating modulation amplitude B_m and static magnetic field offset values with $B_{0,m}$ and without modulation B_0. The resulting field strength at the trap center during modulation is given by

[1] This choice of calculation is unfortunate, but the way, used in the publication [Tiec03].

the square sum of modulated field and static field, since $\vec{B}_m$ is orthogonal to the two parallel $\vec{B}_0$ and $\vec{B}_{0,m}$ at all times during a modulation cycle:

$$B_{res} = \sqrt{B_{0,m}^2 + B_m^2}. \tag{4.34}$$

In the following we denote with g the modulation amplitude, which is defined by making use of equ.(4.33) as

$$(1-g) = (1+b^2)^{-1/4} \quad \text{with} \quad b^2 = (\alpha^2 - \beta)\rho_m^2, \tag{4.35}$$

where we also introduce the modulation depth b. Thus a modulation amplitude of e.g. $g = 0.2$ indicates a decrease of axial frequency of 20%, and thereby results directly in the initial quadrupole oscillation amplitude. By again making use of the harmonic approximation of equ.(4.28) the boundary condition of equal radial frequency before and after modulation switch-off (as demanded in the introduction to this chapter) is expressed by

$$\sqrt{\frac{\alpha_{real}^2}{B_0}} = \sqrt{\frac{\alpha_{real}^2}{B_{0,m}}} \frac{(1+\frac{1}{2}b^2)^{1/2}}{(1+b^2)^{3/4}}. \tag{4.36}$$

Equ.(4.35) can be rewritten as

$$b = \sqrt{(1-g)^{-4} - 1}. \tag{4.37}$$

Inserting this into equ.(4.36) and resolving for $B_{0,m}$ we find

$$B_{0,m} = B_0 \frac{1}{2}\Big[(1-g)^6 + (1-g)^2\Big]. \tag{4.38}$$

By making use of the fact, that to very good approximation

$$b = (\alpha^2 - \beta)^{1/2}\rho_m \approx \alpha\,\rho_m = B_m/B_{0,m}, \tag{4.39}$$

holds, we rewrite equ.(4.35) to

$$\frac{B_m}{B_{0,m}} = \sqrt{(1-g)^{-4} - 1}. \tag{4.40}$$

By inserting equ.(4.38) we find

$$B_m = \frac{1}{2}B_0\Big[(1-g)^6 + (1-g)^2\Big]\sqrt{(1-g)^{-4} - 1}. \tag{4.41}$$

Starting from the desired modulation amplitude g one can thus find the combination of modulation field strength and static axial field during modulation, necessary to cause solely a jump of axial confinement frequency. Also the magnetic field strength without modulation B_0 can be varied, but was in practice left to the standard setting of 0.9G, since no particular advantage can be gained from doing so. Inserting equs.(4.38) and (4.41) into equ.(4.34) we find, that the magnetic field strength at the center changes from

$$\begin{aligned} B_{res} &= \sqrt{\frac{1}{4}B_0\Big[(1-g)^6 + (1-g)^2\Big]^2\Big((1-g)^{-4} - 1 + 1\Big)} \\ &= \frac{1}{2}B_0\Big[(1-g)^4 + 1\Big] \end{aligned} \tag{4.42}$$

back to B_0 at the moment of switch-off of the modulation. The jump occurs between positive values, but still it is apparent, that the modulation should not be switched instantaneously, in order not to depolarize the sample, as discussed in sec.3.2.3.

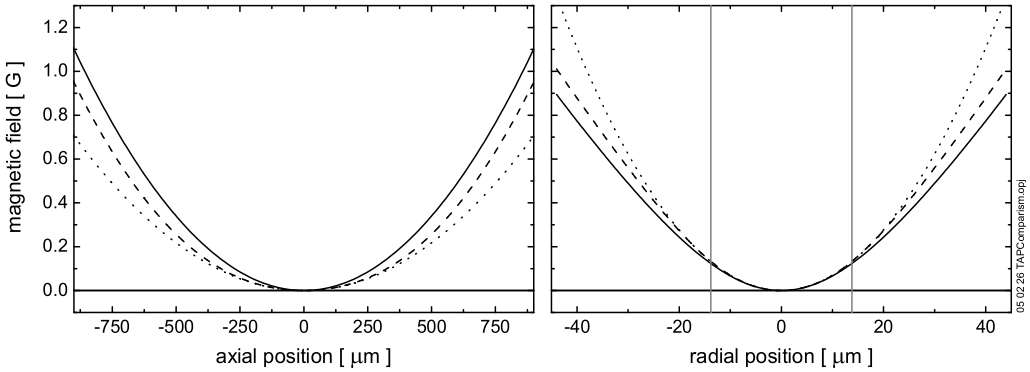

Figure 4.2: Axial (left graph) and radial (right graph) cross sections of potentials, with their individual trap offsets (B_0, B_{res}) subtracted. Straight line: the unmodulated potential. Dashed line: potential under modulation of $g = 0.2$, calculated via the elliptic integral, i.e. equ.(4.25). Dotted line: harmonic approximation with curvatures as given in equs.(4.32) and (4.33) for the same modulation. The displayed ranges are equivalent to ≈ 3 times the $1/e$-sizes of a thermal cloud at 10μK. The vertical lines in the right graph indicate the position of ρ_m for this modulation amplitude.

4.3.3 Comparison of approximation to potential

Equs.(4.32) and (4.33) provide the trap curvature in the trap center (i.e. $x, y, z = 0$) analytically correct. However, already from an intuitive point of view it is clear that in regions, where $(x^2 + y^2)^{1/2} >> \rho_m$ holds, the trap frequency is given by the curvature of the potential according to equ.(3.10), since in far-out regions with high field strengths the modulation represents a negligible disturbance. So the trap frequencies revert to the undisturbed ones with rising radial and axial distance, crossing through a transitional region around ρ_m (as can be seen in fig.4.3). According to its definition in equ.(4.15), this distance scales with the modulation amplitude B_m. It must be carefully checked, if the extent of the cloud under modulation remains well within this boundary.
Getting a quantitative measure, for which range the approximations still provide an appropriate description is analytically not possible, since for that, the second derivative of the elliptic integral in equ.(4.25) must be compared to the approximations for regions of $x, y, z \neq 0$, where no analytic description of the second derivative of the elliptic integral exists.

With mathematical packages like Mathematica (®Wolfram research) such a comparison can be easily done numerically. A thus calculated graphical representation of the two descriptions is presented in figs.4.2 and 4.3. It shows clearly, how for higher distances the trap slope and curvature returns to the original trap values, whereas a harmonic approximation does not reflect this behavior.

Special attention should also be paid to the 3-dimensional structure of the modulated magnetic field. Fig.4.3 shows exemplary, that even the representation via equ.(3.10) with adapted field constants approximates the modulated trapping field well only for regions up to a magnetic field strength of $\approx B(\rho = \rho_m, z = 0)$. It further reveals, that deviations occur in all spatial directions, which cannot be described by a cylindrically symmetric

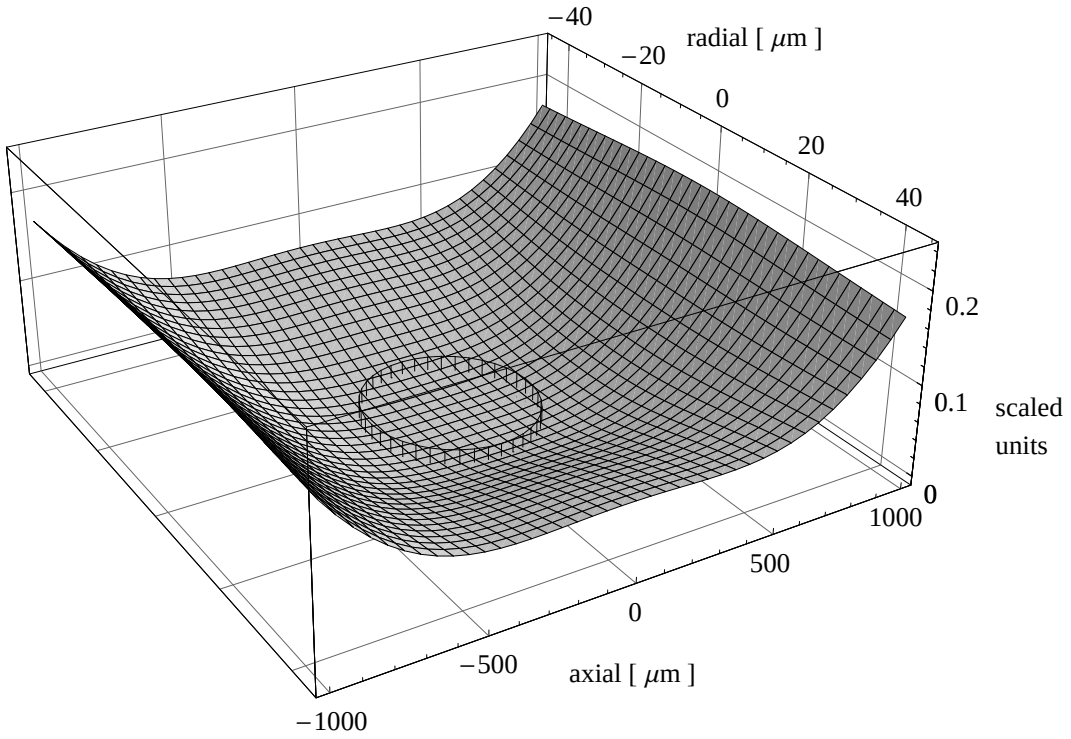

Figure 4.3: 3D representation of the magnetic field in the y-z plane, as calculated from equ.(4.25) subtracted by a representation, calculated from equ.(3.10) with adapted trap parameters α and β, to yield the modulated trap frequencies for $g = 0.2$. The latter one therefore includes more higher order corrections than a harmonic approximation. The difference is scaled to the magnetic field value at the corners of the displayed area, calculated from equ.(4.25). The circle marks the surface of an ellipsoid defined by a sphere with a diameter of $2\rho_m$, stretched in axial direction by the trap aspect ratio.

function. It also shows, that in axial direction, a modulation amplitude of $g = 0.2$ will result in a oscillation amplitude less than 20%, if this region is sampled by the wings of the thermal distribution.

4.3.4 Limits of the TAP approach

To excite the quadrupole mode we remove the modulation field B_m and observe the oscillation in a static potential. The advantage of the TAP approach is the rapid switching between trap frequencies, which is possible because both B_m and B_0 are generated by trim coils, whereas the main currents of the Ioffe-Pritchard trap remain untouched. Further, this approach offers definite knowledge of phase and amplitude.

However, as we have seen, the harmonic range $\rho_{0,m}$ where Eqs. (4.32) and (4.32) hold is proportional to the amplitude of the rotating field: $\rho_{0,m} = B_m/\alpha_{real}$. For regions outside the harmonic range the frequencies revert to the unmodulated ones. This implies a *minimum* required value for B_m to assure that the harmonic radius of the TAP field exceeds the thermal size of the sample, or accordingly lower temperatures. However, for the experiment, intended here, high particle numbers are required to reach deeply into the hydrodynamic regime, which in return implies a high critical temperature for

Bose-Einstein condensation [Ensh96]. On the other hand, the value of ρ_m can be increased only to a limited extent: first of all, since the modulation coils can dissipate only limited current without damage (see section 3.2.2); second, a larger modulation shift ρ_m is inevitably accompanied by a larger oscillation amplitude, which eventually brings the triggered oscillation out of the harmonic regime, and anharmonicities in the oscillation itself would have to be quantified and all data corrected for [LandauM]. Effectively, the cloud temperature has to be balanced between these two limits.

By comparing the magnetic field configurations it turns out, that for a modulation amplitudes of $g \leq 0.1$ a cloud temperature below 1μK would be necessary, to have $\rho_m > 2/3 \times 1/e$-size of the thermal profile, which is not acceptable, since for typical densities of the experiment this would be below the critical temperature for Bose-Einstein condensation. In the collisionless limit, where atom density is low, a lower temperature can be chosen. For a driving amplitude of $g = 0.2$, which represents the technical limit (due to heat dissipation of the helper coil connection wires), temperatures between 1 and 5 μK appear appropriate. In order to make use of the great variational range, this maximal amplitude was experimentally chosen.

Further we have seen, that the cloud density profile deviates from a Gaussian, if the extent of the cloud prepared in the TAP-modulated magnetic field reaches significantly beyond $\rho_{0,m}$. Transferring that distribution into the static magnetic field, in order to trigger the oscillation leads to excitation of higher modes. In particular, the structure of the anharmonicities in the off-axis directions, as presented in fig.4.3, can cause shear like surface modes. If additionally the thermal size of the cloud also exceeds the harmonic range of the static potential (which is *not* related to $\rho_{0,m}$), both anharmonicities will add to the excitation of higher modes.

4.4 Experiment

In our experiment we typically load 10^{10} atoms from the ^{87}Rb source described in ref. [Diec98] into a magneto-optical trap. After an optical molasses stage we optically pump the atoms into the fully stretched $(5S_{1/2}, F = 2, m_F = 2)$ hyperfine state and transfer the cloud into a Ioffe-Pritchard trap with frequencies $\omega_z/2\pi = 7$ Hz and $\omega_\rho/2\pi = 8$ Hz and central field $B_0 = 37$ Gauss. Any remaining population in the $m_F = 1$ magnetic sublevel is removed by gravitational drag. Then, we radially compress the cloud, changing the trap parameters to $\omega_\rho/2\pi = 19$ Hz at $B_0 = 8$ G. After a thermalization time of 100 ms we add, in a linear ramp over 0.5 ms, a magnetic field $B_m = 487\,\mathrm{mG}$, rotating at a frequency of $\nu_m = 7\,\mathrm{kHz}$ orthogonally to the trap axis, using the approach described in section 4.3. This gives rise to a Time-Averaged-Potential (TAP) field with offset $B_{0,m} \equiv (B_m^2 + B_0^2)^{1/2}$ and frequencies

$$\omega_{\rho,m} = \omega_\rho \frac{(1 + 0.5\,b^2)^{1/2}}{(1 + b^2)^{3/4}} \quad \text{and} \quad \omega_{z,m} = \omega_z \frac{1}{(1 + b^2)^{1/4}}, \tag{4.43}$$

where $b = B_m/B_0$ is the modulation depth.

We continue the compression to $\omega_{z,m}/2\pi = 16.8$ Hz, $\omega_{\rho,m}/2\pi = 474$ Hz and $B_{0,m} = 634$ mG ($B_0 = 406$ mG, $b = 1.2$). Then, we cool the sample by forced rf-evaporation to the final temperature of a few microkelvin. After reducing the density to the desired level by laser depletion, the sample is thermalized during plain evaporation periods of up to 2.5 s , which is sufficiently long even for our lowest densities. We then raise the rf-shield energy by a factor of 7 to avoid evaporation losses during the measurements.

The depletion is done with our detection laser. For absorption imaging we typically use 5% of the full detection intensity (2.4 mW) for typically 10 ms at a detuning of 32 MHz red to the $(5S_{1/2}, F = 2) \leftrightarrow (5P_{3/2}, F = 3)$ transition (D_2-line). For phase-contrast imaging we use $> 80\%$ of the full detection intensity at a detuning of -3 GHz for a duration of up to 100 ms. The lasers for phase-contrast and absorption imaging in our experiment are separate devices, the first operating in a region of ± 3 GHz (no online control), the second from -32 to $+15$ MHz (online control) with respect to the D_2-line (for a more complete description of the laser system refer to section 3.1.2). It was not possible to combine laser depletion with one laser source and imaging with the other laser during the same experimental run.

4.4.1 Excitation of the quadrupole mode

To excite the quadrupole mode we remove the modulation field B_m and observe the oscillation in a static potential, as proposed in sec.4.1. As expected, after transfer into the static potential the cloud starts to oscillate inwards as a cosine function with zero phase offset as can be seen in fig. 4.4.

As we remove the modulation, we simultaneously increase the central field to $B_0 = 900$ mG in order to keep ω_ρ constant. The procedure is done with a linear ramp of duration $\tau_{sw} = 230$ μs. This is slow enough to avoid switch-off depolarization and still much faster than the axial oscillation time, $\omega_z \ll \tau_{sw}^{-1} \ll \omega_{Larmor}$. Thus, after switching ω_z, the gas finds itself diabatically in an axially tighter potential. The axial trap frequency has increased to $\omega_z/2\pi = 21.1$ Hz, which changes the aspect ratio to $\omega_\rho/\omega_z \approx 23$ and puts us well into the elongated trap limit of equ. (4.2).

In this way we excite a pure axial oscillation, at least in the collisionless limit. In the hydrodynamic limit, in principle both the low-lying and the high-lying monopole-quadrupole modes could be excited. However, since even at our highest densities, *radially* we remain in the collisionless regime, the high-lying mode cannot be excited due to the lack of coupling.

As has been discussed in the previous section, special attention must be paid, to avoid triggering higher modes with this approach. However, even if such modes are excited, they oscillate at much higher frequencies and damp accordingly faster than the quadrupole mode under investigation.

For our highest-density samples, together with the condition $T \gtrsim 2T_c$, we have $\rho_{0,m} \gtrsim 10$ μm, which implies a required TAP amplitude $B_m > 350$ mG. The value of $B_m = 487$ mG, used in the experiment, represents our technical limit, and corresponds to the harmonic

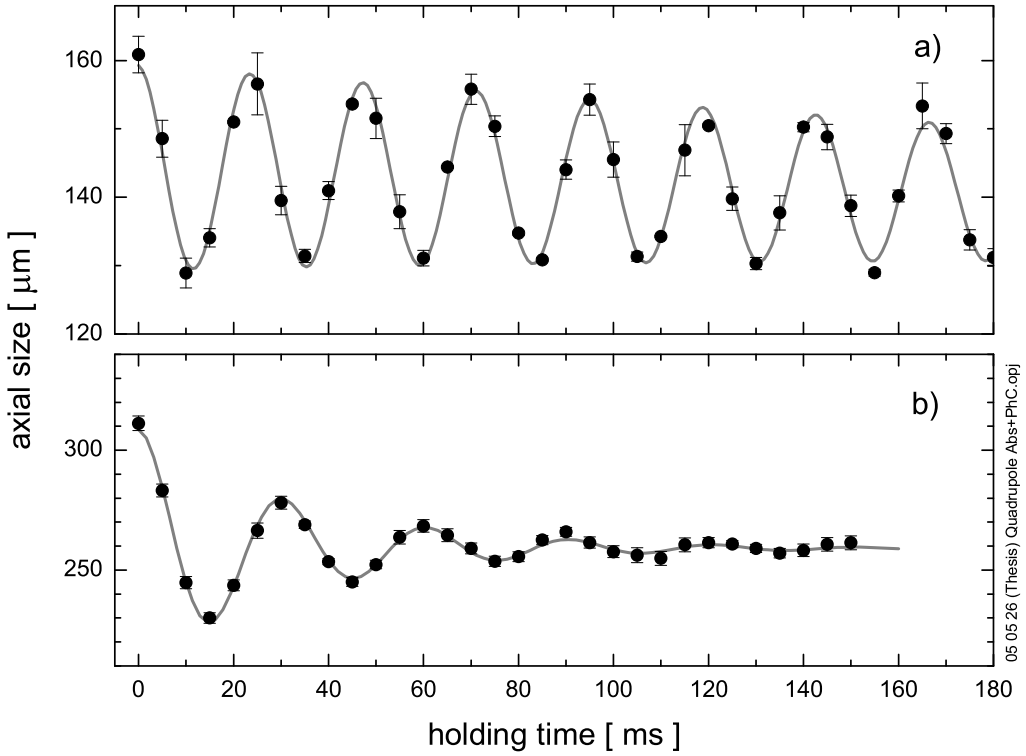

Figure 4.4: Typical quadrupole oscillation traces for fitting frequency and damping; raw data acquired at a temperature of $2\,\mu$K: a) Low density data ($n_0 = 1.7 \times 10^{11}\mathrm{cm}^{-3}$) with fit function (grey line) resulting in $\omega_Q/\omega_z = 2.0$ and $\Gamma/\omega_z = 0.01$. Each point represents the average of 3 absorption images.
b) High density data ($n_0 = 1.1 \times 10^{14}\mathrm{cm}^{-3}$) with fit function (grey line) resulting in $\omega_Q/\omega_z = 1.6$ and $\Gamma/\omega_z = 0.22$. Each point represents the average of 15 phase contrast images. The error bars represent the error in the mean.

$1/e$-size of a thermal cloud at a temperature of $9\,\mu$K. To assure that fitted values for frequency and damping are unaffected by higher modes, we neglect the first two cycles of oscillation traces acquired at temperatures above $7\,\mu$K, and the first cycle for traces acquired above $4\,\mu$K. For lower temperatures also the first cycle is analyzed. Note that the precise reproducibility of the starting phase of our oscillations allows this procedure without degrading the quality of the fits.

4.4.2 Description of the trapping field

During the observation of the quadrupole oscillation the cloud resides in a potential given by $U(\mathbf{r}) = \mu_B[B(\mathbf{r}) - B_0] + mgy$ for the chosen Zeeman-level in this experiment. Here μ_B is the Bohr magneton and g the gravity acceleration along the vertical direction (y-direction). For elongated Ioffe-Pritchard traps the modulus of the trapping field $B(\mathbf{r})$ is accurately described by [Berg87, Surk94]

$$B(x,y,z) = \sqrt{(B_0 + \beta z^2)^2 + \alpha^2(x^2+y^2) + 4\alpha\beta xyz}, \tag{4.44}$$

where $B_0 = 0.9$ G and $\alpha = 353$ G/cm are defined above and $2\beta = 274$ G/cm^2 is the axial curvature. To our knowledge α and β were constant throughout the measurements to within 0.1%; B_0 was monitored to be constant to within 1%. Expanding equ. (4.44) around the trap center and keeping the leading non-linearities [Surk94], the potential can be written as

$$U(\rho, z) = \frac{1}{2}m[\omega_z^2 z^2(1 - \frac{1}{2}\rho^2/\rho_0^2) + \omega_\rho^2 \rho^2(1 - \frac{1}{4}\rho^2/\rho_0^2)] + \cdots, \tag{4.45}$$

where $m\omega_z^2 = 2\mu_B\beta$, $m\omega_\rho^2 = \mu_B\alpha^2/B_0$ and $\rho_0 = B_0/\alpha = 25$ μm the harmonic radius. The gravitational force mg is small as compared to the gradient of the radial trapping field, $mg/\mu_B\alpha \approx 0.04$. Therefore gravity corrections may be neglected to lowest order in the expansion.

4.4.3 Detection procedure

Two imaging methods are used to observe the oscillations. For our highest-density samples we use phase-contrast imaging with red-detuned light (see sec.3.4.2). For densities $n_0 > 5 \times 10^{13}$ cm^{-3} a proper contrast is obtained at a detuning of -3 GHz, where the detection is essentially non-destructive. This allows us to register the oscillations in a sequence of 31 images at 5 ms intervals, taking advantage of the fast 'kinetics' imaging mode of our camera (see sec.3.4 for details on the camera). For lower densities the phase contrast method cannot be used because, at the (smaller) detunings required to maintain adequate phase contrast, photoassociation losses disturb the measurements (see discussion in sec.3.4.2). For densities $n_0 < 5 \times 10^{13}$ cm^{-3}, we used repetitive absorption imaging on the $(5S_{1/2}, F = 2) \leftrightarrow (5P_{3/2}, F = 3)$ transition (D_2-line), varying the holding time of the cloud after excitation of the oscillation (see sec.3.4.1). The lasers for phase-contrast and absorption imaging in our experiment are separate devices, the first operating in a region of ± 3 GHz (no online control), the second from -32 to $+15$ MHz (online control) with respect to the D_2-line. It was not possible to use both detection methods during the same experimental run.

The images were taken *in situ*, just before releasing the cloud from the trap. We apply the usual method of background subtraction and level-normalization to process the images. To retrieve the column density profile $n_2(y, z)$ and the axial and radial Gaussian $1/e$-sizes L_e and R_e, we fit a 2-dimensional Gaussian expression to the optical thickness distribution of our images (for more details on imaging, see section 3.4). The central density follows with $n_0 = n_2(0, 0)/\sqrt{\pi R_e^2}$ and, with equ. (4.12), the relaxation time can be expressed as

$$\omega_z \tilde{\tau} = \frac{3}{2}\frac{\omega_z}{\omega_\rho}\frac{\pi}{n_2(0,0)\sigma}. \tag{4.46}$$

Note that this expression does not depend explicitly on the gas temperature. The collision cross section is $\sigma = 8\pi a^2$ in the zero temperature limit and is calculated with the value $a = 98.98(4)a_0$ for the s-wave scattering length [Kemp02].

To acquire sufficient statistics, at least 30 images are taken to retrieve one oscillation trace for a given density and each trace is acquired at least 3 times. Because the crossover happens over a narrow range of densities, great care was taken to reproduce the initial

conditions from shot to shot. This is done by adjusting the density using laser depletion in a feedback loop with the experimental result of the previous shot. Although this procedure increases the shot to shot fluctuations, long-term drift is virtually eliminated. With this procedure the atom number could be long-term stabilized within a standard deviation of better than 1%. By fitting the expression for an exponentially damped cosine function to the trace (see fig. 4.4), we retrieve the experimental values for the frequency ω_Q and damping rate Γ of the quadrupole mode for the selected density.

4.4.4 Accuracy of density and temperature determination

The *absolute* accuracy of $n_2(0,0)$ is estimated to be $\sim 30\%$. This accuracy is limited by our knowledge of the effective absorption cross section for the $(5S_{1/2}, F=2) \leftrightarrow (5P_{3/2}, F=3)$ transition. We measured a linewidth 30% larger than the literature value (see [Met-Str]). The phase contrast images are calibrated against absorption images of expanded clouds taken 15 ms after release from the trap at zero detuning. This procedure presumes the conservation of atom number during the expansion.

In our analysis we account to leading order for the corrections associated with trap anharmonicities. For temperatures much lower than the harmonic temperature $T_0 = \mu_B B_0/k_B = 60\,\mu$K, equ. (4.45) becomes sufficiently accurate to describe the cloud shape. In this limit the column density on the trap axis (to leading order in the x-integration) can be expressed for $z^2 \ll 2k_BT/m\omega_z^2$ as

$$n_2(0,z) \simeq n_2(0,0)\exp\left(-\frac{m\omega_z^2 z^2}{2k_BT}(1-\frac{1}{2}T/T_0)\right), \tag{4.47}$$

where $T/T_0 = \langle x^2\rangle/\rho_0^2 = k_BT/\mu_B B_0$ with $\langle x^2\rangle = k_BT/m\omega_\rho^2$ the variance of the thermal distribution of the cloud along the x-axis in the harmonic limit.

From equ. (4.47) we estimate the $1/e$-axial-size L_e that will be obtained by fitting a Gaussian to the axial column density profile of the cloud, $L_e = L/(1-\frac{1}{4}T/T_0)$ with L defined by $L^2 = 2k_BT/m\omega_z^2$. We note that L_e is obtained from the column density and does not coincide with the effective length of the cloud. In contrast to harmonic traps, in anharmonic traps the value obtained for the Gaussian length of a thermal cloud by fitting a 2D Gaussian to the column density differs in general from the value obtained by fitting a 3D Gaussian to the full density distribution of the same cloud.

The temperature follows with the expression

$$k_BT \simeq \frac{1}{2}m\omega_z^2 L_e^2(1-\frac{1}{2}T/T_0). \tag{4.48}$$

Hence, for a temperature of 6 μK the harmonic approximation overestimates the temperature by $\sim 5\%$. The correction in the central column density is smaller. Numerically we established that the fit of a 2D Gaussian underestimates the central column density by $\sim 1.4\%$ at $T/T_0 = 0.1$. As these corrections are small, there is no need to go beyond the leading order of anharmonic correction to retrieve these quantities. For measuring oscillation frequencies the situation is different because these can be measured to high precision.

Mean field broadening of the distribution is small [Guer02]. Calculating the variance $\langle z^2\rangle = \frac{1}{2}L^2$ using the recursive expression for the density to first order in mean field $U_{\rm mf}(\mathbf{r}) = 2v_0 n(\mathbf{r})$ leads for $T \ll T_0$ to

$$\frac{1}{2}m\omega_z^2 L^2 \simeq k_B T + E_{\rm mf}, \tag{4.49}$$

where $E_{\rm mf} = v_0 \int n^2(\mathbf{r})d\mathbf{r} / \int n(\mathbf{r})d\mathbf{r} = v_0 n_0/\sqrt{8}$ is the trap averaged interaction energy with $v_0 = (4\pi\hbar^2/m)a$ the interaction coupling constant [Pit-Str]. Equivalently, treating the mean field as an effective potential we may write

$$k_B T = \frac{1}{2}m\omega_z^2 L^2(1-\xi), \tag{4.50}$$

where $\xi = E_{\rm mf}/(k_B T + E_{\rm mf})$ is the mean field correction constant. For the data point with the highest mean field ($n_0 = 1.1\times 10^{14}{\rm cm}^{-3}$, $T = 2\,\mu$K) we calculate $\xi = 0.007$. Therefore, mean field corrections are at least one order of magnitude smaller that the anharmonic corrections and are discarded in this paper.

4.5 Anharmonic frequency shifts

As we operate at temperatures well above T_c, we pay special attention to the issue of trap anharmonicities[2]. We follow the path of argumentation as presented in [Guer99, Pedr03] to derive expressions for the anharmonic shifts. These are both temperature and mode dependent and can also depend on the density. The expressions are suitable for numerical evaluation provided the first and second spatial derivatives of the trapping potential are known.

To describe the dynamical evolution of an observable $\chi = \chi(\mathbf{r},\mathbf{v})$ it is multiplied by equ. (4.1) and averaged over the phase space

$$\frac{d}{dt}\langle\chi\rangle - \langle\mathbf{v}\cdot\nabla_{\mathbf{r}}\chi\rangle - \frac{1}{m}\langle\mathbf{F}\cdot\nabla_{\mathbf{v}}\chi\rangle = -\frac{\langle\chi\rangle - \langle\chi\rangle_{\rm le}}{\tau}, \tag{4.51}$$

where

$$\langle\chi\rangle(t) = \frac{1}{N}\int \chi(\mathbf{r},\mathbf{v})f(t,\mathbf{r},\mathbf{v})d^3r d^3v, \tag{4.52}$$

with N the number of atoms. By choosing the correct set of observables, it is possible to obtain a closed set of equations that describes the dynamics of these observables.

4.5.1 Dipole mode ($L = 1$)

To investigate the effect of trap anharmonicities on the dipole mode oscillation, we make the Ansatz

$$f(t,\mathbf{r},\mathbf{v}) = f_0(r_i - a_i, v_i - \dot{a}_i), \tag{4.53}$$

[2] This section has been worked out in cooperation with Paolo Pedri.

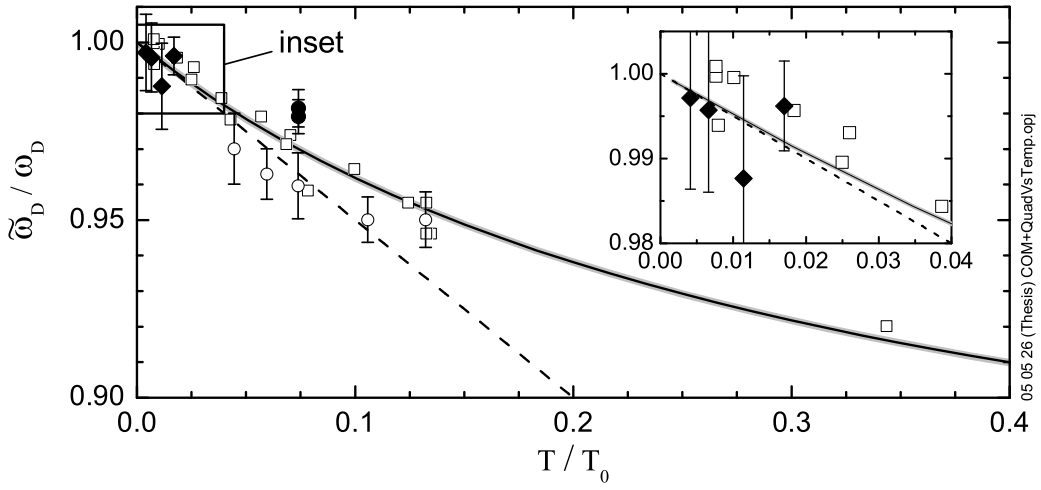

Figure 4.5: Scaled frequencies $\tilde{\omega}_D/\omega_D$ for the axial dipole mode versus temperature. The grey line corresponds to the evaluation of equ. (4.57). The leading slope (dashed line) is given by equ. (4.58). Open circles: phase contrast measurements; closed circles: absorption imaging measurements, both acquired with thermal clouds. Diamonds: measurements with Bose-Einstein condensates, using absorption imaging. Open squares: results acquired at ENS-Paris [LeonTh]. Note, that in the experiment described therein a different element (*He), a different trap (QUIC-trap) and different values for B_0 were used.

where $f_0(\mathbf{r},\mathbf{v}) = \mathcal{C}\exp(-\left(mv^2/2 + U(\mathbf{r})\right)/k_BT)$ is the equilibrium distribution function with $\mathcal{C}$ the normalization factor and $a_i = a_i(t)$. We choose $\chi = v_i$ and obtain the following set of equations

$$\frac{d}{dt}\langle v_i\rangle - \frac{1}{m}\langle F_i(\mathbf{r})\rangle = 0, \quad \text{where} \tag{4.54}$$

$$\langle v_i\rangle = \dot{a}_i \quad \text{and} \quad \langle F(\mathbf{r})\rangle = \langle F(\mathbf{r}+\mathbf{a})\rangle_0. \tag{4.55}$$

Analogously to equ. (4.52) we denote with $\langle\chi\rangle_0$ the average on the phase space using the equilibrium distribution $f_0(\mathbf{r},\mathbf{v})$. Expanding up to first order around the equilibrium position $a_i = 0$, we obtain

$$\ddot{a}_i + \frac{1}{m}\sum_j \langle U''_{ij}\rangle_0 a_j = 0, \tag{4.56}$$

where $U''_{ij} = \frac{\partial^2 U}{\partial r_i \partial r_j}$. Restricting ourselves to potentials with $\langle U''_{ij}\rangle_0 = 0$ for $i \neq j$, we obtain for the effective frequencies of the dipole modes

$$\tilde{\omega}^2_{iD} = \frac{1}{m}\langle U''_{ii}\rangle_0. \tag{4.57}$$

Substituting equ. (4.45) for the potential into equ. (4.57) we obtain for the leading anharmonic shift in the z-direction

$$\tilde{\omega}_{zD} \simeq \omega_z(1 - \frac{1}{2}T/T_0). \tag{4.58}$$

This expression is shown as the dashed line in fig. 4.5. The integral in equ. (4.57) is readily evaluated numerically using equ. (4.44) and requires as input parameters only

the values for α, β and B_0. The resulting curve is shown as the solid line in fig. 4.5. The curve follows the trend of our measurements of center-of-mass oscillations as well as data obtained in Paris [LeonTh].

The zero temperature limit of $\tilde{\omega}_{zD}$ is largely fixed by measurements with Bose-Einstein condensates, which reproduced within 1% over a period of one year. Its value is used to calibrate ω_z and the related β-coefficient. We have no explanation for the remaining deviations for the points taken with thermal samples at higher temperatures[3]. We cannot trace them back to insufficient mechanical or electronic stability of our trap. Non-exponential contributions to the damping may account for a systematic error in the frequency, but should be less than 1%. We speculate that possibly the temperature determinations of the phase contrast measurements could be affected by a molecular contribution to the phase contrast, which tends to narrow-down the distribution and results in an underestimated value for the temperature. This results from the distribution of pairs, that can photoassociate, which is proportional to the square of the atomic density.

4.5.2 Surface modes($L = 0, L = 2$)

In order to calculate the anharmonic shifts for the breathing and the two quadrupole modes we make the Ansatz

$$f(t, \mathbf{r}, \mathbf{v}) = \frac{1}{\prod_j b_j \sqrt{\theta_j}} f_0\left(\frac{r_i}{b_i}, \frac{(v_i - (\dot{b}_i/b_i)r_i)}{\theta_i^{1/2}}\right), \tag{4.59}$$

where b_i and θ_i are time-dependent variables. The parameters b_i take into account shape deformation of the density cloud whereas the parameters θ_i allow an anisotropic momentum distribution which is crucial to calculate the correct frequencies. We choose $\chi = v_i r_i$ and obtain the following set of equations

$$\ddot{b}_i \langle r_i^2 \rangle_0 - \frac{\theta_i}{b_i} \langle v_i^2 \rangle_0 - \frac{1}{m} \langle F_i(b_j r_j) r_i \rangle_0 = 0. \tag{4.60}$$

We impose the stationary solution and find the relation

$$\langle v_i^2 \rangle_0 = -\frac{1}{m} \langle F_i(r_j) r_i \rangle_0. \tag{4.61}$$

Then choosing $\chi = (v_i - (\dot{b}_i/b_i)r_i)^2$ yields

$$\dot{\theta}_i + 2\frac{\dot{b}_i}{b_i}\theta_i = -\frac{\theta_i - \bar{\theta}}{\tau}, \tag{4.62}$$

where $\bar{\theta} = (\sum_i \theta_i)/3$.
Let us now focus our attention on two extreme regimes.

Collisionless limit

In the collisionless limit ($\tau \to \infty$) we obtain the relation

$$\theta_i = \frac{1}{b_i^2}, \tag{4.63}$$

[3]Further investigation of this anharmonicity or reacquisition of the quadrupole oscillation data was not possible, since the experimental apparatus was disassembled prior to the completion of data analysis, as mentioned in the preface to this thesis.

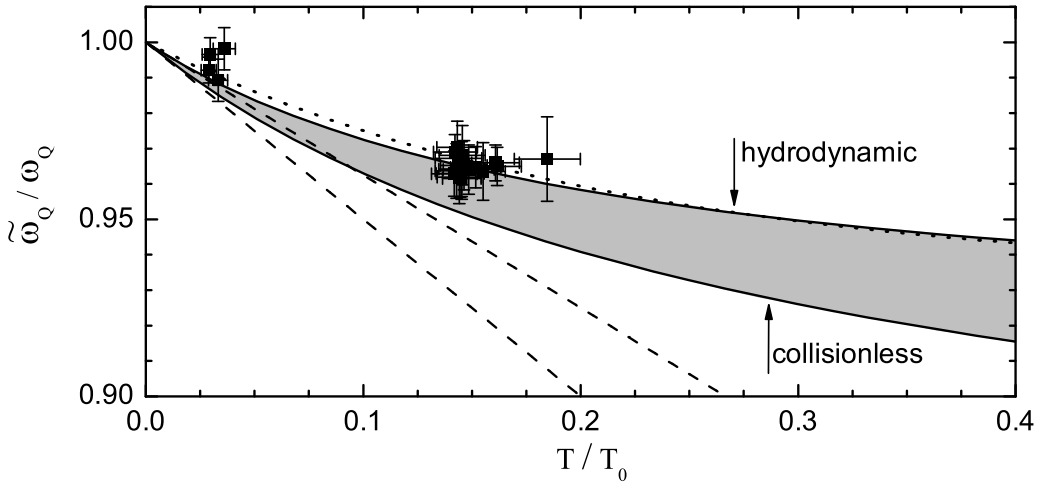

Figure 4.6: Scaled frequencies $\tilde{\omega}_Q/\omega_Q$ for the quadrupole mode versus temperature. The grey sector corresponds to equ. (4.70) evaluated for the cross-over regime (see Sec.4.5.2) with the collisionless and hydrodynamic limits indicated. The dashed lines show the leading slopes given by Eqs. (4.73) and (4.77). All data points correspond to collisionless conditions. The dotted line is used to scale all quadrupole frequency data to zero temperature.

and finally,

$$\ddot{b}_i + \frac{1}{b_i^3}\frac{\langle F_i(r_j)r_i\rangle_0}{m\langle r_i^2\rangle_0} - \frac{\langle F_i(b_j r_j)r_i\rangle_0}{m\langle r_i^2\rangle_0} = 0. \tag{4.64}$$

Linearizing these equations and looking for solution of the form $e^{-i\omega t}$ we obtain the three frequencies. In order to do this explicitly we define the quantities

$$A_{ii} = \frac{3}{m}\frac{\langle r_i U_i'\rangle_0}{\langle r_i^2\rangle_0}, \tag{4.65}$$

where $U_i' = \frac{\partial U}{\partial r_i}$, $A_{ij} = 0$ for $i \neq j$ and

$$B_{ij} = \frac{1}{m}\frac{\langle r_i r_j U_{ij}''\rangle_0}{\langle r_i^2\rangle_0}, \tag{4.66}$$

where $U_{ij}'' = \frac{\partial^2 U}{\partial r_i \partial r_j}$; note that, in general, $B_{ij} \neq B_{ji}$. We have to solve

$$|A + B - \tilde{\omega}^2 I| = 0, \tag{4.67}$$

where I is the identity-matrix, in order to obtain the frequencies. For the quadrupole modes with $M = \pm 2$ we find

$$\tilde{\omega}_{Q2}{}^2 = A_{xx} - A_{xy} + B_{xx} - B_{xy} \tag{4.68}$$

whereas for the modes with $M = 0$ we have

$$\tilde{\omega}_{\mathrm{B}}{}^2 = \mu + \sqrt{\mu^2 - \Delta} \tag{4.69}$$

$$\tilde{\omega}_{Q}{}^2 = \mu - \sqrt{\mu^2 - \Delta}, \tag{4.70}$$

where

$$\mu = (A_{xx} + A_{xy} + A_{zz} + B_{xx} + B_{xy} + B_{zz})/2 \quad (4.71)$$

$$\Delta = (A_{xx} + A_{xy} + B_{xx} + B_{xy})(A_{zz} + B_{zz}) - 2(A_{xz} + B_{xz})(A_{zx} + B_{zx}). \quad (4.72)$$

Here we used $\langle U''_{ij}\rangle_0 = 0$ for $i \neq j$. An analytic approximation for the leading anharmonic shift of the $M = 0$ quadrupole mode is obtained by substituting equ. (4.45) for the trap potential,

$$\tilde{\omega}_Q \simeq \omega_Q(1 - \frac{1}{2}T/T_0), \quad (4.73)$$

where ω_Q is the frequency in the harmonic limit. Note that at this level of approximation the relative shift coincides with that of the dipole mode. The result of the numerical averages based on equ. (4.44) is shown as the lower solid line in fig. 4.6. The lower dashed line corresponds to the leading shift given by equ. (4.73).

Comparison with the experimental points in fig. 4.6 shows agreement as far as the trend of the shift is concerned but a systematic deviation for the slope. This discrepancy can be eliminated by presuming that our axial trap frequency ω_z is underestimated by 1.5%. However, such a correction cannot be justified on the basis of the limited set of data for the dipole mode[4].

Hydrodynamic limit

In the hydrodynamic regime ($\tau \to 0$) the local equilibrium is always maintained, which implies that $\theta_i = \bar{\theta}$. In this case we obtain the relation

$$\theta_i = \bar{\theta} = \frac{1}{\prod_i b_i^{2/3}}, \quad (4.74)$$

and therefore

$$\ddot{b}_i + \frac{1}{b_i(\prod_j b_j)^{2/3}} \frac{\langle F_i(r_j)r_i\rangle_0}{m\langle r_i^2\rangle_0} - \frac{\langle F_i(b_j r_j)r_i\rangle_0}{m\langle r_i^2\rangle_0} = 0. \quad (4.75)$$

By linearizing around the equilibrium we find the frequencies for the $M = \pm 2$ modes and the two $M = 0$ monopole-quadrupole modes. In this case we have to define the A_{ij} matrix as

$$A_{ii} = \frac{5}{3m}\frac{\langle r_i U'_i\rangle_0}{\langle r_i^2\rangle_0} \text{ and } A_{ij} = \frac{2}{5}A_{ii}. \quad (4.76)$$

Note that A_{ij} does not depend on j. The matrix B_{ij} is the same as in the collisionless case. Solving the determinant equ. (4.67) leads again to Eqs. (4.68), (4.69) and (4.70) for the frequencies and Eqs. (4.71) and (4.72) for μ and Δ. Only the expressions for the matrix elements A_{ij} have changed. Substituting equ. (4.45) for the trap potential we find for the leading anharmonic shift of the hydrodynamic $M = 0$ quadrupole mode

$$\tilde{\omega}_Q \simeq \omega_Q(1 - \frac{3}{8}T/T_0), \quad (4.77)$$

[4]Further investigation of this anharmonicity or reacquisition of the quadrupole oscillation data was not possible, since the experimental apparatus was disassembled prior to the completion of data analysis, as mentioned in the preface to this thesis.

which has a slightly weaker slope than in the collisionless case. The result of the numerical averages based on equ. (4.44) are shown as the upper solid line in fig. 4.6. The upper dashed line corresponds to the leading shift given by equ. (4.77).

A comparison with experiment requires densities $n_0 > 4 \times 10^{14}\,\mathrm{cm}^{-3}$ at a temperature $T = 4\ \mu\mathrm{K}$, to have $2\omega_z\tilde{\tau} < 0.1$, which is about three times our maximum density. At our highest density of $n_0 = 1.3 \times 10^{14}\mathrm{cm}^{-3}$, we calculate a 3-body decay rate of $\dot{N}/N = 2\sqrt{3}\,L\,n_0^2 \approx 1\ \mathrm{s}^{-1}$, with $L = 1.8(5) \times 10^{-29}\mathrm{cm}^6\mathrm{s}^{-1}$ the three-body rate constant in the Bose-condensed state [Södi99]. At a three times higher density, the decay rate renders the acquisition of data at approximately constant density impossible for ^{87}Rb.

Crossover regime

In the cross-over region, the same approach can be used, but after linearizing, one has to look for solutions of the form $e^{-i\,\omega t}$ with a complex ω. For the $M = 0$ modes this leads to the equation

$$\left(C[\omega] - \frac{i}{\tau}D[\omega]\right)\left(E[\omega] - \frac{i}{\tau}F[\omega]\right) = 0, \tag{4.78}$$

where $C[\omega] = \omega(\omega^2 - \omega^2_{\mathrm{cl:B}})(\omega^2 - \omega^2_{\mathrm{cl:Q}})$, $D[\omega] = (\omega^2 - \omega^2_{\mathrm{hd:B}})(\omega^2 - \omega^2_{\mathrm{hd:Q}})$, $E[\omega] = \omega(\omega^2 - \omega^2_{\mathrm{cl:Q2}})$ and $F[\omega] = (\omega^2 - \omega^2_{\mathrm{hd:Q2}})$. Each term represents two equations since they contain real and imaginary parts. For an elongated cigar-shape trap it is possible to write the frequencies in the form of equ. (4.3) with rescaled relaxation time $\tilde{\tau} = (\omega^2_{\mathrm{cl:B}}/\omega^2_{\mathrm{hd:B}})\,\tau$, which reaches the value $\tilde{\tau} = 6/5\,\tau$ in the harmonic limit. The numerically calculated results of temperature induced shift, based on equ. (4.44) in the cross-over regime is represented by the grey sector in fig. 4.6.

A comparison with experiment is beyond the scope of this paper because, after scaling to ω_Q, the two limiting cases are spaced by only $\sim 1\%$. Therefore, not only $\tilde{\omega}_Q$ has to be determined to an accuracy much better than 1%, but also the scaling parameter ω_Q. In the limiting cases the latter is fully determined by the trap frequency (i.e. $\omega_{\mathrm{cl}} = 2\omega_z$ and $\omega_{\mathrm{hd}} \approx 1.55\omega_z$). However, in the crossover region knowledge of $\tilde{\tau}$ to much better than 1% is required to calculate ω_Q from equ. (4.10) to adequate precision.

4.6 Results and discussion

We took all our data with the same trap parameters and the same excitation procedure, but at various temperatures. Starting the evaporation with a large atom number and using 'tight' trapping parameters we could reach high densities and thus study the full crossover. However, this choice for a 'tight' trap made us sensitive for anharmonic shifts as discussed in section 4.5. Note from fig. 4.7 that in the collisionless limit frequency shifts as small as 1% are already significant, and anharmonic shifts of that size are expected for $T \gtrsim 2\,\mu\mathrm{K}$ for our trap parameters.

Therefore, we extrapolate all frequency data to the zero-temperature limit ($\tilde{\omega}_Q \to \omega_Q$) using the dotted curve in fig. 4.6. This yields the best estimate for the value in the harmonic limit of our potential. The correction curve is based on the temperature

dependence observed for our data in the collisionless regime ($2\omega_z\tilde{\tau} > 10$, see fig. 4.8), where we may presume $\omega_Q = 2\omega_z$. In this way systematic deviations of our results from the curves in fig. 4.7 and fig. 4.8b were substantially reduced.

In fig. 4.7 we plot the observed, scaled damping rates Γ/ω_z versus the extrapolated quadrupole frequencies normalized to the axial trap frequency, ω_Q/ω_z. The drawn curve corresponds to the crossover expression equ. (4.3) with $\omega_{\rm cl} = 2\omega_z$ and $\omega_{\rm hd} = 1.55\omega_z$. Plots of the same experimental data and the exact solutions of equ. (4.3) separately against $2\omega_z\tilde{\tau}$ are given in fig. 4.8a for Γ/ω_z and fig. 4.8b for ω_Q/ω_z.

From the damping results (fig. 4.8a) we obtain $2\omega_z\tilde{\tau}_0 = 1.0(1)$ for the experimental value of the crossover point. Given the 30% absolute accuracy of our density determination this agreement is fortuitously good (see Sec.4.2).

The determination of the crossover point from the frequency crossover behavior is less straightforward, because errors in the temperature determination add to the error in the extrapolated frequency ω_Q. Further, as the frequency corrections are all positive, they affect the determination of $2\omega_z\tilde{\tau}_0$ from fig. 4.8b. For the crossover region ($0.1 \lesssim 2\omega_z\tilde{\tau} \lesssim 10$) the average applied frequency correction was $\delta\omega_Q/\omega_z = 2.6\%$, which changes the experimental value for $2\omega_z\tilde{\tau}_0$ by a factor 0.85 to yield $2\omega_z\tilde{\tau}_0 = 1.0(1)$. The

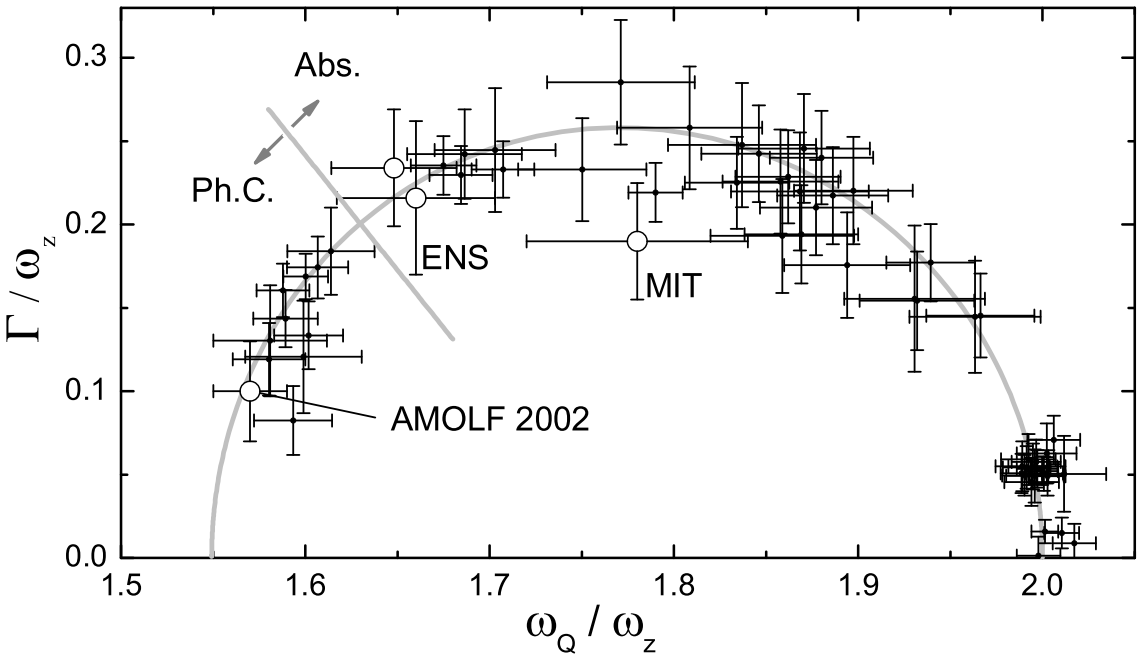

Figure 4.7: Damping (raw data) versus frequency (extrapolated) for the quadrupole mode. Open circles: data acquired at MIT [Kett99], ENS [Ledu02] and AMOLF [Shva02]. The solid line is corresponds to the crossover expression equ. (4.3). The data left of the straight line are obtained with Phase Contrast (Ph.C.) imaging, those on the right with Absorption (Abs.) imaging. The error bars represent a 95% confidence interval of the fit.

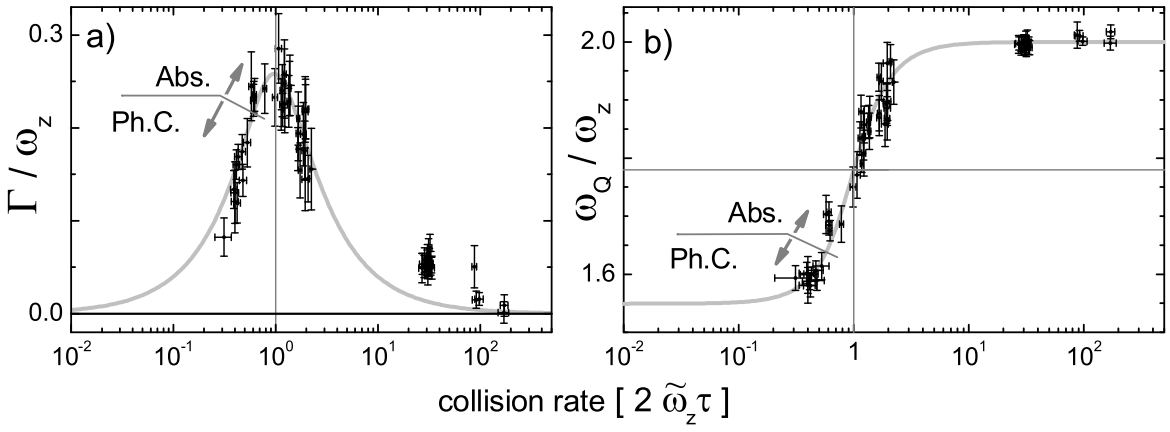

Figure 4.8: Damping (raw data) (a) and frequency (extrapolated to harmonic limit) (b) of the quadrupole mode versus scaled relaxation time. The solid line in figure a) corresponds to the imaginary part ($\Gamma = -\omega''$) of the solution of equ. (4.3); in figure b) to the real part ($\omega_Q = \omega'$). The crosshair marks the location of the crossover point. The vertical error bars are identical to fig. 4.7, the horizontal ones represent the standard deviations.

quoted error corresponds to a conservative (factor of 2) uncertainty in the slope of the correction curve. This value coincides with the result obtained from the damping data and shows that our results are self-consistent.

In the collisionless regime anharmonicities can give rise to dephasing induced damping. These effects were not corrected for as they do not affect to leading order the determination of the crossover point. Here we briefly comment on these effects. Roughly, one may argue that for a given anharmonic spread $\delta\omega_Q$ in frequencies the dephasing time δt will be given by $\delta\omega_Q \delta t \approx 2\pi$. Hence, the dephasing related damping rate is $\delta\Gamma = 2\pi/\delta t \approx \delta\omega_Q$. The cluster of data points at $2\omega_z\tilde{\tau} \approx 30$ in fig. 4.8a best illustrates the significance of the correction as they were taken at the highest temperature (9 μK). For these points the anharmonic frequency shift $\delta\omega_Q$ is $\sim 3.5\%$ (see fig. 4.6). With $\delta\Gamma/\omega_z \simeq \delta\omega_Q/\omega_z = 0.035$ this suggests that the anomalously high damping rates observed for these data points (fig. 4.8a) may be entirely attributed to dephasing effects. Near the crossover point the collisional damping is much faster and dephasing corrections may be neglected $\delta\Gamma/\Gamma \simeq (1/2)\,(\delta\omega_Q/\Gamma)^2 \approx 10^{-3}$.

We also verified that our shot-to-shot variations in the density have a negligible effect on the measured damping rate. The frequency shifts fastest at the density of the crossover point, where $\delta\,(\omega_Q/\omega_z)\,/\delta\,(\omega_{\rm cl}\tilde{\tau}) = (2/\pi)\,(\omega_{\rm cl} - \omega_{\rm hd})\,/\omega_z \approx 0.3$ as follows directly by taking the first derivative of equ. (4.10) with respect to $\tilde{\tau}$. As $\tilde{\tau}$ scales inversely proportional to the central density, a 1% variation in atom number results (at constant temperature) in a $\sim 0.3\%$ variation of the frequency, which is much smaller than to the one considered above and therefore also negligible.

4.7 Summary and Conclusions

With fig. 4.7 and fig. 4.8 we obtain good agreement between experiment and the crossover theory. The frequency shifts down from $2\omega_z$ in the collisionless regime to $1.55\omega_z$ for collisionally hydrodynamic clouds, with ω_z the axial frequency of our trap. Most of the shift occurs over a narrow range of densities around the crossover point. The damping rate peaks over the same range of densities. The determinations of the crossover point from the frequency and the damping behavior agree within 10%, $2\omega_z\tilde{\tau}_0 = 1.0(1)$. The agreement with theory is limited by a 30% absolute uncertainty in density. Further, we present a theory and experimental evidence for anharmonic frequency shifts. The theory allows numerical evaluation for potentials with known first and second spatial derivatives. We show that for elongated Ioffe-Pritchard traps knowledge of the central field B_0 suffices to calculate the leading anharmonic shifts with simple analytic expressions.

Chapter 5
Interferometric determination of the scattering length

The scattering length a, the elastic scattering amplitude in the zero-energy limit, is the central parameter in the theoretical description of quantum gases, as has been extensively discussed in section 2.3 and 2.4 (see also refs.[Pit-Str, Petr04, Fedi96a]). It determines the kinetic properties of these gases as well as the bosonic mean field. Its sign is decisive for the collective stability of the Bose-Einstein condensed state. Near scattering resonances, pairing behavior [Petr04] and three-body lifetime [Fedi96a] can also be expressed in terms of a. As a consequence, the determination of the low-energy elastic scattering properties is a key issue to be settled prior to further investigation of any new quantum gas. Over the past decade the crucial importance of the scattering length has stimulated important advances in collisional physics [Wein99].

In all cases except hydrogen [Frie80] the scattering length has to be determined experimentally as accurate *ab initio* calculations are not possible. An estimate of the modulus $|a|$ can be obtained relatively simply by measuring kinetic relaxation times [Monr93]. In some cases also the sign of a can be determined by such a method, provided p-wave or d-wave scattering can be neglected or accounted for theoretically [Ferr02]. These methods have a limited accuracy since they rely on the knowledge of the atomic density and kinetic properties. Precision determinations are based on photo-association [Hein99], vibrational-Raman [Samu00] and Feshbach-resonance spectroscopy [Chin00, Mart02], or a combination of those. They require refined knowledge of the molecular structure in ground and excited electronic states [Wein99].

In this part we present a stand-alone interference method for the accurate determination of the full (*i.e.* complex) s- and d-wave scattering amplitudes in a quantum gas.

5.1 Experiment principle

As has been discussed in section 2.3 the scattering of atoms at temperatures in the μK regime requires a quantum mechanical treatment. We have shown, that towards the zero temperature limit, all higher partial waves vanish, and scattering occurs solely via s-wave collisions. Inversely this implies, that by increasing the collision energy starting from the zero temperature limit, the next higher partial wave can be populated and interference between all participating scattering channels influences the scattering pattern. Doing so in an uncorrelated way (e.g. rising the cloud temperature) does not allow to retrieve information concerning interference, as many partial waves contribute, according to the Maxwell-Boltzmann statistical distribution of (collision-) energies. By creating two separate clouds at temperatures, where collisions within each cloud are well in the s-wave limit, and then colliding the two at sufficiently high energies, the interference between

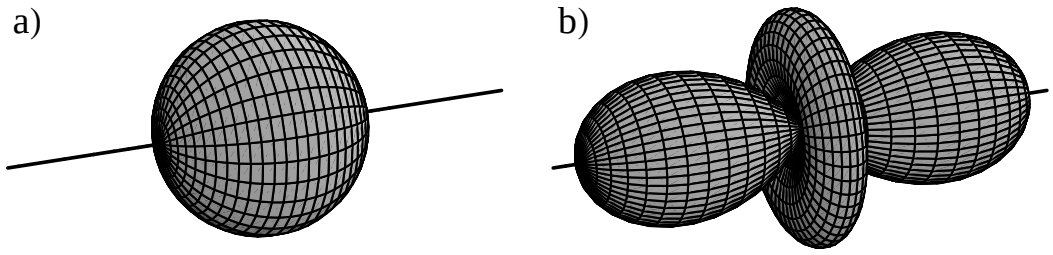

Figure 5.1: 3-dimensional graphical representation of the $Y_{lm}(\vartheta, \varphi)$ spherical harmonics for $(l = 0, m = 0)$ s-wave and $(l = 2, m = 0)$ d-wave with proper relative amplitude scale. The straight line indicates the axis along which the collision occurs.

the partial waves becomes visible in the halo of the scattered atoms.

As shown in section 2.3, in the doubly-spin-polarized state of the atoms in this experiment (where only the valence electron in an s-shell conbtributes) the only possible interaction is given by the triplet interaction potential $^3\Sigma_u$, which implies an interaction with zero angular momentum. As in this isotropic interaction, no angular momentum can be transferred, no uneven partial waves can be populated in a collision. Therefore the first partial wave above the s-wave ($l = 0$), that starts to contribute with rising collision energy in the scattering halo, is the d-wave ($l = 2$). The angular dependance of the scattering amplitude is presented in fig.5.1. The characteristic spherical shape of the s-wave stands in strong contrast to the more complex structure of the d-wave. The distance of a surface point from the center in fig.5.1 represents the amplitude in that spatial direction, not the spatial density distribution. The collision halo is hollow and spherical in both cases, the difference shows in the density distribution in the spherical shell of the halo. With infinitesimally small collision partners and zero momentum spread, the sphere thickness tends to zero. Therefore it is advantageous to conduct this experiment with Bose-Einstein condensates due to their smaller and sharper density profile, though the very same experiment can be conducted with thermal clouds. As a second advantage, the use of condensed clouds allows to observe scattering angles closer to the forward and backward direction, as the unscattered clouds occupy a smaller spatial angle and is easier to discern form the scattered halo due to it's characteristic parabolic profile[1] (see section 2.4). This is of particular value, as the maximum scattering amplitude of the d-wave (the forward and backward lobes of the $Y_{20}(\vartheta, \varphi)$ function) coincides with the trajectory of the unscattered parts of the colliding clouds.

The collision halo is rotationally symmetric (i.e. independent of φ) around the axis of

[1]The angle ϑ is measured from the collision ($z-$) axis, where $\vartheta = 0$ and $\vartheta = 180°$ point along the collision axis, but are indiscernible because of the symmetry of the collision. For the same reason we have $\sigma(\vartheta) = \sigma(180° - \vartheta)$.

the collision. It is imaged from the direction ($\vartheta = 90, \varphi = 0$), where we arbitrarily define $\varphi = 0$ as the direction towards the camera. As absorption imaging integrates the column density in a Cartesian grid, we can extract the angular distribution of the scattering amplitude by a computerized tomography transformation [Born-W] of the images. The angular distribution is directly proportional to the differential cross section which in this particular case is given by the squared modulus of the sum of the interfering s-wave (η_0) and d-wave (η_2) amplitudes

$$\sigma(\vartheta) = \frac{8\pi}{k^2} \left| e^{i\,\eta_0} \sin\eta_0 + \frac{5}{2} e^{i\,\eta_2} \left(3\cos^2\vartheta - 1\right) \sin\eta_2 \right|^2 , \tag{5.1}$$

where k is the incident wave vector of the collision and the η_0 and η_2 the phase shifts of the s- ($l = 0$) and d-wave ($l = 0$) contributions. By defining the new variable $\chi = (3\cos^2\vartheta - 1)$ we rewrite this to

$$\sigma(\vartheta) \propto \left| 1 + \frac{5}{2}\, e^{i\,(\eta_2 - \eta_0)} \frac{\sin\eta_2}{\sin\eta_0}\, \chi \right|^2 , \tag{5.2}$$

which reveals the parabolic shape of this function, when plotted as a function of χ. The absolute scattering amplitude $W(\vartheta)$ is proportional to the differential scattering cross section $\sigma(\vartheta)$ with a proportionality factor, that is dependent on the atom density of the colliding clouds and other geometrical factors (overlap, density profile, time of passing), which are typically difficult to extract with appropriate precision from the image. However, from the prefactor of χ in equ.(5.2) it is possible to extract the asymptotic phase shifts $\eta_l(k)$ of the two scattering channels as a function of the relative momentum k. It can be determined by fitting a parabola to a plot of the number of atoms scattered into the spatial sector ($\delta\vartheta, 0 \leq \varphi \leq 2\pi$) around ϑ plotted as a function of χ. This approach has the advantage, that it does not require knowledge of the density of the colliding and scattered clouds, unlike the stimulated Raman detection approach of ref. [Lege98].

Using these $\eta_l(k)$ as boundary conditions, we integrate the radial Schrödinger equation inwards over the $-C_6/r^6$ tail of the potential and compute the accumulated phase [Verh93] of the wavefunction at radius $20\,a_0$ (with a_0 the Bohr radius). This limitation is well sufficient, as the collision energy is of the order of 1 mK, whereas the potential depth in the inner part of the ground-state triplet ($^3\Sigma_u$) interaction potential, which represents the active potential in this case, is of the order of 100 K, as has been discussed in section 2.3. Under these conditions, the phase development in the region $r < 20\,a_0$ is identical for all partial waves for all considered energies, and we use all data of $\eta_l(k)$ to obtain a single optimized accumulated phase η_{opt} at the point $r = 20\,a_0$. We then infer all the low-energy scattering properties by integrating again the same Schrödinger equation outwards for any collision momentum k and partial wave l, starting at $r = 20\,a_0$ with η_{opt}. The s-wave phase shift $\eta_0(k)$ is of particular interest, because in the zero-energy limit we have

$$\lim_{k\to 0} \eta_0(k) = -k\, a_{triplet}, \tag{5.3}$$

which allows us to infer the triplet scattering length $a_{triplet}$ from η_{opt}. Eventually, the actual value of η_{opt} deviates from the one, retrieved from a more precise potential description, that includes higher order terms, as erratic phase shift accumulates when integrating inwards. However, this does not pose a problem, as we use the same C_6 coefficient when integrating outwards, and we may assume (which will be discussed in

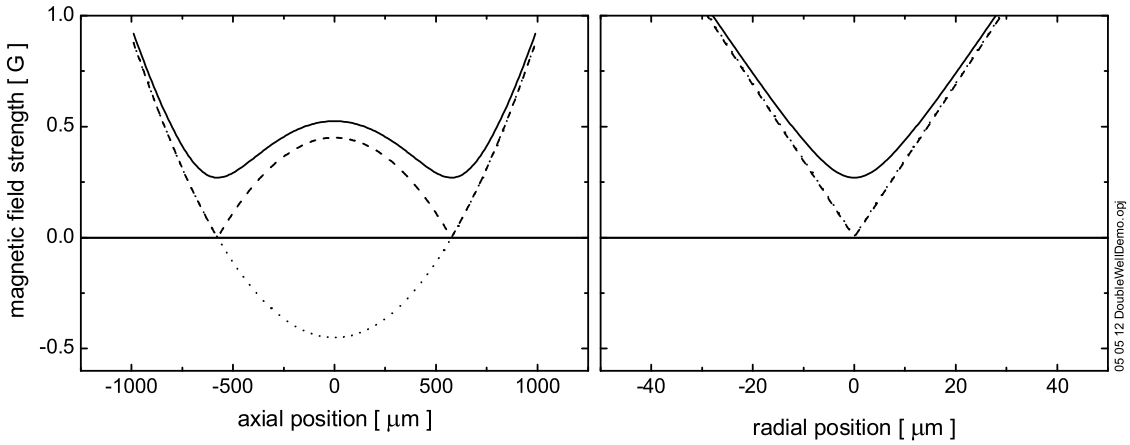

Figure 5.2: Demonstration of the effect of added modulation on a Ioffe-Pritchard type trap with negative offset $|B_0| < 0$. Modulus of the magnetic field a) along the trap axis and b) radially through one of the minima. Dotted line: Magnetic field, taking the vector direction into account. Dashed line: absolute value of field, without modulation. Solid line: modulus of magnetic field with modulation on.

more detail later), that erratic phase shifts de-accumulate out.

5.2 Cloud splitting

The cloud splitting and acceleration technique, used to initiate the collision, can be understood from fig.5.2. If the potential is proportional to a magnetic field with parabolic shape, but the offset is set to a negative value, the field crosses zero at two points, sketched by the dotted line in fig.5.2a. A negative value of the field can be understood from the vector character of the magnetic field, so the region of negative value indicates a region where the vector direction is opposite to the one in a positive region. However, the choice of vector orientation for positive value is arbitrary and of no significance for the argumentation in this chapter. As the potential sensed by atoms is proportional to the modulus of the field strength, low-field seeking atoms experience the potential as a structure with two minima at zero field, indicated by the dashed line in fig.5.2.

In a low field region, i.e. close to the zero crossings of the magnetic field, the polarization field is too weak to keep the atoms spin-polarized as the Larmor frequency ω_{Larmor} tends to zero. When crossing through this region due to their thermal motion, atoms appear in different spin projections on the opposite side of the zero-crossing, which eventually is a non-field sensitive or high-field seeking state, and these atoms are lost from the trap. This so called Majorana depolarization can be avoided, by applying a time averaged potential to the static field, as was first proposed and demonstrated in trapping of low field seeking atoms in a time orbiting potential with a single zero crossing [Petr95]. The first presentation of this modulated double well approach was reported in ref.[Thom02], the first successful experimental realization was reported by our group in ref.[Tiec03]. The effect of the modulation can be understood as an additional field, that (to first approximation;

for a derivation see below) adds in a quadratic sum to all static magnetic fields and lifts the potential values in all regions as sketched as the solid line in fig.5.2. Thus the zero-field value is lifted and Majorana losses are avoided, making this double minimum structure suitable for long-term confinement of atoms. It is obvious, that the value of chosen negative B_0 is decisive for the splitting distance and the barrier height, where we neglect the latter one in the following discussion, as it is of no interest for this experiment.

The technical implementation and mathematical description of this modulation technique is identical to the discussion in section 4.3.1. By applying a fast rotating field, trapped atoms experience the time average of the instantaneously shifted potential, which effectively lifts the potential value in all regions inside the modulated range. Analogous to the discussion of the time averaged potential (TAP) this modulated range is limited by the radius given by the instantaneous displacement of the magnetic field $\rho_m = B_m/\alpha$. As in this case the potential minimum with zero value rotates at the modulation frequency ω_{mod} at a spatial radius of ρ_m, it is referred to as the time orbiting potential (TOP).

In the discussion of the TAP before, the harmonic radius designates a region, where the harmonic approximation that is valid at the center ceases to be acceptable. In this case it signifies additionally a circle, where a zero-field point orbits. The 3 dimensional position of this or (as we later shall see) these two circles is given by $(\rho_m \sin(\omega_m t)\,\vec{e}_x\,,\ \rho_m \cos(\omega_m t)\,\vec{e}_y\,,\ \pm z_0\,\vec{e}_z)$, which defines two circles in the radial plane, centered on the z-axis (for a definition of vector directions see fig.3.10). Atoms, that are occupying a spatial position on this circle experience periodically a zero field on each pass, which results in Majorana depolarization as in a static potential. The loss-rate is smaller, as atoms experience the low field value only for a limited time. However, the loss rate is still significant, which is the reason for the descriptive term 'circle of death' for this region. Its radius is given by

$$\rho_m = B_m/\alpha_{real}. \tag{5.4}$$

The derivation of a closed expression for all spatial regions for the double minimum potential is analogous to the calculations in section 4.3.1. The instantaneous potential is proportional to the magnetic field, which again (compare equ.(3.10)) is given by

$$B(x,y,z) = B_0\sqrt{(1+\beta z^2)^2 + (\alpha^2-\beta)(x^2+y^2)}, \tag{5.5}$$

where the time average has to be calculated over the instantaneous shift of each coordinate $x \to x + \rho_m \sin\phi$ and $y \to y + \rho_m \cos\phi$, where we assume the modulation to be applied in the radial $x-y$-plane. We have to solve

$$B(x,y,z) = \frac{1}{2\pi}\int_0^{2\pi} \sqrt{(B_0+\beta_{real}z^2)^2 + (\alpha_{real}^2 - B_0\beta_{real})((x+\rho_m s_\phi)^2 + (y+\rho_m c_\phi)^2)}\,d\phi. \tag{5.6}$$

where we again use the convenient abbreviations s_ϕ, c_ϕ and the variables, $x = \xi\, s_\psi$, $y = \xi\, c_\psi$, where $\xi^2 = x^2 + y^2$, as introduced in section 4.3.1. Unlike the discussion in section 4.3.1, we cannot use scaled parameters, since in this case B_0 can also have negative values to generate the double minimum structure. Therefore the real trap parameters for axial curvature β_{real} and radial gradient α_{real} have to be used. For convenience,

we neglect the subscript '*real*', as it would have to be applied in all occurrences of α and β. As a first approximation we calculate

$$\begin{aligned} B(x,y,z) &= \frac{1}{2\pi}\int_0^{2\pi}\sqrt{(B_0+\beta z^2)^2+(\alpha^2-B_0\beta)(x^2+y^2+\rho_m^2+2\rho_m(x\,s_\phi+y\,c_\phi))}\,d\phi \\ &= \frac{\sqrt{\mathbf{C}}}{2\pi}\int_0^{2\pi}\sqrt{1+\frac{2(\alpha^2-B_0\beta)}{\mathbf{C}}(x\,s_\phi+y\,c_\phi)}d\phi \\ &\simeq \sqrt{\mathbf{C}}\left(\frac{1}{2\pi}\int_0^{2\pi}\left(1+\frac{(\alpha^2-B_0\beta)}{\mathbf{C}}(x\,s_\phi+y\,c_\phi)\right)d\phi\right) \qquad (5.7) \\ &\simeq \sqrt{(B_0+\beta z^2)^2+(\alpha^2-B_0\beta)(x^2+y^2+\rho_m^2)}, \qquad (5.8) \end{aligned}$$

where we reuse the abbreviations

$$\begin{aligned} \mathbf{C} &= (B_0+\beta z^2)^2+(\alpha^2-B_0\beta)(x^2+y^2+\rho_m^2) \qquad (5.9) \\ \text{and}\quad \mathbf{D} &= (\alpha^2-B_0\beta)2\rho_m\,\xi, \qquad (5.10) \end{aligned}$$

which deviate from the definitions in section 4.3.1 only by the use of non-scaled parameters and the inclusion of B_0. However, the steps towards equs.(5.7) and (5.8) are pathologic, so this derivation can be used only as an intuitive picture and first order approximation.

For a more rigorous derivation the algebraic steps are identical to the discussion between equs.(4.24) and (4.25), and we find the solution

$$\begin{aligned} B(x,y,z) &= \frac{4}{2\pi}\sqrt{\mathbf{C}+\mathbf{D}}\int_0^{\pi/2}\sqrt{1-\mathbf{M}\,s_\theta^2}\,d\theta \qquad (5.11) \\ \text{with}\quad \mathbf{M} &= \frac{2\mathbf{D}}{\mathbf{C}+\mathbf{D}}, \qquad (5.12) \end{aligned}$$

as before, which is the well-known elliptic integral. This solution is again only valid, if $\mathbf{D} \le \mathbf{C}$ holds, so we must evaluate

$$\begin{aligned} 0 &\le (B_0+\beta z^2)^2+(\alpha^2-B_0\beta)(x^2+y^2+\rho_m^2-2\rho_m\sqrt{x^2+y^2}) \qquad (5.13) \\ &\le (B_0+\beta z^2)^2+(\alpha^2-B_0\beta)(\rho_m-\sqrt{x^2+y^2})^2. \qquad (5.14) \end{aligned}$$

Since $\alpha^2 - B_0\beta > 0$ for all experimental values of B_0 ($1\mathrm{G} \ge B_0 \ge -40\mathrm{G}$) and because of the quadratic character of all other terms on the r.h.s. the sum is always positive, but unlike the discussion in section 4.3.1, the limiting case (i.e. the r.h.s. being equal to zero) is realized for the the value of $B_0 = 0$ at the coordinates $(z = 0, \rho_m^2 = x^2 + y^2)$. This designates the moment, when the potential minimum is split into two, if B_0 is infinitesimally further lowered, which occurs during the cloud splitting operation (see below). However, the inequality still holds, and this region is of no interest for the experiment described further-on.

A detailed derivation of the trapping frequencies in each minimum is given in ref.[Thom02]. Here, only a first order approximation shall be given. It is easy to see, that for a parabolic trap with $B(z) = B_0 + \beta z^2$ and $B_0 < 0$ two zero crossings occur at an axial distance of

$z_0 = \pm(|B_0|/\beta)^{1/2}$. At this distance, the first spatial derivative with respect to z is given by

$$\partial_z B(x,y,z)|_{x=y=0,z=z_0} = 2\sqrt{|B_0|\beta}. \tag{5.15}$$

The second spatial derivative is constant, and causes a significant deviation of axial slope on both sides of a single minimum when the splitting distance z_0 is small. However, for large negative B_0, i.e. large splitting distance z_0, these corrections decrease with the square root of B_0, as can be seen from a Taylor expansion of the first derivative around z_0

$$\begin{aligned} \partial_z B(x,y,\delta z)|_{x=y=0} &= 2\sqrt{|B_0|\beta} + \partial_z^2 B(x,y,z)\big|_{x=y=0,z=z_0}(\delta z - z_0) \\ &= 2\sqrt{|B_0|\beta}\left(1 + \sqrt{\frac{\beta}{B_0}}(\delta z - z_0)\right). \end{aligned} \tag{5.16}$$

In this approximation, we may consider the magnetic field to have quadrupole character in both axial and radial direction, and we identify $\alpha_\rho = \alpha$ as the gradient coefficient in the radial direction and

$$\alpha_z = 2\sqrt{|B_0|\beta} \tag{5.17}$$

in the axial direction around z_0. Under these assumptions, we may rewrite the time averaged potential of each separate minimum as

$$B(x,y,z) = \frac{1}{2\pi}\int_0^{2\pi} \sqrt{\alpha_\rho^2\,(x^2+y^2+\rho_m^2+2\rho_m(xs_\phi + yc_\phi)) + \alpha_z^2\delta z^2}\,d\phi \tag{5.18}$$

where we again use the convenient abbreviations s_ϕ and c_ϕ as introduced in section 4.3.1. By changing to the variables, $x = \xi\, s_\psi$, $y = \xi\, c_\psi$, where $\xi^2 = x^2 + y^2$ (ψ can be precisely defined as well, but is irrelevant since it is integrated over), we can make use of the well-known identity

$$\sin(\phi)\cos(\psi) + \cos(\phi)\cos(\psi) = \cos(\phi - \psi) \tag{5.19}$$

and calculate

$$B(x,y,z) = \frac{1}{2\pi}\int_0^{2\pi} \sqrt{\alpha_\rho^2(\rho_m^2 + \xi^2 + 2\rho_m\xi c_{\phi-\psi}) + \alpha_z^2\delta z^2}\,d\phi \tag{5.20}$$

$$\begin{aligned} &= \frac{1}{2\pi}\int_0^{2\pi} \alpha_\rho\rho_m\sqrt{1 + \frac{1}{\rho_m^2}\left(\xi^2 + 2\rho_m\xi c_{\phi-\psi}) + \frac{\alpha_z^2}{\alpha_\rho^2\rho_m^2}\delta z^2\right)}\,d\phi \\ &\simeq \frac{1}{2\pi}\int_0^{2\pi} \alpha_\rho\rho_m\left(1 + \frac{1}{2}\left(\frac{\xi^2}{\rho_m^2} + \frac{2\xi c_\phi}{\rho_m} + \frac{\alpha_z^2}{\alpha_\rho^2\rho_m^2}\delta z^2\right)\right)\,d\phi \\ &= \alpha_\rho\rho_m + \frac{1}{2}\frac{\alpha_\rho\xi^2}{\rho_m} + \frac{1}{2}\frac{\alpha_z^2}{\alpha_\rho\rho_m}\delta z^2 \\ &= B_m + \frac{1}{2}\frac{\alpha_\rho^2}{B_m}(x^2+y^2) + \frac{1}{2}\frac{\alpha_z^2}{B_m}\delta z^2. \end{aligned} \tag{5.21}$$

From these expression we see immediately, that the trapping frequencies in each minimum are given by

$$\omega_{\rho,m} = \sqrt{\frac{\mu_B\,\alpha_\rho^2}{m\,B_m}} \quad \text{and} \quad \omega_{z,m} = \sqrt{\frac{\mu_B\,\alpha_z^2}{m\,B_m}} = \sqrt{\frac{\mu_B\,4|B_0|\,\beta}{m\,B_m}}. \tag{5.22}$$

From this we conclude, that in order to achieve tight compression for evaporation in each separate minimum, low B_m and high negative B_0 are favorable, where 'low B_m' must be balanced against the onset of Majorana losses with decreasing B_m close to z_0. However, splitting the thermal cloud directly after loading from the MOT would result in great losses and inefficient evaporation, as due to technical limitations (compare to section 4.3.2) the maximum possible modulation field was limited to $B_m = 479\,\mathrm{mG}$, and therefore the radius of the circle of death to $\rho_m = 13\,\mu\mathrm{m}$.

The experimental sequence for creating two separated Bose-Einstein condensates therefore starts similarly to the description in section 4.4 by a normal MOT recapture and an early introduction of B_m at positive B_0. Then compression and evaporation proceeds up to the point, that the evaporation knife energy coincides with $U(\rho_m)$ in order to have the cloud entirely inside the circle of death, though at this point, no zero-field value is orbiting yet. Then B_0 is slowly brought to the desired negative value, where sufficient compression in each separate minimum results in effective evaporation. The term 'slowly' only refers to slowly enough, not to excite significant axial center of mass oscillations. During this stage, the circle with radius ρ_m undergoes a principal transformation: for $B_0 \geq 0$, only one circle exists with its center at $z = 0$ but the minimal value, orbiting at ω_{mod} is equal to B_0, i.e. positive. For $B_0 < 0$ the minimal value at the orbit of ρ_m is zero, but as now two zero points of the static axial field exist, we have to consider two circles, centered on the z-axis at $\pm z_0$. Then evaporation continues to the desired temperature, eventually forming BECs in both wells, if the initial number of atoms is high enough to provide enough density for both minima, and the splitting procedure is achieved without major losses.

A principal limitation to the equality of the two BECs is given by the non-rotationally symmetric terms in the magnetic field definition of equ.(3.10), which describe a tetrahedron-like deformation of the magnetic field for large distances. This term had to be excluded from the previous calculations, because it inhibits an analytical solution. As noted there, this deformation is negligible for regions close to the center, but as in this experiment clouds are dragged to large axial distances $\pm z_0$, the two split minima undergo a certain deformation. As this deformation has a different geometrical shape on either side of the center, the gravitational sag introduces an inequality that causes evaporation to proceeds unequally efficient in the two minima, and an imbalanced number of atoms is observed in the two BECs (up to $\approx$20%).

5.3 Collision image generation

We took data with both condensates and thermal clouds. We report only on the condensates, as already indicated in the discussion in the previous chapter. In our experiments, we load about one billion ^{87}Rb atoms in the (fully stretched) $|F = 2, m_F = 2\rangle$ hyperfine level of the electronic ground state from a magneto-optical trap (MOT) into a Ioffe-Pritchard quadrupole trap ($21 \times 477\,\mathrm{Hz}$) with an offset field of $B_0 = +0.9$ G. The modulation field $B_m = 479\,\mathrm{mG}$ is introduced prior to compression, where at this stage its influence on the thermal sample is negligible. We pre-cool the sample by forced evaporative cooling to $\approx 6\,\mu\mathrm{K}$ with a radio-frequency sweep, as discussed in chapter 3.3.

The cloud is then split in two by ramping B_0 from the positive value of 900 mG down to a negative value B_0^-. The actual value is varied, as we intend to vary the splitting distance z_0. As discussed in the previous section, this procedure results in two separate thermal clouds, confined in two minima, spaced by $2z_0$ with local frequencies given by equ. (5.22). We continue evaporative cooling and reach Bose-Einstein condensation with about 10^5 atoms in each cloud and a condensate fraction of $\sim 60\%$.

A diabatic removal of the modulation field B_m with synchronized reversal of B_0 to the usual value of +900 mG changes the magnetic field structure back to the static potential. If this happens on an infinitesimally small timescale, the clouds are at rest and positioned on the far out wings of a parabolic potential, i.e. at z_0. They use the potential energy, supplied by the switch-on of the magnetic field, to accelerate towards the potential minimum at $z = 0$, as sketched in figure 5.3a. It is intuitively clear, that the kinetic energy is limited by the maximum potential energy, that the trapping potential can provide. However, this procedure has the disadvantage, that the sudden rise in the local axial field value from B_m to $B(0, 0, z_0)$ that each BEC experiences, results in an according decrease in local radial frequency. During acceleration, the cloud then moves into the region of lower axial field value (approaching B_0), and the experienced radial frequency rises during acceleration, which gives rise to undesirable shape oscillations.

This effect can be avoided, by jumping the negative B_0^- in an initial step by a smaller amount to $B_{0,i}^-$, when turning off the modulation field B_m. This amount is given by the condition, that after this step, the center of each BEC is supposed to experience the same local field value as in the modulated trap, so we have $|B_{0,i}^-| = |B_0^-| - |B_m|$, as sketched in fig.5.3b. We then sweep the $B_{0,i}^-$ value from its momentary (negative) value in a curve given by a quarter cycle of a sin-function to the static value of $B_0 = 900$ mG. The timescale of this sinosoidal sweep is related to the axial frequency ω_z by $1/4 \times 21.1^{-1}$ s $= 12$ms. In this way we 'lead' the zero-crossing in front of the accelerating cloud such that we keep the radial trapping frequency that is experienced by each BEC constant for all times[2]. As already mentioned in section 3.2.2, an instantaneous switching of the field leads to considerable switch-off depolarization, so the first stepwise switching was in fact done in a linear ramp of 200 μs duration, which is still much shorter than any considered timescale.

The technical implementation of this 2-step scheme is realized by using multiple power supplies and field coils. The static, positive B_0 with a value of $B_0 = 900\text{mG} - |B_m|$ is generated by large volume field coils, whose currents are during an experiment actually not modified. The negative B_0^- is created by using the axial wire trim coils (see fig.3.9) to counteract the $\vec{B}_0$ field. The used powersupply (type SD20-200D, ®Delta Powersupplies) is controlled via the voltage control input in current stabilized mode, which allows to perform the sinosoidal sweep with one of the waveform outputs of the computer control system (see section 3.5). The initial step of B_0^- to $B_{0,i}^-$ is realized by a third powersupply, wired to the axial PCB trim coils to support $\vec{B}_0$. As the timescale of this initial switch is too short for the used powersupply (type δ-SM20-60D, ®Delta Powersupplies) to react on a change on its voltage control input, a FET-switching circuit similar to fig.3.11 is

[2] An intuitive analogon is surfing down a wave at constant vertical height.

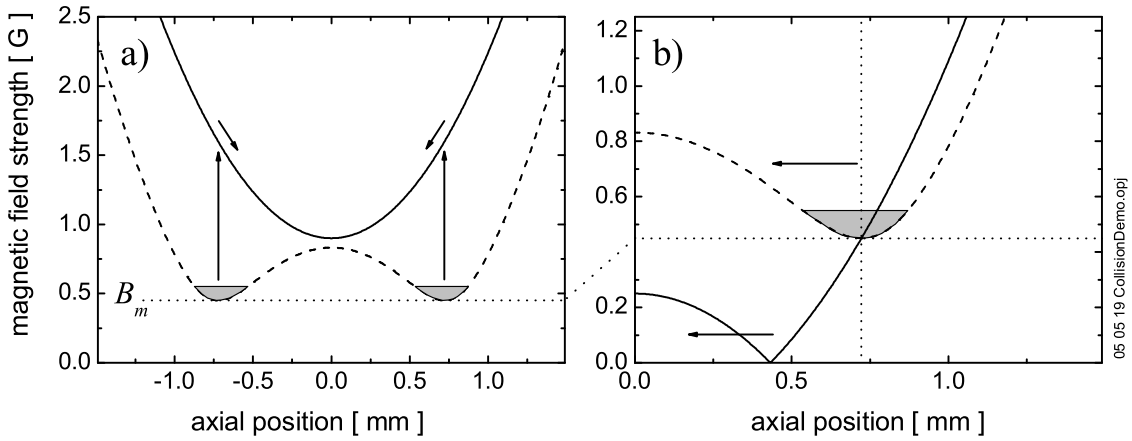

Figure 5.3: Acceleration principle. After preparing 2 BECs in each minimum, a collision is initiated by a diabatic switch from the modulated potential (dashed line) to the unmodulated one (solid line). This switch can occur a) in one step back to the static, positive B_0 or b) by a controlled sweep, guiding the zero crossing at constant energetic distance ahead of the accelerating BEC. Note, that the representation in fig.5.2 and here denotes potential energies, all spatial motion occurs solely along the z-axis.

devised with the powersupply in current stabilized mode. The current is switched solely by the FET, the voltage limit of the powersupply is pre-adjusted to match the desired current, to avoid a current overshoot after opening the FET gate. The sum of the fields of the latter coils and the coils, that were mentioned first in this paragraph add up to 900mG.

The kinetic energy is equal to the potential energy at the moment of switching, which (independent of the precise way of performing the modulation switch-off) is given by $1/2\, m\, v^2 = \mu_B\, B_0^-$, and can be controlled by the current in the wire trim helper coils. The collision occurs in the rest frame of the atoms head on, so the collision energy is twice the individual kinetic energy. The collision energies are linked to the wavevector k by

$$E = |\, 2\mu_B B_0^-| = \hbar^2 k^2 / m, \tag{5.23}$$

with μ_B the Bohr magneton and m the mass of ^{87}Rb and range from 138 μK to 1.23 mK with an overall uncertainty of 3% (RMS), which results from the uncertainty in the coil calibration and measured current.

As the atoms accelerate in a harmonic potential, the time between the modulation switch-off and the collision is independent of the collision energy. Observing the collision with the trap switched on results in more scattered atoms and higher optical density of the halo, as the compression assures a higher cross-section. But this 'in-situ' observation also distorts the shape of the collision halo, as it is not allowed to expand freely, even if the clouds are released immediately after the collision partners have passed each other. As our condensates are sufficiently dense, up to 80% of the colliding 2×10^5 atoms are scattered into the halo (even when released before collision) which results in well sufficient optical density for each part of the halo. This number is measured by acquiring absorption images before and after the collision at large detunings, which is necessary because of the high optical density of the colliding BECs. We therefore release the cloud

by a total magnetic field switch-off just at the moment, when the wings of the BECs start to overlap, and observe the collision in free space. This pre-release time (typically $\approx 0.5\,\mathrm{ms}$) varies slightly with the collision velocity, as the cloud size is constant for all collision velocities. A few ms later we observe the scattering halo by absorption imaging. To improve analysis accuracy, up to 20 individual pictures after the collision are taken and averaged before further processing

Fig.5.4 displays typical (averaged) absorption images for two selected collision energies. Fig.5.4a1 (upper part) displays the s-wave-dominated scattering halo of fully entangled pairs [Chik00], obtained for a collision energy of $E/k_B = 138(4)\,\mu\mathrm{K}$. In fig.5.4b1 (upper part) the halo is entirely different, showing a d-wave-dominated pattern, as it is taken at a significantly higher collision energy of $E/k_B = 1.23(4)\,\mathrm{mK}$. The lower halves of figs.5.4a1 and 5.4b1 display theoretically simulated column densities $n_2(x,z) = \int n\,(x,y,z)\,dy$, where $n(x,y,z)$ is the density of the halo as calculated from the optimized phase η_{opt}, that results from the analysis, that is described in the following section.

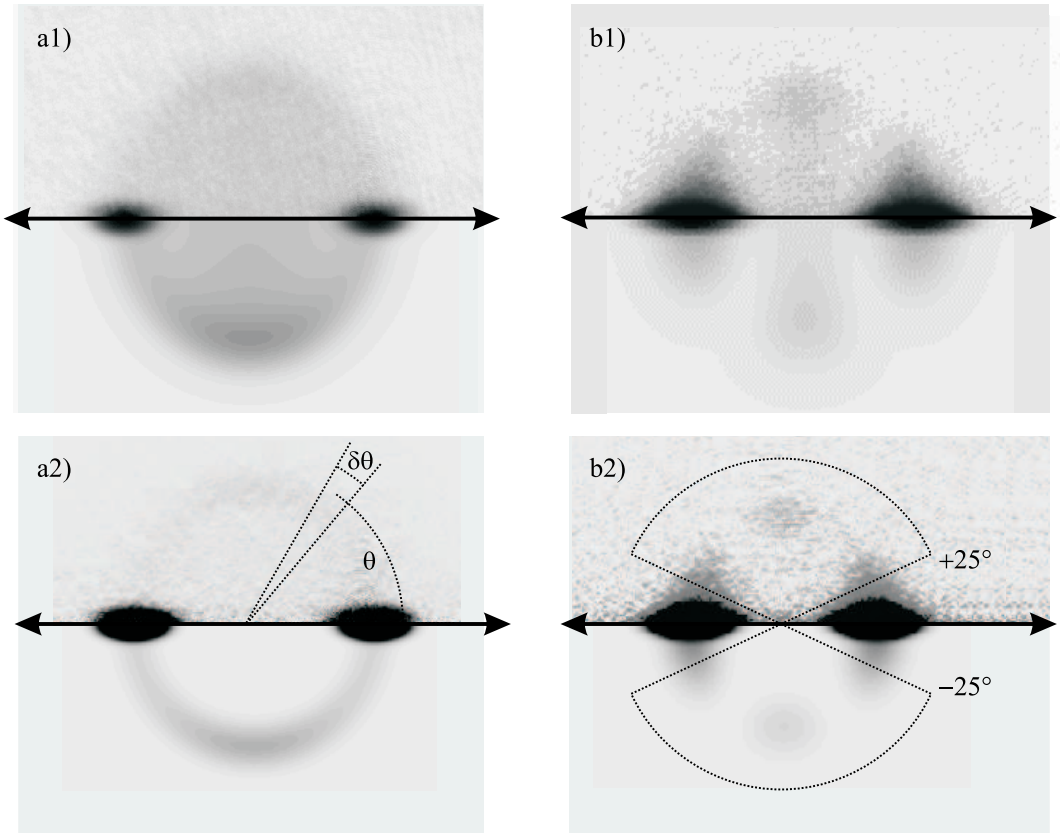

Figure 5.4: Typical absorption images after the collision of 2 BECs. The upper row shows optical densities of the scattering halo for collision energy a1) $E/k_B = 138(4)\,\mu\mathrm{K}$, taken 2.4 ms after the collision, and b1) 1230(40) μK, taken after 0.5 ms. The upper half displays the absorption images as acquired, the lower half a simulated image calculated from η_{opt}. The second row, i.e. a2) and b2) display the images a1) and b1) after the tomography transformation. The sector, indicated in a2) indicates the definition of θ and the shape of the integration sector. In total 30 sectors, covering the area displayed in b2) were used, neglecting the $-25° < \theta < 25°$ sector in forward and backward direction.

5.4 Analysis

5.4.1 Differential scattering amplitude

As discussed in section 5.1 the atoms are scattered by a central field, and the scattering pattern are axially symmetric around the scattering axis, i.e. here the z-axis. As pointed out by the Weizmann group [Ozer02], this allows a computerized tomography transformation [Born-W] to reconstruct the radial density distribution of the halo in cylindrical coordinates by evaluating

$$n(\rho,z) = \frac{1}{4\pi}\int_{-\infty}^{\infty} \tilde{n}_2(\kappa_x, z)\, J_0(\kappa_x \rho)\, |\kappa_x|\, d\kappa_x. \tag{5.24}$$

where ρ is the 1D Fourier transform along the x-direction of the optical density with respect to z

$$\rho = \left(x^2 + y^2\right)^{1/2}\ \tilde{n}_2(\kappa_x, z)\,. \tag{5.25}$$

$J_0(\varrho)$ is the zero-order Bessel function. The transformed plots corresponding to the images of fig.5.4a1 and 5.4b1 are shown as fig.5.4a2 and 5.4b2.

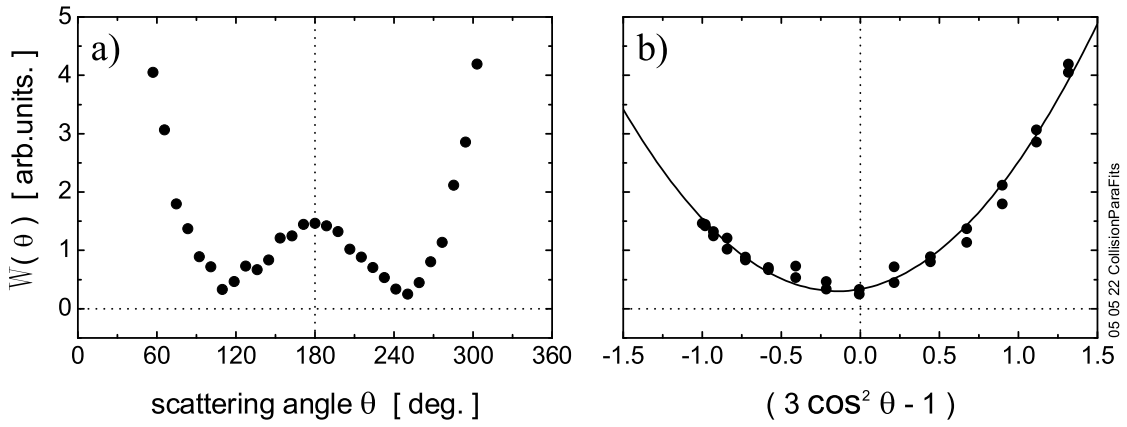

Figure 5.5: Representation of the scattering cross section $W(\vartheta)$ for a collision energy $E/k_B = 1.23(4)\,\mathrm{mK}$, measured 0.5 ms after the collision. Fig. a) shows the number of particles in each of the 30 integrated sectors versus ϑ directly, fig. b) the same, plotted versus $(3\cos^2\vartheta - 1)$. The line in b) is the best parabolic fit.

To obtain the angular scattering distribution $W(\theta)$ we bin the tomographically transformed pictures in 30 discrete angular sectors. These sector have certain angular width $\delta\theta$, and central angle θ as indicated in fig.5.4a2. By counting the total optical density in each sector and transforming it via equ.(3.31) into atom numbers, we retrieve the total number of atoms, scattered into each sector. However, even as up to 80% of the atoms are scattered into the halo, the large halo volume results in low column optical density during imaging, whereas the unscattered clouds appear as objects with high optical density. In absorption imaging on resonance, the halo is very well visible, but the total particle number cannot be retrieved from the same image, as the unscattered clouds appear with saturated optical density. Due to their presence, the two sectors of 50° width

in forward and backwards direction, as shown in fig.5.4b2, are neglected. By repeating the experiment and imaging with different detuning the scattered ratio can be retrieved, but has a larger error attached. However, as argued in section 5.1, this information is not essential for the analysis. As an example fig.5.5a shows the result (in arbitrary units) versus the scattering angle θ for the conditions of the image in fig.5.4b2.

For colliding gas clouds, which are much smaller than the diameter of the halo, $W(\theta)$ is directly proportional to the differential cross section

$$\sigma(\theta) = 2\pi \left| f(\theta) + f(\pi - \theta) \right|^2 . \tag{5.26}$$

Here, the Bose-symmetrized scattering amplitude is given by a summation over the even partial waves,

$$f(\theta) + f(\pi - \theta) = (2/k) \sum_{l=even} (2l+1) e^{i\eta_l} P_l(\cos\theta) \sin\eta_l. \tag{5.27}$$

Unlike in the *total* elastic cross section

$$\sigma = \int_0^{\pi/2} \sigma(\theta) \sin\theta d\theta = \frac{8\pi}{k^2} \sum_{l=even} (2l+1) \sin^2\eta_l, \tag{5.28}$$

the interference between the partial waves is prominent in the *differential* cross section. Given the small collision energy in our experiments, only the s- and d-wave scattering amplitudes contribute, i.e.

$$f_s(\theta) + f_s(\pi - \theta) = \frac{2}{k} e^{i\eta_0} \sin\eta_0 \tag{5.29}$$

$$\text{and} \qquad f_d(\theta) + f_d(\pi - \theta) = \frac{2}{k} \frac{5}{2} e^{i\eta_2} \left(3\cos^2\theta - 1\right) \sin\eta_2. \tag{5.30}$$

Therefore the differential cross section is given by

$$\sigma(\theta) = \frac{8\pi}{k^2} \sin^2\eta_0 \left(1 + 5\cos(\eta_0 - \eta_2)u + \frac{25}{4}u^2\right), \tag{5.31}$$

where $u \equiv (\sin\eta_2/\sin\eta_0)(3\cos^2\theta - 1)$. It is important to realize here, that in the marginal case $\eta_0 = \eta_2$, the expression in the brackets on the r.h.s. of equ.(5.31) becomes phase-shift independent.

To obtain the phase shifts, we plot the measured angular distribution $W(\theta)$ as a function of $(3\cos^2\theta - 1)$ as suggested by equ.(5.31). The results for fig.5.4b2 shown as the solid dots in fig.5.5b. A parabolic fit to $W(\theta)$ directly yields a pair $(\eta_0^{\exp}(k), \eta_2^{\exp}(k))$ of asymptotic phase shifts (defined modulo π) corresponding to the two partial waves involved. This procedure breaks down in the marginal case $\eta_0 = \eta_2$, as noted above. The absolute value of $W(\theta)$ depends on quantities that are hard to measure accurately (like the atom number) so we leave it out of consideration. We rather emphasize that the measurement of the phase shifts is a *complete* determination of the (complex) s- and d-wave scattering amplitudes at a given energy, including the determination of the sign of the phase shift, as will be argued in section 5.4.3.

5.4.2 Phase shift calculation

From the argumentation in section 5.1, we can assume, that the radial wavefunctions corresponding to scattering at different collision energies and different angular momenta in the low energy limit of this experiment should all be in phase at small interatomic distances [Verh93, Grib93] (That this is indeed the case can be seen from fig.5.6). This so-called 'accumulated phase' common to all low-energy wavefunctions can be extracted from the full data set $\{(\eta_0^{\rm exp}(k), \eta_2^{\rm exp}(k))\}$ which are acquired as described in the previous section for various wavevectors k. In practice, we use the experimental phase shifts $\eta_0^{\rm exp}(k)$ and $\eta_2^{\rm exp}(k)$ as boundary conditions to integrate inwards - for given E and l - the Schrödinger equation

$$\hbar^2 \frac{d^2\Psi(r)}{dr^2} + p^2(r)\Psi(r) = 0, \tag{5.32}$$

and obtain the radial wavefunctions $\Psi(r)/r$ down to the radius $r_{in} = 20\,a_0$. Here we have

$$p^2(r) = m\Big(E - V(r)\Big) - \frac{\hbar^2}{r^2}\, l(l+1), \tag{5.33}$$

where $V(r) \simeq -C_6/r^6$ is the tail of the interaction potential (see section 2.3). We used the value $C_6 = 4.698(4) \times 10^3$ a.u. [Kemp02]. At the radius $20\,a_0$, the motion of the atoms is quasi-classical and the accumulated phase can be written as

$$\Phi(r) \simeq \arctan\left(\frac{p(r)}{\hbar\,\partial_r \ln\Psi}\right), \tag{5.34}$$

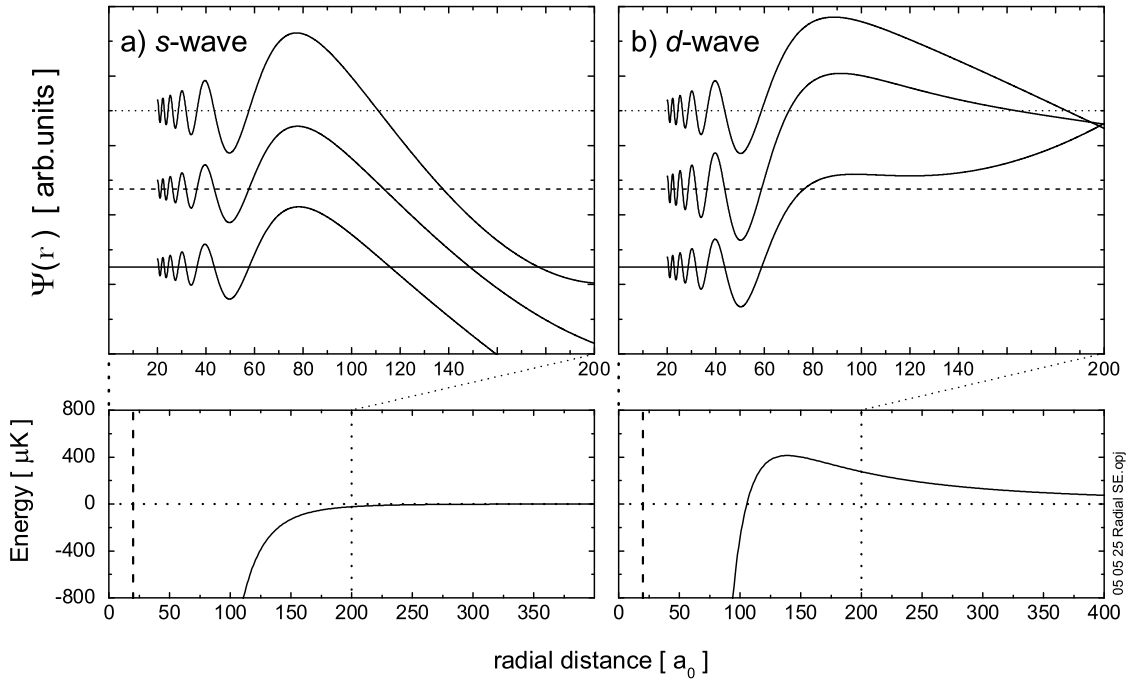

Figure 5.6: Result of integrating the Schrödinger equation, here calculated from η_{opt}. Fig. a) shows the wavefunctions for 3 energies (zero amplitude indicated by the horizontal line: dotted - 500 μK; dashed - 275μK; solid - 50μK) in the C_6/r^6 potential with $l = 0$ (s-wave channel), b) the same for $l = 2$ (d-wave channel). The lower row shows a $\times 2$ zoom out of the potential. The left vertical dashed line in the lower row marks $r = 20a_0$.

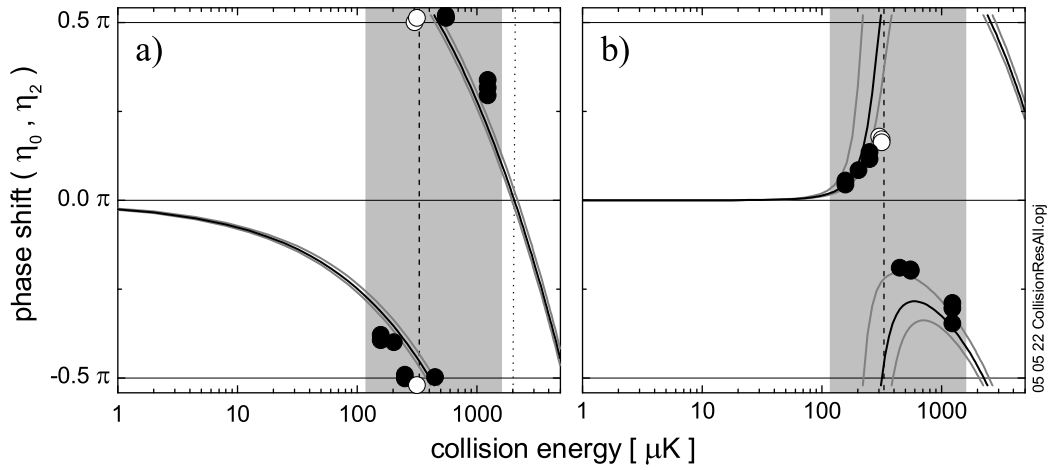

Figure 5.7: a) s-wave and b) d-wave phase shifts versus collision energy in μK. The circles are the results of the parabolic fit of $W(\theta)$ for the individual images. The solid black lines are calculated from the optimized accumulated phase η_{opt}. The grey lines show the effect of adding the uncertainty of $\pm\,0.025\,\pi$ to η_{opt}. The vertical dashed lines indicate the condition $\eta_0 = \eta_2$. Interference between s and d wave is only observed in the grey areas. The first s-wave Ramsauer-Townsend minimum is found at $E_{RT} = 2.1(2)$ mK, marked by the dotted line in a).

where ∂_r represents $\partial/\partial r$. Fig.5.6 shows the resulting wave functions for 3 different collision energies, where fig.5.6a shows the result for the s-wave (with a zoom out of the according potential underneath), and fig.5.6b the same for the d-wave. Note, how the phase development of all waves becomes identical close to $r = 20a_0$.

The distance $20\,a_0$ is small enough for $\Phi(r_{in})$ to be highly insensitive to small variations in E or l [Verh93, Grib93] and large enough that the $-C_6/r^6$ part of the interaction potential is dominant over the full range of integration. We checked that, within the range $15\,a_0 < r < 25\,a_0$, the exact choice of the inner radius of the integration interval is of no influence for the results.

The determination of η_{opt} is done by minimizing

$$\sqrt{\sum_{i=1}^{N}\sum_{l=0,2}\left(\eta_l^{\exp}(k_i) - \eta_l^{\mathrm{opt}}(k_i)\right)^2}, \tag{5.35}$$

where N is the number of data points, and the $\eta_l^{\mathrm{opt}}(k_i)$ are the phase shifts computed from the averaged $\Phi(r_{in})$. As the best value we establish $\eta_{opt} = 1.34 \pm \pi \times 0.025$ for the accumulated phase at $20\,a_0$.

The error reflects the experimental accuracy and not the systematic error related to the choice of C_6, the latter being of less relevance as discussed below. Interestingly, the d-wave scattering resonance [Boes97] results in a sudden variation of $\eta_2^{\exp}$ with the collision energy in the vicinity of that resonance (see fig.5.7a). This imposes a stringent condition on the optimization of Φ_{opt} and constrains its uncertainty.

Once η_{opt} has been established, we use it as a boundary condition to integrate the Schrödinger equation outwards and compute $\eta_l(k)$ for any desired (low) value of k and l. Fig.5.7 shows the resulting phase shifts for collision energies up to 5 mK, the solid dots represent the $\eta_l^{\exp}(k_i)$ obtained from the parabolic fit of $W(\theta)$ from individual images. The g-wave ($l=4$) phase shift can also be computed from the same η_{opt}, but the error made by assuming a constant accumulated phase increases like $l(l+1)$, and the resulting g-wave would be accordingly less accurate. Ramsauer-Townsend minima are observed around collision energies where a phase shift crosses zero (see fig.5.7). The first Ramsauer-Townsend minimum in the s-wave cross section (marked by the dotted line in fig.5.7a) is found at the collision energy $E_{RT}/k_B = 2.1(2)$ mK.

5.4.3 Sign of the phase shift

A certain ambiguity in this procedure persists, since equ.(5.31) is unchanged under reversal of the sign of both $\eta_0^{\exp}(k)$ and $\eta_2^{\exp}(k)$, and the result of the parabolic fit is not unique. We eliminate this ambiguity by comparing the difference in accumulated phases obtained for $\eta_0^{\exp}(k)$ and $\eta_2^{\exp}(k)$ with that obtained for $-\eta_0^{\exp}(k)$ and $-\eta_2^{\exp}(k)$. We find that in almost all cases, this difference - which should be vanishingly small - is much larger for one choice of signs than for the other. We conclude that the correct sign for a pair $(\eta_0^{\exp}(k), \eta_2^{\exp}(k))$ is the one for which the difference between the accumulated phases is the smallest. In all but three cases (at the same collision energy), this criterium is conclusive. These three measurements (the open circles in fig.5.7) are left out of the procedure used to compute η_{opt}. They turn out to correspond to the marginal case that is noted in connection with equ.(5.31), as marked by the vertical dashed lines in fig.5.7. Refinements to the present data analysis may include the occurrence of multiple scattering as well as the influence of the spatial extension of the colliding clouds taking into account the non condensed fraction.

5.5 Results

5.5.1 Triplet scattering length

Knowing the phase shifts, we can infer all the low-energy scattering properties. Our results for the elastic scattering cross section are shown in fig.5.8. The (asymmetric) d-wave resonance emerges pronouncedly at 300(70) μK with an approximate width of 150 μK (FWHM). Most importantly, the scattering length follows from the $k \to 0$ limiting behavior,

$$\lim_{k\to 0} \eta_0(k) = -k\, a_{triplet}, \tag{5.36}$$

which corresponds to the linear approximation from zero energy of the solid line in fig.5.7a. We therefore can extract $a_{triplet}$ with a linear fit to our numerical results. We find $a = +102(6)\, a_0$, whereas the state-of-the-art value is $a = 98.99(2)\, a_0$ [Kemp02]. The d-wave resonance [Boes97] is found at the energy $E_{res} = 300(70)$ μK. These results coincide within experimental error with the precision determinations ($a = 98.99(2)\, a_0$ [Mart02, Kemp02]

and $E_{res} = 270\ \mu$K [Kemp02]), obtained by combining the results of several experiments as input for state-of-the-art theory.

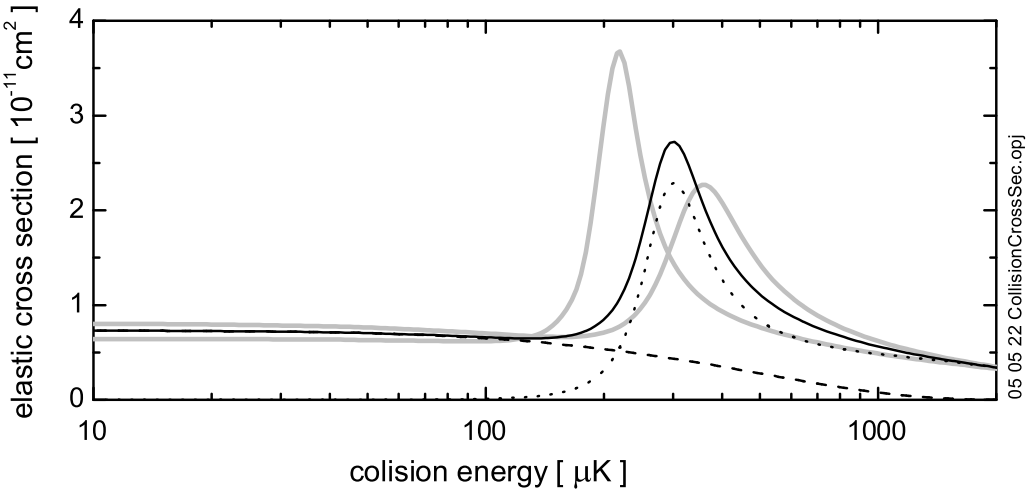

Figure 5.8: s-wave (dashed line), d-wave (dotted line) and total (full black line) elastic cross sections versus collision energy, computed from the optimized accumulated phase η_{opt} as determined in this work. The grey lines are the total elastic cross sections, obtained from $\eta_{opt} \pm 0.025\,\pi$.

5.5.2 Discussion

The comparison with the precision determinations [Mart02, Kemp02] shows that our analysis method readily yields fairly accurate results, relying only on input of the C_6 coefficient, limited predominantly by the quality of the experimental results. In the present case, one does not need to know C_6 to any particular accuracy. Increasing C_6 by 10% results in a 1 %-change of the scattering length. Clearly, the systematic error in η_{opt} accumulated by integrating the Schrödinger equation inward with a wrong C_6 largely cancels when integrating back outward. However, in the case of a s-wave resonance other atomic species may reveal a stronger influence of C_6 on the calculated scattering length. Simple numerical simulations show that the value of C_6 becomes critical only when the (virtual) least-bound state in the interaction potential has an extremely small (virtual) binding energy (less than 10^{-2} level spacing). Hence our method should remain accurate in almost any case.

This method can therefore be applied to other bosonic or fermionic atomic species, provided the gases can be cooled and accelerated in such a way that the lowest-order partial-wave interference can be observed with good energy resolution and image quality. We speculate that the accuracy of the method can be strongly improved by turning to smaller optical-density clouds and fluorescence detection. It will enable higher collision energies and observation of higher-order partial-wave interference. The use of more dilute clouds and longer expansion times will also eliminate multiple-scattering effects

and finite-size convolution broadening of the interference pattern. Finally it will enable precision measurements of the scattered fraction, which in the case of ^{87}Rb will allow us to pinpoint the location of the d-wave resonance to an accuracy of $10\,\mu$K or better. In combination with state-of-the-art theory such improvements are likely to turn our approach into a true precision method.

Chapter 6
BEC Focusing

Since the first observation of Bose-Einstein condensation coherent atom optics is developing into an important field [Rols02], providing tools for the investigation of macroscopic quantum phenomena in dilute atomic gases below their critical temperature. With atom interferometry and quantum information processing as long term goals, atom waveguides as well as atom chips are being developed [Birk01, Brug00, Hind99a]. Mirrors, beam splitters and beam shaping optics of various types have been demonstrated [Roac95, Lau99, Bong99]. Bloch *et al.* [Bloc01] demonstrated the focusing of an atom laser beam by a harmonic potential. A first demonstration of focusing in free flight has been presented by our group in the ballistic expansion of an elongated condensate after release from a Ioffe-Pritchard quadrupole trap [Shva02]. However, in this experiment, the focusing motion has not been triggered actively, but originated from the BEC-formation, that occurred out of equilibrium.

In this part of this thesis we will present BEC-focusing as an universal tool, that can be applied to any initial state of the sample, including equilibrium. This provides a new method for diagnosis of degenerate quantum gases, particularly, as the response of degenerate and non-degenerate clouds differ significantly.

6.1 Focusing principle

To describe the principle of focusing of a condensate in free flight, we consider a cloud of atoms confined in an axially symmetric harmonic trapping potential with angular frequencies ω_z (axial) and ω_ρ (radial) and small aspect ratio $\beta \equiv \omega_z/\omega_\rho \ll 1$, as is the case for the geometry of the experimental device, used in this thesis. The phase space distribution of the trapped cloud is prepared such, that the real space part is given by the cloud shape at equilibrium, i.e. a Gaussian shape with $1/e$-size r_0 according to equ.(2.5) for the non-degenerate fraction and a parabolic shape with Thomas-Fermi size r_{TF} according to equ.(2.44) for the Bose-condensed fraction. In velocity space a linear velocity field $v_{in}(r) = -rv_{in}$ is imposed, that will cause the cloud to contract after release from the trap, so the proper ansatz is given by

$$f(x(0), v(0)) = f(r, v + rv_{in}). \tag{6.1}$$

Note that the unit of v_{in} is s^{-1}. Neglecting all other velocity components and repulsive effects, this linear velocity field would cause all atoms of the sample to arrive on the focused axis center at the same moment, since $t_{focus} = |r/v_{in}(r)| = 1/v_{in}$ is independent of r, as sketched by the dotted line in fig.6.1. In reality, after the release of the cloud at $t = 0$ the cloud evolution will be governed by the competition between the imposed inwards motion and the natural expansion behavior for thermal clouds (see section 2.1.2) and Bose-Einstein condensates (see section 2.5). For sufficient initial inwards velocity, we expect a contraction of the focused axis to a certain, lower value and then the continuation

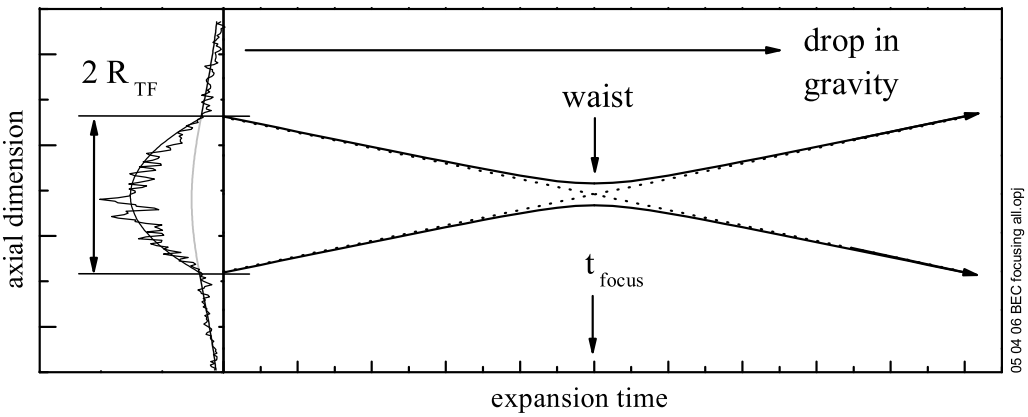

Figure 6.1: Focusing of BEC in free flight. If the initial cloud shape starts from it's size at rest, but is prepared such, that a contraction motion is dominating over the expansion, we expect after an expansion time of t_{focus} the size of that axis to go through a minimum, before re-expanding. Since this procedure occurs in free-flight, the cloud drops in gravity, if no levitation field is applied.

of the expansion, as pictured for a Bose-Einstein condensate in fig.6.1. The moment, when the kinetic trajectory crosses zero, we call in the following the focusing time t_{focus}, the minimal occurring size the focal waist. To first approximation, the focal waist occurs at the moment t_{focus}. However, if broadening effects become noticeable, the moment of minimal size t_{min} shifts to times shorter than t_{focus}, so $t_{min} \leq t_{focus}$, as we will show in the following.

Focusing by oscillation The required inwards velocity can be imposed by preparing the cloud such, that it dilates periodically in a shape oscillation at frequency ω_q (for a collisionless cloud the breathing mode frequency of $\omega_q = 2\omega_z$, for the low-frequency mode of a quadrupole shape oscillation of a BEC $\omega_q \approx 1.58\,\omega_z$ [Kaga96, Dalf99]) with amplitude a_{quad}, so e.g. for a thermal cloud the $1/e$-size scales during holding time as

$$r_e(t) = r_0\,(1 + a_{quad}\sin(\omega_q t_{hold}))\,. \tag{6.2}$$

This can be achieved with the technique presented in section 4.3. By timing the release of the cloud to the moment, when the cloud is in its equilibrium shape ($r(t) = r_0$) during an inwards motion (and thus has maximal velocity of $|v_{in}| = a_{quad}\,\omega_q$) the desired condition is prepared. In this way, the value of the velocity parameter v_{in} can be controlled via the oscillation amplitude. However, the response of the cloud remains in the linear regime only for a limited range of amplitudes, and the technique presented in section 4.3 is limited to $a_{quad} \leq 1$ for principal and to $a_{quad} \leq 0.25$ for technical reasons of this experimental device.

Focusing by acceleration in potential As a second method a switching of the magnetic potential can provide a controllable way of imposing a velocity field. A sudden removal of the radial confinement is equivalent to a full trap switch-off in the radial dimension. If this occurs synchronized with a sudden increase in axial confinement the increased axial force can be exploited to accelerate the distribution. The cloud starts to oscillate inwards in a quadrupole oscillation and accelerates towards the center. The value of v_{in} in this scheme can be controlled by the time passing under acceleration until the total release of the cloud from the potential.

6.1.1 Thermal cloud response

As has been shown in section 2.1.2 the behavior of a thermal cloud in the collisionless regime released from the magnetic trap at equilibrium is given by a Gaussian shape, whose $1/e$-sizes increase linearly in time. Further all axes decouple and the expansion proceeds with the same thermal velocity in all spatial directions. We have shown, that the evolution of the phase-distribution can be calculated by evaluating

$$n_j(r_j,t) = n_0 \iint \exp\left(\frac{-r_j'^2}{r_{j,0}^2} + \frac{-v_j^2}{v_{j,0}^2}\right) \delta(r_j - r_j' - v_j t)\, dr_j' dv_j, \tag{6.3}$$

where the $r_{j,0}$ and $v_{j,0}$ are the $1/e$-sizes in real and velocity space for each axis j, and n_0 is the peak density, given by the normalization of the 3D volume to the particle number.

To find the expansion behavior when starting from a state, where a velocity field is imprinted, we apply the same method and calculate the time evolution of the non-equilibrium phase-space distribution. As has been mentioned in section 2.1.2 in the collision-less regime all axes decouple and we can again treat each axis separately. As has been argued in chapter 4, a quadrupolar shape oscillation in this case is equivalent to a monopole breathing mode oscillation of one axis. Without loss of generality, we assume the focused, thermal fraction to be in the collisionless regime. Then one axis starts its expansion with some contraction velocity, while the remaining two start from thermal equilibrium and expand according to equ.(2.12). For the focused axis (in the experiment the z-axis) we calculate

$$\begin{aligned} n(r,t) &= n_0 \iint \exp\!\left(\frac{-r'^2}{r_0^2} + \frac{-(v + r' v_{in})^2}{v_0^2}\right) \delta(r - r' - vt)\, dr'\, dv \\ &= n_0 \int \exp\!\left(r'^2\left(-A^2 - \frac{v_{in}^2}{v_0^2} + \frac{2v_{in}}{v_0^2 t}\right) + r'\left(\frac{2r}{v_0^2 t^2} - \frac{2r v_{in}}{v_0}\right) - \frac{r^2}{v_0^2 t^2}\right) dr', \end{aligned} \tag{6.4}$$

where we reuse the abbreviation first introduced in section 2.1.2,

$$A^2 = \left(\frac{1}{r_0^2} + \frac{1}{t^2 v_0^2}\right). \tag{6.5}$$

By making use of the identity

$$\int_{-\infty}^{\infty} \exp\!\big(x^2(-a) + xb + c\big)\, dx = \int_{-\infty}^{\infty} \exp\!\big(-a'(x - x_0)^2 + b'\big)\, dx = \exp(b')\frac{\sqrt{\pi}}{\sqrt{a'}} \tag{6.6}$$

we find after some algebra

$$n(r,t) = \mathcal{C}(t) \exp\left(-\frac{r^2}{t^2 v_0^2} + \frac{r_0^2\left(\frac{v_{in}}{t v_0^2} - \frac{1}{v_0^2 t^2}\right)^2}{A^2 - 2\frac{v_{in}}{t v_0^2} + \frac{v_{in}^2}{v_0^2}}\right), \tag{6.7}$$

where the normalization constant $\mathcal{C}(t)$ is again time dependent. Finally we find the scaling behavior of the $1/e$-size during expansion

$$r_0(t)^{-2} = \frac{1}{t^2 v_0^2} - \frac{\left(\frac{v_{in}}{t v_0^2} - \frac{1}{v_0^2 t^2}\right)^2}{A^2 - 2\frac{v_{in}}{t v_0^2} + \frac{v_{in}^2}{v_0^2}} = \frac{A^2 t^2 v_0^2 - 1}{A^2 t^2 v_0^2 - 2 v_{in} t + v_{in}^2 t^2} \tag{6.8}$$

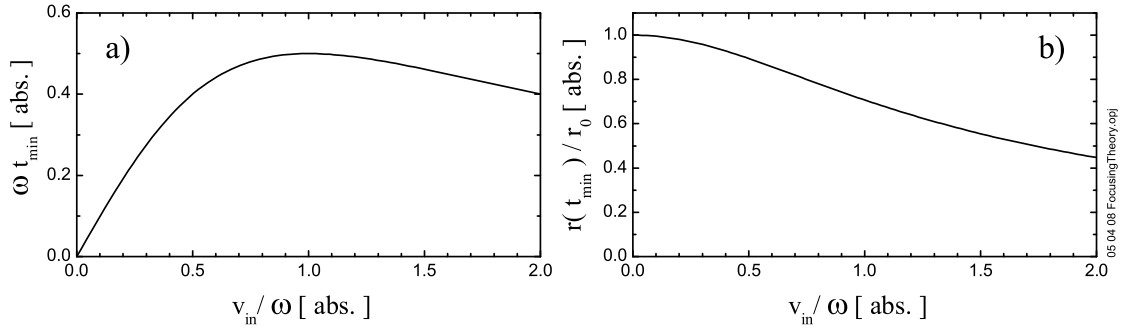

Figure 6.2: Scaled time of minimal size $\omega\, t_{min}$ (a) and scaled focal size $r(t_{focus})/r_0$(b) versus compression motion strength v_{in}/ω. Increasing v_{in} will initially shift the focus time from zero to later times. If it becomes stronger than the thermal expansion ($v_{in} > \omega$), the focus time will return to shorter times. The size at focus, however, monotonously decreases, but a significant drive is necessary to yield substantial focusing. In the experiment, v_{in}/ω remained well below unity for technical limitations.

$$= (r_0^{-2}) \left(1 + \frac{v_0^2 t^2}{r_0^2} - 2v_{in}t + v_{in}^2 t^2\right)^{-1} \tag{6.9}$$

$$\Rightarrow r_0(t) = \sqrt{(r_0 - r_0 v_{in} t)^2 + v_0^2 t^2}. \tag{6.10}$$

This result is conveniently similar to the result, obtained in the case of an expansion from equilibrium (compare equ.(2.12)), and for vanishing imposed velocity ($v_{in} = 0$) returns to the limit of an expansion from equilibrium.

By using equ.(2.5) we rewrite the just found result to

$$r_0(t) = r_0 \sqrt{(1 - v_{in}t)^2 + \omega^2 t^2}, \tag{6.11}$$

where ω is the trap frequency of the axis, that has been focused. It is straightforward to calculate the time of the occurrence of the focal waist

$$t_{min} = \frac{v_{in}}{\omega^2 + v_{in}^2}, \tag{6.12}$$

and the scaled waist of the cloud at this point

$$r(t_{min})/r_0 = \left[1 + \frac{v_{in}^2}{\omega^2}\right]^{-1/2}. \tag{6.13}$$

This results implies, that the scaled focal size is independent of the cloud temperature. As can be seen from fig.6.2a the slowest focusing motion (i.e. maximum t_{min}) occurs for $v_{in} = \omega$. It is also apparent from fig.6.2b, that in order to yield a substantial compression, a significant compression velocity $v_{in} \sim \omega$ is required. For triggering maximum focusing (which results in a compression to 0.71) from a quadrupole oscillation, where $v_{in} = a\omega$, the amplitude would be $a_{quad} = 1$. For a realistic oscillation amplitude of $a_{quad} = 25\%$ we find a scaled focal size of 97% at $\omega_z t_{min} = 0.23$. A detailed evaluation of the potential acceleration method will be given in section 6.2, but has similar limitations. Therefore it is virtually impossible to achieve substantial compression for thermal clouds.

6.1.2 Bose-Einstein condensate response

Initially the axial size is given by the equilibrium Thomas-Fermi radius of equ.(2.46), $R_{TF,z} = (2\mu/m\omega_z^2)^{1/2}$, where μ is the chemical potential of the gas and m the atomic mass as before. The evolution of the axial and radial sizes of the cloud within the Thomas-Fermi approximation is given by the scaling equations (2.57)

$$\ddot{b}_j = \frac{\omega_j^2(0)}{b_j(t)\, b_\rho(t)^2\, b_z(t)} \qquad (j = \rho, z), \tag{6.14}$$

with the initial conditions $b_z(0) = b_x(0) = b_y(0) = 1$, but in this case with the initial conditions for the first derivatives $\dot{b}_z(0) = -v_{in}$ and $\dot{b}_\rho(0) \simeq 0$ unlike the discussion in section 2.5.

Analogously to the result of equ.(2.58) we find to good approximation for the radial expansion $b_\rho(t) = (1 + \omega_\rho^2 t^2)^{1/2}$. For the focused axis, an approximate solution can be found, by separating the time development into 3 parts, marked as sectors **I**, **II** and **III** in fig.6.3: in the initial phase of expansion (sector **I**), the rapid expansion of the unfocused radial dimension leads to a rapid decrease of the second derivative in equ.(6.14). Any velocity development will cease after a time of the order of $1/\omega_\rho$, marked by the first vertical line in fig.6.3. Since this time is short as compared to the axial timescale, we can assume b_z to be constant during this stage. The scaling equation thus simplifies to

$$\ddot{b}_z = \frac{\omega_z^2}{1 + \omega_\rho^2 t^2}, \tag{6.15}$$

which can be directly integrated to

$$\dot{b}_z = \frac{\omega_z^2}{\omega_\rho} \arctan(\omega_\rho t)\Big|_0^\infty + \dot{b}_z(0) = \frac{\omega_z^2}{\omega_\rho}\frac{\pi}{2} + \dot{b}_z(0). \tag{6.16}$$

As to be expected, the release of the mean-field energy leads to a reduction of the contraction velocity $\dot{b}_z(0) = v_{in}$, sketched by the dashed line in fig.6.3.

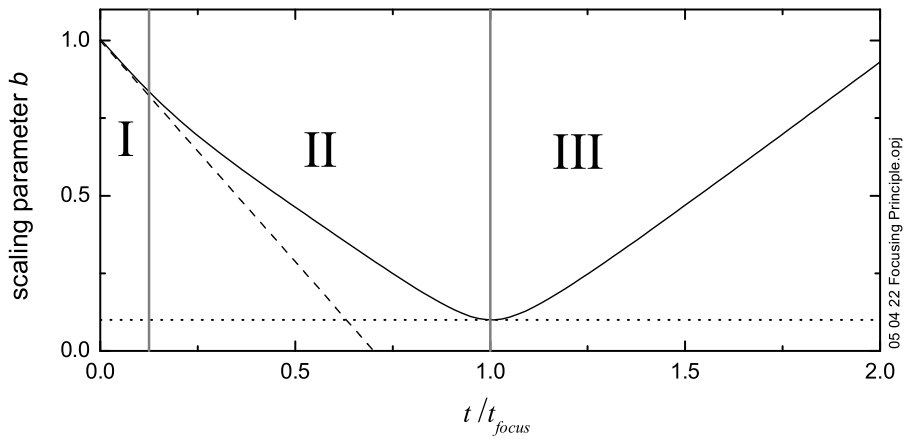

Figure 6.3: Integration regions for focusing. The initial sector **I** has a duration of the order $1/\omega_\rho$, which is strongly enlarged in this schematic. Also the change in slope between sector **I** and **II** is over-emphasized.

During phase **II** the contraction continues linearly, as the second derivative has a negligible value at the end of stage **I** and drops quadratically further in time due to the radial expansion. Around the focusing time t_{focus} its value rises again, as b_z approaches zero. This can be understood as a repulsive force, that forces the contraction motion to halt and 'reflects' the axial size back into an expansion motion. This inversion proceeds symmetric, so the absolute values of the slopes in sectors **II** and **III** are equal. The value is given by equ.(6.16), which can be further approximated by neglecting the first term on the r.h.s., which is equivalent to approximating the axial expansion in equ.(2.59) by a static axial size. At the moment of t_{focus} thus conditions, similar to the starting point of a BEC expansion are restored, and we describe the behavior of the axial size for $t > t_{focus}$ in analogy to the characteristic form of the radial size by

$$b_z(t) = b_f \sqrt{1 + \zeta^2 \, b_f^{-2} \, \omega_z^2 (t - t_{focus})^2}, \tag{6.17}$$

with the yet unknown focal waist $b_f = b_z(t_{focus})$. This form assures, that the slope remains independent of the actual value of b_f at $t = t_{focus}$. For times $0 \leq t < t_{focus}$ this is a good approximation only for $b_f \ll 1$, since then we have $b(t=0) \simeq 1$. Here we also introduce the contraction parameter ζ as

$$\omega_z \zeta = \frac{\omega_z^2}{\omega_\rho} \frac{\pi}{2} + \dot{b}_z(0) = \frac{\omega_z^2}{\omega_\rho} \frac{\pi}{2} - v_{in}. \tag{6.18}$$

We restart from the scaling equation, make use of the approximation equ.(6.17) and calculate

$$2\dot{b_z}\ddot{b}_z = \frac{-2\omega_z^2}{1+\omega_\rho^2 t^2}(-1) b_z^{-2} \dot{b_z} \tag{6.19}$$

$$\partial_t(\dot{b}_z^2) = \frac{-2\omega_z^2}{1+\omega_\rho^2 t^2} \, \partial_t(b_z^{-1}) \tag{6.20}$$

$$\Rightarrow \dot{b}_z^2 = \frac{2\omega_z^2}{1+\omega_\rho^2 t^2} b_z^{-1}(t)\Big|_{t_{focus}}^{\infty} - \int_{t_{focus}}^{\infty} \frac{4\omega_z^2 \omega_\rho^2 t}{(1+\omega_\rho^2 t^2)^2 b_z(t)} \, dt \tag{6.21}$$

$$\approx \frac{2\omega_z^2}{b_\rho(t_{focus})^2 \, b_z(t_{focus})}. \tag{6.22}$$

We match the slope in sector **II** to the one in sector **III** (neglecting the 'kick' that causes the decrease in slope in stage **II** as argued above) and find

$$\omega_z^2 \zeta^2 = \frac{2\omega_z^2}{b_\rho(t_{focus})^2 \, b_z(t_{focus})}. \tag{6.23}$$

Realizing, that to very good approximation the focus time is given by $\omega_z^2 t_{focus} = b_z(0)/\zeta$ and that the radial size has greatly expanded during the time of sector **II** (which implies $\omega_\rho^2 t_{focus}^2 \gg 1$) we find

$$\omega_z^2 \zeta^2 = \frac{2\omega_z^2}{\omega_\rho^2 t_{focus}^2 \, b_f} \quad \Rightarrow \quad b_f = \frac{2}{\omega_\rho^2 \, \zeta^2 t_{focus}^2} = \frac{2\omega_z^2}{\omega_\rho^2}. \tag{6.24}$$

This result implies, that the compression can be very tight, as $2\omega_z^2/\omega_\rho^2 \approx 4 \cdot 10^{-3}$ for the conditions of this experiment. In such cases the optical resolution of the imaging system

used for detection is likely to limit the minimum observable focal size. The typical axial diameter ($2\times R_{TF}$) of BEC's in the trap of our conditions is of the order of 100 μm. With the trap aspect ratio of 23, we expect therefore an axial width of 0.4 μm at the focus, whereas the optical resolution limit is 3.3 μm (see sec.3.4.3).

Beyond a certain expansion time the kinetic energy of the original condensate can no longer be neglected as it gives rise to spreading of the condensate wavefunction. This effect may be accounted for by writing

$$b_z(t) \simeq b_f \sqrt{1 + \zeta^2\, b_f^{-2}\, \omega_z^2 (t - t_{focus})^2 + \eta^2\, b_f^{-2}\, \omega_z^2 t^2}, \tag{6.25}$$

where η is a parameter that expresses the momentum spread, which enlarges the minimum focal waist linearly with the expansion time. Further, it can be concluded from calculating the first derivative of equ.(6.25) that the occurrence of the minimal axial size (t_{min}) is shifted towards earlier times ($t_{min} < t_{focus}$). This effect is shown in fig.6.4, where equ.(6.25) is plotted for two selected parameters sets.

For $\eta = 1$ and $\zeta = 0$, equ.(6.25) represents the spreading of a minimum uncertainty wavepacket. This can be seen from calculating the time-evolution of a Gaussian wavepacket

$$\langle z|\Psi(t)\rangle = \int_{-\infty}^{\infty} dz'\, K(z,t,z',t')\langle z'|\Psi(t')\rangle, \tag{6.26}$$

with the quantum-mechanical propagator

$$K(z,t,z',t') = \int_{-\infty}^{\infty} \frac{dp_z}{2\pi\hbar} \langle z|p_z\rangle \exp\left(-i\frac{E(t-t')}{\hbar}\right) \langle p_z'|z'\rangle \tag{6.27}$$

$$= \left(\frac{m}{i\,2\pi\hbar(t-t')}\right)^{3/2} \exp\left(\frac{i\,m}{2\hbar}\,\frac{(z-z')^2}{(t-t')}\right). \tag{6.28}$$

A minimum uncertainty wavepacket ($\delta z\, \delta p_z = 1/2\,\hbar$) has a Gaussian shape, and is given in 1D (an extension to 3D is trivial because of the superposition principle) by

$$\langle z'|\Psi(t')\rangle = \frac{1}{(2\pi)^{1/4}\delta z} \exp\left(\frac{i}{\hbar} p_0\, z' - \frac{z'}{4\delta z^2}\right), \tag{6.29}$$

where we set in the following the initial momentum p_0 to zero, since the cloud is initially at rest and define the initial time t' also as zero. The density profile is given by the expectation value

$$|\langle z'|\Psi(t)\rangle|^2 = \frac{1}{(2\pi)^{1/2}\delta z'^2} \exp\left(\frac{-z'^2}{2\delta z'^2}\right), \tag{6.30}$$

where the Gaussian $1/e$-size can be matched to the oscillator ground state for the focused axial direction

$$2\delta z'^2 = \frac{\hbar}{\omega_z\, m}. \tag{6.31}$$

By inserting equ.(6.27) in equ(6.26) with the initial wavefunction equ.(6.29) we can explicitly calculate the expansion of the wave function due to the non-zero impulse-spread. We have to solve

$$\langle z|\Psi(t)\rangle = \int_{-\infty}^{\infty} dz' \left(\frac{m}{i2\pi\hbar(t-t')}\right)^{3/2} \frac{2}{(2\pi)^{1/4}\delta z'} \exp\left(\frac{i\,m}{2\hbar}\,\frac{(z-z')^2}{(t-t')} - \frac{z'^2}{4\delta z'^2}\right), \tag{6.32}$$

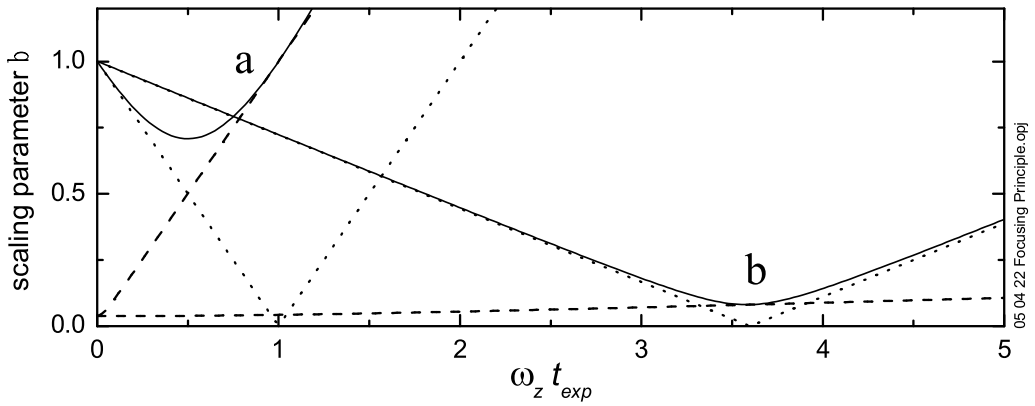

Figure 6.4: Focusing response for a) $\eta = 1$; $\zeta = 1$ and b) $\eta = 0.02$; $\zeta = 0.125$. The dotted lines show the kinetic trajectory, the dashed lines the expansion due to momentum spread and the solid lines the focusing response for the according set of η and ζ-parameters. For the η-parameter, that we assume for our experiment, we expect no slope in the dashed line.

which can be done with little algebra by using again the identity equ.(6.6), and we find

$$\langle z|\Psi(t)\rangle = \frac{\text{const.}}{\sqrt{\frac{1}{4\delta z^2} - \frac{i\,m}{2\hbar t}}} \exp\left(\frac{i\,mz^2}{2\hbar t} + \frac{(\frac{i\,m2z}{2\hbar t})^2}{4(\frac{1}{4\delta z^2} - \frac{i\,m}{2\hbar t})}\right), \tag{6.33}$$

where 'const.' incorporates all non time-dependent normalization constants. By calculating the expectation value $|\langle z|\Psi(t)\rangle|^2$ we can extract the time evolution of the scaled $1/e$-size and after inserting equ.(6.31) we find

$$b(t) = \sqrt{\left(\frac{2\hbar}{m4\delta z^2}\right)^2 t^2 + 1} = \sqrt{\omega_z^2 t^2 + 1}, \tag{6.34}$$

which is identical to the solution in the case of a thermal cloud expansion. Therefore the oscillator ground state wavefunction behaves during expansion from equilibrium ($\zeta = 0$) and also under focusing ($\zeta > 0$) in the same way as a thermal cloud, i.e. according to equ.(6.25) with $\eta = 1$.

Under such conditions, no appreciable focusing is observed except for extreme contraction parameters ζ, as has been discussed at the end of section 6.1.1. For $b_z(t_{focus}) = 1/23$, $\eta = 1$ and $\zeta = 1$, we find $b_{z,min} \approx 0.71$ at $t_{min} \approx 0.5\, t_{focus}$, which is represented as the left solid line in fig.6.4 and identical to the result concluded in section 6.1.1. In general, equ.(6.25) gives rise to substantial focusing only if $\zeta \gg \eta$.

For elongated Thomas-Fermi condensates the situation is different, because the significant initial size, caused by the spreading of the wavefunction due to the mean field pressure, implies a strongly reduced momentum spread. Therefore the condition $\zeta > \eta$ is satisfied and strong focusing can be observed, as sketched by the solid line in fig.6.4 for the value of $\eta = 0.2$. This situation is described by approximating the waist parameter with $\eta = \hbar/2\mu$, which is the value that results from the assumption of

a recovery of the chemical potential and the accompanied mean-field pressure. Then, for $t < t_0 = 2\beta^2 m R_{TF,z}^2/\hbar$, the spreading can be neglected even with respect to the compression minimum $2\beta^2 R_{TF,z}$. For the conditions of this experiment we find $t_0 \approx 52$ ms.

At temperatures above the phase fluctuation temperature, $T > T_\phi = 15\,(\hbar\omega_z)^2 N/32\mu$, equilibrium phase fluctuations will dominate the focal broadening [Petr01, Dett01, Hell01]. In this case the waist parameter may be approximated by $\eta \approx (R_{TF,z}/L_\phi)^2 \hbar\omega_z/\mu \approx (l_h/L_\phi)^2$, where L_ϕ is the phase coherence length and $l_h = [\hbar/m\omega_z]^{1/2}$ the axial harmonic oscillator length. By observing the waist size, it is therefore possible to extract information about the internal momentum spread of the expanding condensate. Any observable width can be attributed to phase fluctuations or other distortions. Further, since free expansion converts velocity components into a spatial density distribution, the axial density cross-section at the focal point is directly proportional to the spectrum of the momentum distribution at the moment of release.

6.2 Experimental sequence

As a method to accelerate the distribution, the method of switching the potential as described in section 6.1 was chosen. A complete removal of the radial confinement ($\omega_\rho \to 0$) can be realized by switching off the current in the Ioffe-bars (see fig.3.9). However, due to technical limitations, this was not feasible without creating transient magnetic fields, that accelerated the cloud in an undesired way. As an alternative, a switch-off of the compensation coils results in a significant increase in B_0, which according to equ.(3.12) gives rise to a decrease in ω_ρ. To describe the effect of the switch off of the compensation coils on the potential, the expression in equ.(3.10) is apparently insufficient. An analytic expression for the field strength along the axis can be derived, by using Biot-Savarts law [Jackso, LandauC].

$$d\vec{B} = \mu_o I n \frac{\vec{dl} \times \vec{r}}{4\pi r^3}, \tag{6.35}$$

where I is the applied current, n the number of windings and $\mu_0 = 4\pi 10^{-7} VsA^{-1}m^{-1}$ the magnetic field constant of the vacuum. Including geometrical factors and integrating the radial symmetry we find for a pair of coils the field along the axis as

$$B_z(z) = \frac{I\,n\,\mu_0}{2}\left(\frac{1}{R}\left(1+\frac{(z-D)^2}{R^2}\right)^{-3/2} + \frac{1}{R}\left(1+\frac{(z+D)^2}{R^2}\right)^{-3/2}\right), \tag{6.36}$$

where R represents the radius and $2D$ the spacing of the coils along the z-axis. By modelling the number and spatial arrangement and current directions of pinch and compensation coils, the field strength and curvature along the trap axis can be calculated.

Thus we find for our experimental apparatus, that the described procedure results in a rise of B_0 from 0.9G to 392G and an increase of axial frequency by 4% from $\omega_z = 2\pi\,21.1$Hz to $\omega_{z,acc} = 2\pi\,22.0$Hz. The increase of B_0, results according to equ.(3.12):

$$\omega_\rho = \sqrt{\frac{\mu_B}{m}\left(\frac{\alpha_{real}^2}{B_0} - \beta_{real}\right)} \tag{6.37}$$

in a decrease of ω_ρ to $\omega_{\rho,acc} = 2\pi\,17.3$Hz. It is interesting to note, that due to the high value of B_0 the first term under the square root becomes comparable to β_{real}, which at usual compression is negligible.

Due to the reduced radial trap frequency, the gravitational sag (which is with 1μm negligible at full compression) shifts the trap minimum to a significantly lower position. By balancing the trapping force versus the gravitational force

$$m\omega_{\rho,acc}^2\rho_g = mg, \tag{6.38}$$

where m is the ^{87}Rb mass and g the gravitational constant, we find the shift $\rho_g = 830\mu$m. So the clouds center-of-mass will oscillate with that amplitude at a frequency of $\omega_{\rho,acc}$ around the point ρ_g if the trap is kept on with the increased B_0. By restricting the time of evolution in that potential to $t_{acc} < 10$ms after this step (which is 2/3 of the first quarter cycle) and then releasing the cloud in all directions, the radial expansion can to good approximation be considered as free.

The development of the axial motion can be calculated by assuming, that the axial distribution oscillates decoupled from the radial expansion in the tightened axial potential. The value of v_{in} rises with the acceleration time t_{acc} between switch-off of the compensation coils and the total trap switch-off sinusoidally and reaches its maximum after a quarter cycle of the monopole oscillation that with the frequency $2\omega_{z,acc}$.

The preparation of the thermal cloud proceeds in the static potential at full compression. In order to assure, that the clouds are well in the collisonless regime, laser depletion stages are applied to lower the density to typically $\approx 2\,10^{12}\mathrm{cm}^{-3}$, which corresponds to a collision rate of $2\omega_z\tilde{\tau} \approx 20$ and therefore collisionless conditions. The clouds are allowed to reach equilibrium by adding 1 second of plain evaporation after laser depletion.

The experimental sequence starts with the switch off of the current in the compensation coils, followed by a variable acceleration time t_{acc}. Then all current is switched off and the development of the cloud shape during expansion time t_{exp} is observed by absorption imaging. As the cloud evolution has to be observed in free space and no field coils are installed to apply a levitation field, the cloud drops in gravity. The camera field of view is limited to $\approx 1 \times 1\,$mm and the cloud leaves the field of view after $\approx 14\,$ms. During expansion the camera field of view has to be adjusted to remain centered on the falling cloud, which can be done to great precision with the mounting mechanics (see section 3.4). However, the displacement range of the mechanics is limited such, that after an expansion time of 35ms the center of the cloud leaves the field of view[1]. This duration can be entirely exploited for the observation of Bose-Einstein condensates, due to their

[1] Due to transient magnetic fields the cloud was accelerated from the center in a trajectory towards the camera. This was clearly identified as being caused by a geometrical mismatch of the field minimum of the pinch and compensation coils, which caused the potential minimum to shift in real space at the moment of switch-off of the compensation coils. This shift turned out to be too strong to compensate with the helper coils. The trajectory was quantified by remeasuring the focal position of the camera for a large number of value pairs of t_{acc} and t_{exp}. This observation showed that the motion could be very well described by an acceleration parabola. In all experimental measurements, the camera was guided to follow the cloud with the field of view and also with the camera focus.

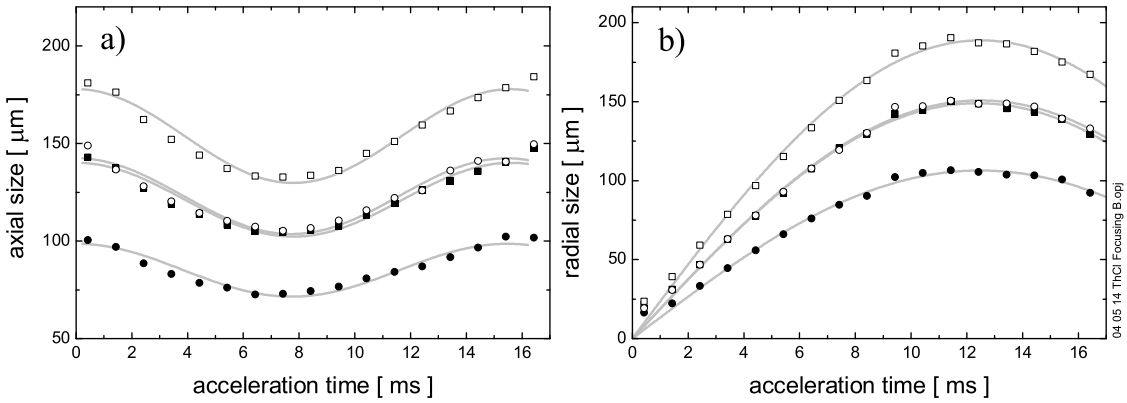

Figure 6.5: Evolution of the cloud sizes after sudden lowering of the radial frequency and slight increase of the axial one for 3 different temperatures 0.8μK, 1.5μK and 2.3μK, ordered from lowest to uppermost curve in both figures and 2 densities. Fig a) axial sizes, b) radial sizes. The grey solid lines represent fit functions in both figures.

smaller size. For thermal clouds the rapid expansion of all thermal sizes makes a successful surface fit difficult, if the cloud does not stay in the center of the field of view, and the maximum observable time is in practice limited to $\approx$20ms.
As argued before, we expect no appearance of mean-field broadening of the focal waist for times $t_{exp} < 52\,\mathrm{ms}$, so we expect to observe focusing to the resolution limit for the Bose-Einstein condensates in our experiment for all possible values of ζ i.e. v_{in}.

6.2.1 Thermal cloud results

In-trap evolution Fig.6.5 shows the response of thermal clouds to the described trap switching, if the cloud is left oscillating in the new trap, which is characterized by $\omega_{z,acc}$ and $\omega_{\rho,acc}$. In order to retrieve the cloud temperatures we fit to the linear part of the radial expansion in fig.6.5b, i.e. including only the data between 3 and 7 ms, and find the temperatures 0.8μK, 1.5μK, 1.5μK and 2.3μK. To retrieve the axial frequency $\omega_{z,acc}$ we fit an undamped cosine with zero phase offset to the oscillation traces in fig.6.5a. Assuming a collisionless breathing mode shape oscillation we find the axial frequency $\omega_{z,acc} = 2\pi\,(32.2 \pm 5)$Hz. The accuracy is mainly limited by the shortness of the trace. From the average axial size we deduce the temperatures a second time and find agreement within 0.1μK. However, the frequency result shows a significantly higher value for the axial frequency, than the anticipated 22Hz; also the averaged amplitude in the traces is with 19% much larger than the expected 5% amplitude.

In order to retrieve the radial frequency $\omega_{\rho,acc}$ we assume, that the cloud starts a breathing oscillation with zero phase offset. From fig.6.5b we see that the oscillation amplitude is far outside the harmonic regime and cannot be described by a cosine. To retrieve the lowest frequency in the spectrum of this oscillation (which we assume to be twice the trap frequency), we measure the time between the lowest and highest turning point of the radial size oscillation by fitting a sine with zero phase offset neglecting all data points below 6ms. The sine peaks at 12.5ms, so the period of the shape oscillation is has a length of 25ms. Since breathing mode oscillations in the collisionless regime proceed at the double trap frequency, we deduce $\omega_{\rho,acc} = 2\pi\,(20.0 \pm 0.8)$Hz, which

agrees with the anticipated value within its principal insecurity (see discussion on page 99).

Despite the discrepancy in the axial dimension, the cloud development proceeds qualitatively as predicted. The increased contraction velocity allows more pronounced observation of the behavior at large v_{in}[2]. From fig.6.5a we conclude for the experimental sequence, that the clouds should not be released later than 7ms after the rise of B_0, and the contraction velocity reaches its maximum for $t_{acc} \approx 3$ms. The radial oscillation period is sufficiently long to exploit this time, without a distortive effect on the radial expansion behavior.

Kinetic focusing To observe the focusing motion in free flight, we trigger the oscillation as described and release the cloud at various times t_{acc}. We monitor the entire development from the moment of switching B_0 on by absorption imaging. This allows us, to cross-check the free expansion of the radial thermal size and provides a mean to test the timing of the release.
Fig.6.6 shows the response of thermal clouds for various values of t_{acc} in the range from 2ms to 8ms (in steps of 1ms). For reference also a release of the cloud from the standard potential was measured, i.e. the magnetic field switching sequence was totally removed from the timeframe control script, but it is still referred to as $t_{acc} = 0$ms.

By applying linear fits to the radial expansion from the moment of B_0-switching on in fig.6.6c we demonstrate, that the radial cloud development is very well described by a free, thermal cloud expansion. From the found linear slope we extract all cloud temperatures, which lie between 1.14 and 1.36μK. We plot the linear expansion again in scaled units (scaled to the average cloud size of all measurements) as a guide to the eye in fig.6.6a. We find that the expansion velocity is to very good approximation (as far, as a comparison is possible with focused clouds) equal in both axes, which confirms, that the clouds are in the collisionless regime [Shva03a]. Fig.6.6a shows the development of the axial sizes of all clouds after release for various t_{acc} scaled to the size of the cloud at the moment of release. We find the anticipated behavior of thermal clouds (compare fig6.4a), which is described by equ.(6.11) (we show the corresponding fit only for the uppermost and the lowest curve).

Fig.6.6b shows the retrieved maximum compression ratios for the corresponding acceleration times. The dashed line shows the expected behavior, which we calculate ab-initio by combining the found breathing oscillation frequency and amplitude (to extract v_{in}) with equ.(6.13). The agreement is outside the statistical error but given the low compression for these conditions and in view of the limited precision of the fitting routines acceptable.

A more detailed quantitative analysis is largely complicated by the unknown reason for the unexpectedly high axial frequency and amplitude. Therefore, we do not present any further analysis and do not draw a definite, quantitative conclusion on the thermal cloud behavior. We assume that the anomalously strong contraction behavior is caused by an artefact in the trap switching procedure and might be removed by adjustments of technical details of the sequence[3].

[2] There is no possibility to investigate the reason for this increased amplitude and frequency, since the experiment has been disassembled prior to data analysis, as mentioned in the preface to this thesis.

[3] In this case any investigation of this behavior is impossible, because it is likely to be an artefact of

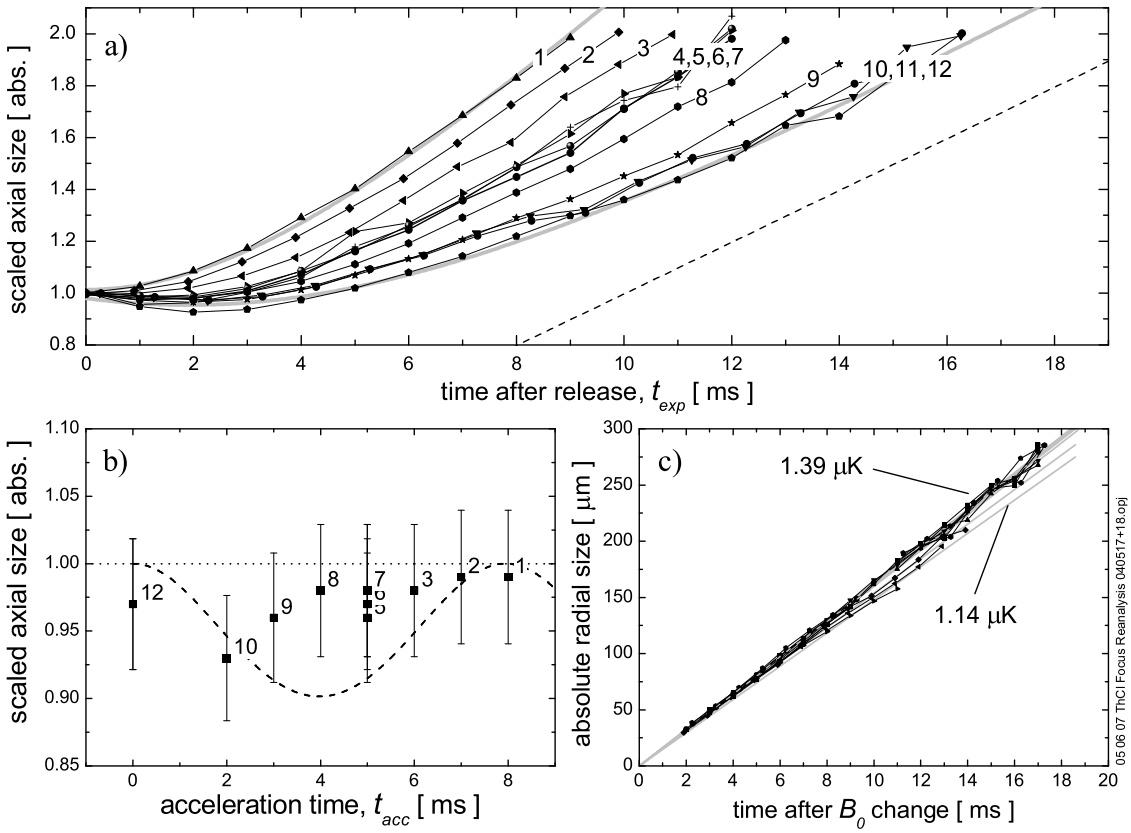

Figure 6.6: Fig.a) Thermal cloud development for various acceleration times from t_{acc} = 0ms and t_{acc} = 2ms to t_{acc} = 8ms in steps of 1ms, scaled to the size at the moment of release. Fig.b shows the resulting compression ratios for each t_{acc}, the numeric labels allow an identification of the corresponding time development trace in fig.a. Fig.c, show the absolute sizes of the radial time development after release from the radial confinement, i.e. the moment of B_0-rise. The temperatures deduced from the radial expansion vary between 1.14μK and 1.39μK. The dashed line in fig.a shows the linear slope corresponding to a temperature of 1.39μK as a guide to the eye. The grey solid lines in fig.a show exemplary 2 fits of equ.(6.11) to the uppermost and lowest data set. The dashed line in fig.b shows an ab-initio calculation of the expected focusing compression.

We conclude, that the response of thermal clouds is in qualitative agreement with equ.(6.11). For the parameters of this experiment, no focusing of thermal clouds to a compression smaller than 0.9 is observed, which confirms the conclusion of section 6.1.1, that no significant focusing of thermal clouds can be achieved.

6.2.2 BEC results

By excluding the laser-depletion stage and evaporating to lower temperatures, we go above the critical phase-space density of Bose-Einstein condensation and reach condensate fractions > 80%. We let the condensate reach equilibrium by allowing 1s of plain evaporation and then apply the identical magnetic switching sequence as described in section 6.2. Then we observe the dynamic evolution of radially free expanding and

the device itself, which after re-assembly might not reappear.

axially focusing condensate, as described in the previous section for thermal clouds. The magnetic trap switching sequences here are identical in all cases and details except the durations of t_{acc} and t_{exp}. As argued before, the condensate drops in free flight, and the time of observation is limited by the maximum vertical displacement of the camera to 30ms.

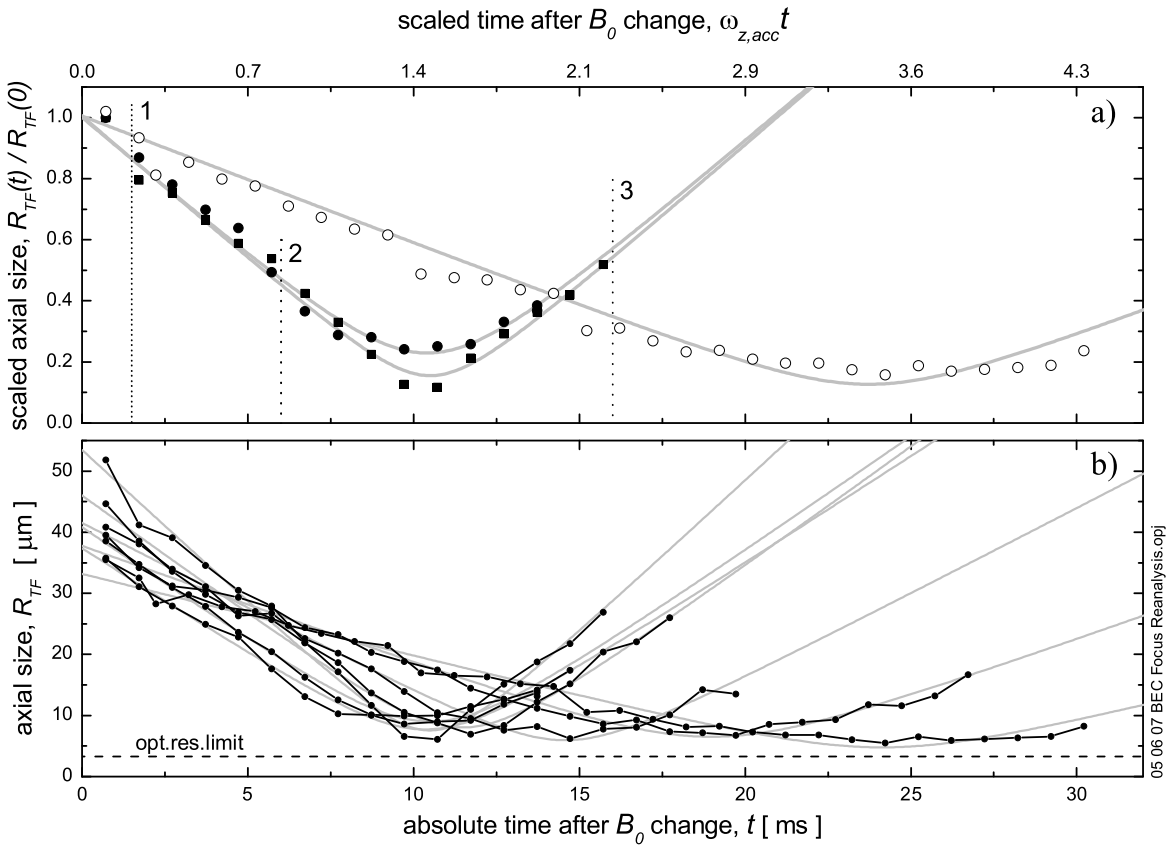

Figure 6.7: Results of active, kinetic BEC focusing. Fig.a shows a selection of 3 observed BEC focusing trajectories for release at $t_{acc}=3$ms (vertical dashed marker 1, hollow circles), $t_{acc}=7$ms (vertical dashed marker 2, full circles), and one in-field focusing trajectory (release at $t_{acc}=15$ms, vertical dashed marker 3, full boxes). Axial sizes are scaled to the in-trap size. Fig.b shows all acquired trajectories in absolute sizes. The grey solid lines represent in both graphs a fit of equ.(6.25) to the data points. The horizontal dashed line in fig.b marks the resolution limit. The time is shown in absolute units in fig.b and in scaled units in fig.a.

Fig.6.7 shows the observed behavior of the axial Thomas-Fermi size of equ.(2.46) for the time after the switching of B_0. From Fig.6.7a we see, that the contraction motion for a Bose-Einstein condensate is significantly different compared to a thermal cloud, which was presented in fig.6.6. The compression ratio is well below 0.3, which is in agreement with the discussion in section 6.1.2. We note, that the focusing behavior for fast inwards motion, i.e. large v_{in}, does not decrease for $t_{acc} > 3$ms, as it is observed in thermal clouds: The compression of the in-field focused cloud (full boxes in fig.6.7a) is tighter than for the one, which is released before the focus (full circles), but the time of t_{min} is equal. We also see from both fig.6.7a and b, that for decreasing t_{acc} the occurrence

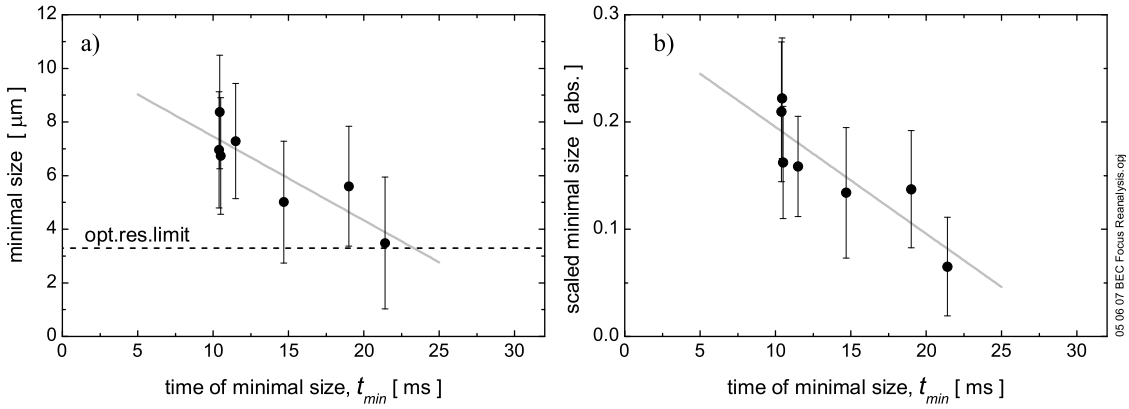

Figure 6.8: Observed absolute (a) Thomas-Fermi sizes and compression ratio $b(t_{min})/b(t{=}0ms)$ (b) plotted as a function of t_{min}. The optical resolution limit is deconvoluted for all data. The grey lines represent a free linear fit, but serves only as a guide to the eye.

of the minimal axial size shifts monotonously to larger t_{min}, which is in agreement with the argumentation in section 6.1.2. From fig.6.7a we conclude a value of $\zeta = 0.7$ for the contraction motion of the clouds released at marker 2 and 3, which is an unexpectedly large value. However, this observation is in agreement with the unexpected large axial frequency change and the large oscillation amplitude, that was observed in thermal clouds.

In fig.6.8 we plot the minimum observed size vs. the moment of its occurrence t_{min}. We de-convolute the optical resolution limit of 3.3μm from the smallest observed axial size of $\approx 4.8\mu$m and find a minimum axial Thomas-Fermi size of $\approx$ 3.4μm, which is of the order of but still larger than the optical resolution limit of 3.3μm. As anticipated from the conclusion of section 6.1.2, the value does not rise with t_{min}. On the contrary, we observe that both compression and absolute minimum size *decrease* in an approximately linear fashion on the range of our observations with t_{min}.

As to the effect of the influence of phase fluctuations on the waist size, we can only compare the results on equilibrium phase fluctuations with the non-equilibrium fluctuations, reported in refs.[Shva00, Shva03b][4]. The result presented therein is shown as the full dots fig.6.9. We plot in the same figure the trace from fig.6.7 for $t_{acc} = 2$ms as hollow dots. From the fit we find, that the non-equilibrium phase fluctuations increase the minimum waist size by a factor of $\approx$2.5 from the waist of an equilibrium BEC. This is in qualitative agreement with the model presented in section 6.1.2, but due to the unknown reason for the large waist size for equilibrium BEC's and the time dependency of the waist on t_{min} we cannot state the actual value of the phase coherence length for either cases.

6.3 Discussion

Comparing the response of thermal clouds in fig.6.6 with the one of Bose-Einstein condensed clouds in fig.6.7 we find the anticipated principally contrary behavior: Thermal

[4] A deeper investigation of this dependency was abandoned, due to lack of time before the scheduled moving of the experiment.

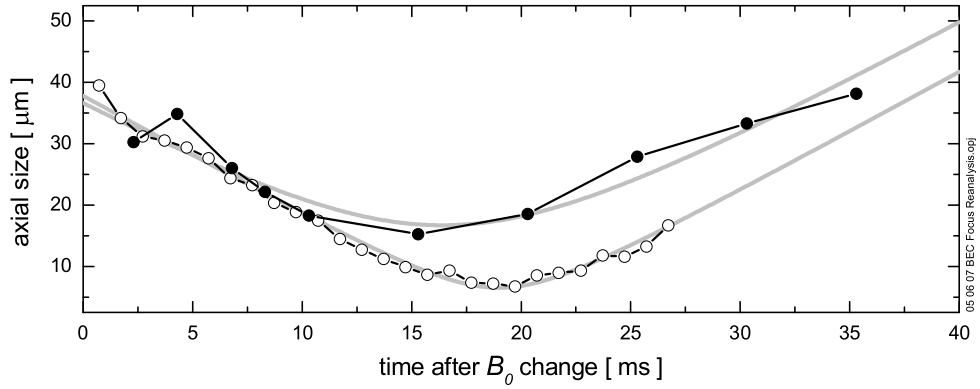

Figure 6.9: Focusing of a BEC with strong non-equilibrium phase fluctuations as reported in refs.[Shva00, Shva03b] (full dots) compared to active focusing with $t_{acc} = 2$ms of an equilibrium condensate. The grey, solid lines represent fits of equ.(6.25) to the data points.

clouds show a significantly weaker compression (> 0.9) than degenerate clouds (< 0.3) for the same inwards velocity v_{in}. We have also shown that the theoretical model for the focusing motion is in qualitative agreement with the observed behaviors for both cases.

The anomalous strong focusing motion is likely to be an artefact of the experimental device. Without further experimental investigation, a conclusion on the dependency of the compression on v_{in} cannot be made. The observation of a *decreasing* minimum axial waist in focusing for larger t_{min} in BECs is also not predicted by the theoretical model. We note, that with the typical radial diameter of 60μm at $t_{min} \approx 15$ms an angle between camera and orthogonal axis of 4.6 degrees would cause an infinitesimally thin disk of that diameter to appear with a thickness of 3μm. Such a deviation in camera position is unlikely, but cannot be verified. Though a combination of technical details might add to yield the observed size, all of them would result in a static axial waist, or one, that *increases* with t_{min}. If all technical limitations can be ruled out, we speculate, that the effect of the mean field pressure built-up is largely underestimated and further investigations appear necessary, as the observations contradict the conclusions made in ref.[Shva03b].

According to the calculation presented in section 6.1.2, the phase coherence state can be deduced from the focal waist. A first application of the focusing technique with that goal was reported in ref.[Shva02]. The intention of the experiments shown in this chapter were to confirm the underlying theory. However, with the available data, and in particular the uncertainties in the driving parameters, this definite conclusion cannot be made.

Still the found results confirm the applicability of BEC focusing as a tool to compress Bose-Einstein condensed and (to lower extent) thermal clouds initially at rest in expansion. The dependance of the waist size on the phase coherence state of the degenerate cloud is proven and an upper boundary of the effect of Heisenberg-uncertainty broadening is given. Due to the disassembly of the Bose-Einstein condensation experiment, with which the experiments in this thesis have been performed, the mentioned further investigations are beyond the possibilities of the author of this thesis.

Bibliography

[AlKh00] U. Al Khawaja, C.J. Pethick, H. Smith, *Kinetic theory of collective modes in atomic clouds above the Bose-Einstein transition temperature*, J.Low Temp.Phys. **118**, 127 (2000).

[Ande95] M.H. Anderson, J.R. Ensher, M.R. Matthews, C.E. Wieman, E.A. Cornell, *Observation of Bose-Einstein condensation in a dilute atomic vapor*, Science **269**, 198 (1995).

[Andr96] M.R. Andrews, M.-O. Mewes, N.J. van Druten, D.S. Durfee, D.M. Kurn, W. Ketterle, *Direct non-destructive imaging of BEC*, Science **273**, 84 (1996).

[Andr97] M.R. Andrews, C.G. Townsend, H.-J. Miesner, D.S. Durfee, D.M. Kurn, W. Ketterle, *Observation of interference between two bose condensates*, Science **275**, 637 (1997).

[Bard57] J. Bardeen, L.N. Cooper, J.R. Schrieffer, *Theory of Superconductivity*, Phys.Rev. **108**, 1175 (1957).

[Baym96] G. Baym, C.J. Pethick, *Ground-State Properties of Magnetically Trapped Bose-Condensed Rubidium Gas*, Phys.Rev.Lett. **76**, 6 (1996).

[Bech67] R.J. Becherer, G.B. Parrent jr., *Nonlinearity in optical imaging systems*, J.Opt.Soc.Am. **57**, 1479 (1967).

[Berg87] T. Bergeman, G. Erez, H.J. Metcalf, *Magnetostatic trapping fields for neutral Atoms*, Phys.Rev. A **35**, 1535 (1987).

[Beth35] H. Bethe, *Theory of disintegration of nuclei by neutrons*, Phys.Rev. **47**, 747 (1935).

[Beth99] H.A. Bethe, *Quantum theory*, Rev.Mod.Phys. **71**, S1 (1999).

[Birk01] G. Birkl, F.B.J. Buchkremer, R. Dumke, W. Ertmer, *Atom optics with microfabricated optical elements*, Opt.Commun. **191**, 67 (2001).

[Bloc01] I. Bloch, M. Köhl, M. Greiner, T.W. Hänsch, T. Esslinger, *Optics with an atom laser beam*, Phys.Rev.Lett. **87**, 030401 (2001).

[Boes97] H.M.J.M. Boesten, C.C. Tsai, J.R. Gardner, D. J. Heinzen, B.J. Verhaar, *Shape resonances in the collision of cold ^{87}Rb*, Phys.Rev. A **55**, 636 (1997).

[Bond00] M. Bondiou, R. Gabet, G.M. Stéphan, P. Besnard, *Linewidth of an optically injected semiconductor laser*, J.Opt. B **2**, 41 (2000).

[Bong99] K. Bongs, S. Burger, G. Birkl, K. Sengstock, W. Ertmer, K. Rzazewski, A. Sanpera, M. Lewenstein, *Coherent Evolution of Bouncing Bose-Einstein Condensates*, Phys.Rev.Lett. **83**, 3577 (1999).

[Born-W] M. Born, E. Wolf, *Principles of Optics*, 7th (expanded) Edition, Cambridge University Press, Cambridge (1999).

[Bose24] S.N. Bose, *Plancks Gesetz und Lichtquantenhypothese*, Zeitschrift für Physik **26**, 178 (1924).

[Bour03] T. Bourdel, J. Cubizolles, L. Khaykovich, K.M.F. Magalhaes, S.J.J.M.F. Kokkelmans, G.V.Shlyapnikov, C. Salomon, *Measurement of the Interaction Energy near a Feshbach Resonance in Li-6*, Phys.Rev. Lett. **91**, 20402 (2003).

[Brad95] C.C. Bradley, C.A. Sackett, J.J. Tollet, R.G. Hulet, *Evidence of Bose-Einstein condensation in an atomic gas with attractive interactions*, Phys.Rev.Lett. **75**, 1687 (1995).

[Brad97] C.C. Bradley, C.A. Sackett, R.G. Hulet, *Analysis of in situ images of Bose-Einstein condensates of Lithium*, Phys.Rev. A **55**, 3951 (1997).

[Brug00] K. Brugger, T. Calarco, D. Cassetari, R. Folman, A. Haase, P.B. Hessmo, P. Krüger, T. Maiers, J. Schmiedmayer, *Nanofabricated atom optics: atom chips*, J.Mod.Opt. **47**, 2789 (2000).

[Buch00] F.B.J. Buchkremer, R. Dumke, Ch. Buggle, G. Birkl, W. Ertmer, *Low-cost setup for generation of 3 GHz frequency difference phase-locked laser light*, Rev.Sci.Instr. **71**, 3306 (2000).

[Bugg04a] Ch. Buggle, I. Shvarchuck, W. von Klitzing, J.T.M. Walraven, *Hydrodynamic clouds and Bose-Einstein condensation*, J.Phys.IV France **116**, 211 (2004).

[Bugg04b] Ch. Buggle, J. Léonard, W. von Klitzing, J.T.M. Walraven, *Interferometric Determination of the s and d-Wave Scattering Amplitudes in ^{87}Rb*, Phys.Rev.Lett. **93**, 173202 (2004).

[Bugg05] Ch. Buggle, P. Pedri, W. von Klitzing, J.T.M. Walraven, *Shape oscillations in non-degenerate Bose gases - transition from the collisionless to the hydrodynamic regime*, cond-mat/0505136, submitted to Phys.Rev. A (2005).

[Burn02] K. Burnett, P.S. Julienne, P.D. Lett, E. Tiesinga, C.J. Williams, *Quantum encounters of the cold kind*, Nature **416**, 225 (2002).

[Buss85] B. Bussery, M. Aubert-Frécon, *Multipolar long-range electrostatic, dispersion, and induction energy terms for the interactions between two identical alkali atoms, Li, Na, K, Rb, and Cs in various electronic states*, J.Phys.Chem. **82**, 3224 (1985).

[Cast96] Y. Castin, R. Dum, *Bose-Einstein condensates in time dependant traps*, Phys.Rev.Lett. **77**, 5315 (1996).

[Cha-Cow] S. Chapman, T.G. Cowling, *The Mathematical Theory of Non-Uniform Gases*, Cambridge University Press, Cambridge (1970).

[Chik00] A.P. Chikkatur, A. Görlitz, D.M. Stamper-Kurn, S. Inouye, S. Gupta, W. Ketterle, *Suppression and Enhancement of Impurity Scattering in a Bose-Einstein Condensate*, Phys.Rev.Lett., **85**, 483 (2000).

[Chin00] C. Chin, V. Vuletic, A.J. Kerman, S. Chu, *High Resolution Feshbach Spectroscopy of Cesium*, Phys.Rev.Lett. **85**, 2717 (2000).

[Clin80] R.W. Cline, D.S. Smith, T.J. Greytak, D. Kleppner, *Magnetic confinement of Spin-polarized atomic hydrogen*, Phys.Rev.Lett. **45**, 2117 (1980).

[Corn02] E.A. Cornell, C.E. Wieman, *Nobel lecture: Bose-Einstein condensation in a dilute gas*, Rev.Mod.Phys. **74**, 875 (2002).

[Cubi03] J. Cubizolles, T. Bourdel, S.J.J.M.F. Kokkelmans, G.V. Shlyapnikov, C. Salomon, *Production of Long-Lived Ultracold Li-2 Molecules from a Fermi Gas*, Phys.Rev.Lett. **91**, 240401 (2003).

[Dalf99] F. Dalfovo, S. Giorgini, L.P. Pitaevskii, S. Stringari, *Theory of Bose-Einstein condensation in trapped gases*, Rev.Mod.Phys. **71**, 463 (1999).

[Datz99] S. Datz, G.W.F. Drake, T.F. Gallagher, H. Kleinpoppen, G. zu Putlitz, *Atomic Physics*, Rev.Mod.Phys. **71**, S223 (1999).

[Davi95a] K.B. Davis, M.-O. Mewes, M.A. Joffe, M.R. Andrews, W. Ketterle, *Evaporative cooling of Sodium atoms*, Phys.Rev.Lett. **74**, 5202 (1995).

[Davi95b] K.B. Davis, M.-O. Mewes, M.R. Andrews, N.J. van Druten, D.S. Durfee, D.N. Kurn, W. Ketterle, *Bose-Einstein condensation in a gas of Sodium atoms*, Phys.Rev.Lett. **75**, 3696 (1995).

[Dean03] D.J. Dean, M. Hjorth-Jensen, *Pairing in nuclear systems: from neutron stars to finite nuclei*, Rev.Mod.Phys. **75**, 607 (2003).

[Demtrö] W. Demtröder, *Laserspectroscopy*, Springer Verlag, Berlin, ISBN 3-540-57171-X 2nd edition (1998).

[Dett01] S. Dettmer, D. Hellweg, P. Ryytty, J.J. Arlt, W. Ertmer, K. Sengstock, D.S. Petrov, G.V. Shlyapnikov, H. Kreutzmann, L. Santos, M. Lewenstein, *Observation of phasefluctuations in elongated Bose-Einstein condensates*, Phys.Rev.Lett. **87**, 160406 (2001).

[Diec98] K. Dieckmann, R.J.C. Spreeuw, M. Weidemüller, J.T.M. Walraven, *Two-dimensional magneto-optical trap as a source of slow atoms*,Phys.Rev. A **58**, 3891 (1998).

[DiecTh] K. Dieckmann, *Bose-Einstein condensation with high atom number in a deep magnetic trap*, Ph.D. thesis, University of Amsterdam (2001).

[Dodd96] R.J. Dodd, M. Edwards, C.J. Williams, C.W. Clark, M.J. Holland, P.A. Ruprecht, K. Burnett, *Role of attractive interactions on Bose-Einstein condensation*, Phys.Rev. A **54**,661 (1996).

[Edwa96] M. Edwards, R.J. Dodd, C.W. Clark, P.A. Ruprecht, K. Burnett, *Properties of a Bose-Einstein condensate in an anisotropic harmonic potential*, Phys.Rev. A **53**, R1950 (1995).

[Eike01] K.S.E. Eikema, J. Walz, T.W. Hänsch, *Continuous Coherent Lyman-α Excitation of Atomic H*, Phys.Rev.Lett. **86**, 5679 (2001).

[Eins24] Einstein, *Quantentheorie des einatomigen idealen Gases - Erste Abhandlung*, Sitzungsber.Preuss.Akad.Wiss. 261 (1924).

[Eins25] Einstein, *Quantentheorie des einatomigen idealen Gase - Zweite Abhandlung*, Sitzungsber.Preuss.Akad.Wiss. 3 (1925).

[Ensh96] J.R. Ensher, D.S. Jin, M.R. Matthews, C.E. Wieman, E.A. Cornell, *Bose-Einstein Condensation in a Dilute Gas: Measurement of Energy and Ground-State Occupation*, Phys.Rev.Lett. **77**, 4984 (1996).

[Ette75] R.D. Etters, J.V. Dugan, Jr. and R.W. Palmer, *The ground state properties of spin aligned atomic hydrogen, deuterium and tritium*,J.Chem.Phys. **62**, 313 (1975).

[Fedi96a] P.O. Fedichev, M.W. Reynolds, G.V. Shlyapnikov, *Three body recombination of Ultracold Atoms*, Phys.Rev.Lett. **77**, 2921 (1996).

[Fedi96b] P.O. Fedichev, Yu. Kagan, G.V. Shlyapnikov, J.T.M. Walraven, *Influence of Nearly Resonant Light on the Scattering Length in Low-Temperature Atomic Gases*, Phys.Rev.Lett. **77**, 2921 (1996).

[Ferr02] G. Ferrari, M. Inguscio, W. Jastrzebski, G. Modugno, G. Roati, A. Simoni, *Collisional properties of ultracold K-Rb Mixtures*, Phys.Rev.Lett. **89**, 53202 (2002).

[Frie80] D.G. Friend, R.D. Etters, *A dilute Hard-Sphere Bose-Gas Model Calculation of Low-Density Atomic Hydrogen Properties*,J.Low Temp.Phys. **39**, 409 (1980).

[Frie98] D.G. Fried, T.C. Killian, L. Willmann, D. Landhuis, S.C. Moss, D. Kleppner, T.J. Greytak, *Bose-Einstein condensation of atomic hydrogen*,Phys.Rev.Lett. **81**, 3811 (1998).

[Gard95] J.R. Gardner, R.A. Cline, J.D. Miller, D.J. Heinzen, H.M.J.M. Boesten, B.J. Verhaar, *Collisions of doubly spin polarized, ultracold ^{85}Rb atoms*, Phys.Rev.Lett. **74**, 3764 (1995).

[Gard97] C.W. Gardiner, P. Zoller, R.J. Ballagh, M.J. Davis, *Kinetics of Bose-Einstein Condensation in a Trap*, Phys.Rev.Lett. **79**, 1793 (1997).

[Gard98] C.W. Gardiner, M.D. Lee, R.J. Ballagh, M.J. Davis, P. Zoller, *Quantum Kinetic Theory of Condensate Growth: Comparison of Experiment and Theory*, Phys.Rev.Lett. **81**, 5266 (1998).

[Gens01] S.D. Gensemer, D.S. Jin, *Transition from collisionless to hydrodynamic behaviour in an ultracold Fermi gas*, Phys.Rev.Lett. **87**, 173201 (2001).

[Gerb04] F. Gerbier, J.H. Thywissen, S. Richard, M. Hugbart, P. Bouyer, A. Aspect, *Critical temperature of a trapped, weakly interacting Bose gas*, Phys.Rev.Lett. **92**, 030405 (2004).

[Gert00] J.M. Gerton, D. Strekalov, I. Prodan, R.G. Hulet, *Direct observation of growth and collapse of a Bose-Einstein condensate with attractive interactions*, Nature **408**, 692 (2000).

[Gibb95] K. Gibble, S. Chang, R. Legere, *Direct Observation of s-wave atomic Collisions*, Phys.Rev.Lett. **75**, 2666 (1995).

[Gold81] V.V. Goldman, I.F. Silvera, A.J. Leggett, *Atomic hydrogen in an inhomogeneous magnetic field: Density profile and Bose-Einstein condensation*, Phys.Rev. B **24**, 2870 (1981).

[Golu79] R. Golub, J.M. Pendlebury, *Ultra-cold neutrons*, Rep.Prog.Phys. **42**, 439 (1979).

[Gott62] Yu.V. Gott, M.S. Ioffe, V.G. Tel'kovsky, *Some new results on plasma confinement in a magnetic trap*, Academy of Sciences of the USSR, J.Nucl.Phys. **3**, 1045 (1962).

[Grei02] M. Greiner, O. Mandel, T. Esslinger, T.W. Hänsch, I. Bloch, *Quantum phase transition from a superfluid to a Mott insulator in a gas of ultracold atoms*, Nature **415**, 39 (2002).

[Grei03] M. Greiner, C.A. Regal, D.S. Jin, *Emergence of a molecular Bose-Einstein condensate from a Fermi gas*, Nature **426**, 537 (2003).

[Grib93] G.F. Gribakin, V.V. Flaumbaum, *Calculation of the scattering length using the semiclassical approximation*, Phys.Rev.A **48**, 546 (1993).

[Grif97] A. Griffin, W.C. Wu, S. Stringari, *Hydrodynamic modes in a trapped Bose gas above the Bose-Einstein Transition*, Phys.Rev.Lett. **78**, 1838 (1997).

[Guer02] D. Guéry-Odelin, *Mean-field effects in a trapped gas*, Phys.Rev. A **66**, 033613 (2002).

[Guer99] D. Guéry-Odelin, F. Zambelli, J. Dalibard, S. Stringari, *Collective oscillations of a classical gas confined in harmonic traps*, Phys.Rev. A **60**, 4851 (1999).

[Gust97] T.L. Gustavson, P. Bouyer, M.A. Kasevich, *Precision Rotation measurements with an atomic interferometer gyroscope*, Phys.Rev.Lett. **78**, 2046 (1997).

[Hecht] E. Hecht, *Optics*, Addison-Wesley, Reading, 2nd edition, ISBN 0-201-11611-1 (1987).

[Hein99] D. Heinzen, in:, *Proceedings of the international School of Physics - Enrico Fermi*, M. Inguscio, S. Stringari and C. Wieman (Eds.), IOS Press, Amsterdam (1999).

[Hell01] D. Hellweg, S. Dettmer, P. Ryytty, J.J. Arlt, W. Ertmer, K. Sengstock, D.S. Petrov, G.V. Shlyapnikov, H. Kreutzmann, L. Santos and M. Lewenstein, *Phase fluctuations in Bose-Einstein condensates*, App.Phys.B **73**, 781 (2001).

[Hess86] H.F. Hess, *Evaporative cooling of magnetically trapped and compressed spin-polarized hydrogen*, Phys.Rev. B **34**, 3476 (1986).

[Hess87] H.F. Hess, Greytak, *Magnetic trapping of spin-polarized atomic hydrogen*, Phys.Rev.Lett. **59**, 672 (1987).

[Hijm93] T.W. Hijmans, Yu. Kagan, G.V. Shlyapnikov, J.T.M. Walraven, *Bose condenstaion and relaxatio explosion in magnetically trapped hydrogen*, Phys.Rev. B **48**, 12886 (1993).

[Hind99a] E.A. Hinds, I.G. Hughes, *Magnetic atom optics: mirros, guides, traps and chips for atoms*, J.Phys.D: Appl.Phys. **32**, R119 (1999).

[Hind99b] H. Hinderthür, F. Ruschewitz, H.-J. Lohe, S. Lechte, K. Sengstock, W. Ertmer, *Time-domain high finesse atom interferometry*, Phys.Rev.A **59**, 2216 (1999).

[Hols97] B. Holst, W. Allison, *An atom focusing mirror*, Nature **390**, 244 (1997).

[Hutc97] D.A.W. Hutchinson, E. Zaremba, A. Griffin, *Finite temperature excitations of a trapped Bose gas*, Phys.Rev.Lett. **78**, 1842 (1997).

[Inou98] S. Inouye, M.R. Andrews, J. Stenger, H.-J. Miesner, D.M. Stamper-Kurn, W. Ketterle, *Observation of Feshbach resonances in a Bose-Einstein condensate*, Nature **392**, 151 (1998).

[Jackso] J.D. Jackson, *Classical electrodynamics*, 3rd edition, John Wiley and sons inc., ISBN 0-471-30932-X (New York) (1999).

[Jess96] P.S. Jessen, I.H. Deutsch, *Optical lattices*, in Adv.At.Mol.Opt.Phys. **37**, 95 (1996).

[Joch03b] S. Jochim, M. Bartenstein, A. Altmeyer, G. Hendl, S. Riedl, C. Chin, J. Hecker Denschlag, R. Grimm, *Bose-Einstein condensation of molecules*, Science **302**, 2101 (2003).

[Kaga96] Yu. Kagan, E.L. Surkov, G.V. Shlyapnikov, *Evolution of a Bose-condensed gas under variations of the confining potential*, Phys.Rev. A **54**, R1753 (1996).

[Kaga97] Yu. Kagan, E.L. Surkov, G.V. Shlyapnikov, *Evolution of a Bose gas in anisotropics time dependant traps*, Phys.Rev. A **55**, R18 (1996).

[Kapl02] D.B. Kaplan, S. Reddy, *Novel phases and transitions in color flavor locked matter*, Phys.Rev. D, **65**, 054042 (2002).

[Kavo98] G.M. Kavoulakis, C.J. Pethick, H. Smith, *Damping of hydrodynamic modes in a trapped Bose gas above the Bose-Einstein transition temperature*,Phys.Rev. A **57**, 2938 (1998).

[Kemm04] M. Kemmann, I. Mistrik, S. Nussmann, H. Helm, C.J. Williams, P.S. Julienne, *Near-threshold photoassociation of* $^{87}Rb_2$,Phys.Rev. A **69**, 022715 (2004).

[Kemp02] E.G.M. van Kempen, S.J.J.M.F. Kokkelmans, D.J. Heinzen, B.J. Verhaar, *Interisotope determination of ultracold Rubidium interactions from three high-precision experiments*, Phys.Rev.Lett. **88**, 93201 (2002).

[Kett96] W. Ketterle, N.J. van Druten, *Evaporative cooling of trapped atoms*, ed. by B.Bederson and H.Walther, Adv.At.Mol.Opt.Phys. **37**, 181 (1996).

[Kett99] W. Kett99, D.S. Durfee, D.M. Stamper-Kurn, *Making, probing and understanding of Bose-Einstein condensates*, in: *Bose-Einstein condensation in atomic gases*, Proceedings of the International School of Physics "Enrico Fermi", Course CXL, edited by M. Inguscio, S. Stringari and C.E. Wieman (IOS Press, Amsterdam 1999) pp. 67-176; e-print cond-mat/9904034 (1999).

[Knud09] M. Knudsen, *Die Gesetze der Molekularströmung und der inneren Reibungsströmung der Gase durch Röhren*, Annalen der Physik (Leipzig) **28**, 75 (1909).

[Koeh02] M. Köhl, M.J. Davis, C.W. Gardiner, T.W. Hänsch, T. Esslinger, *Growth of Bose-Einstein Condensates from Thermal Vapor*, Phys.Rev.Lett. **88**, 080402 (2002).

[Kolo65] W. Kolos, L. Wolniewicz, *Potential-Energy curves for the* $X^1\Sigma_g^+$, $b^3\Sigma_u^+$, *and* $C^1\Pi_u$ *states of the hydrogen molecule*, J.Chem.Phys. **43**, 2429 (1965).

[Kroo76] M. Krook, T.T. Wu, *Formation of Maxwellian tails*, Phys.Rev.Lett. **36**, 1107 (1976).

[Laha04] T. Lahaye, J.M. Vogels, K.J. Günter, Z. Wang, J. Dalibard, D. Guéry-Odelin, *Realization of a magnetically guided atomic beam in the collisional regime*, Phys.Rev.Lett. **93**, 093003 (2004).

[LandauC] L.D. Landau, E.M. Lifschitz, *Classical field theory*, Butterworth-Heinemann, Oxford (1987).

[LandauF] L.D. Landau, E.M. Lifschitz, *Fluid Mechanics*, Butterworth-Heinemann, Oxford (1987).

[LandauM] L.D. Landau, E.M. Lifschitz, *Mechanics*, Butterworth-Heinemann, Oxford (1987).

[LandauQ] L.D. Landau, E.M. Lifschitz, *Quantum Mechanics*, Butterworth-Heinemann, Oxford (1987).

[LandauS] L.D. Landau, E.M. Lifschitz, *Statistical physics Part 1*, Butterworth-Heinemann, Oxford (1987).

[Lau99] D.C. Lau, R.J. Mclean, A.I. Sidorov, D.S. Gough, J. Koperski, W.J. Rowlands, B.A. Sexton, G.I. Opat, P. Hannaford, *Magnetic mirrors with micron-scale periodicities for slowly moving neutral atoms*, J.Opt.B **1**, 371 (1999).

[Ledu02] M. Leduc, J. Léonard, F. Pereira dos Santos, E. Jahier, S. Schwartz, C. Cohen-Tannoudji, Acta Phys.Pol.B **33**, 2213 (2002).

[Lege98] R. Legere, K. Gibble, *Quantum Scattering in a Juggling Fountain*,Phys.Rev.Lett. **81**, 5780 (1998).

[Legg01] A.J. Leggett, *Bose-Einstein condensation in the alkali gases: Some fundamental concepts*, Rev.Mod.Phys. **73**, 307 (2001).

[Legg04] A.J. Leggett, *Nobel Lecture: Superfluid 3He: the early days as seen by a theorist*, Rev.Mod.Phys. **76**, 999 (2001).

[Legg99] A.J. Leggett, *Superfluidity*, Rev.Mod.Phys. **71**, S318 (1999).

[LeonTh] J. Léonard, *Photoassociation de l'helium metastable*, Ph.D. thesis, ENS-Paris (2003).

[LeRo70] R.J. LeRoy, R.B. Bernstein, *Dissociation energy and long-range potential of diatomic molecules from vibrational spacings of higher levels*, J.Chem.Phys. **52**, 3869 (1970).

[Lett88] P.D. Lett, R.N. Watts, C.I. Westbrook, W.D. Phillips, P.L. Gould, H.J. Metcalf, *Observation of atoms laser cooled below the doppler limit*, Phys.Rev.Lett. **61**, 169 (1988).

[Lett95] P.D. Lett, P.S. Julienne, W.D. Phillips, *Photoassociative spectroscopy of laser-cooled atoms*, Ann.Rev.Phys.Chem. **46**, 423 (1995).

[Lifsch] E.M. Lifschitz, L.P. Pitaevskii, *Physical Kinetics*, Butterworth-Heinemann, Oxford (1981).

[Loudon] R. Loudon, *The quantum theory of light*, Oxford University Press, Oxford, ISBN 0-19-850177-3 (2000).

[Luit96] O.J. Luiten, M.W. Reynolds, J.T.M. Walraven, *Kinetic theory of the evaporative cooling of a trapped gas*, Phys.Rev.A **53**, 381 (1996).

[Magn93] S. Magnier, Ph. Millié, O. Dulieu, F.Masnou-Seeuws, *Potential curves for the ground and excited states of the Na2 molecule up to the (3s+5p) dissociation limit: Results of two different effective potential calculations*, J.Chem.Phys. **98**, 7113 (1993).

[Majo32] E. Majorana, Il Nuovo Cimento **9**, 43 (1932).

[MaKu97] T. Mayer-Kuckuk, *Atomphysik*, Teubner Studienbücher, Stuttgart, ISBN 3-519-43042-8 (1997).

[Mari98] M. Marinescu, L. You, *Controlling Atom-Atom Interaction at Ultralow Temperatures by dc Electric Fields*, Phys.Rev.Lett. **81**, 4596 (1998).

[Mart02] A. Marte, T. Volz, J. Schuster, S. Dürr, G. Rempe, E.G.M. van Kempen, B.J. Verhaar, *Feshbach resonances in rubidium 87: precision measurement and analysis*,Phys.Rev.Lett.**89**, 283202 (2002).

[Masu88] N. Masuhara, J.M. Doyle, J.C. Sandberg, D. Kleppner, T.J. Greytak, *Evaporative cooling of spin-polarized atomic hydrogen*, Phys.Rev.Lett. **61**, 935 (1988).

[McGu02] J.M. McGuirk, G.T. Foster, J.B. Fixler, M.J. Snadden, M.A. Kasevich, *Sensitive absolute-gravity gradiometry using atom interferometry*, Phys.Rev. A, **65**, 033608 (2002).

[Met-Str] H.J. Metcalf, P. van der Straten, *Laser cooling and trapping*, Springer Verlag, Berlin, ISBN 0-387-98728-2, (1999).

[Mies98] H.-J. Miesner, D.M. Stamper-Kurn, M.R. Andrews, D.S. Durfee, S. Inouye, W. Ketterle, *Bosonic Stimulation in the Formation of a Bose-Einstein Condensate*, Science **279**, 1005, (1998).

[Migd85] A.L. Migdall, J.V. Prodan, W.D. Phillips, *First Observation of magnetically trapped neutral atoms*, Phys.Rev.Lett. **54**, 2596 (1985).

[Mill93] J.D. Miller, R.A. Cline, D.J. Heinzen, *Photoassociation spectrum of ultracold Rb atoms*, Phys.Rev.Lett. **71**, 2204 (1993).

[Mish97] A. Mishra, P.K. Panda, S. Schramm, J. Reinhardt, W. Greiner, *Structure of the vacuum in nuclear matter: a nonperturbative approach*,Phys.Rev. C **56**, 1380 (1997).

[Moer96] A.J. Moerdijk, B.J. Verhaar, T.M. Nagtetaal, *Collisions of dressed ground state atoms*, Phys.Rev. A **53**, 4343 (1996).

[Monr93] C.R. Monroe, E.A. Cornell, C.A. Sackett, C.J. Myatt, C.E. Wieman, *Measurement of Cs-Cs elastic scattering at T=30 μK*, Phys.Rev.Lett. **70**, 414 (1993).

[Niku04] T. Nikuni, A. Griffin, *Frequency and damping of hydrodynamic modes in a trapped Bose-condensed gas*, Phys.Rev.A **69**, 23604 (2004).

[Niku98] T. Nikuni, A. Griffin, *Hydrodynamic Damping in trapped Bose Gases*, J.Low Temp.Phys. **111**, 793 (1998).

[OHar02a] K.M. O'Hara, S.L. Hemmer, M.E. Gehm, S.R. Granade, J.E. Thomas, *Observation of a Strongly Interacting Degenerate Fermi Gas*, Science **298,**,2179 (2002).

[Ozer02] R. Ozeri, J. Steinhauer, N. Katz, N. Davidson, *Direct Observation of the Phonon Energy in a Bose-Einstein Condensate by Tomographic Imaging*, Phys.Rev.Lett. **88**, 220401, (2002).

[Pedr03] P. Pedri, D. Guéry-Odelin, S. Stringari, *Dynamics of classical gas including dissipative and mean-field effects*, Phys.Rev. A **68**, 043608 (2003).

[Petr01] D.S. Petrov, G.V. Shlyapnikov, J.T.M. Walraven, *Phase-fluctuating 3D Bose-Einstein condensates in elongated traps*, Phys.Rev.Lett. **87**, 050404 (2001).

[Petr04] D.S. Petrov, C. Salomon, G.V. Shlyapnikov, *Weakly bound dimers of fermionic atoms*,Phys.Rev.Lett. **93**, 090404 (2004).

[Petr95] W. Petrich, M.H. Anderson, J.R. Ensher, E.A. Cornell, *Stable tight confining magnetic trap for evaporative cooling of neutral atoms*, Phys.Rev.Lett. **74**, 3352 (1995).

[Pet-Smi] C.J. Pethick, H. Smith, *Bose-Einstein condensation in dilute gases*, Cambridge University Press, Cambridge (2002).

[Pfau02] T. Pfau, *Continuous progress on atom lasers*, Science **296**, 2155 (2002).

[Phil98] W.D. Phillips, *Laser cooling and trapping of neutral atoms*, Rev.Mod.Phys. **70**, 721 (1998).

[Pink98] P.W.H. Pinkse, A. Mosk, M. Weidemüller, M.W. Reynolds, T.W. Hijmans, J.T.M. Walraven, *One-dimensional evaporative cooling of magnetically trapped atomic hydrogen*, Phys.Rev.A **57**, 4747 (1998).

[Pit-Str] L.P. Pitaevskii, S. Stringari, *Bose-Einstein Condensation*, Clarendon Press, Oxford ISBN 0 19 850719 4 (2003).

[Prit83] D.E. Pritchard, *Cooling neutral atoms in a magnetic trap for precision spectroscopy*, Phys.Rev.Lett. **51**, 1336 (1983).

[Raab87] E.L. Raab, M. Prentiss, A. Cable, S. Chu, D.E. Pritchard, *Trapping of neutral sodium atoms with radiation pressure*, Phys.Rev.Lett. **59**, 2631 (1987).

[Rabi36] I.I. Rabi, *On the process of space quantization*, Phys.Rev. **49**, 324 (1936).

[Rees47] A.L.G. Rees, *Calculation of Potential Energy Curves from Spectroscopic Data*, Proc.Phys.Soc. London **59**, 998 (1947).

[Rega03] C.A. Regal, D.S. Jin, *Measurement of positive and negative scattering lengths in a Fermi gas of atoms*, Phys.Rev.Lett. **90**, 230404 (2003).

[Roac95] T.M. Roach, H. Abele, M.G. Boshier, H.L. Grossman, K.P. Zetie, E.A. Hinds, *Realization of a magnetic mirror for cold atoms*, Phys.Rev.Lett. **75**, 629 (1995).

[Roij88] R. van Roijen, J.J. Berkhout, S. Jaakkola, J.T.M. Walraven, *Experiments with atomic hydrogen in a magnetic trap*, Phys.Rev.Lett. **61**, 931 (1988).

[Rols02] S.L. Rolston, W.D. Phillips, *Nonlinear and quantum atom optics*, Nature **416**, 219 (2002).

[Rubb81] J.R. Rubbenmark, M.M. Kahs, M.G. Littman, D. Kleppner, *Dynamical effects at avoided level crossing: A study of the Landau-Zener effect using Rydberg atoms*, Phys.Rev. A, **23**, 3107 (1981).

[Södi99] J. Söding, D. Guéry-Odelin, P. Desbiolles, F. Chevy, H. Inamori, J. Dalibard, *Three-body decay of a rubidium BoseŰEinstein condensate*,Appl.Phys. B **69**, 257 (1999).

[Samu00] C. Samuelis, E. Tiesinga, T. Laue, M. Elbs, H. Knöckel, E. Tiemann, *Cold atomic collisions studied by molecular spectroscopy*, Phys.Rev. A **63**, 12710 (2000).

[Sant99] G. Santarelli, Ph. Laurent, P. Lemonde, A. Clairon, A.G. Mann, S. Chang, A.N. Luiten, C. Salomon, *Quantum projection noise in an atomic fountain: A high stability cesium frequency standard*, Phys.Rev.Lett. **82**, 4619 (1999).

[Schü99] U. Schünemann, H. Engler, R. Grimm, M. Weidemüller, M. Zielonkowski, *Simple scheme for tunable frequency offset locking of two lasers*, Rev.Sci.Instr. **70**, 242 (1999).

[Seid04] S. Seidelin, J. Viana Gomes, R. Hoppeler, O. Sirjean, D. Boiron, A. Aspect, C.I. Westbrook, *Getting the Elastic Scattering Length by Observing Inelastic Collisions in Ultracold Metastable Helium Atoms*, Phys.Rev.Lett. **93**, 090409 (2004).

[Self83] S.A. Self, *Focusing of shperical Gaussian beams*, App.Opt. **22**, 658 (1983).

[Seti93] I.D. Setija, H.G.C. Werij, O.J. Luiten, M.W. Reynolds, T.W. Hijmans, J.T.M. Walraven, *Optical cooling of atomic hydrogen in a magnetic trap*, Phys.Rev.Lett. **70**, 2257 (1993).

[Shva00] I. Shvarchuck, K. Dieckmann, M. Zielonkowski, J.T.M. Walraven, *Broad-area diode-laser system for a rubidium Bose-Einstein condensation experiment*, Appl.Phys. B **71**, 475Ű480 (2000).

[Shva02] I. Shvarchuck, Ch. Buggle, D.S. Petrov, K. Dieckmann, M. Zielonkowski, M. Kemmann, T.G. Tiecke, W. von Klitzing, G.V. Shlyapnikov, J.T.M. Walraven, *Bose-Einstein condensation into non-equilibrium states studied by condensate focusing*, Phys.Rev.Lett. **89**, 270404 (2002).

[Shva03a] I. Shvarchuck, Ch. Buggle, D.S. Petrov, M. Kemmann, W. von Klitzing, G.V. Shlyapnikov, J.T.M. Walraven, *Hydrodynamic behavior in expanding thermal clouds of $^{8}7Rb$*, Phys.Rev. A **68**, 063603 (2003).

[Shva03b] I. Shvarchuck, Ch. Buggle, D.S. Petrov, M. Kemmann, T.G. Tiecke, W. von Klitzing, *Focusing of Bose-Einstein condensates in free flight*, Interactions in ultracold gases, Wiley-VCH, ISBN 3-527-40389-2 pg. 415 (2003).

[ShvaTh] I. Shvarchuck, *Bose-einstein condensation into non-equllibrium states*, Ph.D. Thesis, University of Amsterdam (2003).

[Silv80] I.F. Silvera, J.T.M. Walraven, *Stabilization of atomic hydrogen at low temperature*,Phys.Rev.Lett. **44**, 164 (1980).

[Silv86] I.F. Silvera, J.T.M. Walraven, *Spin polarized atomic hydrogen*, Progr.Low Temp.Phys. **X**, 139 (1986).

[Simu05] T.P. Simula, P. Engels, I. Coddington, V. Schweikhard, E.A. Cornell, R.J. Ballagh, *Observations on Sound Propagation in Rapidly Rotating Bose-Einstein Condensates*, Phys.Rev.Lett. **66**, 050404 (2005).

[Stam98] D.M. Stamper-Kurn, H.J. Miesner, S. Inouye, M.R. Andrews, W. Ketterle, *Collisionless and Hydrodynamic Excitations in a BEC*, Phys.Rev.Lett. **81**, 500 (1998).

[Stri04] S. Stringari, *Collective Oscillations of Superfluid Fermi gas near Feshbach Resonance*,Europhys.Lett. **65**, 749 (2004).

[Suom95] K.A. Suominen, M.J. Holland, K. Burnett, *Optical shielding of cold collisions*, Phys.Rev. A **51**, 1446 (1995).

[Surk94] E.L. Surkov, J.T.M. Walraven, G.V. Shlyapnikov, *Collisionless motion in magnetostatic traps*, Phys.Rev. A **49**, 4778 (1994).

[Surk96] E.L. Surkov, J.T.M. Walraven, G.V. Shlyapnikov, *Collisionless motion and evaporative cooling in magnetic traps*, Phys.Rev. A **53**, 3403 (1996).

[Thom02] N.R. Thomas, A.C. Wilson, C.J. Foot, *Double well magnetic trap for Bose-Einstein condensates*, Phys.Rev. A **65**, 63406 (2002).

[Thom04] N.R. Thomas, N. Kjäergaard, P.S. Julienne, A.C. Wilson, *Imaging of s and d Partial-Wave Interference in Quantum Scattering of Identical Bosonic Atoms*, Phys.Rev.Lett. **93**, 173201 (2004).

[Tiec03] T.G. Tiecke, M. Kemmann, Ch. Buggle, I. Schvarchuck, W. von Klitzing, J.T.M. Walraven, *Bose-Einstein condensation in a magnetic double-well potential*,J.Opt.B **5**, S119 (2003).

[Ties93] E. Tiesinga, B.J. Verhaar, H.T.C. Stoof, *Threshold and resonance phenomena in ultracold ground-state collisions*, Phys.Rev. A **47**, 4114 (1993).

[Tiem03] E. Tiemann, *Cold Molecules*, in: Interactions in ultracold gases, Wiley-VCH, ISBN 3-527-40389-2 pg. 175 (2003).

[Tosc03] F. Toschi, P. Vignolo, S. Succi, M.P. Tosi, *Dynamics of trapped two-component Fermi gas: Temperature dependence of the transition from collisionless to collisional regime*,Phys.Rev. A **67**, 041605(R) (2003).

[Tosc04] F. Toschi, P. Capuzzi, S. Succi, P. Vignolo, M.P. Tosi, *Transition to hydrodynamics in colliding fermion clouds*,J.Phys.B: At.Mol.Opt.Phys. **37**, S91 (2004).

[Town95] C.G. Townsend, N.H. Edwards, C.J. Cooper, K.P. Zetie, C.J. Foot, A.M. Steane, P. Szriftgiser, H. Perrin, J. Dalibard, *Phase-space density in the magneto-optical trap*, Phys.Rev. A **52**, 1423 (1995).

[ValcMs] P. Valckering, *Optimization of evaporative cooling of rubidium atoms in a magnetic trap*, M.Sc. thesis, University of Utrecht (1999).

[Verh93] B. Verhaar, K. Gibble, S. Chu, *Cold collision properties derived from frequency shifts in a cesium fountain*, Phys.Rev. A **48**, R3429 (1993).

[Vida79] C.A. Vidal, *Determination of vibrational quantum numbers of diatomic molecules using a variational method*, Chem.Phys.Lett. **65**, 81 (1979).

[Walr96] J.T.M. Walraven, *Atomic Hydrogen in magnetostatic traps*, published in:, *Quantum dynamics of simple systems*, IOP: Bristol, (SUSSP Proceedings, Vol. 77) (1996).

[Wein99] J. Weiner, V.S. Bagnato, S. Zilio, P.S. Julienne, *Cold and Ultracold collisions*, Rev.Mod.Phys. **71**, 1 (1999).

[Weit94] M. Weitz, B.C. Young, S. Chu, *Atom manipulation based on delayed laser pulses in three- and four-level systems*, Phys.Rev.A **50**, 2438 (1994).

[Wiem91] C.E. Wieman, L. Hollberg, *Using diode lasers for atomic physics*, Rev.Sci.Instr. **62**, 1 (1991).

[Wing84] W.H. Wing, *On neutral particle trapping in quasistatic electromagnetic fields*, Prog.Quant.Electr. **8**, 181 (1984).

[Wu96] H. Wu, C.J. Foot, *Direct Simulation of evaporative Cooling*, J.Phys. B: At.Mol.Opt.Phys. **29**, L321 (1996).

[Wu97] H. Wu, E. Arimondo, C.J. Foot, *Dynamics of evaporative cooling for Bose-Einstein condensation*, Phys.Rev. A **56**, 560 (1997).

[Wu98] H. Wu, E. Arimondo, *Expansion of the non-condensed trapped Bose gas in Bose-Einstein condensation*, Europhys.Lett. **43**, 141 (1998).

[You96] L. You, M. Holland, *Ballistic expansion of trapped thermal atoms*, Phys.Rev. A **53**, R1 (1996).

[Zene32] C. Zener, *Non-adiabatic crossing of energy levels*, Proceedings of the Royal Society of London Series A, **137**, 696 (1932).

[Zwie03] M.W. Zwierlein, C.A. Stan, C.H. Schunck, S.M.F. Raupach, S. Gupta, Z. Hadzibabic, W. Ketterle, *Observation of BEC of Molecules*,Phys.Rev.Lett. **91**, 250401 (2003).

Appendix A
Summaries

A.1 Summary

This thesis describes the scientific work, conducted by the author, Christian Buggle, and co-workers in the years 2003 till 2005, in order to achieve the title: Doctor of physics of the University of Amsterdam. The field of research, addressed by the experimental work herein is generally referred to as 'ultracold quantum gases'. From a theoretical point of view, this research addresses questions in the framework of quantum mechanics and many-body theory; from the experimental point of view, the investigated object, a cloud of ultracold (i.e. below 1 μK cold) Rubidium 87 atoms, links techniques of atomic physics, laser cooling and di-atomic collisional interactions, i.e. molecular physics with each other. The experiments herein are also situated in the context of Bose-Einstein condensation.

Introduction (Chapter 1) In the first chapter of this thesis, we outline the importance of the research on ultra-cold quantum gases. Bose-Einstein condensation as a theoretical concept dates back as early as 1924 and has been successfully applied to many physical problems in the course of the 20th century. It can be understood as a direct consequence of quantum-statistics. Therefore, direct experimental evidence is of vital importance for testing the validity of quantum-statistics as a correct description of nature. Due to this importance, the first successful direct experimental observations of Bose-Einstein condensation in magnetically trapped alkali gases in 1995 have been awarded the Nobel prize in 2001.

Background (Chapter 2) In chapter 2 we offer a short introduction to theoretical concepts, as far as they are involved in the experiments of this thesis. A thermal gas can be well understood by a statistical entity of point-like particles interacting with each other via collisions. Einstein noted that Boses quantumstatistics implies that in the limit of low temperature and high density, the statistical distribution of particle energies cannot contain all particles. The abundant particles fall into the lowest possible quantum state, figurately condensing into the bottom of the trap. This effect sets in as a sharp phase transition when crossing beyond a critical phase-space density, i.e. the product of real-space density and and momentum-space density. In a gas cloud of Rubidium 87 atoms, that is trapped in a magnetic field with parabolic potential shape, this implies particle densities of $\approx 10^{14}$ atoms per cm^3 at temperatures of $\approx 1\mu$K. The Bose-Einstein condensate (BEC) appears as a small, very dense part of the gas cloud inside the more dilute uncondensed part. The key feature of interest in a BEC is phase coherence: it results from the fact, that all atoms are described by the common ground state wave function. Also collisions at such low temperatures have to be described as potential scattering of quantummechanical waves.

Apparatus (Chapter 3) In the third chapter we describe the methods and devices, required to conduct the experiments. A BEC is created in the following steps: in a magneto-optical trap (MOT) appox. 10^{10} atoms are collected from a source stream of

Rubidium 87 atoms and laser-cooled to $\approx 40\,\mu$K. The cloud is then transferred into a magnetic Ioffe-Pritchard trap in the (F=2, m_F=2) polarization state and compressed, which raises the temperature to $750\,\mu$K. The phase-space density is then increased by forced radio-frequency induced evaporative cooling until the desired density and temperature is reached. Typically, the cloud then still contains $\approx 10^6$ atoms and has a real-space size of $\approx 100\,\mu$m, which makes it accessible to direct observation by an optical imaging system and a CCD-camera. In the experiments of this thesis various collective excitations are triggered by modifying the magnetic potential. The response of the cloud is observed by either absorption or phase contrast imaging.

Hydrodynamic shape oscillations (Chapter 4) As Boltzmann and Knudsen pointed out around the end of the 19th century, at high collisional densities hydrodynamic effects alter the collective behavior of classical trapped gases. These effects mimic the superfluid hydrodynamics of a BEC. As collisional hydrodynamics is of great importance in modern BEC-experiments, this classical effect deserves renewed attention. To yield a description of the gas behavior in the regime between the collisionless and hydrodynamic limit, theoretical work has focused on the frequency of the low-lying m=0 quadrupole mode shape oscillation in cigar-shaped clouds. We trigger this oscillation by a new modulation technique, which is based on time-averaged potentials and allows fast modifications of the trapping frequencies by as much as 20% for our technical installations. Within the theoretical framework we also point out that this technique has a certain critical limitation: as the harmonic range of the modulated potential is proportional to the modulation amplitude, we find a link between a *minimum* amplitude and a *maximum* cloud temperature to remain in harmonic conditions. By loading the gas cloud in an axially elongated trap and then instantly tightening it, we trigger the oscillation in the experiment. We cover the major part of the cross-over regime by controlling the atom density, taking special care for stable conditions within each trace. In agreement with theory we find, that the frequency of the oscillation shifts down from $2\,\omega_z$ to $1.55\,\omega_z$ with rising collisional density, where $\omega_z/2\pi$ is the trap frequency of the long cloud axis. In both limiting cases no damping of the oscillation is expected: in the hydrodynamic limit due to the conservation of entropy; in the collisionless limit due to energy conservation of the particle trajectories in an ideal harmonic trap, which we confirm for the collisionless limit. In the cross-over regime theories indicate strong damping, which peaks around the cross-over point at $2\,\omega_z\tilde{\tau} = 1$ (where $\tilde{\tau}$ is the relaxation time towards thermal equilibrium), which we confirm from the experiment. We further show that anharmonicities in the trapping field add a cloud size dependant frequency down-shift, which reduces the observed frequencies by up to 5%. We present, how this results from the reduction of the restoring force in the off-center regions of the potential.

S-D-wave interference in collisions (Chapter 5) At temperatures below 1 mK collisions between atoms must be described by quantummechanical wave scattering, where the interaction potential scatters the incoming wave into an outgoing one. These can be decomposed into a set of spherical harmonics, labelled with rising complexity and energy *s*-, *p*-, *d*-wave etc. The intensity of the collisional interactions, which is characteristic for the collision partners, is expressed in terms of the scattering length a, the real-space displacement, which corresponds to the phase shift between incoming and outgoing wave in an *s*-wave collision. At typical BEC temperatures collisions occur as *s*-wave collisions for bosonic alkali atoms, which makes a a central parameter. To trigger a collision of 2 BECs

we prepare a single, thermal cloud and then slowly ramp the axial magnetic field from a positive offset to a negative one; simultaneously we apply a fast rotating homogeneous field in the radial plane. As the Zeeman effect and thus the trapping potential is not dependant on the sign of the magnetic field, the negative offset transforms the potential from a parabolic well into a double minimum potential, and we thus split the thermal cloud in two. The rotating radial field lifts in the time-average the field minimum of each well to a non-zero value, thus avoiding Majorana depolarization losses. We continue evaporative cooling and reach BEC in both clouds. Then we return the magnetic field configuration to the harmonic potential in a rapid sweep. In this sweep the 2 BECs are accelerated by the potential gradient towards the field minimum and collide in the center. We observe the halo of scattered particles by absorption imaging for collision energies up to 1.3 mK and find, that in energy regimes of $\approx 1\,\mathrm{mK}$ the scattering pattern is given by the interference of s- and $d-$wave contributions (the p-wave is not present due to the identical polarization of the collision partners). As the atom distribution in the scattered halo is dependant on the relative amplitudes of the interfering s- and d-waves, we extract the collision phase-shifts for various energies. This analysis is based on a numerical evaluation of the Schrödinger equation with relatively limited theoretical and numerical effort. We use the "accumulated phase" method to extract the scattering length a and calculate a value of $+102(6)\,a_0$, which in view of the significantly smaller experimental and theoretical effort than in state-of-the-art methods (resulting in $+98.99(2)\,a_0$) is fairly accurate.

BEC-focusing (Chapter 6) As a third experiment we demonstrate a method to actively compress one axis of a BEC in expansion after switch-off of the trap. The quantum degenerate gas can also be used as a tool for applications or other fundamental research by making use of the quantum matter wave. This raises direct analogies to applications that are well known for laser-light sources. Great experimental effort is undertaken (but at the moment of publication of this thesis still underway) to produce a continuous coherent stream of matter waves, the 'atom-laser'. In parallel, also coherent atom optical elements are in development. In both theory and experiment we address the question, how a BEC can be focused and how a thermal cloud responds under the same conditions. A contraction motion of one axis is induced by an asynchronous release of the cloud from the trapping potential: we first release the radial dimensions of a cigar-shaped trap and after some delay the long, axial one. The axial dimension is pushed to contract by a small change in the axial magnetic field. We control the contraction motion by timing of this release sequence. By calculating the phase-space development we find that for thermal clouds the expansion motion dominates over the induced contraction motion as soon as the force is removed for essentially all accessible experimental conditions. In the experiment we find this very behavior and we cannot achieve a contraction to less than 0.9 times the thermal in-trap size. For BECs we calculate, that the absolute observed focal size should be limited by the optical resolution limit (3μm), as the compression should be much tighter ($\approx 1/100$), also for very weak contraction motions. Experimentally we observe a significantly larger size of $\approx 5\,\mu$m, i.e. ≈ 0.1 times the in-trap size. Nevertheless, we do find qualitative agreement with our theoretical model, and thus demonstrate the devised technique as a new atom-optical element.

A.2 Zusammenfassung

Dieses Buch beschreibt die wissenschaftliche Arbeit, die vom Autor, Christian Buggle, durchgeführt wurde in den Jahren 2003 bis 2005 zur Erlangung des Titels: Doktor der Universität von Amsterdam. Das Arbeitsfeld, auf das sich die experimentellen Arbeiten beziehen, wird als 'ultrakalte Quantengase' bezeichnet. Theoretisch nimmt dieses wissenschaftliche Gebiet Bezug auf Fragen der Quantenmechanik und der Vielteilchensysteme; von der experimentellen Seite her kombiniert das untersuchte System, eine Wolke aus ultrakalten (d.h. weniger als 10μk kalten) Rubidium 87 Atomen, Techniken aus der Atomphysik, der Laserkühlung und der zwei-Teilchenstöße d.h. Molekularphysik mit einander. Die Experimente stehen auch im Kontext der Bose-Einstein Kondensation.

Einleitung (Kapitel 1) Im ersten Kapitel dieser Arbeit umreißen wir den Stellenwert der Forschung an ultra-kalten Quantengasen. Bose-Einstein Kondensation as theoretisches Konzept datiert zurück auf 1924, und wurde im Verlauf des 20sten Jahrhunderts erfolgreich auf verschiedene physikalische Probleme angewandt. Es folgt direkt als Konsequenz der Quantenstatistik. Daher sind direkte experimentelle Nachweise von hohem Wert als Test der Verlässlichkeit der Quantenstatistik als korrekte Beschreibung der Natur. Dieses Umstandes wegen wurde die erfolgreiche, direkte Beobachtung von Bose-Einstein Kondensation in magnetisch eingeschlossenen Alkali-Gasen in 1995 mit dem Nobelpreis 2001 gewürdigt.

Grundlagen (Kapitel 2) In Kapitel 2 geben wir eine kurze Einleitung in die theoretischen Grundlagen, soweit sie für die Experimente in dieser Arbeit von Belang sind. Ein thermisches Gas läßt sich sehr gut beschrieben als Boltzmann-statistisches Ensemble von punkt-artigen Teilchen, die miteinander über Kollisionen wechselwirken. Einstein merkten an, dass Boses Quantenstatistik impliziert, dass bei ausreichend niedrigen Temperaturen und ausreichend hohen Dichten die statistische Energieverteilung nicht mehr alle Teilchen enthalten kann. Die verbliebenen Teilchen fallen in den niedrigstmöglichen Quantenzustand, und kondensieren bildlich in den Boden der Falle. Dieser Effekt setzt mit einem Phasenübergang ein, sobald eine gewisse Phasenraumdichte, das Produkt aus der Dichte im realen Raum und im Impulsraum, überschritten wird. Für ein Gas aus Rubidium 87 Atomen bedeutet dies Dichten von ca. 10^{14} Atomen per cm^3 bei Temperaturen van ca. 1μK. Das Bose-Einstein Kondensat (BEC) erscheint als kleiner, sehr dichter Bestandteil der Gaswolke innerhalb der umgebenden weniger dichten thermischen Wolke. Von besonderem Interesse ist die Kohärenz eines solchen BEC's: diese rührt daher, dass alle Atome durch dieselbe Grundzustandswellenfunktion beschrieben werden. Auch Kollisionen bei solch niedrigen Temperaturen müssen im Rahmen der Wellenmechanik beschrieben werden.

Experimentelle Techniken (Kapitel 3) Im dritten Kapitel beschreiben wir die Methoden und Instrumente, die für die Experimente benötigt werden. Ein BEC wird in den folgenden Schritten erzeugt: In einer magneto-optischen Falle (MOT) werden ca. 10^{10} Atome aus dem Strom einer Rubidium 87 Quelle gesammelt und laser-gekühlt auf ca. 40μK. Die Wolke wird dann in eine magnetische Falle vom Ioffe-Pritchard Typ im (F=2, m_F=2) Polarisationszustand umgeladen und komprimiert, wodurch die Temperatur auf 750μK ansteigt. Die Phasenraumdichte wird dann durch Radiofrequenz-induziertes evaporatives Kühlen erhöht bis die gewünschte Dichte und Temperatur erreicht ist. Typischerweise

enthält die Wolke dann noch 10^6 Atome und hat eine tatsächliche Größe von ca. 100μm, was ausreicht, um sie mit Hilfe eines optischen Systems und einer CCD-Kamera abzubilden. In den Experimenten in dieser Arbeit werden verschiedene kollektive Anregungen durch Veränderungen des magnetischen Potentials ausgelöst. Die Reaktion der Wolke wird dann entweder durch Absorptions- oder Phasenkontrastbildgebung beobachtet.

Hydrodynamische kollektive Oszillationen (Kapitel 4) Wie Boltzmann und Knudsen bereits gegen Endes des 19ten Jahrhunderts anmerkten, beeinflussen hydrodynamische Effekte das kollektive Verhalten klassischer, eingeschlossener Gase. Diese Effekte imitieren die Superfluid-Hydrodynamik von BEC's. Da kollisionsinduzierte Hydrodynamik in modernen BEC-Experimenten eine wichtige Rolle spielt, verdient diese Phänomen der klassischen Physik erneute Aufmerksamkeit. Um eine Beschreibung des Gasverhaltens in dem Regime zwischen dem kollisionsfreien und hydrodynamischen Grenzfall zu erhalten, haben sich theoretische Arbeiten mit der niederfrequenten m=0 Quadrupole Oszillation in Zigarrenförmigen Wolken beschäftigt. Wir lösen diese Oszillation im Experiment aus mit Hilfe einer neuartigen Modulationstechnik, die auf Zeit-gemittelten Potentialen basiert und schnelle Veränderungen der Fallenfrequenzen um bis zu 20% mit unserer Ausrüstung erlaubt. Innerhalb der theoretischen Beschreibung weisen wir auch auf eine kritische Beschränkung dieser Technik hin: Da die harmonische Reichweite des Potentials der Modulationsamplitude proportional ist, finden wir einen Zusammenhang von minimaler Amplitude zu maximaler Temperatur der Wolke, um mit dem Ausmaß der Wolke innerhalb der harmonischen Bereiches zu bleiben. Wir starten die Oszillation, indem wir die Wolke in eine axial ausgedehnte Falle laden und diese plötzlich wieder verkürzen. Indem wir die Atomdichte modifizieren erfassen wir den größten Teil des Übergangsgebietes, wobei wir besondere Sorgfalt stabilen Atomdichten innerhalb eines Oszillationszuges widmen. In Übereinstimmung mit der Theorie beobachten wir, daß die Oszillationsfrequenz mit wachsender Kollisionsdichte von $2\omega_z$ auf $1.55\omega_z$ absinkt, wobei $\omega_z/2\pi$ die axiale Fallenfrequenz ist. In den beiden Grenzfällen wird keine Dämpfung erwartet: im hydrodynamischen Grenzfall wegen der Erhaltung der Entropie, im kollisionsfreien Grenzfall wegen der Energieerhaltung der Partikeltrajektorien in einer idealen harmonischen Falle, was wir für den kollisionlosen Grenzfall bestätigen können. Im Übergangsgebiet weisen die Theorien eine starke Dämpfung auf, die um den Übergangspunkt bei $2\omega_z\tilde{\tau} = 1$ (wobei $\tilde{\tau}$ die Zeit ist, die das Gas zur Relaxation ins thermische Gleichgewicht benötigt) ein Maximum erreicht, was wir experimentell vollständig bestätigen können. Weiterhin zeigen wir, daß Anharmonizitäten im Fallenpotential eine Frequenzverringerung verursachen, die von der Wolkengröße abhängt und die beobachtete Frequenz um bis zu 5% reduziert. Wir zeigen, wie dies aus einer Verringerung der Rückstellkraft in den Regionen abseits des Zentrums folgt.

S-D-Wellen Interferenz in Kollisionen (Kapitel 5) Bei Temperaturen unter 1mK müssen Kollisionen zwischen Atomen durch quantenmechanische Potentialstreuung beschrieben werden, wobei das Interaktionspotential eine eingehende de Broglie-Welle in eine ausgehende streut. Diese können durch eine Partialwellenzerlegung umgeschrieben werden in eine Serie aus Kugelflächenfunktionen, die mit steigender Komplexität und Energie s-, p-, d-Welle usw. benannt sind. Die Streustärke, die charakteristisch für die Streupartner ist, wird in der Streulänge a ausgedrückt, der räumlichen Verschiebung, die mit der Phasenverschiebung zwischen der eingehenden und gestreuten Welle in einer s-Wellenkollision einher geht. Bei den für BEC's typischen Temperaturen erfolgen alle Kol-

lisionen für Alkali-Atome als s-Wellenkollisionen, wodurch a zu einem zentralen Parameter wird. Um eine Kollision zwischen zwei BEC's auszulösen, bereiten wir eine einzelne thermische Wolke vor und rampen den Wert der axialen magnetischen Feldstärke im minimum des harmonischen Potentials langsam von einem posivitiven zu einem negativen; gleichzeitig legen wir in der radialen Ebene ein schnell rotierendes, homogenes Feld an. Da der Zeeman Effekt und somit das Fallenpotential nicht vom Vorzeichen des magnetischen Feldes abhängen, wird durch den negativen zentralen Wert der Charakter des Potentials von einem einzelnem parabolischem Topf zu einer Doppel-Minimum Struktur verändert, und wir spalten die thermische Wolke dadurch in zwei. Das rotierende radiale Feld hebt im Zeitmittel den minimalen Wert in jedem der beiden Minima auf einen von Null verschiedenen Wert und vermeidet so Verluste durch Majorana Depolarisierung. Wir setzen das evaporative Kühlen fort und erreichen BEC in beiden Wolken. Dann kehren wir in einer schnellen Rampe zu dem ursprünglichen harmonischen Potential zurück. In diesem Zug werden die beiden BEC's durch die Gradienten des Potentials zum Potentialminimum hin beschleunigt und kollidieren im Zentrum. Wir beobachten die Winkelverteilung der gestreuten Atome in Absorptionsbildern für Kollisionsenergien bis zu 1.3 mK und finden, daß für Energien im Bereich von ca. 1 mK das Streumuster durch die Interferenz der Beiträge aus s- und d-Wellen gebildet wird (die p-Welle kommt nicht vor wegen der identischen Polarisation der Kollisionspartner). Da die Verteilung der Atome im Streumuster vom anteiligen Verhältnis der interferierenden s- und d-Wellen abhängt, können wir auf die Phasenverschiebung der Kollision für verschiedene Energien schliessen. Diese Analyse basiert auf einer numerischen Auswertung der Schrödinger Gleichung mit relativ begrenztem theoretischem und numerischen Aufwand, für die wir nur den Van der Waals C_6-Koeffizienten des Interaktionspotentials benötigen. Insbesondere verwenden wir keine Information aus der Atomdichte, die schwierig mit genügender Genauigkeit zu messen ist. Wir wenden die Methode der 'akkumulierten Phase' an, um den Wert der Streulänge a zu finden, und berechnen einen Zahlenwert von $+102(6)a_0$, was in Anbetracht des beträchtlich geringeren experimentellen und theoretischem Aufwandes im Vergleich mit aktuellen Präzisionsmethoden zur Bestimmung (die $+98.99(2)a_0$ ergeben) recht präzise ist.

BEC-Fokussierung (Kapitel 6) As drtittes Experiment demonstrieren wir eine Methode, um aktiv ein BEC bei der Expansion nach dem Abschalten der Falle in einer Dimension zu komprimieren. Das quantendegenerierte Gas kann auch als Hilfsmittel bei Anwendungen oder anderer Grundlagenforschung dienen, wo von der Quantenmechanischen Materiewelle Gebrauch gemacht wird. Solche stehen in direkter Analogie zu bekannten Anwendungen für Laserlicht. Großer experimenteller Aufwand wird getrieben (der zum Zeitpunkt der Publikation dieser Arbeit noch nicht abgeschlossen ist), um eine kontinuierliche Quelle eines kohärenten Materiewellenstroms zu verwirklichen, den 'Atomlaser'. Gleichzeitig werden auch optische Elemente für kohärente Materiewellen entwickelt. Sowohl in Theory als auch im Experiment gehen wir auf die Frage ein, inwieweit ein BEC fokussiert werden kann und wie eine thermische Wolke unter diesen Bedingungen reagiert. Die Kontraktionsbewegung von einer Achse wird erreicht durch ein nicht gleichzeitiges Abschalten des Fallenpotentials: wir entlassen zunächst die beiden radialen Achsen der Zigarrenförmigen Wolke aus dem Potential, und erst mit einiger Verzögerung die lange, axiale Achse. Diese wird durch eine kleine Veränderung im axialen Magnetfeldprofil in eine Kontraktionsbewegung getrieben. Dieser letzte Schritt

ist prinzipiell nur für thermische Wolken notwendig, da deren Geschwindigkeitsverteilungen in verschiedenen Dimensionen unabhängig voneinander sind; BEC's kollabieren axial bereits durch die Entladung des chemischen Potentials in die radiale Richtung. Wir kontrollieren die Stärke der Kontraktionsbewegung über die Zeitabfolge in dieser Sequenz. Aus einer Berechnung der Entwicklung der Phasenraumdichte schließen wir, daß für thermische Wolken die Expansionsbewegung über die induzierte Kontraktion für praktisch alle zugänglichen experimentellen Parameter dominiert, sobald das Magnetfeld abgeschaltet wird. Im Experiment finden wir eben dieses Verhalten, und auch daß wir keine Kontraktion auf einen Wert von weniger als das 0.9-fache der thermischen Größe im Fallenpotential erzielen können. Für BEC's berechnen wir, daß unsere beobachtete Größe im Fokus durch das optische Auflösungsvermögen von 3.3μm limitiert sein sollte, da die skalierte Kontraktion (mit ca. 1/100) deutlich stärker ausfallen sollte. Im Experiment beobachten wir jedoch einen größeren Wert von ca. 5μm, d.h. das 0.1-fache der Größe im Fallenpotential. Davon abgesehen finden wir dennoch eine qualitative Übereinstimmung mit unserem theoretischen Modell, und demonstrieren die vorgestellte Technik als neues atom-optisches Element.

A.3 Samenvatting

Dit proefschrift beschrijft het wetenschappelijke werk, dat de auteur, Christian Buggle, en medewerkers tijdens de jaren 2003 tot 2005 hebben gedaan, ter verkrijging van de graad van doctor van de Universiteit van Amsterdam. Het onderzoeksgebied, waarbinnen de experimenten zijn uitgevoerd staat bekend als 'kwantumgassen'. Het onderzoek betreft vragen op het gebied van kwantummechanisch gedrag, botsingsgedrag en hydrodynamisch gedrag van kwantumgassen. De experimenten zijn gedaan met wolkjes van ultrakoude (temperaturen $< 10\mu$K) Rubidium 87 atomen, en maken gebruik van methoden uit de atoomfysica, atomaire botsingfysica en statistieke fysika. Het onderzoek maakt deel uit van het vakgebied Bose-Einstein condensatie.

Introductie (Hoofdstuk 1) In het eerste hoofdstuk bespreken we het belang van onderzoek met ultrakoude kwantumgassen. Het begrip Bose-Einstein condensatie gaat terug tot 1924 en heeft een belangrijke rol gespeeld binnen de fysica van de 20ste eeuw. Het kan begrepen worden als het directe gevolg van kwantumstatistiek. Daarom is de experimentele studie van dit verschijnsel van vitaal belang voor het testen van de kwantumstatistiek als een correcte beschrijving van de natuur. Gezien dit belang zijn de eerste experimentele studies van de eigenschappen van Bose-Einstein condensaten (1995) bekroond met de Nobelprijs.

Achtergrond (Hoofdstuk 2) In hoofdstuk 2 geven we een korte inleiding in de theoretische concepten voor zover die van belang zijn voor de experimenten beschreven in dit proefschrift. Een thermisch gas kan goed beschreven worden als een Boltzmann-statistisch ensemble van atomen, die met elkaar botsen als gevolg van interacties. Einstein liet zien dat de quantumstatistiek van Bose impliceerd, dat in de limiet van voldoende lage temperaturen en voldoende hoge dichtheid niet alle deeltjes binnen de Bose-distributie ondergebracht kunnen worden. De resterende deeltjes bezetten de laagst mogelijke translatietoestand. Bij wijze van spreken condenseren op de bodem van de val waarin het gas is opgesloten. Dit verschijnsel toont zich als een faseovergang zodra een kritische faseruimtedichtheid wordt overschreden. In een gas van Rubidium atomen opgeslagen in een parabolisch magnetisch potentiaalveld impliceert dit temperaturen van rond de 1μK en dichtheiden rond de 10^{14} atomen per cm^3. Het Bose-Einstien condensaat (BEC) is herkenbaar als een zeer dichte kern in het centrum van een ijle, niet gecondenseerde wolk. Een sleutelbegrip is fasecoherentie als gevolg van eén gemeenschappelijke golffunctie (grondtoestand). Ook botsingen moeten bij deze lage temperaturen kwantummechanisch beschreven worden.

Instrumentatie (Hoofdstuk 3) In het derde hoofdstuk beschrijven we de methoden en apparaten die nodig waren om de experimenten uit te voeren. Een BEC wordt gemaakt in een aantal stappen: eerst worden ongeveer 10^{10} atomen uit een koude bundel van Rubidium atomen verzameld in een magneto-optische val (MOT) en optisch gekoeld tot ongeveer 40μK. De wolk wordt overgeladen in een magnetostatische Ioffe-Pritchard val en vervolgens gecomprimeerd. De temperatuur neemt hierbij toe tot 750μK. Daarna wordt de faseruimtedichtheid vergroot met gedwongen afdampkoeling totdat de gewenste dichtheid en temperatuur is bereikt. De wolk bevat dan nog steeds ongeveer 10^6 atomen en heeft een afmeting van ongeveer 100μm. Dit maakt BEC's direct toegankelijk voor optische microscopie vastgelegd met een CCD camera. In de experimenten beschreven in dit proefschrift

wordt de vorm van de gaswolk beinvloed door variatie van het magnetisch potentiaalveld. De reactie van de wolk kan dan worden vastgelegd met lichtabsorptiemicroscopie of fasecontrastmicroscopie.

Hydodynamische vormoscillaties (Hoofdstuk 4) Zoals reeds naar voren gebrachd door Boltzmann en Knudsen rond de vorige eeuwwisseling vertonen klassieke gassen hydrodynamisch gedrag mits de dichtheid voldoende hoog is. Deze effecten lijken in bepaalde opzichten veel op de superfluide hydrodynamica van een BEC. Omdat botsinghydrodynamica een belangrijke rol speelt in modern onderzoek met kwantumgassen trekt dit klassieke gedrag hernieuwde aandacht. Om het gedrag in de overgang van de botsingsvrije limiet naar de hydrodynamische limiet te beschrijven is in theoretisch onderzoek bijzondere aandacht besteed aan frequentieverschuivingen en demping van de laagste m=0 quadrupole vormoscillatie in sigaarvormige wolken. Experimenteel brengen wij de oscillatie op gang met een nieuwe modulatiemethode, die resulteert in tijdgemiddelde potentialen in de Ioffe-Pritchard val. Met deze methode wordt bij onze experimenten de valfrequentie met zo'n 20% veranderd in 100 μs. Ook de beperkingen van deze methode worden besproken: zo blijkt het, dat de harmonische dracht van de gemoduleerde potentiaal evenredig is met de modulatieamplitude. Dit leidt tot een verband tussen een minimale amplitude en maximale temperatuur, om ervoor te zorgen dat de gehele wolk zich in het harmonische gebied bevindt. De oscillatie wordt experimenteel gestart, door eerst het gas te laden in een in de lengterichting uitgerekte val en dan plotseling de uitrekking te verminderen. Onze experimenten bestrijken het grootste deel van het overgangsgebied. Het bleek van groot belang om bijzondere aandacht te besteden aan de reproduceerbaarheid van de atomaire dichtheid. In goede overeenstemming met de theorie hebben wij aangetoond dat de frequentie van de oscillatie omlaag schuift van $2\,\omega_z$ naar $1.55\,\omega_z$ met toenemende dichtheid. Hierbij is $\omega_z/2\pi$ de valfrequentie in de lengterichting. Opmerkelijk genoeg treedt zowel in het botsingsvrije als in de hydrodynamische limiet geen demping op. De demping blijkt zich te beperken tot het overgangsgebied en bereikt een maximum rond het kantelpunt bij $2\omega_z\tilde{\tau} = 1$, waarbij $\tilde{\tau}$ de relaxatietijd is waarop lokaal het thermische evenwicht wordt bereikt. Verder laten we zien dat valanharmoniciteiten eveneens aanleiding geven tot een frequentieverlaging. Bij onze metingen gaf dit aanleiding tot frequentieverschuivingen van maximaal 5%. De oorsprong van dit effect wordt besproken en beschreven in de vorm van een aantal compacte uitdrukkingen.

S-D-golf interferentie in botsingen (Hoofdstuk 5) In dit hoofdstuk bespreken we een nieuwe methode om een centrale parameter uit de theorie van de kwantumgassen, de strooilengte a, te bepalen. Deze strooilengte is een maat voor de sterkte van de wisselwerking in het gas. Bij lage temperaturen moeten de botsingen tussen atomen kwantummechanisch beschreven worden. Hierbij worden de botsenden atomen beschreven met de de Broglie-golven. Bij een ontwikkeling in zogenaamde deelgolven blijken alleen de laagste deelgolven (s-, p-, d-golven etc.) een rol te spelen. De verstrooide golven worden wiskundig beschreven als harmonische bolfuncties. Omdat de botsingen elastisch zijn ligt alle botsingsinformatie opgesloten in de faseverschuiving van de deelgolven. Deze faseverschuiving kan bepaald worden door de interferentie tussen de laagste voorkomende deelgolven (s en d bij verstrooiing van identieke bosonen) te meten. Bij typische BEC-temperaturen (1μK) is alleen s-golf verstrooiing van belang. Om de d-golf te kunnen exciteren en daarmee de s-d-interferentie mogelijk te maken, zijn botsingsenergien van minimal enkele honderden μK nodig. Dit wordt gedaan door 2 BEC's ten opzichte van elkaar te versnellen en tot bots-

ing te brengen. Hiertoe prepareren we eerst een thermische wolk, die in twee delen wordt gesplitst door het axiale magneetveld in het centrum van het val langzaam te reduceren tot nul en vervolgens te laten groeien in negatieve richting. Om te voorkomen dat het gas depolariseert, wordt loodrecht op de lengterichting een draaiend magnetveld aangelegd, zodat ter plaatse van de atomen het tijdgemiddelde magneetveld nooit nul wordt. Het gas wordt door afdampen gekoeld totdat BEC optreedt in beide wolken. Daarna keren we terug naar de oorspronkelijke val. Hiermee worden de twee BEC's versneld. Vlak voordat de BEC's botsen wordt de val uitgezet zodat de botsing kan plaatsvinden onder veldvrije condities en de halo niet vervormd wordt door de valpotentiaal. De interferentie tussen de deelgolven is zichtbaar in de halo van verstrooide atomen. De botsingsenergie kan gevarieerd worden door de BEC's voór het versnellen meer of minder uiteen te trekken. Zo kan de faseverschuiving van de de Broglie-golven als functie van de energie bepaald worden. We laten zien dat kennis van de Van der Waals C_6 parameter voldoende is, om met numerieke integratie van de Schrödinger vergelijking de energieafhankelijkheid van de verstrooiing vast te leggen. Hiertoe maken we gebruik van de zogenaamde 'geaccumuleerde fase'. De kennis van de geakkumuleerde fase stelt ons in staat om de strooilengte a voor Rubidium te bepalen tot een nauwkeurigheid van 6% met de waarde van $a = +102(6)a_0$. Omdat de methode is gebaseerd op een interferentieverschijnsel, is kennis van de dichtheid niet nodig om het botsingsgedrag vast te leggen.

BEC-focussering (Hoofdstuk 6) Als derde experiment demonstreren we een methode om de BEC-golffunctie te manipuleren na het uitzetten van de val. Dit is van belang voor toepassingen waarbij men gebruik wil maken van de eigenschappen van coherente materiegolven. Hierbij kan men bijvoorbeeld denken aan toepassingen analoog aan die van laserlicht. Er bestaat momenteel grote belangstelling voor het produceren van een coherente bron van materiegolven, de atoom-laser. Evenzeer is er belangstelling voor atoomoptische componenten, waarmee materiegolven gemanipuleerd kunnen worden. Zowel theoretisch als experimenteel gaan we in op de vraag, hoe een BEC gefocusseerd kan worden en hoe een thermische wolk zich gedraagt onder dezelfde condities. Wij hebben ons beperkt tot het focusseren van sigaarvormige wolken in axiale richting onder botsingvrije condities na het uitzetten van de val. Met BEC's kan dit worden bereikt door de val in twee stappen uit te zetten: eerst de radiale opsluiting, en daarna de axiale opsluiting. Zodra de radiale opsluiting wordt beeindigd zal het gas in radiale richting expanderen zodat de interacties (chemische potentiaal) al snel verwaarloosbaar zijn. Omdat de chemische potentiaal is weggevallen zal het condensaat in axiale richting samentrekken. Deze contractie zet zich voort, ook nadat het axiale veld is uitgezet. De minimale lengte is experimenteel bepaald en kan gezien worden als een 1-dimensional focus van de BEC-golffunctie. Thermische wolken tonen dit gedrag niet, omdat na het uitzetten van de val in radiale richting de thermische snelheid behouden blijft. We vergelijken onze resultaten met een eenvoudig model. Voor BEC's berekenen we dat de waarneembare focale afmeting beperkt moet worden door de optische resolutie limiet (3μm) van onze microscoop. Experimenteel vinden we de iets grotere waarde van ongeveer 5μm. Dit correspondeert met 10% van de axiale lengte bij de start van het experiment. Voor thermische wolken meten we een contractie tot 90% van de oorspronkelijke afmeting. Dit kan worden verklaard door een versterking van de axiale opsluiting bij het uitschakelen van de radiale veld in rekening te brengen.

Appendix B
Acknowledgements

The work, which I was able to create was supported and aided by a lot of people, both from professional and private circles.

First, I want to thank my mother, Brigitte Buggle, since during all my life she encouraged me always to reach out for the next higher level. I would not be on this path without her.

I want to thank Prof. Dr. med. Kallfels and the medical teams of the cardiology of the Medizinische Hochschule Hannover. Without their medical skills, none of the things I did, I would be capable of even imagining.
I want to thank Dr. med. Harringer and again the medical teams of the cardioology of the Medizinische Hochschule Hannover. Without their help for a second time, I would probably not be here to write these lines.
Many die in this world for the lack of small things, so I want to express my thanks to the people of Germany, who paid for the survival of only one a high price. This thanks also includes the unknown person, whose death helped me to live. I hope, that with this thesis I could proof this investment not to be wasted.

I thank my supervisor Prof.Dr. J.T.M. Walraven for the honor and privilege having worked for his group for such a long time. His guidance was always friendly, professional and aiming for the best of the group. I learned very much about how to do proper, scientific work and keep the connection between theory and experiment.
I thank Dr. Kai Dieckmann, Dr. Igor Shvarchuck and all the postdocs, mentioned in the preface, for the excellent work they did on constructing the experiment. The high quality of the results, that I could acquire, stands testimony also to the quality of my predecessors work.
I thank Igor Shvarchuck, since it was a great pleasure working with such a joyful and at the same time skilled companion in the lab for 2 years. From him I learned 'the way, how the Russians won the space race'.
I thank Mark Kemmann for the work he did in the lab, in particular the reconstruction of the imaging optics. His quiet positivism and solid work made me expect a good working relationship. I deeply regret, that this talented man simply left the lab.
I thank Wolf von Klitzing for being an un-irritable source of good mood in the group, and the work he did in the analysis of all image data with Mathematica. No matter, how bad things would go in the lab, he would have some joyful remark about it. His input in terms of theoretical guidance and numerical analysis in particular with the hydrodynamic shape oscillation project was decisive for the progress of this thesis.
I thank Jeremi Léonard for his professionalism and joyful personality. He was member of the group only for a very short time, but made the most of it. His input was decisive for the speed of progress of the publication concerning the collision project, which influenced also the experimental progress.
I want to acknowledge Tobias Tiecke for the input in the TAP technique, that he

and Wolf von Klitzing prepared theoretically. However, had the reference [Tiec03] included the argumentations of section 4.3.1, and had the responsible authors not insisted on their own derivation in 2003, the date of this thesis would have been potentially earlier.

From the theoretical side I want to thank Dimitri Petrov, who not only had vital input in the collision and BEC focusing project, but was also always a quiet source of sharp minded advice.
I want to thank Paolo Pedri for his energetic and skilled help with the hydrodynamic oscillation project. After the state of the project analysis became evident, he offered the essential input to bring the project to a good end. It is worth mentioning, that he is a person, who puts his personal honor above authorship on a publication: just because the theory presented in reference [Bugg05] deviated from the measurements by 20%, it took me some persuasion to have him be second author.
I thank Carlos Lobo, who was my office neighbor after the group moved to the UVA, and Micha Baranov, who was next door. From them I received countless times good advice in smaller and greater calculations.

Scientific research, in particular with technologically advanced machinery like a BEC experiment, cannot succeed without the skills of the technicians, who design the instrumentation, and the quality of the results reflects the quality of the AMOLF technical support.
I want to thank Hinco Schoenmaker, who not only could make the most complicated metal pieces for any bizarre application appear after a few minutes. He also was a never-ending source of good mood, 'biertjes' and help in repairing my motorbike.
I want to thank Wim Brouwer, Henk Sodenkamp, Ilia Cerjak and all the personnel from the metal work shop for the design and machining of metal pieces of any structure, material and effort, that was slipped within minutes in the workshop pipeline. Without this kindness countless days would have been lost with waiting for the right piece.
I want to thank Duncan Verhijde, Idsard Attema, Henk Dekker and Ton Vijftigschild for their professional and swift help for the quite numerous electronic problems I came up with. Whatever electronics they designed or optimized from my hands, it would always work way better than it was meant to, even when it was soldered together by myself, which shows the high quality of their tutoring.
I want to thank Hans Alberda, Marco Konijnenburg and Sjourd Wouda for their sharp insight in programming, which was of great help when I did maintenance and expansion work on the experiment control hardware and software, which they had designed years before.
I want to thank the just mentioned people of electronics and programming for the construction of the DDS rf-evaporation source. The design was way ahead the common technology market and allowed experiments with unprecedented precision, whose value in particular for the quadrupole project cannot be underestimated.
I want to thank the people from the computer maintenance and network administration department, Richard Schaafsma, Rutger Schoone and Ben Onkhuizen. Their advice was always valuable, and in particular I have to thank for the one or two closed eyes, that were granted to me, to keep the somewhat unusual PC hardware and laboratory subnetwork running under my own supervision.

All of AMOLF I want to express my thanks, since the atmosphere is very special: a place where everyone is friendly to everyone, and everyone can be asked for help, with a near unit probability of receiving it. Both from the preference and also from the real time spent there, I considered AMOLF my home. From the administration I thank specially Roudy van der Wijk (who organized my very nice apartment) and Wouter Harmsen (who helped me with a lot of bureaucracy).
As we say in Germany: 'shared suffering is halved suffering' and without the collective suffering of all fellow PhD students together and mutual moral support (specially by Anna Tchebotareva and Denitza Lambreva) the pressure would have been unbearable. You are too many to list all the names, but you know, whom I mean.
Also at the UVA I found cool people to talk to, but the time had there, was too short to talk enough: still I want to thank for the time and words of nice people.

The time as a PhD student was dominated by lab-time, and the few friends I had in my private life, had to accept the usual answer 'too busy', so I am thankful that still so many had the patience and remembered, that I was still alive somewhere in the lab:
My bunch of Dutch friends, where I include Annemieke Petrignani-Taubes vast and lovely family, one fellow DJ (three-decks-Charlie) and two musicians (Junkbeat'ers), who are always in search of the DDS ('directe duitse sound'), my German bunch, who managed to lure me quite often out of the lab to the light 'Lux' or the valley 'Bloemendaal', the French, who more or less franco-formed me ('*les allemands ont le savoir faire, mais les français ont le savoir vivre!*'), my dear Spanish lady and the multinational bunch of AMOLF, who proved the belief, that scientists cannot party totally wrong.
All you guys are the most faithful and funny public, a part-time DJ like me could dream of.

Well, the time in the Netherlands was a time of unexpected things happening and outside of AMOLF it was in even more respects different. In particular, new years eve 2004 had a special surprise in store, delivered by certain parts of the Dutch society, which apparently is out of control, combined with the insight, that police and hospitals in this country operate differently than a German would expect. The 'Dutch experience' was so stunning, it will certainly keep ringing in my mind for all eternity.